

Neural Plasticity

# Brain Network Architecture and Plasticity: MR Neuroimaging Perspectives

Guest Editors: Feng Shi, Yong Liu, Shuyu Li, Xiaobo Li, and Martin Walter





---

# **Brain Network Architecture and Plasticity: MR Neuroimaging Perspectives**

Neural Plasticity

---

## **Brain Network Architecture and Plasticity: MR Neuroimaging Perspectives**

Guest Editors: Feng Shi, Yong Liu, Shuyu Li, Xiaobo Li,  
and Martin Walter



---

Copyright © 2016 Hindawi Publishing Corporation. All rights reserved.

This is a special issue published in “Neural Plasticity.” All articles are open access articles distributed under the Creative Commons Attribution License, which permits unrestricted use, distribution, and reproduction in any medium, provided the original work is properly cited.

---

## Editorial Board

Shimon Amir, Canada  
Michel Baudry, USA  
Michael S. Beattie, USA  
Clive R. Bramham, Norway  
Anna K. Braun, Germany  
Sumantra Chattarji, India  
Rajnish Chaturvedi, India  
Vincenzo De Paola, UK  
Michele Fornaro, USA  
Zygmunt Galdzicki, USA  
Preston E. Garraghty, USA

Anthony J. Hannan, Australia  
George W. Huntley, USA  
Alexandre H. Kihara, Brazil  
Jeansok J. Kim, USA  
Eric Klann, USA  
Malgorzata Kossut, Poland  
Stuart C. Mangel, USA  
Aage R. Møller, USA  
Diane K. O'Dowd, USA  
Martin Oudega, USA  
Maurizio Popoli, Italy

Bruno Poucet, France  
Timothy Schallert, USA  
Menahem Segal, Israel  
Panagiotis Smirniotis, USA  
Naweed I. Syed, Canada  
Christian Wozny, UK  
Chun-Fang Wu, USA  
Long-Jun Wu, USA  
James M. Wyss, USA  
Lin Xu, China

# Contents

## **Brain Network Architecture and Plasticity: MR Neuroimaging Perspectives**

Feng Shi, Yong Liu, Shuyu Li, Xiaobo Li, and Martin Walter

Volume 2016, Article ID 6952169, 2 pages

## **Topological Properties of Large-Scale Cortical Networks Based on Multiple Morphological Features in Amnesic Mild Cognitive Impairment**

Qionglin Li, Xinwei Li, Xuotong Wang, Yuxia Li, Kuncheng Li, Yang Yu, Changhao Yin, Shuyu Li, and Ying Han

Volume 2016, Article ID 3462309, 14 pages

## **State and Training Effects of Mindfulness Meditation on Brain Networks Reflect Neuronal Mechanisms of Its Antidepressant Effect**

Chuan-Chih Yang, Alfonso Barrós-Loscertales, Daniel Pinazo, Noelia Ventura-Campos, Viola Borchardt, Juan-Carlos Bustamante, Aina Rodríguez-Pujadas, Paola Fuentes-Claramonte, Raúl Balaguer, César Ávila, and Martin Walter

Volume 2016, Article ID 9504642, 14 pages

## **Multilevel Deficiency of White Matter Connectivity Networks in Alzheimer's Disease: A Diffusion MRI Study with DTI and HARDI Models**

Tao Wang, Feng Shi, Yan Jin, Pew-Thian Yap, Chong-Yaw Wee, Jianye Zhang, Cece Yang, Xia Li, Shifu Xiao, and Dinggang Shen

Volume 2016, Article ID 2947136, 14 pages

## **Node Detection Using High-Dimensional Fuzzy Parcellation Applied to the Insular Cortex**

Ugo Vercelli, Matteo Diano, Tommaso Costa, Andrea Nani, Sergio Duca, Giuliano Geminiani, Alessandro Vercelli, and Franco Cauda

Volume 2016, Article ID 1938292, 8 pages

## **Abnormal Resting-State Functional Connectivity Strength in Mild Cognitive Impairment and Its Conversion to Alzheimer's Disease**

Yuxia Li, Xiaoni Wang, Yongqiu Li, Yu Sun, Can Sheng, Hongyan Li, Xuanyu Li, Yang Yu, Guanqun Chen, Xiaochen Hu, Bin Jing, Defeng Wang, Kuncheng Li, Frank Jessen, Mingrui Xia, and Ying Han

Volume 2016, Article ID 4680972, 12 pages

## **The Exercising Brain: Changes in Functional Connectivity Induced by an Integrated Multimodal Cognitive and Whole-Body Coordination Training**

Traute Demirakca, Vita Cardinale, Sven Dehn, Matthias Ruf, and Gabriele Ende

Volume 2016, Article ID 8240894, 11 pages

## **Compensation through Functional Hyperconnectivity: A Longitudinal Connectome Assessment of Mild Traumatic Brain Injury**

Armin Iraj, Hanbo Chen, Natalie Wiseman, Robert D. Welch, Brian J. O'Neil, E. Mark Haacke, Tianming Liu, and Zhifeng Kou

Volume 2016, Article ID 4072402, 13 pages

## **Functional Reorganizations of Brain Network in Prelingually Deaf Adolescents**

Wenjing Li, Jianhong Li, Jieqiong Wang, Peng Zhou, Zhenchang Wang, Junfang Xian, and Huiguang He

Volume 2016, Article ID 9849087, 10 pages

**Closely Spaced MEG Source Localization and Functional Connectivity Analysis Using a New Prewhitening Invariance of Noise Space Algorithm**

Junpeng Zhang, Yuan Cui, Lihua Deng, Ling He, Junran Zhang, Jing Zhang, Qun Zhou, Qi Liu, and Zhiguo Zhang

Volume 2016, Article ID 4890497, 12 pages

**Reorganization of Anatomical Connectome following Electroconvulsive Therapy in Major Depressive Disorder**

Jinkun Zeng, Qinghua Luo, Lian Du, Wei Liao, Yongmei Li, Haixia Liu, Dan Liu, Yixiao Fu, Haitang Qiu, Xirong Li, Tian Qiu, and Huaqing Meng

Volume 2015, Article ID 271674, 8 pages

**Alterations of Regional Spontaneous Brain Activity and Gray Matter Volume in the Blind**

Aili Jiang, Jing Tian, Rui Li, Yong Liu, Tianzi Jiang, Wen Qin, and Chunshui Yu

Volume 2015, Article ID 141950, 12 pages

## Editorial

# Brain Network Architecture and Plasticity: MR Neuroimaging Perspectives

**Feng Shi,<sup>1</sup> Yong Liu,<sup>2</sup> Shuyu Li,<sup>3</sup> Xiaobo Li,<sup>4</sup> and Martin Walter<sup>5</sup>**

<sup>1</sup>*Department of Radiology and Biomedical Research Imaging Center, University of North Carolina at Chapel Hill, Chapel Hill, NC 27599, USA*

<sup>2</sup>*Brainnetome Center, Institute of Automation, Chinese Academy of Sciences, Beijing 100190, China*

<sup>3</sup>*School of Biological Science and Medical Engineering, Beihang University, Beijing 100191, China*

<sup>4</sup>*Department of Biomedical Engineering, New Jersey Institute of Technology, Newark, NJ 07102, USA*

<sup>5</sup>*Eberhard Karls University, 72074 Tübingen, Germany*

Correspondence should be addressed to Feng Shi; [fengshi@med.unc.edu](mailto:fengshi@med.unc.edu)

Received 14 March 2016; Accepted 14 March 2016

Copyright © 2016 Feng Shi et al. This is an open access article distributed under the Creative Commons Attribution License, which permits unrestricted use, distribution, and reproduction in any medium, provided the original work is properly cited.

Recent advances in brain connectivity research suggest that the human brain operates as a complex but economic global network. Novel approaches from graph theory have been applied to a variety of neuroimaging studies and have achieved great success. However, the brain network architecture and plasticity patterns vary across different brain developmental periods, learning activities, and disease effects. Translation of descriptive imaging levels into clinical and other exploitation crucially depends on the potential to induce and monitor plastic changes in the network of interest. This special issue is intended to stimulate the continuing efforts in understanding the architecture and plasticity patterns of brain networks. It also aims to broaden the attention not only to the researchers who are currently working on these areas but to the general scientific audience who are interested in the brain structures and functions as well.

This special issue includes eleven papers that presented an up-to-date progress of MR neuroimaging methods on brain network architecture and plasticity investigation employing various neuroimaging modalities: structural MRI, diffusion MRI, and functional MRI. In these papers, there are five studies focused on brain diseases, including Alzheimer's disease, mild cognitive impairment, mild traumatic brain injury, and major depressive disorder. Two studies investigated the brain plasticity changes after visual or hearing deprivations. Also, there are two studies that assessed volunteers after mediation

or cognitive training, and, finally, the remaining two studies are on the methodological development for brain network construction.

*Brain Diseases.* In the paper entitled "Abnormal Resting-State Functional Connectivity Strength in Mild Cognitive Impairment and Its Conversion to Alzheimer's Disease" by Y. Li et al., an investigation was performed for individuals diagnosed with mild cognitive impairment. With a 2-year follow-up, those individuals converted to Alzheimer's disease were compared with nonconverters for their alterations on functional connectivity strength and seed-based functional connections.

The paper entitled "Topological Properties of Large-Scale Cortical Networks Based on Multiple Morphological Features in Amnesic Mild Cognitive Impairment" by Q. Li et al. investigated the topological properties of cortical networks based on geometric measures (i.e., sulcal depth, curvature, and metric distortion) change in aMCI patients compared with normal controls.

The paper entitled "Multilevel Deficiency of White Matter Connectivity Networks in Alzheimer's Disease: A Diffusion MRI Study with DTI and HARDI Models" by T. Wang et al. conducted an evaluation of how the fiber tractography method could influence the construction of brain white matter network and eventually affect the extraction of brain

network properties, as well as group comparison using Alzheimer's disease patients as examples.

In the paper entitled "Compensation through Functional Hyperconnectivity: A Longitudinal Connectome Assessment of Mild Traumatic Brain Injury" by A. Iraj et al., patients with mild traumatic brain injury were studied for possible brain functional alterations. Brain functional network was constructed through predefined seeds in a 358-landmark mask and a groupwise clustering algorithm was employed to identify general patterns of functional hyperconnectivity.

The paper entitled "Reorganization of Anatomical Connectome following Electroconvulsive Therapy in Major Depressive Disorder" by J. Zeng et al. presented a study for patients with major depressive disorder that were treated by electroconvulsive therapy. The plasticity of white matter pathway was evaluated.

*Sensory Deprivation.* In the paper entitled "Alterations of Regional Spontaneous Brain Activity and Gray Matter Volume in the Blind" by A. Jiang et al., authors investigated how the early blindness shapes the regional spontaneous brain activity and gray matter volume in visual areas compared to sighted controls. A correlation analysis is also performed between the onset age of blindness and the brain structure and functions.

In the paper entitled "Functional Reorganizations of Brain Network in Prelingually Deaf Adolescents" by W. Li et al., authors used resting-state fMRI to study prelingually deaf adolescents to access the possible brain network reorganizations due to their experience.

*Training Influence.* The paper entitled "State and Training Effects of Mindfulness Meditation on Brain Networks Reflect Neuronal Mechanisms of Its Antidepressant Effect" by C.-C. Yang et al. designed a longitudinal analysis investigating resting-state fMRI both before and after 40 days of meditation training. Differences in functional connectivity both between states (rest versus meditation) and between timepoints (before versus after training) were assessed and reveal functional specificity of plastic reconfiguration of key networks implied in MDD.

The paper entitled "The Exercising Brain: Changes in Functional Connectivity Induced by an Integrated Multimodal Cognitive and Whole-Body Coordination Training" by T. Demirakca et al. investigated the impact of "life kinetic" training on brain plasticity in terms of an increased functional connectivity during resting-state functional magnetic resonance imaging (rs-fMRI). The training is an integrated multimodal training that combines motor and cognitive aspects and challenges the brain by introducing new and unfamiliar coordinative tasks.

*Methodology Development.* The paper entitled "Closely Spaced MEG Source Localization and Functional Connectivity Analysis Using a New Prewhitening Invariance of Noise Space Algorithm" by J. Zhang et al. proposed a prewhitening invariance of noise space as a new method for localizing closely spaced and highly correlated cortical sources under real magnetoencephalography (MEG) noise, to facilitate the source-level functional connectivity analysis.

The paper entitled "Node Detection Using High-Dimensional Fuzzy Parcellation Applied to the Insular Cortex" by U. Vercelli et al. investigated a fuzzy parcellation scheme that partitions insular cortex into a number of regions based on the variances of their functional signals. Furthermore, the identified 12 clusters located in the insular cortex are found to best correlate with distinct brain areas that subserve different brain circuits/functions.

## Acknowledgments

We would like to thank all authors for their contributions and the reviewers for their tremendous efforts in reviewing the manuscripts submitted in response to this special issue and providing constructive comments for the authors to improve their work. We are also grateful to the editorial board for providing us the great support in publishing this special issue.

Feng Shi  
Yong Liu  
Shuyu Li  
Xiaobo Li  
Martin Walter

## Research Article

# Topological Properties of Large-Scale Cortical Networks Based on Multiple Morphological Features in Amnestic Mild Cognitive Impairment

Qionglng Li,<sup>1</sup> Xinwei Li,<sup>1</sup> Xuotong Wang,<sup>1</sup> Yuxia Li,<sup>2,3,4</sup> Kuncheng Li,<sup>5</sup>  
Yang Yu,<sup>6</sup> Changhao Yin,<sup>6</sup> Shuyu Li,<sup>1</sup> and Ying Han<sup>2,3</sup>

<sup>1</sup>Key Laboratory for Biomechanics and Mechanobiology of Ministry of Education, School of Biological Science & Medical Engineering, Beihang University, Beijing 100191, China

<sup>2</sup>Center of Alzheimer's Disease, Beijing Institute for Brain Disorders, Beijing 100053, China

<sup>3</sup>Department of Neurology, Xuanwu Hospital, Capital Medical University, Beijing 100053, China

<sup>4</sup>Department of Neurology, Tangshan Gongren Hospital, Tangshan 063000, China

<sup>5</sup>Department of Radiology, Xuanwu Hospital, Capital Medical University, Beijing 100053, China

<sup>6</sup>Department of Neurology, Hongqi Hospital, Mudanjiang Medical University, Mudanjiang 157011, China

Correspondence should be addressed to Shuyu Li; [shuyuli@buaa.edu.cn](mailto:shuyuli@buaa.edu.cn) and Ying Han; [13621011941@163.com](mailto:13621011941@163.com)

Received 26 July 2015; Revised 20 December 2015; Accepted 30 December 2015

Academic Editor: Stuart C. Mangel

Copyright © 2016 Qionglng Li et al. This is an open access article distributed under the Creative Commons Attribution License, which permits unrestricted use, distribution, and reproduction in any medium, provided the original work is properly cited.

Previous studies have demonstrated that amnestic mild cognitive impairment (aMCI) has disrupted properties of large-scale cortical networks based on cortical thickness and gray matter volume. However, it is largely unknown whether the topological properties of cortical networks based on geometric measures (i.e., sulcal depth, curvature, and metric distortion) change in aMCI patients compared with normal controls because these geometric features of cerebral cortex may be related to its intrinsic connectivity. Here, we compare properties in cortical networks constructed by six different morphological features in 36 aMCI participants and 36 normal controls. Six cortical features (3 volumetric and 3 geometric features) were extracted for each participant, and brain abnormalities in aMCI were identified by cortical network based on graph theory method. All the cortical networks showed small-world properties. Regions showing significant differences mainly located in the medial temporal lobe and supramarginal and right inferior parietal lobe. In addition, we also found that the cortical networks constructed by cortical thickness and sulcal depth showed significant differences between the two groups. Our results indicated that geometric measure (i.e., sulcal depth) can be used to construct network to discriminate individuals with aMCI from controls besides volumetric measures.

## 1. Introduction

Mild cognitive impairment (MCI) is considered to be a transitional period between normal aging and Alzheimer's disease (AD), which is a progressive, neurodegenerative disease characterized by cognitive decline greater than expected for one's age and educational level yet not fulfilling the criteria of AD [1]. Amnestic MCI (aMCI), as the most common subtype of MCI, is characterized by primary memory impairments with single or multiple cognitive domains impaired and likely progresses to AD [2–4]. Current studies of aMCI have shown disrupted functional integration [5] and abnormal structural

connections between regions [6]. Morphological features have been widely used to characterize brain structures [7, 8] and also served as structural measures to investigate topological properties in large-scale cortical networks [9–11]. Previous studies on large-scale cortical network in MCI mostly used cortical thickness and gray matter volume as descriptors to construct structural network of the human cortex [12, 13].

However, different morphological features reveal different intrinsic properties of cerebral cortex. For example, volumetric measures (i.e., cortical thickness, gray matter volume) reflect the size, density, and arrangement of cells

(neurons, neuroglia, and nerve fibers) [14, 15], and surface area is linked to the number of mini columns in the cortical layer [16]. Using large-scale cortical network analysis based on cortical thickness, several studies have found disrupted small-world properties (i.e., lower clustering coefficient and shorter path length) in MCI patients compared to normal controls [13, 17, 18]. A cortical network study using surface area can reveal topological properties of the networks resulting from the concurrent changes between different anatomical regions [10]. In addition, geometric measures (i.e., sulcal depth, curvature, and metric distortion) mainly reflect cortical folding pattern [19–21]. For instance, sulcal depth and curvature measure specific aspects of the cortical geometry, and metric distortion is a wider measure of the overall degree of cortical folding [22]. These geometric measures related to cortical folding may vary with the changes of intrinsic as well as extrinsic connectivity according to the tension theory of the cerebral cortex morphogenesis [19] and could be more suitable descriptors for finding the anatomical-axonal and morphological connectivity correlation [10]. Thus, we assume that geometric measures can be used to construct cortical network that may detect the alterations from structural disconnection in aMCI and show different topological properties compared with volumetric measures (i.e., cortical thickness, gray matter volume, and surface area).

Here, we investigated topological properties of large-scale human cortical network based on graph theory analysis method by employing multiple morphological features in aMCI patients. Then we compared the topological properties of different cortical networks constructed by different morphological features. We expected that topological properties of cortical networks based on geometric measures in aMCI patients may be different from normal controls and can be used to discriminate individuals with aMCI from controls.

## 2. Materials and Methods

*2.1. Participants.* Seventy-two right-handed participants, including thirty-six aMCI and demography matched healthy normal controls, participated in this study. The aMCI participants were recruited from a clinical research program at Xuanwu Hospital, Beijing, China. The healthy normal controls were recruited from the local community through advertisements. This study was approved by the Research Ethics Review Board of Xuanwu Hospital, and written informed consent was obtained from each participant.

All the aMCI participants were identified according to the criteria for amnesic MCI [23–26], which included (a) memory complaint, preferably confirmed by an informant; (b) objective memory impairment, adjusted for age and education; (c) normal or near-normal performance on general cognitive functioning and no or minimum impairment of daily life activities; (d) the Clinical Dementia Rating (CDR) score of 0.5; and (e) not meeting the criteria for dementia according to the DSM-IV (Diagnostic and Statistical Manual of Mental Disorders, 4th Edition, revised). Participants with aMCI were diagnosed by experienced neurologists. Participants were excluded if they met the following clinical characteristics: (a) a clear history of stroke; (b) severe depression that led

TABLE I: Subject demographics.

	aMCI ( $n = 36$ )	Control ( $n = 36$ )	$p$ value
Gender (M/F)	14/22	15/21	0.813
Age	$66.0 \pm 8.7$ (50–83)	$63.9 \pm 6.1$ (56–79)	0.258
Education	$10.2 \pm 4.4$ (2–21)	$10.7 \pm 3.2$ (5–17)	0.651
MMSE	$24.4 \pm 3.2$ (17–30)	$28.1 \pm 1.7$ (20–30)	<0.001
MoCA	$20.6 \pm 3.7$ (15–27)	$26.4 \pm 2.4$ (18–30)	<0.001

Age, education, MMSE, and MoCA data are expressed as mean  $\pm$  SD (range). No significant differences were between two groups in gender, age, and education years. Groups for aMCI and NC showed significant differences in MMSE and MoCA scores ( $p < 0.01$ ). Statistical  $p$  value was analyzed using two-sample  $t$ -test, in which gender was converted into a virtual variable.

to mild cognitive impairment (Hamilton Depression Rating Scale score  $>24$  points); (c) other nervous system diseases, which can cause cognitive impairment (such as brain tumors, Parkinson’s disease, encephalitis, and epilepsy); (d) cognitive impairment caused by traumatic brain injury; (e) other systemic diseases, which can cause cognitive impairment, such as thyroid dysfunction, severe anemia, syphilis, and HIV; and (f) a history of psychosis or congenital mental growth retardation. Clinical and demographic data for the participants are shown in Table 1.

*2.2. MRI Data Acquisition.* MRI data acquisition was performed on a 3.0 T Siemens scanner by employing a sagittal magnetization-prepared rapid gradient echo (MP-RAGE) sequence with the following imaging parameters: repetition time ( $T_R$ ) = 1900 ms; echo time ( $T_E$ ) = 2.2 ms; inversion time = 900 ms; flip angle =  $90^\circ$ ; field of view (FOV) = 250 mm  $\times$  250 mm; matrix = 256 $\times$ 256; 176 slices, thickness = 1.0 mm. Brain MR images were inspected by an experienced neuroradiologist, and no gross abnormalities were observed for any subject.

*2.3. Cortical Reconstruction and Morphological Features Extraction.* Both the cortical reconstruction and morphological features extraction were obtained by using the FreeSurfer software (<http://surfer.nmr.mgh.harvard.edu/>) with a standard cortical automatic handling protocol. First, the data were normalized to a standard anatomical template [27] and corrected for bias-field inhomogeneity. Then the images were skull-stripped using a watershed algorithm [28] and subsequently segmented into subcortical white matter and deep gray matter volumetric structures [29, 30]. The initial tessellation was formed by reconstructing the gray matter/white matter boundary (white surface) and the outer cortical surface (pial surface) [31, 32]. Subsequently, a series of deformable procedures were performed, including surface inflation [31], registration to a spherical atlas [33], and parcellation of the cerebral cortex into units based on gyral and sulcal structures [30]. All reconstructed surfaces were visually inspected for gross-anatomical topological defects. Finally, a variety of morphological features at each vertex on the pial surface were computed, including volumetric

(cortical thickness, surface area, and GM volume) and geometric (sulcal depth, metric distortion, and mean curvature) measures, more details seen in this paper [34]. The thickness maps of both NC and aMCI groups are shown in Figure 1(a).

**2.4. Cortical Network Construction.** We employed a cortical scheme comprised of 148 regions from Destrieux Atlas. Cortical networks were built from partial correlation of interregional cortical morphological features. Prior to the correlation analysis, a linear regression was performed at every region to remove the effects of age, gender, and the total morphological feature value for each measure. And the resulting residuals were used to substitute for the raw morphological feature values. In this experimental design, the number of observations (participants,  $N = 36$ ) is smaller than the number of dependent variables (regions,  $P = 148$ ). “Small  $N$ , large  $P$ ” lead to inaccurate estimations of the covariance matrix [35]. A method based on the Ledoit-Wolf lemma was used to shrink the covariance estimates [36]. Finally, the partial correlation coefficients were computed with R software (<http://www.r-project.org/>). The partial correlation matrixes (adjacent matrix) of cortical networks constructed by thickness are shown in Figure 1(b).

The adjacent matrix was then binarized to an undirected and unweighted graph as shown in Figure 1(c) (at the sparsity of 5%) using a wide range of sparsity values (from 5% to 35%, step = 0.01). Sparsity of 5% meant that only the strongest 5% of the connections remained and 95% of the connectivity matrixes were removed. If the sparsity was less than 5%, the small-world properties were not estimable. And if the sparsity was greater than 35%, more noise would be included in the graph and it would be more like random network [37, 38]. The same sparsity range was applied for all network analyses.

**2.5. Graph Theoretical Characterization.** Graph theory is usually considered an attractive model for the mathematical treatment of cortical network connectivity [39]. In general, a complex network can be represented as a graph  $G$ , which consists of a set of nodes and a set of edges. Several important parameters of the graph  $G$  for the connectivity matrixes were estimated in this study.

Degree is the number of links connected to the node. Degree of a node “ $i$ ” is defined as

$$k_i = \sum_{j \in N} a_{ij}, \quad (1)$$

where  $N$  is the set of all nodes in the network;  $a_{ij}$  is the connection status between nodes “ $i$ ” and “ $j$ ” and  $a_{ij} = 1$  when link exists; otherwise  $a_{ij} = 0$ .

The clustering coefficient  $C_i$  of a node “ $i$ ” with degree  $k_i$  is defined as the ratio of the existing connections ( $e_i$ ) between the node’s neighbors and the maximum possible connections between neighbors of the node. The clustering coefficient of node “ $i$ ” is given as

$$C_i = \frac{2e_i}{k_i(k_i - 1)}. \quad (2)$$

The clustering coefficient is an index of local structure, while the clustering coefficient of the whole network is the average  $C_i$  over all nodes

$$C = \frac{1}{N} \sum_{i=1}^N C_i. \quad (3)$$

The shortest path length  $L_{i,j}$  between two nodes “ $i$ ” and “ $j$ ” of the graph  $G$  is the smallest number of edges that is required to connect “ $i$ ” and “ $j$ .” The shortest path length of a node “ $i$ ” can be calculated as the distance between a node “ $i$ ” and all other nodes [37]:

$$L_i = \frac{1}{N} \sum_{j=1, j \neq i}^N L_{i,j}. \quad (4)$$

The characteristic path length is defined as the mean of path length  $L_{i,j}$  over all pairs of nodes:

$$L = \frac{1}{N} \sum_{i=1}^N L_i. \quad (5)$$

The small-worldness network parameter  $\sigma$  is defined as those with small path length, like random network, and high clustering coefficient networks, much higher than random network. Small-world properties of a given network may be influenced by its intrinsic features, such as the number of nodes, edges, and the degree distribution. Thus, 1000 random networks were generated by using a random rewiring process [40], which preserves the number of nodes, mean degree, and degree distribution. This results in a normalized clustering coefficient  $\gamma = C_p/C_{\text{rand}} \gg 1$  and a normalized path length  $\lambda = L_p/L_{\text{rand}} \approx 1$ . Then a simple quantitative measurement of small-worldness  $\sigma$  is acquired [41]:

$$\sigma = \frac{\gamma}{\lambda}. \quad (6)$$

The real cortical network  $G$  is considered to be a small-world network if it meets the following criteria [37]:

$$\sigma = \frac{\gamma}{\lambda} > 1. \quad (7)$$

Betweenness centrality is a measure of network hubs that are crucial to efficient communication. BC is defined as the ratio of the number of shortest path passing through node “ $i$ ” to the total number of shortest paths between pairs of nodes “ $j$ ” and “ $k$ ”:

$$BC_i = \sum_{\substack{j, k \in N \\ j \neq k}} \frac{\rho_{j,k(i)}}{\rho_{j,k}}, \quad (8)$$

where  $\rho_{j,k}$  is the number of shortest paths between “ $j$ ” and “ $k$ ” and  $\rho_{j,k(i)}$  is the number of shortest path between “ $j$ ” and “ $k$ ” that passes through “ $i$ .” For further comparison, the betweenness  $BC_i$  would be normalized as  $bc_i = BC_i/BC$ , where  $BC$  is the average betweenness of the network. Cortex regions were defined as hubs, whose betweenness values were more than twice the average betweenness of the network ( $bc_i > 2$ ).

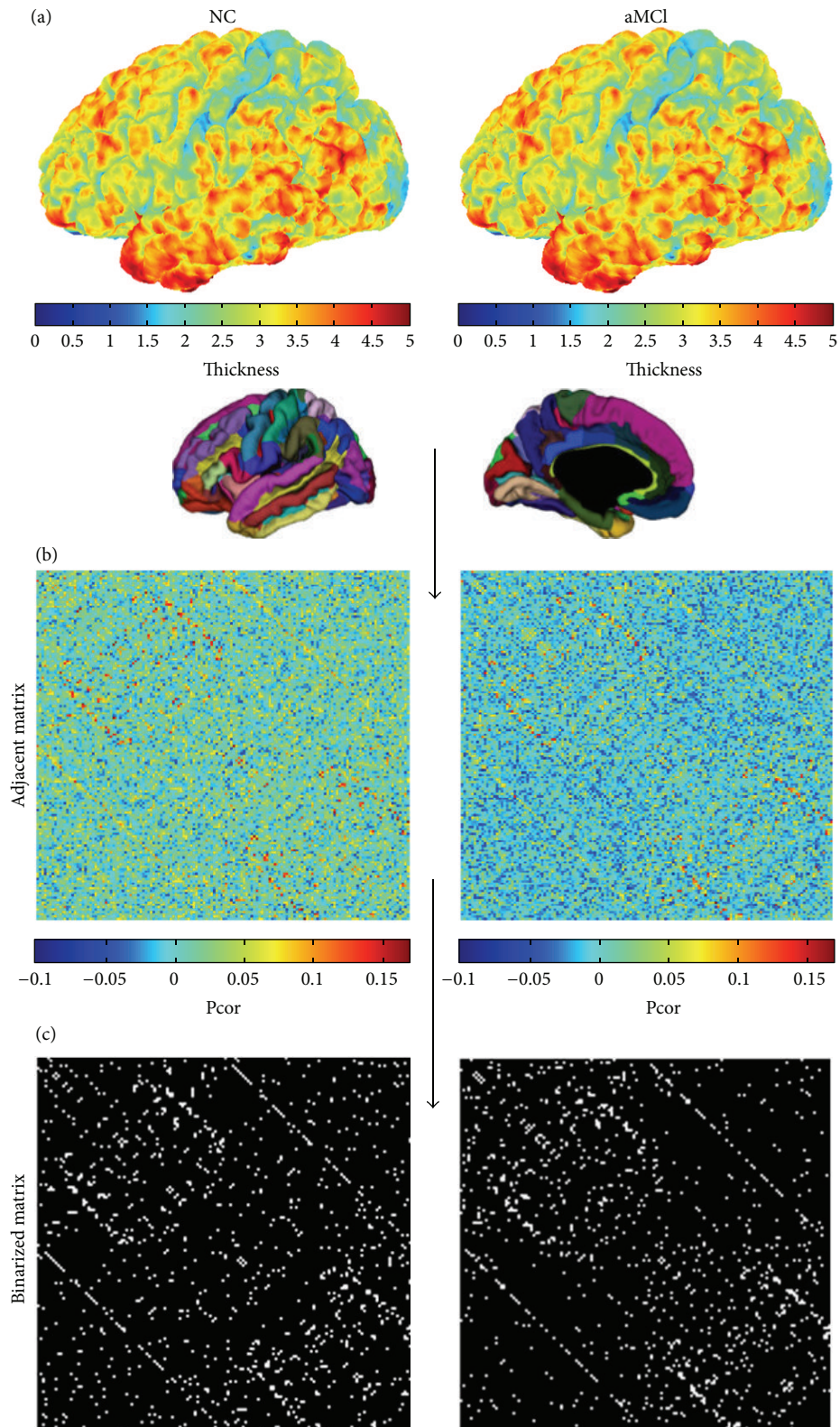


FIGURE 1: Flowchart for the construction of structural cortical networks. (a) Two representative cortical thickness maps (left for a control subject and right for an aMCI subject) were obtained from anatomical MRI. The color bar indicating the range of thickness is shown on the right. (b) The cortical thickness was mapped into 148 regions and the partial correlation matrices were obtained between regional thicknesses across subjects within each group (left for NC and right for aMCI). The color bar indicating the partial correlation coefficient between regions is shown on the right. (c) The correlation matrices of (b) were thresholded into the binarized matrices (left for NC and right for aMCI) by sparsity of 5%. NC, normal controls.

**2.6. Statistical Analysis.** Two-sample  $t$ -test was used to test the demographics, in which gender was converted into a virtual variable. To test the statistical significance of the between-group differences in the parameters of the cortical networks, a nonparametric permutation test was employed [42]. In this permutation test, we calculated possible values of the test statistic on a reference distribution after repeatedly rearranging the observed data from NC and aMCI groups. First, characteristics of the cortical network, such as  $C_p$ ,  $L_p$ , and  $bc_i$ , were calculated for NC and aMCI groups, respectively. Then NC and aMCI data were mixed. From the mixed data, the same number of subjects as aMCI patients was randomly chosen to be considered as aMCIs and the rest to be NCs. Next, partial correlation matrix for each randomized group was recalculated and corresponding binarized matrix was obtained using the same sparsity as in the real cortical networks. Third, network parameters for each randomized group were computed. This process was repeated 1000 times and the 95 percentile points of each distribution used as the critical values for a one-tailed procedure were repeated at every sparsity value of the cortical networks.

### 3. Results

**3.1. Demographics.** Two-sample  $t$ -test was used to test the demographics, in which gender was converted into a virtual variable, and results are shown in Table 1. There were no significant differences in gender, age, or years of education between aMCI and NC. Groups for aMCI and NC showed significant differences in MMSE and MoCA scores ( $p < 0.01$ ).

**3.2. Small-World Properties of Cortical Networks.** Compared with random networks, small-world networks had higher clustering coefficients and similar characteristic path length. Over a range of sparsity values ( $5\% \leq \text{sparsity} \leq 35\%$ ), clustering coefficient and characteristic path length were calculated for both the NC and aMCI networks based on different morphological features. The small-world attributes of the networks are shown in Figure 2. Compared with matched random networks which had the same number of nodes and degree distribution, all morphological networks had similarly characteristic path length ( $\lambda \approx 1$ ) and larger clustering coefficients ( $\gamma \gg 1$ ) in both NC and aMCI networks. Compared with NC, aMCI showed slightly larger small-world characteristics (larger  $\sigma$ ) in the cortical networks obtained for volumetric measures (cortical thickness and GM volume) and there were no great differences between NC and aMCI cortical networks based on surface area and geometric measures (mean curvature, metric distortion, and sulcal depth).

**3.3. Abnormal Changes in Nodal Betweenness Centrality.** As crucial components required for efficient communication in a network, hubs regulated information flow and played a key role in network resilience against attacks. To study the nodal characteristics, the cortical networks were constructed at certain sparsity of 11%. This sparsity ensured that all regions

were included in the cortical networks while minimizing the number of false-positive paths. Based on the results, some regions were identified as hubs in the cortical network of both the NC and aMCI groups. Details of the hub regions in the cortical networks are shown in Table 2.

In this study, the identified hub in networks based on volumetric measures, as shown in Figures 3(a) and 3(b), was involved in the frontal, temporal, parietal, and insula association cortex in the NC and temporal lobe, superior parietal lobule, cingulate cortex, precentral sulcus, callosum, and insula in the aMCI. High betweenness in network based on geometric measures was similar to volumetric measures. It was worth noting that hubs in networks using sulcal depth as descriptor included frontal polar, lingual sulcus, medial occipitotemporal sulcus, precentral sulcus, temporal gyrus (Heschl), and corpus callosum in NC group. And in aMCI group, regions included collateral sulcus, precentral sulcus, postcentral sulcus, temporal-occipital incisures, frontal gyrus, and corpus callosum (Figure 3(c)).

Permutation test was used to detect the significant differences in betweenness between NC and aMCI. Regions showing significant increase ( $p < 0.05$ ) in the betweenness of cortical networks using volumetric measures in aMCI patients included collateral sulcus, occipital gyrus, temporal gyrus, temporal pole, parietooccipital sulcus, postcentral gyrus, and subcallosal gyrus. And decreased betweenness ( $p < 0.05$ ) regions were located in subparietal sulcus, middle occipital gyrus, precuneus, and superior temporal sulcus as shown in Figures 4(a) and 4(b). Betweenness in inferior temporal gyrus, superior temporal gyrus, inferior frontal gyrus, and pericallosal sulcus showed significant increase ( $p < 0.05$ ) in network constructed by sulcal depth in aMCI patients. And betweenness in lateral sulcus, medial occipitotemporal sulcus, lateral occipitotemporal sulcus, cingulate sulcus, and short insular gyri significantly decreased ( $p < 0.05$ ).

#### 3.4. Comparing Networks from Different Morphological Features between Groups

**3.4.1. Volumetric Measures.** As shown in Figures 5(a) and 5(b), clustering coefficient and characteristic path length were higher in the structural cortical networks obtained from volumetric measures (both cortical thickness and GM volume) of aMCI. A permutation test was used to detect the between-group differences. The arrows indicated the significant differences between NC and aMCI in the clustering coefficient ( $p < 0.05$ ) of networks constructed by cortical thickness at the sparsity of 12% and 14% as shown in Figure 5(a). Significant differences in characteristic path length ( $p < 0.05$ ) of networks constructed by cortical thickness had been detected between NC and aMCI at the sparsity of 11%, 12%, and 14%. In the cortical networks obtained from GM volume, as shown in Figure 5(b), no significant differences were found in clustering coefficient between NC and aMCI ( $p > 0.05$ ). Only at the sparsity of 35% was a significant difference found in characteristic path length ( $p < 0.05$ ). Our findings provided further evidence for which networks constructed by cortical thickness had a small-world characteristic loss in aMCI.

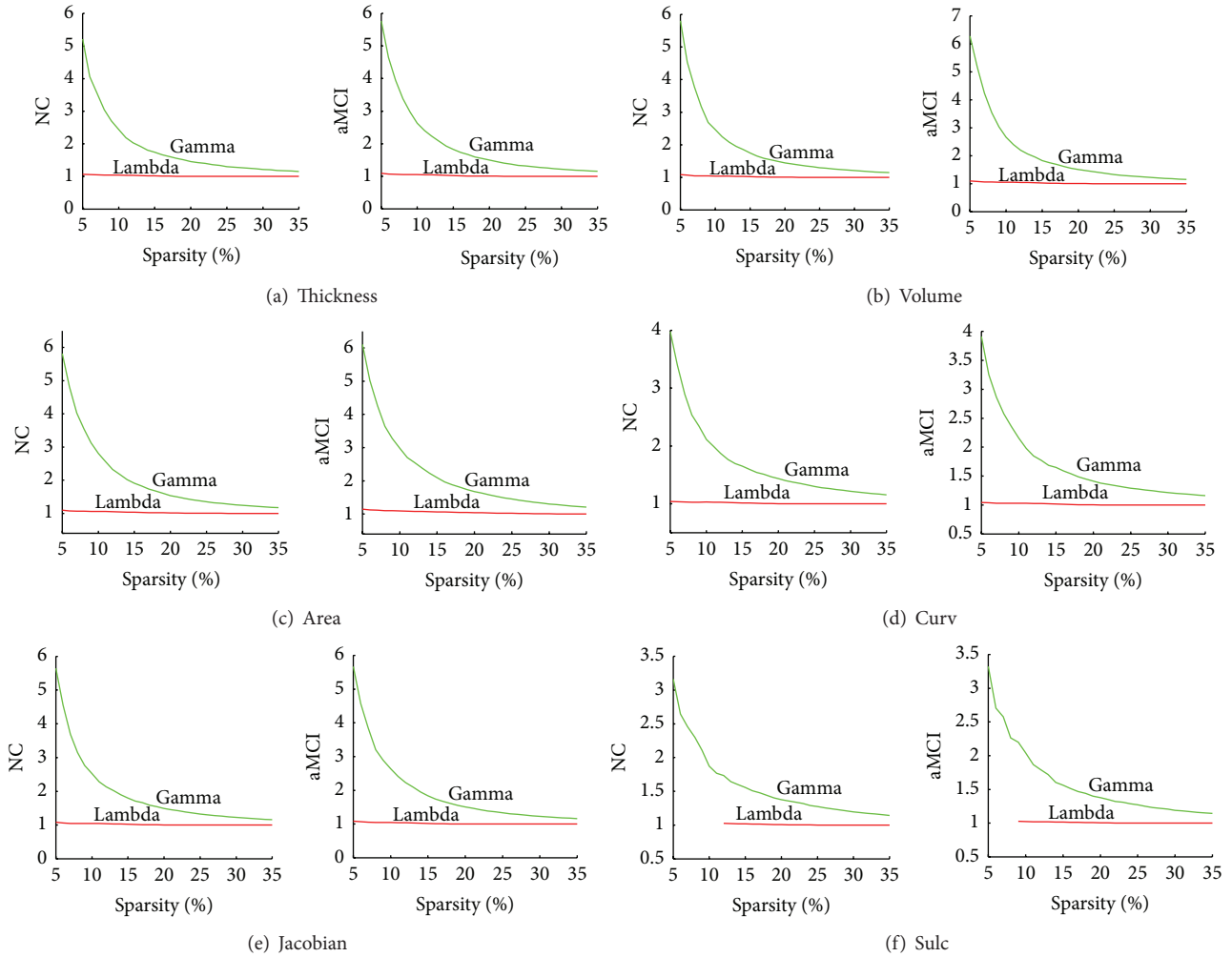


FIGURE 2: Small-world properties of volumetric measures networks and geometric measures networks. The graph shows the normalized characteristic path length ( $\lambda$ ,  $\lambda = L_p/L_{\text{rand}}$ ) and clustering coefficients ( $\gamma$ ,  $\gamma = C_p/C_{\text{rand}} \gg 1$ ) over a range of sparsity values ( $5\% \leq \text{sparsity} \leq 35\%$ ). All the networks have  $\gamma \gg 1$  (green lines) and  $\lambda \approx 1$  (red lines), which imply small-world properties. (a) The values of gamma and lambda in NC and aMCI of cortical thickness networks. (b) The values of gamma and lambda in NC and aMCI of GM volume networks. (c) The values of gamma and lambda in NC and aMCI of surface area networks. (d) The values of gamma and lambda in NC and aMCI of mean curvature networks. (e) The values of gamma and lambda in NC and aMCI of metric distortion (Jacobian) networks. (f) The values of gamma and lambda in NC and aMCI of sulcal depth networks. Thickness, cortical thickness. Volume, gray matter volume. Area, surface area. Curv, mean curvature. Sulc, sulcal depth. NC, normal controls.

In Figure 5(c), the clustering coefficient and characteristic path length were much larger for aMCI in cortical network using surface area as descriptor. However, no significant differences ( $p > 0.05$ ) were found in all permutation tests for small-world properties of cortical network based on surface area.

**3.4.2. Geometric Measures.** Small-world properties of cortical network using sulcal depth were very similar to properties in network using thickness for both NC and aMCI. As shown in Figure 5(f), the clustering coefficient was higher for aMCI, and the characteristic path length had no much difference between aMCI and NC. Statistical analysis further revealed significant differences in the clustering coefficient ( $p < 0.05$ ) at  $9\% \leq \text{sparsity} \leq 11\%$ ,  $\text{sparsity} = 13\%$ ,  $16\%$ , and  $18\%$ , and

$\text{sparsity} = 24\%$  and  $25\%$ . Significant differences were found in the characteristic path length between NC and aMCI at the range of sparsity values ( $\text{sparsity} = 25\%$  and  $30\% \leq \text{sparsity} \leq 33\%$ ).

In Figure 5(e), small-world properties analysis using metric distortion as a descriptor showed similar results to properties in network based on cortical thickness. As shown in Figure 5(e), the clustering coefficient was larger for the aMCI compared with NC subjects. What is more, the characteristic path length had no much difference between NC and aMCI. However, statistical analysis revealed no significant differences ( $p > 0.05$ ) in all the topological parameters over the whole range of sparsity values. Similar to metric distortion, no significant differences were found when using mean curvature as descriptor in cortical network ( $p > 0.05$ ).

TABLE 2: The abbreviations of Destrieux Atlas.

Index	Long name	Abbreviations
1	Frontomarginal gyrus (of Wernicke) and sulcus	GSF
2	Inferior occipital gyrus (O3) and sulcus	GSOI
3	Paracentral lobule and sulcus	GSP
4	Subcentral gyrus (central operculum) and sulci	GSS
5	Transverse frontopolar gyri and sulci	GSTF
6	Anterior part of the cingulate gyrus and sulcus (ACC)	GSCA
7	Middle-anterior part of the cingulate gyrus and sulcus (aMCC)	GSCMA
8	Middle-posterior part of the cingulate gyrus and sulcus (pMCC)	GSCMP
9	Posterior-dorsal part of the cingulate gyrus (dPCC)	GCPD
10	Posterior-ventral part of the cingulate gyrus (vPCC, isthmus of the cingulate gyrus)	GCPV
11	Cuneus (O6)	GC
12	Opercular part of the inferior frontal gyrus	GFIOper
13	Orbital part of the inferior frontal gyrus	GFIOrb
14	Triangular part of the inferior frontal gyrus	GFIT
15	Middle frontal gyrus (F2)	GFM
16	Superior frontal gyrus (F1)	GFS
17	Long insular gyrus and central sulcus of the insula	GILSCI
18	Short insular gyri	GIS
19	Middle occipital gyrus (O2, lateral occipital gyrus)	GOM
20	Superior occipital gyrus (O1)	GOS
21	Lateral occipitotemporal gyrus (fusiform gyrus, O4-T4)	GOTLF
22	Lingual gyrus, lingual part of the medial occipitotemporal gyrus (O5)	GOTML
23	Parahippocampal gyrus, parahippocampal part of the medial occipitotemporal gyrus (T5)	GOTMP
24	Orbital gyri	GO
25	Angular gyrus	GPIA
26	Supramarginal gyrus	GPIS
27	Superior parietal lobule (lateral part of P1)	GPS
28	Postcentral gyrus	GPost
29	Precentral gyrus	GPCen
30	Precuneus (medial part of P1)	GPCun
31	Straight gyrus, gyrus rectus	GR
32	Subcallosal area, subcallosal gyrus	GS
33	Anterior transverse temporal gyrus (of Heschl)	GTSGTT
34	Lateral aspect of the superior temporal gyrus	GTSL
35	Planum polare of the superior temporal gyrus	GTSPP
36	Planum temporale or temporal plane of the superior temporal gyrus	GTSPPT
37	Inferior temporal gyrus (T3)	GTI
38	Middle temporal gyrus (T2)	GTM
39	Horizontal ramus of the anterior segment of the lateral sulcus (or fissure)	LFAH
40	Vertical ramus of the anterior segment of the lateral sulcus (or fissure)	LFAV
41	Posterior ramus (or segment) of the lateral sulcus (or fissure)	LFP
42	Occipital pole	PO
43	Temporal pole	PT
44	Calcarine sulcus	SCal
45	Central sulcus (Rolando's fissure)	SCen
46	Marginal branch (or part) of the cingulate sulcus	SCM
47	Anterior segment of the circular sulcus of the insula	SCIA
48	Inferior segment of the circular sulcus of the insula	SCII
49	Superior segment of the circular sulcus of the insula	SCIS
50	Anterior transverse collateral sulcus	SCTA

TABLE 2: Continued.

Index	Long name	Abbreviations
51	Posterior transverse collateral sulcus	SCTP
52	Inferior frontal sulcus	SFI
53	Middle frontal sulcus	SFM
54	Superior frontal sulcus	SFS
55	Sulcus intermedius primus (of Jensen)	SIPJ
56	Intraparietal sulcus (interparietal sulcus) and transverse parietal sulci	SIPT
57	Middle occipital sulcus and lunatus sulcus	SOML
58	Superior occipital sulcus and transverse occipital sulcus	SOST
59	Anterior occipital sulcus and preoccipital notch (temporooccipital incisure)	SOA
60	Lateral occipitotemporal sulcus	SOTL
61	Medial occipitotemporal sulcus (collateral sulcus) and lingual sulcus	SOTML
62	Lateral orbital sulcus	SOL
63	Medial orbital sulcus (olfactory sulcus)	SOMO
64	Orbital sulci (H-shaped sulci)	SOHS
65	Parietooccipital sulcus (or fissure)	SPO
66	Pericallosal sulcus (S of corpus callosum)	SPer
67	Postcentral sulcus	SPost
68	Inferior part of the precentral sulcus	SPIP
69	Superior part of the precentral sulcus	SPSP
70	Suborbital sulcus (sulcus rostrales, supraorbital sulcus)	SSO
71	Subparietal sulcus	SSP
72	Inferior temporal sulcus	STI
73	Superior temporal sulcus (parallel sulcus)	STS
74	Transverse temporal sulcus	STT

#### 4. Discussion

In this study, we explored the properties of large-scale human brain cortical networks using multiple morphological features (including 3 volumetric measures, cortical thickness, surface area, and gray matter volume, and 3 geometric measures, sulcal depth, metric distortion, and mean curvature) based on graph theory analysis in cognitively normal older adults and amnesic mild cognitive impairment (aMCI) patients. We found that all networks constructed by these morphological features showed small-world properties which implied high efficiency of information transformation in human cognition. Properties in networks constructed by cortical thickness and sulcal depth showed significant differences between NC and aMCI patients. Besides, regions showing significant differences mainly located in the medial temporal lobe and supramarginal and right inferior parietal lobe. Our results indicated that geometric measure (i.e., sulcal depth) can be used to construct network to discriminate individuals with aMCI from controls besides volumetric measures and provided new insights into the study of the pathophysiological mechanism of amnesic MCI.

Previous studies have demonstrated that the cortical thickness and GM volume can be used as morphological descriptors to study the complex cortical networks, and networks based on the cortical thickness and GM volume followed the small-world properties [10–12, 43, 44]. Similar

to previous studies, networks based on volumetric measures showed altered small-world properties (i.e., increased clustering coefficient and path length) in aMCI patients compared with NC subjects. Short path length and high clustering coefficient in cortical network mean effective and rapid transfers of information between and across remote regions that are believed to constitute the basis of cognitive processes. Large  $\sigma$  means an optimal balance between local specialization and global integration. The cortical thickness changes are related to myelination of gray matter or the underlying white matter, as we know damage of myelin sheath is often associated with decreased functional efficiency. Here, we found longer path length and higher clustering coefficient in aMCI that may indicate a disturbance of the normal balance [45].

Consistent with the volumetric measures, all networks based on geometric measures also followed the small-world properties but less optimal small-worldness in aMCI network, while properties in network constructed by sulcal depth showed much more significant differences between NC and aMCI patients compared with properties in networks based on other geometric measures through a range of sparsity values. Previous studies have demonstrated that geometric differences are predominantly linked with the development of neuronal connections and cortical pattern of connectivity [19, 46] and are thus a marker for cerebral development or abnormal cortical connectivity due to disorders.

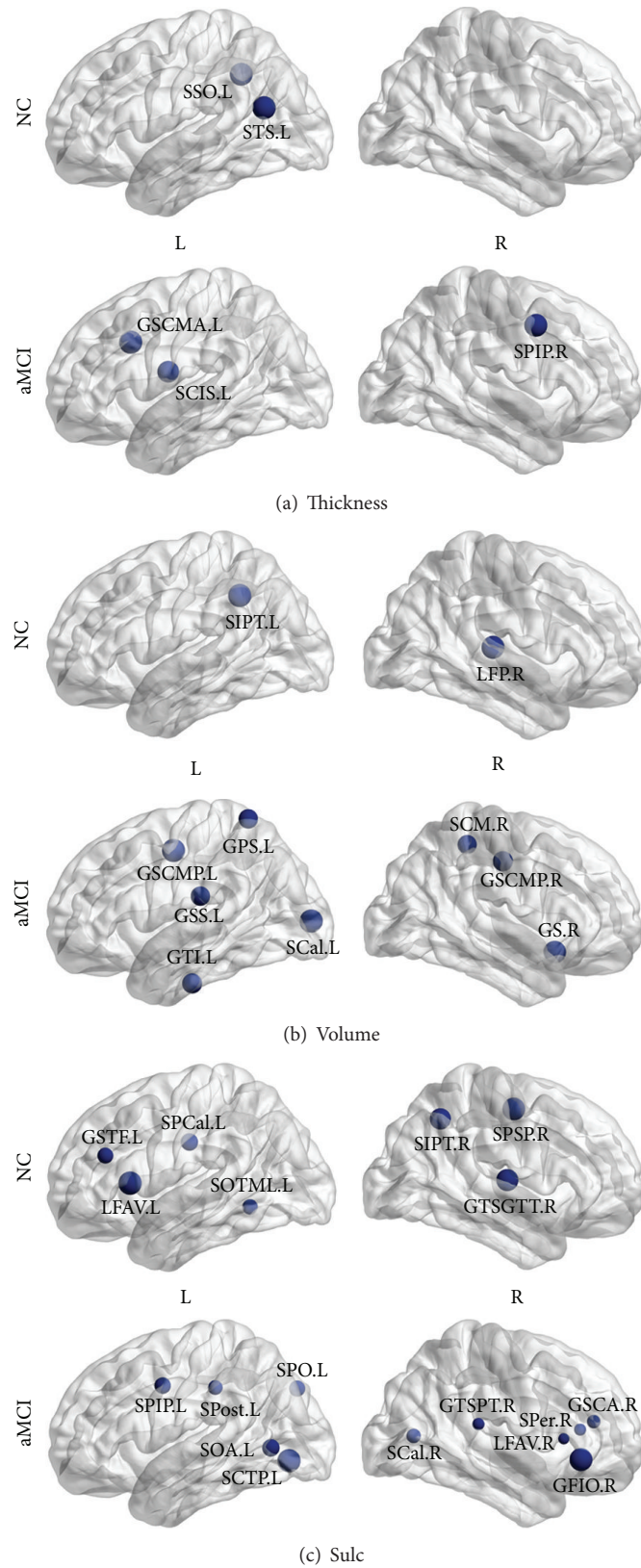


FIGURE 3: Hubs regions in cortical networks. Global hub regions derived from normalized nodal betweenness centrality in NC and amCI. The blue spheres indicate the global hubs whose betweenness is more than twice the average betweenness of the network. (a) Global hubs in cortical thickness networks. (b) Global hubs in gray matter volume networks. (c) Global hubs in sulcal depth networks. Thickness, cortical thickness. Volume, gray matter volume. NC, normal controls. For the abbreviations of regions, see Table 2.

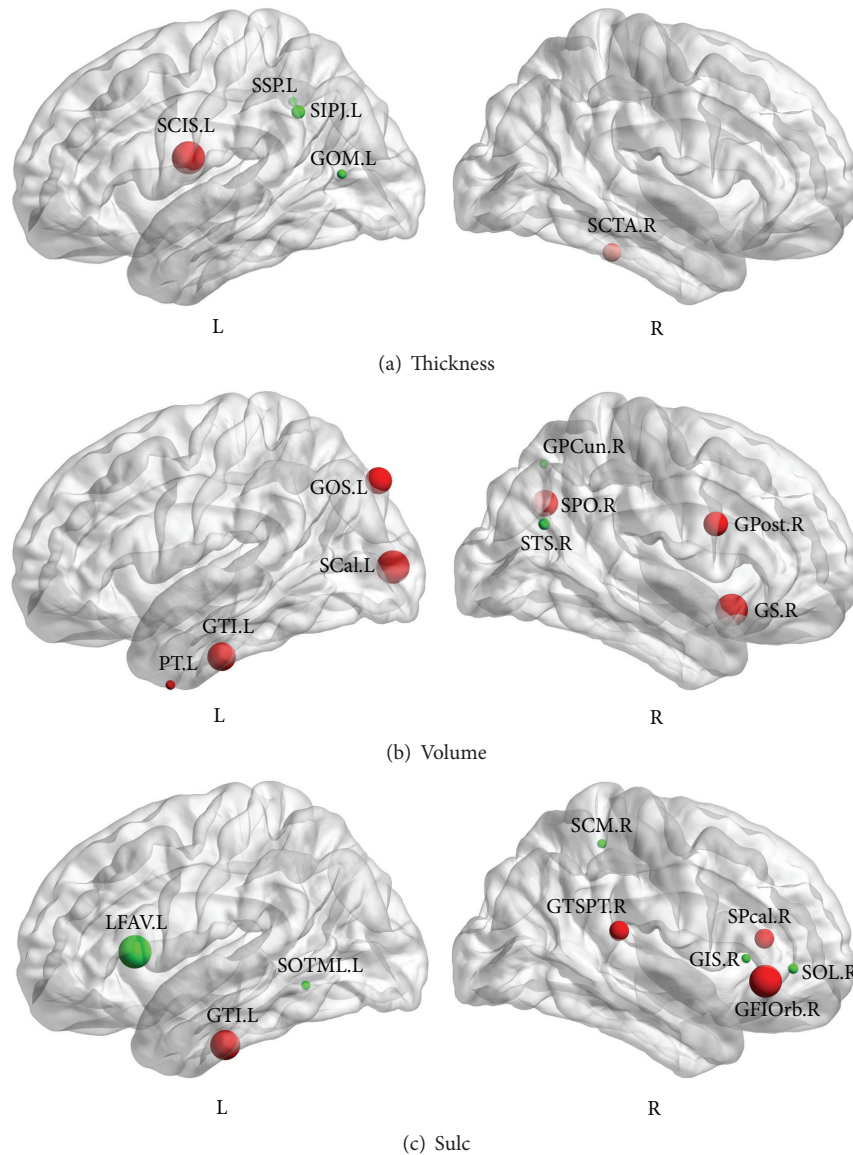


FIGURE 4: Abnormal changes in nodal betweenness centrality. The graph shows significant difference ( $p < 0.05$ ) in betweenness between two groups. The green spheres indicate significant decreases in between-group nodal centrality. The red spheres indicate significant increases in between-group nodal centrality. (a) Abnormal changes in cortical thickness networks. (b) Abnormal changes in gray matter volume networks. (c) Abnormal changes in sulcal depth networks. Thickness, cortical thickness. Volume, gray matter volume. NC, normal controls. For the abbreviations of regions, see Table 2.

Here networks constructed by sulcal depth in aMCI with less optimal small-worldness implied abnormal structural connections between specific regions in aMCI patients.

Previous studies indicated that hubs were mainly in regions of the parietal, temporal, and frontal heteromodal association cortex (SPL, SMG, MTG, STG, IFG, and SFG) and highly connected primary motor cortex (PrCG) [45]. Hubs in this study were predominately in frontal, temporal, parietal, and insula association cortex in NC of networks based on volumetric measures. Many previous studies ignore the insula when constructing cortical network because the insula is covered by other lobes. Compared with NC, there were more hubs in aMCI involved in temporal lobe, superior

parietal lobe, cingulate cortex, precentral sulcus, callosum, and insula. In networks based on sulcal depth, hub regions in NC were compatible with previous studies of functional and structural cortical network [47]. These hub regions, which are considered to be the substrates of human cognition and consciousness, are in the association cortex that receives convergent inputs from multiple other cortical regions [12]. And in networks based on sulcal depth, hub regions in aMCI had more hubs compared with NC, which was similar to regions in networks based on volumetric measures.

Evidences from previous studies have shown the shrunk brain regions in aMCI patients located in parahippocampal gyrus, medial temporal lobe, entorhinal cortex, cingulum,

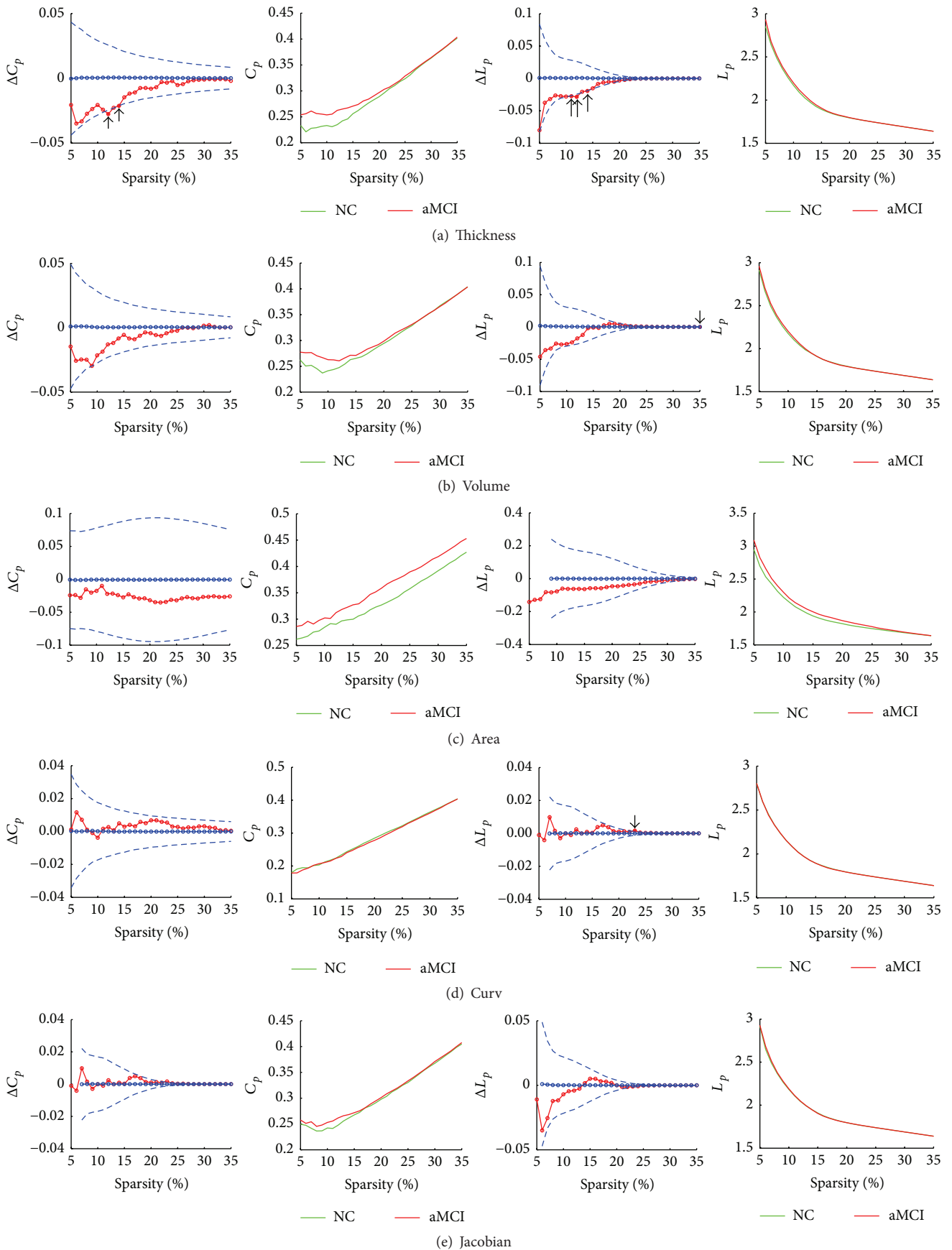


FIGURE 5: Continued.

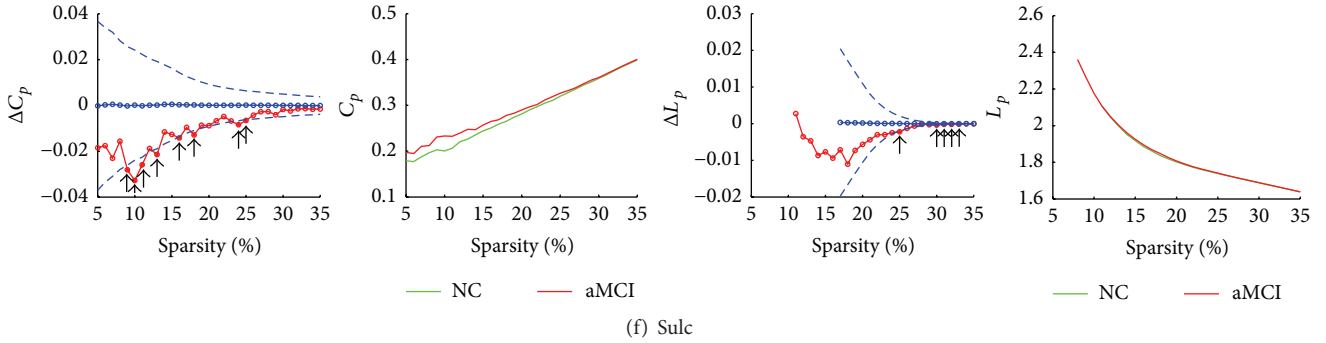


FIGURE 5: Between-group differences in clustering coefficient ( $C_p$ ) and characteristic path length ( $L_p$ ) of different morphological features based networks. The graph shows the differences in  $C_p$  and  $L_p$  between NC and aMCI as a function of sparsity of geometric measures networks. The blue lines represent the mean values (open circles) and 95% confidence intervals of the between-group differences obtained from 1000 permutation tests at each sparsity value. The arrows indicate significant ( $p < 0.05$ ) difference in  $C_p$  or  $L_p$  between the two groups. (a) Between-group differences in  $C_p$  and  $L_p$  as a function of sparsity of cortical thickness networks. (b) Between-group differences in  $C_p$  and  $L_p$  as a function of sparsity of gray matter volume networks. (c) Between-group differences in  $C_p$  and  $L_p$  as a function of sparsity of surface area networks. (d) Between-group differences in  $C_p$  and  $L_p$  as a function of sparsity of mean curvature networks. (e) Between-group differences in  $C_p$  and  $L_p$  as a function of sparsity of metric distortion (Jacobian) networks. (f) Between-group differences in  $C_p$  and  $L_p$  as a function of sparsity of sulcal depth networks. Thickness, cortical thickness. Volume, gray matter volume. Area, surface area. Curv, mean curvature. Sulc, sulcal depth. NC, normal controls.

insula, and thalamus [48, 49]. Our results were partially consistent with previous studies. Abnormal changes in the temporal, occipital gyrus and cingulate sulcus in aMCI group have been reported as being related to memory performance. What is more, significantly higher nodal centrality in aMCI was considered as increased functional connectivity occurred in various brain regions [50]. This may serve as a compensatory mechanism that enables patients with aMCI to use other additional resources to maintain normal cognitive performance [51, 52]. The abnormal characteristics of the cortical networks observed in aMCI may reflect anatomical structural abnormalities. Our findings may contribute to an understanding of the cerebral organization in aMCI.

Some limitations should be addressed in the future. Firstly, several studies have demonstrated that network resolution has an effect on topological properties of human neocortex by using volumetric measures as descriptors of anatomical connectivity [10, 53, 54]. In our network analysis, we only used 148 nodes to construct the network. In the future, it is interesting to investigate the relationship between network resolution and topological properties of human neocortex by using geometric measures. Secondly, topological properties of a given network may be influenced by intrinsic features of that network, such as the number of nodes, number of connections, and degree distribution. To counteract these effects, we used random networks with the same number of nodes and edges as surrogates to normalize the corresponding graph measures. Without any correction, the small-world index cannot be used to compare the small-worldness of different empirical networks. However, random surrogates may increase the sensitivity to differences in nodes number and degrees for the commonly used small-world index [55]. The minimum spanning tree (MST) [56],

a mathematically defined and unbiased subnetwork, provides similar information about network topology as conventional graph measures. It is noted that the MST discards all loop connections that the clustering coefficient and path length in the small-world index are highly correlated. Several network characteristics such as modularity, hierarchy, and rich club cannot be interpreted with the MST. There is still no optimal method to normalize network measures. Thirdly, different thresholding may lead to different network topological organizations [47]. Notably, connectivity values often vary depending on subjects and conditions, which can result in differences in average degree when using the same threshold for all networks. In the future, it is important to study the optimal thresholding methods in constructing networks.

## 5. Conclusions

This work demonstrated that besides cortical thickness and gray matter volume, sulcal depth can also be used to study the topological properties of cortical networks. We found that networks based on both the volumetric measures and geometric measures showed small-world properties and properties in these networks were different from aMCI to NC. Notably, properties in cortical network constructed by sulcal depth showed significant differences between the two groups. Our results indicate that geometric measure (sulcal depth) can be used to construct network to discriminate individuals with aMCI from controls.

## Conflict of Interests

The authors declare that there is no conflict of interests regarding the publication of this paper.

## Acknowledgments

This work was supported by the National Natural Science Foundation of China (Grants nos. 31371007, 81430037, 81171403, 81301188, and 81471731), Beijing Municipal Science & Technology Commission (Grant no. Z131100006813022), Kallikrein Medical Research Program (Grant no. 201206006), and the National Key Department of Neurology funded by Chinese Health and Family Planning Committee.

## References

- [1] C. A. Luis, D. A. Loewenstein, A. Acevedo, W. W. Barker, and R. Duara, "Mild cognitive impairment: directions for future research," *Neurology*, vol. 61, no. 4, pp. 438–444, 2003.
- [2] R. C. Petersen, R. O. Roberts, D. S. Knopman et al., "Mild cognitive impairment: ten years later," *Archives of Neurology*, vol. 66, no. 12, pp. 1447–1455, 2009.
- [3] L. R. Clark, L. Delano-Wood, D. J. Libon et al., "Are empirically-derived subtypes of mild cognitive impairment consistent with conventional subtypes?" *Journal of the International Neuropsychological Society*, vol. 19, no. 6, pp. 635–645, 2013.
- [4] R. C. Petersen, J. E. Parisi, D. W. Dickson et al., "Neuropathologic features of amnesic mild cognitive impairment," *Archives of Neurology*, vol. 63, no. 5, pp. 665–672, 2006.
- [5] L. Wang, H. Li, Y. Liang et al., "Amnesic mild cognitive impairment: topological reorganization of the default-mode network," *Radiology*, vol. 268, no. 2, pp. 501–514, 2013.
- [6] N. Shu, Y. Liang, H. Li et al., "Disrupted topological organization in white matter structural networks in amnesic mild cognitive impairment: relationship to subtype," *Radiology*, vol. 265, no. 2, pp. 518–527, 2012.
- [7] R. A. Barton and P. H. Harvey, "Mosaic evolution of brain structure in mammals," *Nature*, vol. 405, no. 6790, pp. 1055–1058, 2000.
- [8] D. A. Clark, P. P. Mitra, and S. S.-H. Wang, "Scalable architecture in mammalian brains," *Nature*, vol. 411, no. 6834, pp. 189–193, 2001.
- [9] Y. He, Z. J. Chen, and A. C. Evans, "Small-world anatomical networks in the human brain revealed by cortical thickness from MRI," *Cerebral Cortex*, vol. 17, no. 10, pp. 2407–2419, 2007.
- [10] G. Sanabria-Diaz, L. Melie-García, Y. Iturria-Medina et al., "Surface area and cortical thickness descriptors reveal different attributes of the structural human brain networks," *NeuroImage*, vol. 50, no. 4, pp. 1497–1510, 2010.
- [11] B. M. Tijms, C. Möller, H. Vrenken et al., "Single-subject grey matter graphs in Alzheimer's disease," *PLoS ONE*, vol. 8, no. 3, Article ID e58921, 2013.
- [12] Z. Yao, Y. Zhang, L. Lin et al., "Abnormal cortical networks in mild cognitive impairment and Alzheimer's disease," *PLoS Computational Biology*, vol. 6, no. 11, Article ID e1001006, 2010.
- [13] Y. Zhou and Y. W. Lui, "Small-world properties in mild cognitive impairment and early Alzheimer's disease: a cortical thickness MRI study," *ISRN Geriatrics*, vol. 2013, Article ID 542080, 11 pages, 2013.
- [14] A. Parent, *Carpenter's Human Neuroanatomy*, Lippincott Williams & Wilkins, 1996.
- [15] K. L. Narr, R. M. Bilder, A. W. Toga et al., "Mapping cortical thickness and gray matter concentration in first episode schizophrenia," *Cerebral Cortex*, vol. 15, no. 6, pp. 708–719, 2005.
- [16] P. Rakic, "Defects of neuronal migration and the pathogenesis of cortical malformations," *Progress in Brain Research*, vol. 73, pp. 15–37, 1988.
- [17] A. C. Burggren, B. Renner, M. Jones et al., "Thickness in entorhinal and subicular cortex predicts episodic memory decline in mild cognitive impairment," *International Journal of Alzheimer's Disease*, vol. 2011, Article ID 956053, 9 pages, 2011.
- [18] L. Wang, F. C. Goldstein, E. Veledar et al., "Alterations in cortical thickness and white matter integrity in mild cognitive impairment measured by whole-brain cortical thickness mapping and diffusion tensor imaging," *American Journal of Neuroradiology*, vol. 30, no. 5, pp. 893–899, 2009.
- [19] D. C. Van Essen, "A tension-based theory of morphogenesis and compact wiring in the central nervous system," *Nature*, vol. 385, no. 6614, pp. 313–318, 1997.
- [20] G. Lohmann, D. Y. Von Cramon, and A. C. F. Colchester, "Deep sulcal landmarks provide an organizing framework for human cortical folding," *Cerebral Cortex*, vol. 18, no. 6, pp. 1415–1420, 2008.
- [21] A. Cachia, J.-F. Mangin, D. Rivière et al., "A primal sketch of the cortex mean curvature: a morphogenesis based approach to study the variability of the folding patterns," *IEEE Transactions on Medical Imaging*, vol. 22, no. 6, pp. 754–765, 2003.
- [22] C. Ecker, A. Marquand, J. Mourão-Miranda et al., "Describing the brain in autism in five dimensions—magnetic resonance imaging-assisted diagnosis of autism spectrum disorder using a multiparameter classification approach," *The Journal of Neuroscience*, vol. 30, no. 32, pp. 10612–10623, 2010.
- [23] R. C. Petersen, R. Doody, A. Kurz et al., "Current concepts in mild cognitive impairment," *Archives of Neurology*, vol. 58, no. 12, pp. 1985–1992, 2001.
- [24] R. C. Petersen, G. E. Smith, S. C. Waring, R. J. Ivnik, E. G. Tangalos, and E. Kokmen, "Mild cognitive impairment: clinical characterization and outcome," *Archives of Neurology*, vol. 56, no. 3, pp. 303–308, 1999.
- [25] R. Petersen, J. Stevens, M. Ganguli, E. Tangalos, J. Cummings, and S. DeKosky, "Practice parameter: early detection of dementia: mild cognitive impairment (an evidence-based review) report of the quality standards subcommittee of the american academy of neurology," *Neurology*, vol. 56, no. 9, pp. 1133–1142, 2001.
- [26] R. Petersen, *Mild Cognitive Impairment: Aging to Alzheimer's Disease*, Oxford University Press, New York, NY, USA, 2003.
- [27] J. Talairach and P. Tournoux, *Co-Planar Stereotaxic Atlas of the Human Brain. 3-Dimensional Proportional System: An Approach to Cerebral Imaging*, 1988.
- [28] F. Ségonne, A. M. Dale, E. Buxa et al., "A hybrid approach to the skull stripping problem in MRI," *NeuroImage*, vol. 22, no. 3, pp. 1060–1075, 2004.
- [29] B. Fischl, D. H. Salat, E. Buxa et al., "Whole brain segmentation: automated labeling of neuroanatomical structures in the human brain," *Neuron*, vol. 33, no. 3, pp. 341–355, 2002.
- [30] B. Fischl, A. van der Kouwe, C. Destrieux et al., "Automatically parcellating the human cerebral cortex," *Cerebral Cortex*, vol. 14, no. 1, pp. 11–22, 2004.
- [31] A. M. Dale, B. Fischl, and M. I. Sereno, "Cortical surface-based analysis: I. Segmentation and surface reconstruction," *NeuroImage*, vol. 9, no. 2, pp. 179–194, 1999.
- [32] B. Fischl and A. M. Dale, "Measuring the thickness of the human cerebral cortex from magnetic resonance images," *Proceedings of the National Academy of Sciences of the United States of America*, vol. 97, no. 20, pp. 11050–11055, 2000.

- [33] B. Fischl, M. I. Sereno, and A. M. Dale, "Cortical surface-based analysis: II. Inflation, flattening, and a surface-based coordinate system," *NeuroImage*, vol. 9, no. 2, pp. 195–207, 1999.
- [34] S. Li, X. Yuan, F. Pu et al., "Abnormal changes of multidimensional surface features using multivariate pattern classification in amnesic mild cognitive impairment patients," *The Journal of Neuroscience*, vol. 34, no. 32, pp. 10541–10553, 2014.
- [35] J. Peng, P. Wang, N. Zhou, and J. Zhu, "Partial correlation estimation by joint sparse regression models," *Journal of the American Statistical Association*, vol. 104, no. 486, pp. 735–746, 2009.
- [36] R. Opgen-Rhein and K. Strimmer, "Accurate ranking of differentially expressed genes by a distribution-free shrinkage approach," *Statistical Applications in Genetics and Molecular Biology*, vol. 6, no. 1, 2007.
- [37] D. J. Watts and S. H. Strogatz, "Collective dynamics of 'small-world' networks," *Nature*, vol. 393, no. 6684, pp. 440–442, 1998.
- [38] S. Achard, R. Salvador, B. Whitcher, J. Suckling, and E. Bullmore, "A resilient, low-frequency, small-world human brain functional network with highly connected association cortical hubs," *The Journal of Neuroscience*, vol. 26, no. 1, pp. 63–72, 2006.
- [39] E. Bullmore and O. Sporns, "Complex brain networks: graph theoretical analysis of structural and functional systems," *Nature Reviews Neuroscience*, vol. 10, no. 3, pp. 186–198, 2009.
- [40] S. Maslov and K. Sneppen, "Specificity and stability in topology of protein networks," *Science*, vol. 296, no. 5569, pp. 910–913, 2002.
- [41] J. D. Humphries, A. Byron, and M. J. Humphries, "Integrin ligands at a glance," *Journal of Cell Science*, vol. 119, no. 19, pp. 3901–3903, 2006.
- [42] E. T. Bullmore, J. Suckling, S. Overmeyer, S. Rabe-Hesketh, E. Taylor, and M. J. Brammer, "Global, voxel, and cluster tests, by theory and permutation, for a difference between two groups of structural mr images of the brain," *IEEE Transactions on Medical Imaging*, vol. 18, no. 1, pp. 32–42, 1999.
- [43] B. Lv, J. Li, H. He et al., "Gender consistency and difference in healthy adults revealed by cortical thickness," *NeuroImage*, vol. 53, no. 2, pp. 373–382, 2010.
- [44] W. Zhu, W. Wen, Y. He, A. Xia, K. J. Anstey, and P. Sachdev, "Changing topological patterns in normal aging using large-scale structural networks," *Neurobiology of Aging*, vol. 33, no. 5, pp. 899–913, 2012.
- [45] Y. He, Z. Chen, and A. Evans, "Structural insights into aberrant topological patterns of large-scale cortical networks in Alzheimer's disease," *Journal of Neuroscience*, vol. 28, no. 18, pp. 4756–4766, 2008.
- [46] E. Armstrong, A. Schleicher, H. Omran, M. Curtis, and K. Zilles, "The ontogeny of human gyrification," *Cerebral Cortex*, vol. 5, no. 1, pp. 56–63, 1995.
- [47] Z. Dai and Y. He, "Disrupted structural and functional brain connectomes in mild cognitive impairment and Alzheimer's disease," *Neuroscience Bulletin*, vol. 30, no. 2, pp. 217–232, 2014.
- [48] Y. Fan, N. Batmanghelich, C. M. Clark, and C. Davatzikos, "Spatial patterns of brain atrophy in MCI patients, identified via high-dimensional pattern classification, predict subsequent cognitive decline," *NeuroImage*, vol. 39, no. 4, pp. 1731–1743, 2008.
- [49] A. J. Saykin, H. A. Wishart, L. A. Rabin et al., "Older adults with cognitive complaints show brain atrophy similar to that of amnesic MCI," *Neurology*, vol. 67, no. 5, pp. 834–842, 2006.
- [50] A. L. W. Bokde, P. Lopez-Bayo, T. Meindl et al., "Functional connectivity of the fusiform gyrus during a face-matching task in subjects with mild cognitive impairment," *Brain*, vol. 129, no. 5, pp. 1113–1124, 2006.
- [51] J. L. Woodard, S. T. Grafton, J. R. Votaw, R. C. Green, M. E. Dabraski, and J. M. Hoffman, "Compensatory recruitment of neural resources during overt rehearsal of word lists in Alzheimer's disease," *Neuropsychology*, vol. 12, no. 4, pp. 491–504, 1998.
- [52] J. Pariente, S. Cole, R. Henson et al., "Alzheimer's patients engage an alternative network during a memory task," *Annals of Neurology*, vol. 58, no. 6, pp. 870–879, 2005.
- [53] R. Romero-Garcia, M. Atienza, L. H. Clemmensen, and J. L. Cantero, "Effects of network resolution on topological properties of human neocortex," *NeuroImage*, vol. 59, no. 4, pp. 3522–3532, 2012.
- [54] A. Zalesky, A. Fornito, I. H. Harding et al., "Whole-brain anatomical networks: does the choice of nodes matter?" *NeuroImage*, vol. 50, no. 3, pp. 970–983, 2010.
- [55] B. C. M. Van Wijk, C. J. Stam, and A. Daffertshofer, "Comparing brain networks of different size and connectivity density using graph theory," *PLoS ONE*, vol. 5, no. 10, Article ID e13701, 2010.
- [56] P. Tewarie, E. Van Dellen, A. Hillebrand, and C. J. Stam, "The minimum spanning tree: an unbiased method for brain network analysis," *NeuroImage*, vol. 104, pp. 177–188, 2015.

## Research Article

# State and Training Effects of Mindfulness Meditation on Brain Networks Reflect Neuronal Mechanisms of Its Antidepressant Effect

**Chuan-Chih Yang,<sup>1,2,3</sup> Alfonso Barrós-Loscertales,<sup>1</sup> Daniel Pinazo,<sup>4</sup> Noelia Ventura-Campos,<sup>1,5</sup> Viola Borchardt,<sup>2,3</sup> Juan-Carlos Bustamante,<sup>6</sup> Aina Rodríguez-Pujadas,<sup>1</sup> Paola Fuentes-Claramonte,<sup>1</sup> Raúl Balaguer,<sup>4</sup> César Ávila,<sup>1</sup> and Martin Walter<sup>2,3,7,8,9</sup>**

<sup>1</sup>Departamento de Psicología Básica, Clínica y Psicobiología, Universitat Jaume I, 12071 Castellón, Spain

<sup>2</sup>Clinical Affective Neuroimaging Laboratory, 39120 Magdeburg, Germany

<sup>3</sup>Department of Behavioral Neurology, Leibniz Institute for Neurobiology, 39118 Magdeburg, Germany

<sup>4</sup>Departamento de Psicología Evolutiva, Educativa, Social y Metodología, Universitat Jaume I, 12071 Castellón, Spain

<sup>5</sup>Departamento de Didáctica de la Matemática, Facultad de Magisterio de la Universidad de Valencia, 46022 Valencia, Spain

<sup>6</sup>Departamento de Psicología y Sociología, Universidad de Zaragoza, 50009 Zaragoza, Spain

<sup>7</sup>Department of Psychiatry and Psychotherapy, Otto-von-Guericke University, 39120 Magdeburg, Germany

<sup>8</sup>Center for Behavioral Brain Sciences (CBBS), 39120 Magdeburg, Germany

<sup>9</sup>Department of Psychiatry and Psychotherapy, Eberhard Karls University, 72076 Tuebingen, Germany

Correspondence should be addressed to Alfonso Barrós-Loscertales; [barros@uji.es](mailto:barros@uji.es)

Received 17 August 2015; Revised 10 January 2016; Accepted 11 January 2016

Academic Editor: Bruno Poucet

Copyright © 2016 Chuan-Chih Yang et al. This is an open access article distributed under the Creative Commons Attribution License, which permits unrestricted use, distribution, and reproduction in any medium, provided the original work is properly cited.

The topic of investigating how mindfulness meditation training can have antidepressant effects via plastic changes in both resting state and meditation state brain activity is important in the rapidly emerging field of neuroplasticity. In the present study, we used a longitudinal design investigating resting state fMRI both before and after 40 days of meditation training in 13 novices. After training, we compared differences in network connectivity between rest and meditation using common resting state functional connectivity methods. Interregional methods were paired with local measures such as Regional Homogeneity. As expected, significant differences in functional connectivity both between states (rest versus meditation) and between time points (before versus after training) were observed. During meditation, the internal consistency in the precuneus and the temporoparietal junction increased, while the internal consistency of frontal brain regions decreased. A follow-up analysis of regional connectivity of the dorsal anterior cingulate cortex further revealed reduced connectivity with anterior insula during meditation. After meditation training, reduced resting state functional connectivity between the pregenual anterior cingulate and dorsal medial prefrontal cortex was observed. Most importantly, significantly reduced depression/anxiety scores were observed after training. Hence, these findings suggest that mindfulness meditation might be of therapeutic use by inducing plasticity related network changes altering the neuronal basis of affective disorders such as depression.

## 1. Introduction

Mindfulness meditation has been shown to be therapeutic in emotion regulation [1–5]. Mindfulness practice, inherited from the ancient Buddhist tradition, involves observing thoughts nonjudgmentally in the present moment.

Mindfulness-based meditation (MBM) or mindfulness-based intervention (MBI) is increasingly being employed in western psychology to alleviate a variety of mental and physical conditions including obsessive compulsive disorder and anxiety and in the prevention of relapse in depression and drug addiction [6–10]. Despite the fact that recent

neuroimaging studies indicate the several positive aspects of mindfulness practice, its neuronal mechanisms are still poorly understood.

A main theme in meditation research is the question if the observed effects are dependent on practice/expertise or on personal characteristics. Usually, studies on meditation compare expert practitioners with novice practitioners in cross-sectional studies [11–13]. Functional studies have employed fMRI block designs to investigate the blood-oxygen level dependent (BOLD) signal changes during meditation [11, 12, 14], as well as exploring resting state fMRI (rs-fMRI) differences between experienced meditators and novices [11, 13, 15]. Crucially, longitudinal studies of the impact of short-term meditation practice on the same novice group have the potential to reflect effects of meditation independently of individual differences, for example, personal interest in meditation or previous meditation experience. Hölzel et al. [4] observed changes in gray matter density in a longitudinal study with 8 weeks of a mindfulness-based stress reduction (MBSR) programme.

Resting state functional connectivities (RSFC) methods provide one approach for exploring how mindfulness meditation alters neural plasticity among brain regions. The interregional dynamics of RSFC specifically afford the advantages of being task independent, rendering reliable estimates of neural circuit functionality corresponding to structural topography [16, 17].

To investigate the impact of mindfulness practice on the neuronal level and its antidepressant effects, alteration in the activation pattern of the Default Mode Network (DMN) is of particular interest and the DMN is thus selected as the target brain network [13]. We know that the DMN involves several brain regions active when the brain is not actively engaged in a cognitively demanding task but rather is in a relaxed state [18]. Consistently, the DMN includes areas at the medial posterior cortex, specifically the posterior cingulate cortex (PCC; areas 23/31), the precuneus, and the medial frontal cortex (MFC, including areas 24/10-m/32), as well as bilateral inferior parietal and posterior temporal areas around the temporoparietal junction area (TPJ) [19].

Recent findings suggested that the DMN has altered resting state functional connectivity between networks when depressed patients were compared to healthy participants [20]. Among these DMN regions, dmPFC was shown to be involved in self-inspection [21] and emotion regulation [22] and demonstrated increased activity in depression [23]. Thus, major depressive disorder (MDD) patients show more neural functional connectivity between the posterior cingulate cortex and the subgenual-cingulate cortex during rest periods compared to healthy individuals [24].

Several regions of anterior cingulate are of importance in depression-related disorders. Pregenual anterior cingulate cortex (pgACC) has been shown to be hypoactivated in MDD [25]. The dorsal anterior cingulate cortex (dACC) is associated with the involvement of cognitive control over attentional resources [26, 27], and it is strongly impaired in MDD. van Tol et al. [28] showed that dACC and pgACC are also structurally affected in MDD, while pgACC was furthermore found to be molecularly affected by altered

glutamate concentrations. In contrast to the dACC, the pgACC belongs to an affective subdivision of the ACC [26] and was shown to mediate the increased internal focus present in the ruminative thinking style of depressed patients. Furthermore, the pgACC is specifically impaired in highly anhedonic patients [29].

The neurobiological model of depression [30] states that impaired cognitive control, mediated by regions in the prefrontal cortex (PFC), cooccurs with hyperactivation of the amygdala, which facilitates encoding and retrieval of emotional stimuli via modulation of hippocampal activity. Activity in the medial prefrontal cortex (MPFC), which is associated with internal representations of the self, is consequently increased as well. The suppressed regulatory influence of PFC regions facilitates an undesired recall of negative (mood-congruent) events. The DMN has been shown to support internally oriented and self-referential thoughts and MDD has been associated with both hyperconnectivity within the DMN and hyperconnectivity between frontoparietal control systems and regions of the default network [31]. Furthermore, MDD has been characterized by hypoconnectivity within the frontoparietal network, a set of regions involved in cognitive control of attention and emotion regulation, and hypoconnectivity between frontal systems and parietal regions of the dorsal attention network involved in attending to the external environment [31]. These networks modulate affective and cognitive processes disturbed in depression.

In the cases described here, impairment refers to increase or decrease of an existing functional connection. Alterations reflect changes in operational properties of interregional connections and their local resting state activity. As much as MDD is characterized by hyperactivity in, for example, ventral and subcortical regions, this was discussed to be directly related to hypoactivity and resulting disinhibition from dorsal cortical regions [30]. Likewise, within-network connectivity can be altered in opposite direction compared to between-network connectivity (in terms of functional connectivity) as soon as a hub region is concerned, which connects both to its own functional module and towards regions outside its own functional subnetwork.

Recent neuroimaging publications benefit from the utilization of multiple imaging methods. Resting state fMRI widely used seed-based correlation analysis between regions of interest (ROIs) by investigating interregional functional connectivity to reveal highly consistent patterns of functional connectivity across regions [32]. In this study we selected two ROIs in the ACC, pgACC, and dACC, due to their role in emotion regulation and as portions of the DMN. Earlier studies showed that the pgACC was associated with internal monitoring [33, 34] and Mood States [35]. Likewise, the dACC has been shown to relate to focused attention [26, 27] and recent study from Dickenson and colleagues had found that the dACC was recruited during mindfulness meditation as compared to the mind wandering for the novice practitioner [36]. Both pgACC and dACC are therefore target regions for specific symptoms in depression related to mindfulness and emotional/interoceptive awareness, and we focused our analysis on these two regions with supposedly differential,

if not contrary, effects, as previously reported in patient studies and suggested by their involvement in potentially antagonistic networks. The method of seed-based functional connectivity was used to test their resting state behavior both before and after training. Furthermore, independent component analysis (ICA), which neither relies on *a priori* model of brain activity, parcellation into ROIs, nor choice of seed regions but has been widely used to detect resting state networks [37], was chosen as a complementary, data-driven approach. We hypothesized that some regions within DMN would be relevant to emotional regulation and ICA was used for functional parcellation of the DMN. In addition to seed-based functional connectivity method and ICA, which reflect the interregional neuronal properties between distant brain regions, ReHo was used to map the level of regional activity synchronization across the whole brain [38]. Regional Homogeneity (ReHo) measures the similarity of the time series of a given voxel to those of neighbouring voxels [39], which reflects the temporal homogeneity of localized neural dynamics [40–42].

Therefore, our aims were to analyze both the interregional and local features of fMRI signal during resting state (RS) in a longitudinal study of RS activation, as well as comparing RS activation to meditation state (MS) activation. We hypothesized that the training of mindfulness meditation will lead to changes in the following: (1) the interregional functional connectivity of our *a priori* seed ROIs—pgACC and dACC (by means of seed-based FC); (2) the internal consistency of the DMN (by means of ICA); and (3) the regional synchronization of fMRI time series (by means of ReHo).

## 2. Materials and Methods

**2.1. Subjects.** Thirteen university students (Spanish native speakers) were recruited by university advertisement to participate in 40 days of mindfulness meditation course. Sample demographic characteristics are detailed in Table 1. All study protocols were approved by the Institutional Review Board of the Universitat Jaume I of Castellón and informed consent was obtained from all subjects. Participants were screened for psychiatric or neurological conditions prior to enrollment in the meditation course. No previous meditation experience was reported by the subjects.

**2.2. Mindfulness Meditation Training.** The mindfulness training programmes consisted of 8-week courses, with daily practice at home in sessions of around 45 minutes [43]. The mindfulness-based stress reduction (MBSR) programme [44] as well as acceptance and commitment therapy [45] was used to design the meditation-mindfulness training programme based on self-observation training. The self-observation training programme consisted of eight 1.5-hour sessions over a period of 8 weeks. The first hour of the sessions was devoted to simple physical and breathing exercises during which the participants were instructed to perform Vipassana meditation exercises, by focusing their attention on thoughts that came to their mind without dwelling on any of them. After the exercises, participants meditated in silence,

TABLE 1: Characteristics of the subject sample. Wherever relevant, group mean ( $\pm$  standard deviation) is given.

Number of participants	13
Ratio of males and females	3/10
Age	24.53 ( $\pm$ 5.89)
Ratio of handedness	right = 13, left = 0
Minutes of meditation practice per day	10.67 ( $\pm$ 1.66)
Total number of meditation days until scanning	39.23 ( $\pm$ 3.63)
Total number of minutes of meditation practice until scanning	418.07 ( $\pm$ 71.45)

continuing to observe their thoughts without censoring them. The time devoted to meditation without the physical exercises gradually increased over the course. The final half hour was used to talk about the experience and explain the characteristics of meditation and mindfulness in which videos and fables reflecting the most significant aspects of the meditation and self-observation experience were used. Participants were also encouraged to do the meditation exercises at home; they were given a meditation diary in which to record their daily experiences, which was handed in to the course instructor. A quantification of the participants' amount of meditation practice at the end of the course is detailed in Table 1.

**2.3. Self-Report Measures.** Three self-assessment questionnaires were administered to participants both before and after the training period. We applied the Profile of Mood States (POMS) throughout the study in its abbreviated, Spanish version [46] of the original POMS [47]. It is a 44-item inventory, which measures current mood state by rating statements on a Likert scale (0 to 4). It consists of six subscales: anger, fatigue, tension, depression, vigor, and friendliness. To evaluate changes in depressive symptoms of our sample, we used the Center for Epidemiologic Studies Depression Scale (CES-D) which is a well-validated, 20-item inventory [48]. Subjects were asked to rate statements based on the previous week on a Likert scale (0–3) and scores range from 0 to 60, whereat higher scores indicate higher levels of depression. The State-Trait Anxiety Inventory [49] is a 40-item scale designed to measure the state and trait anxiety based on a Likert scale (1–4), which was also applied. Scores range from 20 to 80 whereat higher scores relate to higher levels of anxiety.

**2.4. Data Acquisition.** In this longitudinal study participants were scanned twice. Before the training of mindfulness meditation, subjects underwent a single resting state (RS) scan (time point 1, TP1). Later on, at day 40 (time point 2, TP2), subjects underwent two scans, RS scan and a scan during which they practiced meditation (MS). During the RS, subjects were instructed to close their eyes, be at the normal relaxing condition without engaging in any specific task or mental activity, and not fall into meditation. During meditation scan, subjects were instructed to close their eyes, openly monitor the surrounding environment by accepting all sensations rise and fall nonjudgmentally, and specifically to be aware of the present moment as they were trained. At

time point 2 (TP2), RS scan was measured for 9 minutes followed by continuous MS lasting for 12 minutes. Long time acquisition for both conditions was set to obtain sufficient power for the functional connectivity analyses given the relatively small sample size [37].

**2.5. MR Sequence Parameters.** MR measurements were performed on 1.5 T Siemens AVANTO scanner (Siemens Erlangen, Germany). A structural image was acquired from each subject with a magnetization-prepared rapid gradient-echo (MP-RAGE) sequence (TR = 2200 ms, TE = 3.79 ms, flip angle (FA) = 15°, 160 slices, matrix size = 256 × 256, field-of-view (FOV) = 256 mm × 256 mm, and slice thickness = 1 mm). For both RS and MS, a standard EPI sequence was used (TR = 2300 ms, TE = 55 ms, FA = 90°, FOV = 224 mm × 224 mm, matrix size = 64 × 64, and slice thickness = 4 mm,) with 25 axial slices for whole brain coverage. Finally, an extra gradient field mapping sequence (*gre\_field\_mapping*) was acquired followed by each EPI sequence (TR = 487 ms, TE1 = 8 ms, TE2 = 12.76 ms, FA = 65°, FOV = 224 mm × 224 mm, matrix size = 64 × 64, and slice thickness = 4 mm) with 25 slices with the same coverage used in EPI sequence.

**2.6. Data Preprocessing.** B0 inhomogeneity correction was performed to reduce static field inhomogeneity using an EpiUnwarping tool based on FSL (<http://surfer.nmr.mgh.harvard.edu/fswiki/epidewarp.fsl>) [50]. Preprocessing was performed using Statistical Parametric Mapping (SPM8, <http://www.fil.ion.ucl.ac.uk/spm/>) and Data Processing Assistant for resting state fMRI (DPARSF v 2.3 [51]). Functional images were slice-time corrected. Motion correction was performed by using a least squares approach and a six-parameter (rigid body) linear transformation. Spatial normalization to MNI space was carried out by using unified segmentation of T1-weighted acquired images, and the extracted normalization parameters from segmentation were applied to normalize the functional volumes for each participant (normalized images were then resampled to 3-mm isotropic cubic voxels). Finally, functional volumes were smoothed by applying a 4 mm FWHM Gaussian kernel. Smoothed volumes were used for ICA and seed-based FC. ReHo analysis was performed on nonsmoothed functional volumes and images were smoothed after the analysis, because smoothing prior to ReHo calculation would increase regional similarity [51].

We conducted additional preprocessing for seed-based FC and ReHo analyses using the DPARSF tool through the following steps: (i) removing a linear trend in the time series and (ii) temporal band-pass filtering (0.01–0.08 Hz) to reduce the effect of low frequency drift and high-frequency noise [52, 53]. For the seed-based FC analysis, several sources of spurious variance were removed from the data through linear regression: six parameters from rigid body correction of head motion, white matter signal, cerebrospinal fluid signal, and the global mean signal [54].

For MS, the first and the last 40 volumes of the functional images were discarded (total 313 volumes were acquired before removing the 80 volumes). The reason for removing the first 40 volumes was to allow the participants to get used

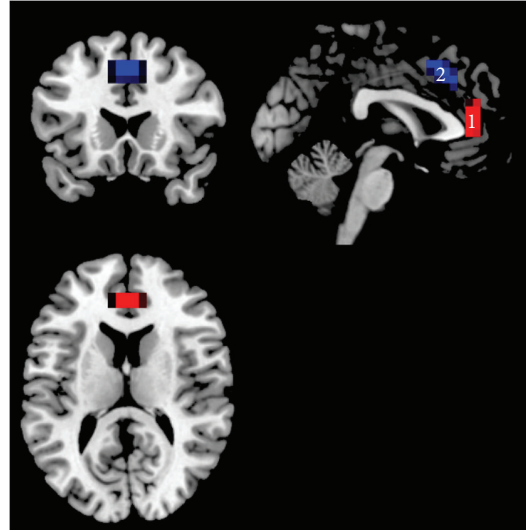


FIGURE 1: Seed ROIs used for RSFC analysis. ROI1: pregenual ACC (pgACC) as marked in red color. ROI2: dorsal ACC (dACC) as marked in blue color overlaid on the T1 anatomical MNI space.

to the scanning environment and ensure a reasonable establishment of the meditation state. The reason for removing the last 40 volumes was aiming at avoiding distraction effects at the end of the meditation, yielding a duration similar to the RS. The central 233 (8 min 33 sec) functional volumes of the time series were sufficient for estimation of independent components (ICs) [37].

**2.7. Seed-Based Functional Connectivity.** In addition to a data-driven approach, we performed a hypothesis-driven seed-based FC analysis. Two independent seed ROIs placed in the pregenual anterior cingulate cortex (pgACC) and the dorsal anterior cingulate cortex (dACC) were chosen based on previous reports on their involvement in meditation and affective disorders such as depression [55].

To examine FC in the pgACC and the dACC in a whole brain voxel-wise analysis, these two seed regions were defined by the Montreal Neurological Institute (MNI) coordinates ( $x, y, z$ ): 0, 41, and 9 (pgACC) and 0, 27, and 30 (dACC). Both ROIs had a radius of 10 mm resulting in a volume of approximately 4 mL, maximizing the gray matter contribution as described previously [56], as shown in Figure 1. The averaged time course from each seed region was obtained for each subject at both time points and for both conditions (RS, MS) separately. An individual FC map for each seed was generated by calculating the voxel-wise correlation coefficients in the whole brain, which were then converted into  $z$ -maps by Fisher's  $Z$  transformation to enhance normality. The  $z$ -maps of the dACC and pgACC of each individual were entered into second-level paired  $t$ -test.

**2.8. Group Independent Component Analysis (Group ICA).** A group independent component analysis was performed using GIFT (v 2.0e, <http://mialab.mrn.org/software/gift/>) [57] to investigate the following: (a) the training-related RSFC changes and (b) the FC difference between RS and MS.

These analyses were performed based on FC analysis from spontaneous BOLD activity from the average fMRI time course of the entire brain.

In the analysis of training-related RSFC changes over time, the longitudinal resting state data were grouped together when conducting group ICA following a previous report [58]. In the analysis of FC differences between RS and MS experimental conditions, a single ICA was performed at the group level for RS and MS conditions separately, in agreement with previous studies [59, 60]. The data of each condition was restricted to twenty-four independent components (ICs) using the MDL criteria and extracted by ICA decomposition using the Infomax algorithm [61]. To determine the reliability of the ICA algorithm, multiple runs of ICA were performed using ICASSO. Each IC consists of a spatial map and an associated time course. The ICs which resembled the DMN most were firstly spatially sorted by using the DMN template built-in in GIFT [57] and then further identified by visual inspection by two different raters for RS and MS separately. Subsequently, individual subject maps were back reconstructed to obtain single-subject results. Finally, the resulting individual IC maps were converted into voxel-wise  $z$ -score maps representing the degree to which each voxel belongs to the overall ICA component map.

Individual subject  $z$ -maps were entered into SPM random-effect analyses. The RSFC analysis involved a longitudinal analysis of changes in temporal correlations in connectivity fluctuations before and after training. To compare RS and MS conditions, one paired  $t$ -test was performed. In the IC decomposition, only DMN was extracted to be compared between time points and conditions. We computed the DMN from the average fMRI time course from the entire network as described before. Furthermore, in the analysis between RS and MS, the DMN comparison was not restricted to a mask of the conjunction between both conditions, since it would involve the restriction of any other regions that may be identified as the DMN in the MS as different from the DMN in the RS, but to the addition of the masks for the DMN identified under RS and MS.

Additionally, exploratory mask restricted analysis was performed but not reported because its contribution was similar to the unrestricted comparison in the target regions of the DMN, although covering differences in other out regions.

**2.9. Regional Homogeneity (ReHo).** ReHo images of the whole brain for both MS and RS were generated using DPARSF. Voxel-by-voxel Kendall’s coefficient of concordance (KCC, [39]) of the time series of a given cluster of 27 neighbouring voxels was calculated [62]. To reduce the global effects of individual variability across participants, the ReHo of each voxel was scaled by the mean value of whole brain ReHo for each participant [20].

A paired  $t$ -test was performed to identify the effects of meditation on ReHo during resting state activity between TP1 and TP2. A second paired  $t$ -test was performed to identify the differences in ReHo between the resting states (RS) and meditation state (MS) at TP2. The resulting  $t$ -value maps of each contrast of interest was displayed after applying a statistical height threshold of  $p < 0.001$  for each voxel and

TABLE 2: Profile of Mood States (POMS), Center for Epidemiologic Studies Depression Scale (CES-D), and State-Trait Anxiety Inventory (STAI) scores before and after meditation training. Group means and standard deviations are listed. Significant group differences are listed as follows: \*\*\*: significant at  $p < 0.001$ , \*\*: significant at  $p < 0.01$ , and \*: significant at  $p < 0.05$ . †: before training, 6 out of 13 subjects surpassed the cutoff for depression. (+): positive mood state factor, (-): negative mood state factor.

Questionnaire	Before training	After training
POMS		
Anger (-)	2.84 ( $\pm 3.78$ )	3.30 ( $\pm 6.07$ )
Fatigue (-)	4.84 ( $\pm 2.67$ )	3.69 ( $\pm 4.57$ )
Vigor (+)	11.92 ( $\pm 5.31$ )	12.30 ( $\pm 5.36$ )
Friendliness (+)	18.92 ( $\pm 2.98$ )	19.46 ( $\pm 4.27$ )
Tension (-)	8.00 ( $\pm 3.36$ )	5.38 ( $\pm 5.18$ )*
Depression (-)	3.76 ( $\pm 3.94$ )	4.53 ( $\pm 8.04$ )
CES-D	16.23 ( $\pm 9.54$ )*	9 ( $\pm 6.20$ )***
STAI, state	17.84 ( $\pm 4.75$ )	14.38 ( $\pm 10.16$ )
STAI, trait	21.30 ( $\pm 8.6$ )	16.84 ( $\pm 9.56$ )**

a corrected cluster threshold at  $p < 0.05$ , as determined by a Monte Carlo simulation (see AlphaSim in AFNI <http://afni.nimh.nih.gov/pub/dist/doc/manual/AlphaSim.pdf>).

### 3. Results

**3.1. Behavioral Self-Report Measures.** A paired  $t$ -test analysis of the total scores of CES-D indicated a significant reduction of depression scores after meditation training ( $t(12) = 4.43$ ;  $p < 0.001$ ). Before meditation training, the mean CES-D score of the sample was  $16.23 \pm 9.54$ , which slightly surpassed the cutoff score for depression (a CES-D above 16 indicates depression; see [63]). After training, the mean CES-D score was reduced to  $9 \pm 6.20$ .

Pre-post comparisons of the STAI measures revealed a significant reduction in trait anxiety ( $t(12) = 2.76$ ;  $p < 0.01$ ), but not in state anxiety scores. Neither the sum score of the POMS nor its sub-scores showed a significant change (all  $p < 0.05$ , controlled for multiple comparisons). However, the tension subscore did show a change ( $t(12) = 1.883$ ,  $p < 0.05$ , uncorrected); see Table 2.

As an exploratory step, the changes in CES-D scores were correlated with the changes in connectivity of the FC components, but the results were not significant for dACC ( $r = .122$ ,  $p > 0.1$ ) and pgACC ( $r = -.064$ ,  $p > 0.1$ ).

#### 3.2. Seed-Based Functional Connectivity

**3.2.1. Comparison of FC Differences between RS and MS.** For the contrast between resting and meditation states (RS > MS), the pgACC showed a reduced connectivity with the bilateral inferior parietal gyri but an increased connectivity with the MPFC, the left superior temporal gyrus (STG), and the right TPJ during MS as shown in Figure 2(a) and Table 3 ( $p < 0.05$ , FWE-corrected).

TABLE 3: Regions showing functional differences between conditions (rest versus meditation).

Analysis	Rest > meditation					Meditation > rest				
	Region	Side	K	MNI coordinates	z-score	Region	Side	K	MNI coordinates	z-score
ICA	$(p < 0.001, \text{FWE}^{\text{a}}$ -corrected cluster threshold at $p < 0.05$ ) <sup>b</sup>									
	dACC	R	202	9 21 36	5.70	Precuneus	R	178	3 -66 27	4.94
	sgACC	R	349	9 27 0	5.60	TPJ/IPL	L	157	-51 -57 27	4.31
	AI	L	336	-39 9 0	5.02					
	AI	R	37	45 18 0	4.34					
	IFG/BA9	R	21	60 18 27	4.26					
Seed-based FC	$(p < 0.001, \text{FWE}$ -corrected cluster threshold at $p < 0.05$ ) <sup>b</sup>									
(ROI: pgACC)	IPL	L	42	-45 -39 36	4.31	TPJ	R	58	57 -66 36	4.51
	IPL	R	45	39 -51 51	4.17	MPFC	R	36	9 51 9	4.49
						STG	L	23	-42 -60 18	3.86
(ROI: dACC)	AI	L	20	-36 18 3	4.2	n.s.				
ReHo	$(p < 0.001, \text{FWE}$ -corrected cluster threshold at $p < 0.05$ ) <sup>b</sup>									
	n.s.					dACC	R	125	0 36 15	5.32
						MPFC	R	125	6 48 12	4.24
						Putamen	L	77	-21 6 3	4.40

Notes: AI, anterior insula; dACC, dorsal anterior cingulate cortex; IPL, inferior parietal lobe; K, cluster size; MPFC, medial prefrontal cortex; pgACC, pregenual anterior cingulate cortex; sgACC, subgenual anterior cingulate cortex; STG, superior temporal gyrus; TPJ, temporoparietal junction; and BA: brodmann area.

<sup>a</sup>Family-wise error.

<sup>b</sup>A combined threshold of  $p < 0.001$  and a minimum cluster size determined by AlphaSim<sup>c</sup> algorithm in AFNI, resulting in FWE-corrected threshold of  $p < 0.05$ . An estimate of the spatial correlation across voxels was modeled using the program 3dFWHM<sup>d</sup> in AFNI.

<sup>c</sup>AlphaSim: <http://afni.nimh.nih.gov/pub/dist/doc/manual/AlphaSim.pdf>.

<sup>d</sup>3dFWHM: [http://afni.nimh.nih.gov/pub/dist/doc/program\\_help/3dFWHM.html](http://afni.nimh.nih.gov/pub/dist/doc/program_help/3dFWHM.html).

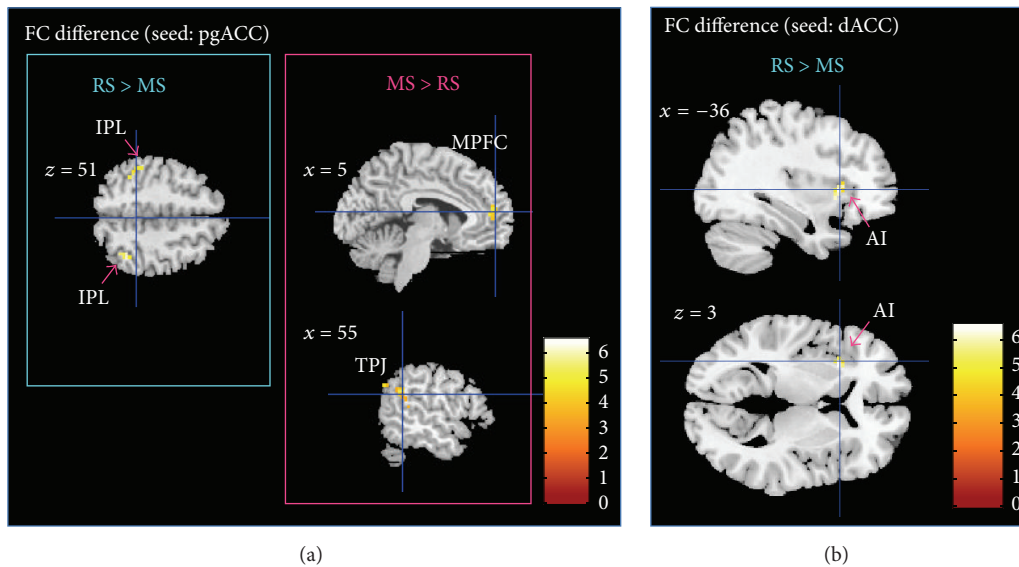


FIGURE 2: (a) Paired comparison of seed-based FC maps (seed = pgACC) between rest and meditation at TP2 ( $p < 0.05$ , FWE-corrected). Bar plot represents the  $t$ -values. White labels indicate the coordinate of each slice in the MNI frame of reference ( $x, z$ ). (b) Paired comparison of seed-based FC maps (seed = dACC) between rest and meditation at TP2. FC decreases between dorsal ACC and left AI during meditation as compared to rest ( $p < 0.05$ , FWE-corrected). Bar plot represents the  $t$ -values. White labels indicate the coordinate of each slice in the MNI frame of reference ( $x, z$ ).

The dACC showed a decreased FC with the left anterior insula (AI) during MS ( $p < 0.05$ , FWE-corrected); see Figure 2(b) and Table 3.

The voxel-wise significance level was set at  $p < 0.001$  with a spatial extent threshold of 16 contiguous voxels, yielding

a whole brain threshold of  $p < 0.05$  corrected for multiple comparisons using AlphaSim algorithm implemented in AFNI (data dimension:  $61 \times 73 \times 61$  voxels, Gaussian filter widths:  $\text{FWHM}_x = 6.66$ ,  $\text{FWHM}_y = 6.88$ , and  $\text{FWHM}_z = 6.79$ ).

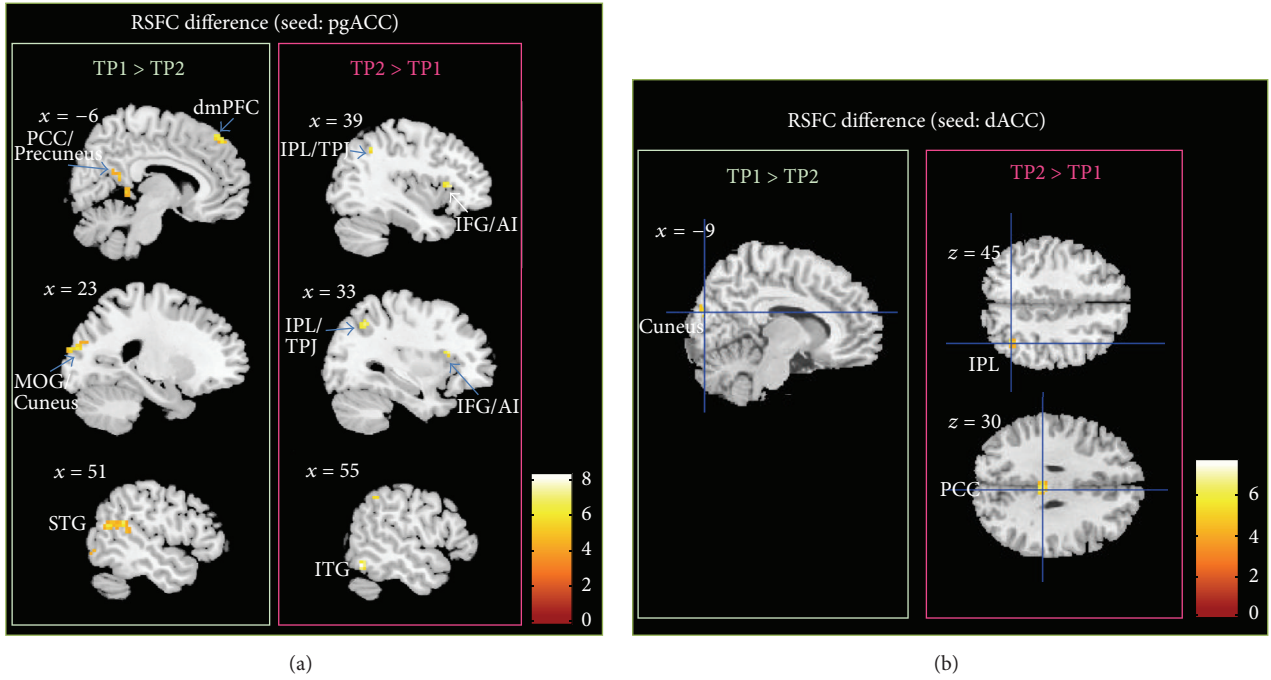


FIGURE 3: (a) Longitudinal seed-based RSFC results (seed = pgACC) ( $p < 0.05$ , FWE-corrected). Bar plot represents the  $t$ -values. White labels indicate the coordinate of each slice in the MNI frame of reference ( $x, z$ ). (b) Longitudinal seed-based RSFC results (seed = dACC) ( $p < 0.05$ , FWE-corrected). Bar plot represents the  $t$ -values. White labels indicate the coordinate of each slice in the MNI frame of reference ( $x, z$ ).

**3.2.2. Longitudinal Analysis of RSFC Changes due to Meditation.** The longitudinal effect of meditation practice (TP1 > TP2) on RSFC was tested separately for pgACC and dACC. For pgACC, a decreased connectivity to the left PCC/precuneus, the left dorsal medial prefrontal cortex (dmPFC), the right superior temporal gyrus (STG), the left middle occipital gyrus, and left inferior temporal gyrus was observed, while connectivity to the right inferior temporal gyrus, the right inferior frontal gyrus (IFG), and the right TPJ/IPL increased after meditation training ( $p < 0.05$ , FWE-corrected; see Figure 3(a) and Table 4).

In dACC, meditation training entailed a reduction of RSFC to calcarine sulcus and the cuneus but an increased RSFC towards cerebellum, the right inferior parietal lobe (IPL), and the posterior cingulate cortex (PCC) ( $p < 0.05$ , FWE-corrected; see Figure 3(b) and Table 4).

The voxel-wise significance level was set at  $p < 0.001$  with a spatial extent threshold of 16 contiguous voxels, yielding a whole brain threshold of  $p < 0.05$  corrected for multiple comparisons using AlphaSim algorithm implemented in AFNI (data dimension:  $61 \times 73 \times 61$  voxels, Gaussian filter widths:  $\text{FWHM}_x = 6.66$ ,  $\text{FWHM}_y = 6.88$ , and  $\text{FWHM}_z = 6.79$ ).

### 3.3. Group Independent Component Analysis

**3.3.1. Comparison of the DMN Independent Component between RS and MS.** To ensure that our DMN comparison between these two conditions was performed in the same low frequency band, power density spectra were obtained. The results revealed that both DMNs were derived from the same

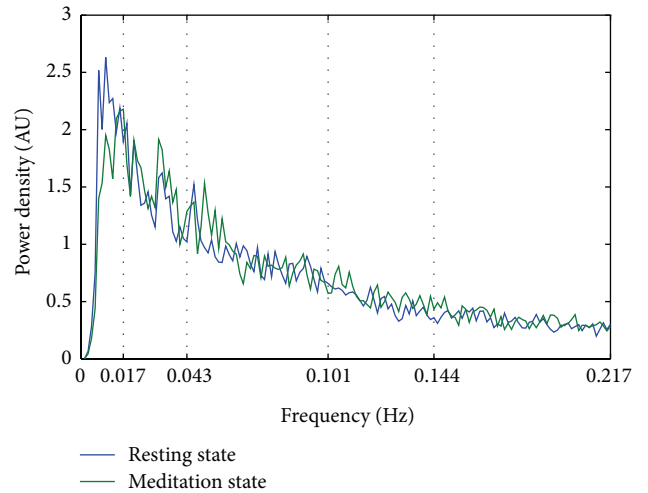


FIGURE 4: Mean power spectral density of the Default Mode Network (DMN) component. The peak power density was observed below 0.04 Hz for both conditions (resting state and meditation state). AU stands for arbitrary unit.

very low frequency band ( $< 0.04$  Hz). This insured that the comparison between RS and MS were performed in the same “expected” very low frequency domain [60]; see Figure 4.

At TP2, ICA revealed reduced activation during meditation in dACC, sgACC, bilateral insula, superior frontal gyrus, and inferior frontal gyrus (IFG) when compared to rest ( $p < 0.05$ , FWE-corrected). The precuneus and the left

TABLE 4: Regions showing RSFC differences between time points.

Analysis	Region	Side	TP1 > TP2			TP2 > TP1				
			K	MNI coordinates	z-score	Region	Side	K	MNI coordinates	z-score
ICA	n.s. ( $p < 0.001$ , FWE <sup>a</sup> -corrected cluster threshold at $p < 0.05$ ) <sup>b</sup>									
Seed-based FC	$(p < 0.001$ , FWE-corrected cluster threshold at $p < 0.05$ ) <sup>b</sup>									
(ROI: pgACC)	PCC/precuneus	L	58	-12 -51 15	4.71	ITG	R	16	54 -63 -18	4.23
	dmPFC	L	49	-12 45 54	4.35	IFG	R	17	39 24 6	3.84
	STG	R	53	54 -63 15	4.34	IPL/TPJ	R	18	33 -60 42	3.76
	MOG	L	22	-24 -102 6	4.19					
	ITG	L	21	-57 0 -24	4.01					
(ROI: dACC)	Calcarine/cuneus	L	18	-9 -84 21	4.37	Cerebellum	L	22	-30 -54 -30	4.56
	BA19	L	26	-27 -90 21	4.01	IPL	R	16	36 -60 45	4.20
						PCC	R	19	3 -30 30	4.13
ReHo	n.s. ( $p < 0.001$ , FWE-corrected cluster threshold at $p < 0.05$ ) <sup>b</sup>									

Note: dmPFC, dorsal medial prefrontal cortex; IFG, inferior frontal gyrus; IPL, inferior parietal lobe; ITG, inferior temporal gyrus; K, cluster size; PCC, post cingulate cortex; STG, superior temporal gyrus; MOG, middle occipital gyrus; and BA: brodmann area.

<sup>a</sup>Family-wise error.

<sup>b</sup>A combined threshold of  $p < 0.001$  and a minimum cluster size determined by AlphaSim<sup>c</sup> algorithm in AFNI, resulting in corrected threshold of  $p < 0.05$ .

An estimate of the spatial correlation across voxels was modeled using the program 3dFWHM<sup>d</sup> in AFNI.

<sup>c</sup>AlphaSim: <http://afni.nimh.nih.gov/pub/dist/doc/manual/AlphaSim.pdf>.

<sup>d</sup>3dFWHM: [http://afni.nimh.nih.gov/pub/dist/doc/program\\_help/3dFWHM.html](http://afni.nimh.nih.gov/pub/dist/doc/program_help/3dFWHM.html).

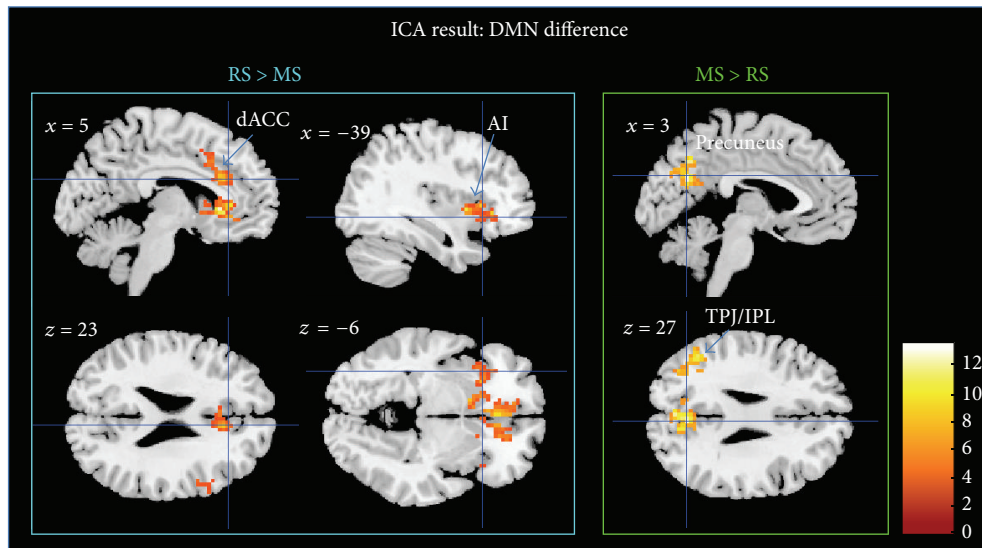


FIGURE 5: ICA results. DMN differences at TP2 for RS > MS and MS > RS ( $p < 0.05$ , FWE-corrected). Bar plot represents the  $t$ -values. White labels indicate the coordinate of each slice in the MNI frame of reference ( $x, z$ ).

temporoparietal junction (TPJ) showed an increased internal consistency in the ICs during MS; see Figure 5 and Table 3.

The voxel-wise significance level was set at  $p < 0.001$  with a spatial extent threshold of 16 contiguous voxels, yielding a whole brain threshold of  $p < 0.05$  corrected for multiple comparisons using AlphaSim algorithm implemented in AFNI (data dimension:  $61 \times 73 \times 61$  voxels, Gaussian filter widths:  $\text{FWHM}_x = 7.39$ ,  $\text{FWHM}_y = 8.18$ , and  $\text{FWHM}_z = 8.19$ ).

**3.3.2. Longitudinal Analysis of RS Changes in the DMN Independent Component due to Meditation.** The paired  $t$ -test at a threshold of  $p < 0.05$ , FWE-corrected, did not reveal longitudinal changes within the DMN independent

components. The voxel-wise significance level was set at  $p < 0.001$  with a spatial extent threshold of 23 contiguous voxels, yielding a whole brain threshold of  $p < 0.05$  corrected for multiple comparisons using AlphaSim algorithm implemented in AFNI (data dimension:  $61 \times 73 \times 61$  voxels, Gaussian filter widths:  $\text{FWHM}_x = 7.84$ ,  $\text{FWHM}_y = 8.68$ , and  $\text{FWHM}_z = 8.53$ ).

#### 3.4. Regional Homogeneity (ReHo) Analysis

**3.4.1. ReHo Comparison between MS and RS.** The comparison of MS and RS (MS > RS) showed an increased ReHo in dACC, left striatum (putamen), MPFC, and TPJ

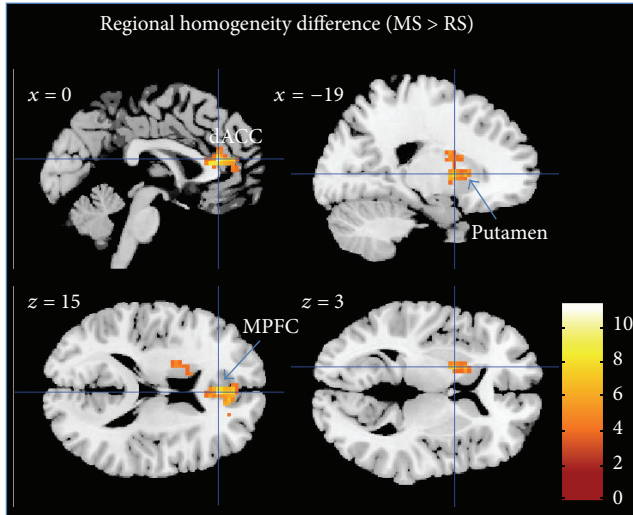


FIGURE 6: Regional homogeneity difference between MS and RS ( $p < 0.05$ , FWE-corrected). Bar plot represents the  $t$ -values. White labels indicate the coordinate of each slice in the MNI frame of reference ( $x, z$ ).

(supramarginal gyrus), FWE-corrected at  $p < 0.05$ ; see Figure 6 and Table 3.

The voxel-wise significance level was set at  $p < 0.001$  with a spatial extent threshold of 63 contiguous voxels, yielding a whole brain threshold of  $p < 0.05$  corrected for multiple comparisons using AlphaSim algorithm implemented in AFNI (data dimension:  $61 \times 73 \times 61$  voxels, Gaussian filter widths:  $\text{FWHM}_x = 13.25$ ,  $\text{FWHM}_y = 13.98$ , and  $\text{FWHM}_z = 12.13$ ).

**3.4.2. Longitudinal Analysis of ReHo Changes.** Longitudinal effects of meditation on the ReHo of RS activity were tested between time points using a paired  $t$ -test. However, no significant differences between time points were found. The voxel-wise significance level for this analysis was set at  $p < 0.001$  with a spatial extent threshold of 70 contiguous voxels, yielding a whole brain threshold of  $p < 0.05$  corrected for multiple comparisons using AlphaSim algorithm implemented in AFNI (data dimension:  $61 \times 73 \times 61$  voxels, Gaussian filter widths:  $\text{FWHM}_x = 14.28$ ,  $\text{FWHM}_y = 14.53$ , and  $\text{FWHM}_z = 12.48$ ).

## 4. Discussion

**4.1. Summary.** In the current study, for the first time, we investigated longitudinal effects of mindfulness meditation training on changes in functional connectivity between brain areas. To our knowledge, no previous study has directly compared a meditation condition with a resting condition using sophisticated methods like ICA, ReHo, and FC. During the analyses, we specifically focused on target regions and resting state network playing a role in affective disorders like depression such as the pgACC, the dACC, and the DMN.

We found significant differences in functional connectivity both between states (rest versus meditation) and

between time points (before versus after training). The ICA analysis showed differences in the internal consistency in the precuneus and the temporoparietal junction, increased during meditation, while the internal consistency of frontal brain regions decreased. The dACC further revealed reduced connectivity with anterior insula during meditation. As an indication of plastic changes following mindfulness meditation, reduced RSFC between the pgACC and dorsal medial prefrontal cortex was observed after meditation training.

### 4.2. Detailed Findings, Previous Work, and Explanations

**4.2.1. Imaging Findings.** ICA revealed that, during MS, in comparison to RS, the DMN component had stronger association of TPJ and precuneus, while activity in frontal, cingulate, and insular cortex was less associated with DMN. This may reflect the expected network dissociation as a function of cognitive task during meditation.

**4.2.2. Psychometry Findings.** Our findings indicate that the short-term practice of mindfulness meditation leads to differences in CES-D score before and after training. Nearly 50% reduction in depressive symptoms after mindfulness meditation training is consistent with recent meta-analyses reported by [3, 64].

Short-term meditation training yielded lowered acute feelings of tension at the time of scanning in our study. Likewise, our results emulate previous reports on the effects of meditation on well-being in anxiety trait and depression self-reports [65].

**4.2.3. Implication for Acute Effects and Plasticity Induction during Supporting Therapeutic Efficacy of Meditation.** The reported beneficial effects of mindfulness meditation for the treatment of emotional dysregulation in major depression and other affective disorders led us to hypothesize longitudinal changes in the RSFC. Changes in self-reports suggest that meditation training are very well in accordance with enduring changes in brain function as found in the literature and also in our study [66, 67]. In this sense, the longitudinal observation of RSFC decreases is very well in line with cross-sectional observations of altered functional responses [25] and RS connectivity, especially in the DMN. As one key region mediating depression-related symptoms, pgACC showed a longitudinal reduction in its connectivity with the PCC/precuneus region and conversely increased its connectivity with the right IPL. Such a reduction of intrinsic connectivity between pgACC and the posterior DMN components in precuneus would indeed reflect the expected directionality of connectivity changes if a hyperconnectivity within DMN in major depressive disorder (MDD), being considered a target of the antidepressant efficacy of meditation training. Sheline and colleagues [20] reported that such hyperconnectivity in the DMN exists for MDD; and, in their study, they highlighted the importance of abnormal hyperconnectivity of a “dorsal nexus.” Quite consistently, we also found a reduction of connectivity between pgACC and dmPFC, close to the previously reported dorsal nexus region. That such changes of RSFC after interventions of antidepressant action can

also be observed in healthy subjects was recently supported by a finding from Scheidegger and colleagues [68], who showed that, similar to our finding, a connectivity decrease of anterior and posterior DMN components, located in pgACC and PCC, was observed after 24 hrs of ketamine injection, mirroring the substances' maximum antidepressant effects in patients. In other words, the neuronal effects observed after 40 days of meditation, which was shown to affect depression-related psychometry, also reduced connectivity in a network that is hyperconnected in MDD, and, given the predominance of pgACC findings, this further suggests some specificity given the overall role of its dysfunction and abnormal connectivity in depression [29].

Longitudinal meditation training effects on functional connectivity are expected to be subserved by acute meditation effects when compared to resting conditions. Similar to the observed longitudinal reduction of RSFC between anterior and posterior DMN components we found an opposite pattern of connectivity changes from rest for pgACC compared to lateral and medial parietal DMN subcomponents. At the same time, the frontal DMN subcomponents seemed to aggregate as indicated by the increased RSFC between pgACC and dmPFC during meditation. Next to within-network connectivities our results showed convergence of state (between conditions) and trait (between time points) effects on the alteration of the functional connectivity between pgACC and right TPJ. Here increased connectivities between these two regions would be in line with functional role of TPJ in reorienting of attention [69]. In the meditation technique applied here, both focused attention and open monitoring aspects were combined. While increased pgACC-TPJ connectivity very well fits together with an improvement of open monitoring behavior such as "present moment awareness," it would equally well fit into potential antidepressant efficacy reversing narrowed or biased attention [30], although we did not include a direct measure of such behavioral effects.

When investigating the effects on the attention maintenance network [27], dACC was found to exert a reduced connectivity with its functional counterpart in the AI in MS compared to RS (Figure 2(b)). Previous studies reported insula activity during meditation [12] and anatomical changes in terms of increased gray matter [70, 71]. The dACC region was however not found to show increased gray matter in either study. This structural distinction of subregions with and without volumetric differences within the cingulo-opercular network would be in line with our structural decoupling during meditation. In the literature there are also findings of increases in dACC activity, especially in expert meditators [72] and recent investigations of focused breathing versus mind wandering reported increased activation in both dACC and AI [36]. When interpreting our findings in line with functional involvements of dACC and AI, next to specifications of the explicit study design, one also has to acknowledge that one region can be part of several networks. This is especially true for AI, which next to its involvement in focused attention, together with dACC, is activated together with MPFC during self-referential conditions and further plays an important role in orchestrating different networks

[73]. In contrast to the observed decoupling of AI and dACC in our seed-based analysis, the finding of reduced correlation with the DMN independent components of these two regions appears within a general observation of reduced IC connectivity in all task-positive regions (Figure 5). Here dACC and AI both showed similar effects of functional decoupling with DMN as an effect of differentiated task behavior during meditation, which however does not imply that they were necessarily any more functionally coupled. The differential effects on dACC and AI are also supported by the local metrics of the ReHo analysis.

Here, the comparison between RS and MS conditions revealed increased ReHo during MS in the MPFC and the dACC and subcortical regions but not in insula cortices. Since this is the first paper to our knowledge to apply ReHo measures to resting or active states in meditators, we cannot directly relate our observations to other findings. When trying to relate changes of temporal synchrony [62] to cross-sectional changes in patient populations, one likewise has to acknowledge that for MPFC both increases and decreases have been reported. While decreases have been for MPFC and ACC in depression [74], but also social anxiety [75] or Alzheimer disease [76], a recent study in bipolar depression rather indicated an increase in MPFC ReHo [74]. If indeed the functional distinction in increased versus decreased ReHo in bipolar versus MDD patients would mirror functional states that also discern rest versus active meditation, this would need to be subject to future investigations targeting the specificity and the physiological meaning of this observation. One important addition to the other connectivity-based findings is however provided by altered ReHo in putamen. This structure has been repeatedly reported in meditation studies [14, 77–80] but, distinct from the other main regions frequently reported, was not revealed by our connectivity analyses.

*4.3. Strengths and Limitations of the Current Study.* Mindfulness meditation and its neural correlates have been investigated in several studies [36, 81] by means of block-design fMRI. A limitation of such a design is that meditation is difficult to perform with a short on-and-off period (30–45 sec), especially for novice meditators. This limitation also results from the GLM itself, in which a longer epoch will decrease the design efficiency. However, the study of Barentsen et al., 2010, investigated continuous meditation by means of fMRI. They performed both SPM GLM and ICA on continuous meditation and focused on the difference between the meditation onset period and the maintained state of meditation.

One may argue that independent component comparison still would best be performed for components identified across all conditions. In our case, however, similar to Harrison et al., 2008, who used a continuous sad mood induction paradigm compared to RS, we decided to decompose independent components for both conditions separately, also following the method of Calhoun et al., 2008, who used ICASSO to insure ICA stability.

As we did not recruit a control group, our findings cannot be causally attributed solely to mindfulness meditation so

this will be important improvement for future directions of further investigation.

Moreover, the small sample size, due to discarding of incomplete subjects and imaging artifacts due to motion inside the scanner, limits the generalizability of findings. An increased sample size will increase the statistical power in a future study.

At baseline, the CES-D score of our sample slightly surpassed the clinical cutoff for depression (CES-D > 16), which could be a potential selection bias. Despite a negative diagnosis of depression based on a personal interview, some of the participants may have had a subclinical depression. In this aspect, our sample may still be representative of the general population due to the high prevalence of subclinical depression in general population; however inference to entirely healthy population is limited.

In our present study we did not collect physiological data. Future studies might consider inclusion of certain parameters, such as heart rate, breath rate, and respiration amplitude. High-frequency heart rate variability (HF-HRV) which is a measure of parasympathetic nervous system output that has been associated with enhanced self-regulation [80] would be of particular interest. Since meditation has been shown to increase HF-HRV, this might serve as a biomarker for meditation training-related effects. Recent findings however also suggest a direct relationship especially between HF-HRV and RSFC of, for example, cingulate regions [82], so that functional interpretation of connectivity changes could thus be directly related to autonomous nervous system tone. Further studies on MDD and other affective disorders may help to clarify the actual role of these changes in emotional regulation after short-term meditation, as well as its therapeutic effects.

## 5. Conclusion

We were able to show that the 40-day mindfulness meditation training resulted not only in amelioration of depression-related symptoms but also in changes in whole brain networks towards connectivity states usually found when comparing healthy controls to MDD patients in clinical studies. These longitudinal changes were in part mirrored in short-term effects when directly comparing RS and MS. This was especially evident in the involvement of the temporoparietal junction and its connectivity to anterior cingulate cortex, demonstrating cross-network interaction. Within-network consistency was most strongly affected in the DMN where anterior and posterior subcomponents segregated both longitudinally and in direct comparison of MS and RS. In particular effects in dACC which also showed altered local fluctuations during MS and in consequence strongest decoupling from DMN in direct comparison to RS spatially overlap with a network related to attention maintenance [27]; however individual analysis steps revealed variable cluster locations within anatomical boundaries of the midcingulate cortex. These network effects were in part paralleled by observations of altered local fluctuations, which further supported distinct effects in subregions of the salience network, as also supported by reduced connectivity between insula and dACC. Finally we could again identify the putamen as an important subcortical

region during meditation, characterized by increased local synchronization of signal variations. Critically, our results may provide insight into the brain circuits that potentially subserve the plastic antidepressant effects of mindfulness meditation training.

## Conflict of Interests

There is no conflict of interests in this paper.

## Acknowledgments

The authors would like to thank the mindfulness meditation training teacher Raúl Balaguer for his kindness for contributing his knowledge to the mindfulness research, Professor Dr. Daniel Pinazo Calatayud for his enthusiastic contribution to initializing the meditation study, Professor Dr. César Ávila for the kind support in fMRI study, Dr. Alfonso Barrós-Loscertales for his full support of research design, data analysis, and paper writing, Dr. Martin Walter for his expertise in clinical affective imaging research and paper preparation, and Viola Borchardt for her kind support in preparing the paper. This study is based on work supported by grants to MINECO (PSI2012-33054) and the Spanish National Drug Strategy (4623/2011) to Alfonso Barrós-Loscertales, as well as Spanish State Secretary of Research MINECO (CSO2012-34066) to Daniel Pinazo and Martin Walter (DFG-SFB779).

## References

- [1] R. Chambers, E. Gullone, and N. B. Allen, "Mindful emotion regulation: an integrative review," *Clinical Psychology Review*, vol. 29, no. 6, pp. 560–572, 2009.
- [2] N. A. S. Farb, A. K. Anderson, and Z. V. Segal, "The mindful brain and emotion regulation in mood disorders," *Canadian Journal of Psychiatry*, vol. 57, no. 2, pp. 70–77, 2012.
- [3] S. G. Hofmann, A. T. Sawyer, A. A. Witt, and D. Oh, "The effect of mindfulness-based therapy on anxiety and depression: a meta-analytic review," *Journal of Consulting and Clinical Psychology*, vol. 78, no. 2, pp. 169–183, 2010.
- [4] B. K. Hölzel, J. Carmody, M. Vangel et al., "Mindfulness practice leads to increases in regional brain gray matter density," *Psychiatry Research: Neuroimaging*, vol. 191, no. 1, pp. 36–43, 2011.
- [5] Y.-Y. Tang and M. I. Posner, "Special issue on mindfulness neuroscience," *Social Cognitive and Affective Neuroscience*, vol. 8, no. 1, pp. 1–3, 2013.
- [6] D. J. Siegel, "Mindfulness training and neural integration: differentiation of distinct streams of awareness and the cultivation of well-being," *Social Cognitive & Affective Neuroscience*, vol. 2, no. 4, pp. 259–263, 2007.
- [7] S. Bowen, N. Chawla, S. E. Collins et al., "Mindfulness-based relapse prevention for substance use disorders: a pilot efficacy trial," *Substance Abuse*, vol. 30, no. 4, pp. 295–305, 2009.
- [8] S. Rosenzweig, J. M. Greeson, D. K. Reibel, J. S. Green, S. A. Jasser, and D. Beasley, "Mindfulness-based stress reduction for chronic pain conditions: variation in treatment outcomes and role of home meditation practice," *Journal of Psychosomatic Research*, vol. 68, no. 1, pp. 29–36, 2010.
- [9] E. L. Garland, S. A. Gaylord, C. A. Boettiger, and M. O. Howard, "Mindfulness training modifies cognitive, affective, and physiological mechanisms implicated in alcohol dependence: results

- of a randomized controlled pilot trial,” *Journal of Psychoactive Drugs*, vol. 42, no. 2, pp. 177–192, 2010.
- [10] B. K. Hölzel, E. A. Hoge, D. N. Greve et al., “Neural mechanisms of symptom improvements in generalized anxiety disorder following mindfulness training,” *NeuroImage: Clinical*, vol. 2, pp. 448–458, 2013.
  - [11] J. A. Brewer, P. D. Worhunsky, J. R. Gray, Y.-Y. Tang, J. Weber, and H. Kober, “Meditation experience is associated with differences in default mode network activity and connectivity,” *Proceedings of the National Academy of Sciences of the United States of America*, vol. 108, no. 50, pp. 20254–20259, 2011.
  - [12] A. Lutz, J. Brefczynski-Lewis, T. Johnstone, and R. J. Davidson, “Regulation of the neural circuitry of emotion by compassion meditation: effects of meditative expertise,” *PLoS ONE*, vol. 3, no. 3, Article ID e1897, 2008.
  - [13] V. A. Taylor, V. Daneault, J. Grant et al., “Impact of meditation training on the default mode network during a restful state,” *Social Cognitive and Affective Neuroscience*, vol. 8, no. 1, pp. 4–14, 2013.
  - [14] J. A. Brefczynski-Lewis, A. Lutz, H. S. Schaefer, D. B. Levinson, and R. J. Davidson, “Neural correlates of attentional expertise in long-term meditation practitioners,” *Proceedings of the National Academy of Sciences of the United States of America*, vol. 104, no. 27, pp. 11483–11488, 2007.
  - [15] J. H. Jang, W. H. Jung, D.-H. Kang et al., “Increased default mode network connectivity associated with meditation,” *Neuroscience Letters*, vol. 487, no. 3, pp. 358–362, 2011.
  - [16] M. D. Fox and M. E. Raichle, “Spontaneous fluctuations in brain activity observed with functional magnetic resonance imaging,” *Nature Reviews Neuroscience*, vol. 8, no. 9, pp. 700–711, 2007.
  - [17] M. D. Greicius, K. Supekar, V. Menon, and R. F. Dougherty, “Resting-state functional connectivity reflects structural connectivity in the default mode network,” *Cerebral Cortex*, vol. 19, no. 1, pp. 72–78, 2009.
  - [18] M. E. Raichle, A. M. MacLeod, A. Z. Snyder, W. J. Powers, D. A. Gusnard, and G. L. Shulman, “A default mode of brain function,” *Proceedings of the National Academy of Sciences of the United States of America*, vol. 98, no. 2, pp. 676–682, 2001.
  - [19] R. B. Mars, F.-X. Neubert, M. P. Noonan, J. Sallet, I. Toni, and M. F. S. Rushworth, “On the relationship between the ‘default mode network’ and the ‘social brain,’” *Frontiers in Human Neuroscience*, vol. 6, article 189, 2012.
  - [20] Y. I. Sheline, J. L. Price, Z. Yan, and M. A. Mintun, “Resting-state functional MRI in depression unmasks increased connectivity between networks via the dorsal nexus,” *Proceedings of the National Academy of Sciences of the United States of America*, vol. 107, no. 24, pp. 11020–11025, 2010.
  - [21] D. A. Gusnard, E. Akbudak, G. L. Shulman, and M. E. Raichle, “Medial prefrontal cortex and self-referential mental activity: relation to a default mode of brain function,” *Proceedings of the National Academy of Sciences of the United States of America*, vol. 98, no. 7, pp. 4259–4264, 2001.
  - [22] K. N. Ochsner and J. J. Gross, “The cognitive control of emotion,” *Trends in Cognitive Sciences*, vol. 9, no. 5, pp. 242–249, 2005.
  - [23] C. Lemogne, G. le Bastard, H. Mayberg et al., “In search of the depressive self: extended medial prefrontal network during self-referential processing in major depression,” *Social Cognitive and Affective Neuroscience*, vol. 4, no. 3, pp. 305–312, 2009.
  - [24] M. G. Berman, S. Peltier, D. E. Nee, E. Kross, P. J. Deldin, and J. Jonides, “Depression, rumination and the default network,” *Social Cognitive and Affective Neuroscience*, vol. 6, no. 5, pp. 548–555, 2011.
  - [25] M. Walter, A. Henning, S. Grimm et al., “The relationship between aberrant neuronal activation in the pregenual anterior cingulate, altered glutamatergic metabolism, and anhedonia in major depression,” *Archives of General Psychiatry*, vol. 66, no. 5, pp. 478–486, 2009.
  - [26] G. Bush, P. Luu, and M. I. Posner, “Cognitive and emotional influences in anterior cingulate cortex,” *Trends in Cognitive Sciences*, vol. 4, no. 6, pp. 215–222, 2000.
  - [27] N. U. F. Dosenbach, D. A. Fair, A. L. Cohen, B. L. Schlaggar, and S. E. Petersen, “A dual-networks architecture of top-down control,” *Trends in Cognitive Sciences*, vol. 12, no. 3, pp. 99–105, 2008.
  - [28] M.-J. van Tol, N. J. A. van der Wee, O. A. van den Heuvel et al., “Regional brain volume in depression and anxiety disorders,” *Archives of General Psychiatry*, vol. 67, no. 10, pp. 1002–1011, 2010.
  - [29] D. I. Horn, C. Yu, J. Steiner et al., “Glutamatergic and resting-state functional connectivity correlates of severity in major depression—the role of pregenual anterior cingulate cortex and anterior insula,” *Frontiers in Systems Neuroscience*, vol. 4, article 33, 2010.
  - [30] S. G. Disner, C. G. Beevers, E. A. P. Haigh, and A. T. Beck, “Neural mechanisms of the cognitive model of depression,” *Nature Reviews Neuroscience*, vol. 12, no. 8, pp. 467–477, 2011.
  - [31] R. H. Kaiser, J. R. Andrews-Hanna, T. D. Wager, and D. A. Pizzagalli, “Large-scale network dysfunction in major depressive disorder: a meta-analysis of resting-state functional connectivity,” *JAMA Psychiatry*, vol. 72, no. 6, pp. 603–611, 2015.
  - [32] B. B. Biswal, M. Mennes, X.-N. Zuo et al., “Toward discovery science of human brain function,” *Proceedings of the National Academy of Sciences of the United States of America*, vol. 107, no. 10, pp. 4734–4739, 2010.
  - [33] D. L. Schacter, D. R. Addis, and R. L. Buckner, “Episodic simulation of future events: concepts, data, and applications,” *Annals of the New York Academy of Sciences*, vol. 1124, no. 1, pp. 39–60, 2008.
  - [34] F. Schneider, F. Bermpohl, A. Heinzl et al., “The resting brain and our self: self-relatedness modulates resting state neural activity in cortical midline structures,” *Neuroscience*, vol. 157, no. 1, pp. 120–131, 2008.
  - [35] S. Krüger, D. Seminowicz, K. Goldapple, S. H. Kennedy, and H. S. Mayberg, “State and trait influences on mood regulation in bipolar disorder: blood flow differences with an acute mood challenge,” *Biological Psychiatry*, vol. 54, no. 11, pp. 1274–1283, 2003.
  - [36] J. Dickenson, E. T. Berkman, J. Arch, and M. D. Lieberman, “Neural correlates of focused attention during a brief mindfulness induction,” *Social Cognitive and Affective Neuroscience*, vol. 8, no. 1, pp. 40–47, 2013.
  - [37] S. M. Smith, K. L. Miller, G. Salimi-Khorshidi et al., “Network modelling methods for FMRI,” *NeuroImage*, vol. 54, no. 2, pp. 875–891, 2011.
  - [38] B. Zhang, M. Li, W. Qin et al., “Altered functional connectivity density in major depressive disorder at rest,” *European Archives of Psychiatry and Clinical Neuroscience*, 2015.
  - [39] J. D. Kendall and M. G. Gibbons, *Rank Correlation Methods*, Edward Arnold, London, UK, 5th edition, 1990.
  - [40] Z. Yao, L. Wang, Q. Lu, H. Liu, and G. Teng, “Regional homogeneity in depression and its relationship with separate depressive symptom clusters: a resting-state fMRI study,” *Journal of Affective Disorders*, vol. 115, no. 3, pp. 430–438, 2009.

- [41] Z. Liu, C. Xu, Y. Xu et al., "Decreased regional homogeneity in insula and cerebellum: a resting-state fMRI study in patients with major depression and subjects at high risk for major depression," *Psychiatry Research—Neuroimaging*, vol. 182, no. 3, pp. 211–215, 2010.
- [42] M.-J. van Tol, L. R. Demenescu, N. J. A. van der Wee et al., "Functional magnetic resonance imaging correlates of emotional word encoding and recognition in depression and anxiety disorders," *Biological Psychiatry*, vol. 71, no. 7, pp. 593–602, 2012.
- [43] R. A. Baer, "Mindfulness training as a clinical intervention: a conceptual and empirical review," *Clinical Psychology: Science and Practice*, vol. 10, no. 2, pp. 125–143, 2006.
- [44] J. Kabat-Zinn, *Full Catastrophe Living: Using the Wisdom of Your Body and Mind to Face Stress, Pain, and Illness*, Rev Upd Edition, Bantam, New York, NY, USA, 1990.
- [45] S. C. Hayes, J. B. Luoma, F. W. Bond, A. Masuda, and J. Lillis, "Acceptance and commitment therapy: model, processes and outcomes," *Behaviour Research and Therapy*, vol. 44, no. 1, pp. 1–25, 2006.
- [46] E. Andrade, C. Arce, J. Torrado, J. Garrido, C. De Francisco, and I. Arce, "Factor structure and invariance of the POMS mood state questionnaire in Spanish," *Spanish Journal of Psychology*, vol. 13, no. 1, pp. 444–452, 2010.
- [47] D. M. McNair, M. Lorr, and L. F. Droppleman, *Manual for the Profile of Mood States*, Educational and Industrial Testing Service, San Diego, Calif, USA, 1971.
- [48] L. S. Radloff, "The CES-D scale: a self-report depression scale for research in the general population," *Applied Psychological Measurement*, vol. 1, no. 3, pp. 385–401, 1977.
- [49] C. D. Spielberger, R. L. Gorsuch, P. R. Lushene, P. R. Vagg, and G. A. Jacobs, *Manual for the State-Trait Anxiety Inventory*, Consulting Psychologists Press, 1983.
- [50] S. M. Smith, M. Jenkinson, M. W. Woolrich et al., "Advances in functional and structural MR image analysis and implementation as FSL," *NeuroImage*, vol. 23, supplement 1, pp. S208–S219, 2004.
- [51] C.-G. Yan and Y.-F. Zang, "DPARSF: a MATLAB toolbox for 'pipeline' data analysis of resting-state fMRI," *Frontiers in System Neuroscience*, vol. 4, article 13, 2010.
- [52] B. Biswal, F. Zerrin Yetkin, V. M. Haughton, and J. S. Hyde, "Functional connectivity in the motor cortex of resting human brain using echo-planar MRI," *Magnetic Resonance in Medicine*, vol. 34, no. 4, pp. 537–541, 1995.
- [53] M. J. Lowe, B. J. Mock, and J. A. Sorenson, "Functional connectivity in single and multislice echoplanar imaging using resting-state fluctuations," *NeuroImage*, vol. 7, no. 2, pp. 119–132, 1998.
- [54] K. Murphy, R. M. Birn, D. A. Handwerker, T. B. Jones, and P. A. Bandettini, "The impact of global signal regression on resting state correlations: are anti-correlated networks introduced?" *NeuroImage*, vol. 44, no. 3, pp. 893–905, 2009.
- [55] J. L. Price and W. C. Drevets, "Neurocircuitry of mood disorders," *Neuropsychopharmacology*, vol. 35, no. 1, pp. 192–216, 2010.
- [56] A. Lord, D. Horn, M. Breakspear, and M. Walter, "Changes in community structure of resting state functional connectivity in unipolar depression," *PLoS ONE*, vol. 7, no. 8, Article ID e41282, 2012.
- [57] V. D. Calhoun, T. Adali, G. D. Pearlson, and J. J. Pekar, "A method for making group inferences from functional MRI data using independent component analysis," *Human Brain Mapping*, vol. 14, no. 3, pp. 140–151, 2001.
- [58] S. Chen, T. J. Ross, W. Zhan et al., "Group independent component analysis reveals consistent resting-state networks across multiple sessions," *Brain Research*, vol. 1239, pp. 141–151, 2008.
- [59] V. D. Calhoun, K. A. Kiehl, and G. D. Pearlson, "Modulation of temporally coherent brain networks estimated using ICA at rest and during cognitive tasks," *Human Brain Mapping*, vol. 29, no. 7, pp. 828–838, 2008.
- [60] B. J. Harrison, J. Pujol, H. Ortiz, A. Fornito, C. Pantelis, and M. Yücel, "Modulation of brain resting-state networks by sad mood induction," *PLoS ONE*, vol. 3, no. 3, Article ID e1794, p. 12, 2008.
- [61] A. J. Bell and T. J. Sejnowski, "The 'independent components' of natural scenes are edge filters," *Vision Research*, vol. 37, no. 23, pp. 3327–3338, 1997.
- [62] Y. Zang, T. Jiang, Y. Lu, Y. He, and L. Tian, "Regional homogeneity approach to fMRI data analysis," *NeuroImage*, vol. 22, no. 1, pp. 394–400, 2004.
- [63] P. M. Lewinsohn, J. R. Seeley, R. E. Roberts, and N. B. Allen, "Center for Epidemiologic Studies Depression Scale (CES-D) as a screening instrument for depression among community-residing older adults," *Psychology and Aging*, vol. 12, no. 2, pp. 277–287, 1997.
- [64] M. De Vibe, A. Bjørndal, E. Tipton, K. T. Hammerstrøm, and K. Kowalski, "Mindfulness based stress reduction (MBSR) for improving health, quality of life, and social functioning in adults," *Campbell Systematic Reviews*, vol. 8, no. 3, 127 pages, 2012.
- [65] S. L. Shapiro, G. E. Schwartz, and G. Bonner, "Effects of mindfulness-based stress reduction on medical and premedical students," *Journal of Behavioral Medicine*, vol. 21, no. 6, pp. 581–599, 1998.
- [66] G. Desbordes, L. T. Negi, T. W. W. Pace, B. A. Wallace, C. L. Raison, and E. L. Schwartz, "Effects of mindful-attention and compassion meditation training on amygdala response to emotional stimuli in an ordinary, non-meditative state," *Frontiers in Human Neuroscience*, vol. 6, article 292, 2012.
- [67] H. A. Slagter, R. J. Davidson, and A. Lutz, "Mental training as a tool in the neuroscientific study of brain and cognitive plasticity," *Frontiers in Human Neuroscience*, vol. 5, p. 17, 2011.
- [68] M. Scheidegger, M. Walter, M. Lehmann et al., "Ketamine decreases resting state functional network connectivity in healthy subjects: implications for antidepressant drug action," *PLoS ONE*, vol. 7, no. 9, Article ID e44799, 2012.
- [69] N. U. F. Dosenbach, D. A. Fair, F. M. Miezin et al., "Distinct brain networks for adaptive and stable task control in humans," *Proceedings of the National Academy of Sciences of the United States of America*, vol. 104, no. 26, pp. 11073–11078, 2007.
- [70] S. W. Lazar, C. E. Kerr, R. H. Wasserman et al., "Meditation experience is associated with increased cortical thickness," *NeuroReport*, vol. 16, no. 17, pp. 1893–1897, 2005.
- [71] B. K. Hölzel, U. Ott, H. Hempel et al., "Differential engagement of anterior cingulate and adjacent medial frontal cortex in adept meditators and non-meditators," *Neuroscience Letters*, vol. 421, no. 1, pp. 16–21, 2007.
- [72] A. Lutz, L. L. Greischar, D. M. Perlman, and R. J. Davidson, "BOLD signal in insula is differentially related to cardiac function during compassion meditation in experts vs. novices," *NeuroImage*, vol. 47, no. 3, pp. 1038–1046, 2009.
- [73] V. Menon and L. Q. Uddin, "Saliency, switching, attention and control: a network model of insula function," *Brain Structure & Function*, vol. 214, no. 5–6, pp. 655–667, 2010.

- [74] C.-H. Liu, X. Ma, F. Li et al., "Regional homogeneity within the default mode network in bipolar depression: a resting-state functional magnetic resonance imaging study," *PLoS ONE*, vol. 7, no. 11, Article ID e48181, 2012.
- [75] C. Qiu, W. Liao, J. Ding et al., "Regional homogeneity changes in social anxiety disorder: a resting-state fMRI study," *Psychiatry Research. Neuroimaging*, vol. 194, no. 1, pp. 47–53, 2011.
- [76] Z. Zhang, Y. Liu, T. Jiang et al., "Altered spontaneous activity in Alzheimer's disease and mild cognitive impairment revealed by Regional Homogeneity," *NeuroImage*, vol. 59, no. 2, pp. 1429–1440, 2012.
- [77] T. W. Kjaer, C. Bertelsen, P. Piccini, D. Brooks, J. Alving, and H. C. Lou, "Increased dopamine tone during meditation-induced change of consciousness," *Cognitive Brain Research*, vol. 13, no. 2, pp. 255–259, 2002.
- [78] S. W. Lazar, G. Bush, R. L. Gollub, G. L. Fricchione, G. Khalsa, and H. Benson, "Functional brain mapping of the relaxation response and meditation," *Neuroreport*, vol. 11, no. 7, pp. 1581–1585, 2000.
- [79] Y.-Y. Tang, Y. Ma, Y. Fan et al., "Central and autonomic nervous system interaction is altered by short-term meditation," *Proceedings of the National Academy of Sciences of the United States of America*, vol. 106, no. 22, pp. 8865–8870, 2009.
- [80] D. J. Libby, P. D. Worhunsky, C. E. Pilver, and J. A. Brewer, "Meditation-induced changes in high-frequency heart rate variability predict smoking outcomes," *Frontiers in Human Neuroscience*, vol. 6, article 54, 2012.
- [81] K. B. Børntsen, H. Stødkilde-Jørgensen, B. Sommerlund et al., "An investigation of brain processes supporting meditation," *Cognitive Processing*, vol. 11, no. 1, pp. 57–84, 2010.
- [82] C. Chang, C. D. Metzger, G. H. Glover, J. H. Duyn, H.-J. Heinze, and M. Walter, "Association between heart rate variability and fluctuations in resting-state functional connectivity," *NeuroImage*, vol. 68, pp. 93–104, 2013.

## Research Article

# Multilevel Deficiency of White Matter Connectivity Networks in Alzheimer's Disease: A Diffusion MRI Study with DTI and HARDI Models

Tao Wang,<sup>1,2,3</sup> Feng Shi,<sup>2</sup> Yan Jin,<sup>2</sup> Pew-Thian Yap,<sup>2</sup> Chong-Yaw Wee,<sup>2</sup>  
Jianyue Zhang,<sup>4</sup> Cece Yang,<sup>1,3</sup> Xia Li,<sup>1,3</sup> Shifu Xiao,<sup>1,3</sup> and Dinggang Shen<sup>2,5</sup>

<sup>1</sup>Department of Geriatric Psychiatry, Shanghai Mental Health Center, Shanghai Jiao Tong University School of Medicine, Shanghai, China

<sup>2</sup>IDEA Lab, Department of Radiology and BRIC, University of North Carolina at Chapel Hill, Chapel Hill, NC, USA

<sup>3</sup>Alzheimer's Disease and Related Disorders Center, Shanghai Jiao Tong University, Shanghai, China

<sup>4</sup>Department of Radiology, Shanghai Mental Health Center, Shanghai Jiao Tong University School of Medicine, Shanghai, China

<sup>5</sup>Department of Brain and Cognitive Engineering, Korea University, Seoul, Republic of Korea

Correspondence should be addressed to Shifu Xiao; [xiaoshifu@msn.com](mailto:xiaoshifu@msn.com) and Dinggang Shen; [dgshen@med.unc.edu](mailto:dgshen@med.unc.edu)

Received 23 June 2015; Accepted 22 November 2015

Academic Editor: Clive R. Bramham

Copyright © 2016 Tao Wang et al. This is an open access article distributed under the Creative Commons Attribution License, which permits unrestricted use, distribution, and reproduction in any medium, provided the original work is properly cited.

Alzheimer's disease (AD) is the most common form of dementia in elderly people. It is an irreversible and progressive brain disease. In this paper, we utilized diffusion-weighted imaging (DWI) to detect abnormal topological organization of white matter (WM) structural networks. We compared the differences between WM connectivity characteristics at global, regional, and local levels in 26 patients with probable AD and 16 normal control (NC) elderly subjects, using connectivity networks constructed with the diffusion tensor imaging (DTI) model and the high angular resolution diffusion imaging (HARDI) model, respectively. At the global level, we found that the WM structural networks of both AD and NC groups had a small-world topology; however, the AD group showed a significant decrease in both global and local efficiency, but an increase in clustering coefficient and the average shortest path length. We further found that the AD patients had significantly decreased nodal efficiency at the regional level, as well as weaker connections in multiple local cortical and subcortical regions, such as precuneus, temporal lobe, hippocampus, and thalamus. The HARDI model was found to be more advantageous than the DTI model, as it was more sensitive to the deficiencies in AD at all of the three levels.

## 1. Introduction

Alzheimer's disease (AD) is the most common form of dementia in elderly people and is characterized by chronic cortical atrophy and neurodegeneration, resulting in behavioral changes, loss of memory and language function, and general cognitive decline [1]. It is an irreversible and progressive brain disease and usually diagnosed in people older than 65. Nearly 36 million people worldwide are affected by AD, with 5.2 million alone just in the United States [2].

Tau and amyloid beta ( $A\beta$ ) in cerebrospinal fluid are considered to be reliable biomarkers of AD [3]. However, the invasiveness, cost, and availability associated with the measurement of these quantities are significant drawbacks.

On the other hand, magnetic resonance imaging (MRI) has been widely recognized as a noninvasive means for neurodiagnosis and disease staging. Previous studies using T1-weighted structural MRI revealed AD-induced gray matter (GM) atrophy in multiple brain regions, including the hippocampal and entorhinal cortices [4, 5], the temporal and cingulate gyri, the precuneus, the insular cortices, the caudate nuclei, the frontal cortices [6], the sensorimotor cortices, the occipital poles, the cerebellum, and the medial thalami [7].

On the other hand, diffusion-weighted magnetic resonance imaging (DWI) [8] can recover the local profile of water diffusion in tissue, yielding information on white matter (WM) integrity and connectivity that is not available from standard structural MRI. Specifically, tractography methods

[9, 10] can be used to fit continuous streamlines through directional diffusion data at each voxel for reconstructing WM fiber tracts. With the obtained tractography, WM integrity can be analyzed with both region-of-interest- (ROI-) based analysis, for example, tract-based spatial statistics (TBSS) [11] and fiber clustering [12, 13], and parcellation-based connectome analysis [14].

WM abnormalities in AD were reported in previous studies. Liu et al. [15] performed voxelwise TBSS to compare fractional anisotropy (FA) between the AD patients and the healthy controls. Multiple WM tracts, such as parahippocampal WM, cingulum, uncinate fasciculus, inferior and superior longitudinal fasciculus, and corpus callosum, showed decreased FA in the AD group. Jin et al. [16] used the tract-based clustering method to relate fornix degeneration to cognitive decline in AD with various diffusion-derived measures. Mean diffusivity (MD) was shown to be more sensitive to the group difference among AD and normal controls than FA did. Li et al. [17] proposed a spectral diffusional connectivity framework to explore the connectivity deficit in AD. The framework was based on studying eigenvalues of the Laplacian matrix of the diffusion tensor field at the voxel level. The peaks of the diffusional connectivity spectra were shifted in the AD group compared to the normal controls that did not shift. Daianu et al. [18] found widespread breakdown in AD in the 68-ROI based connectivity networks with multiple connectivity metrics on the “ $k$ -core” structure.

Importantly, WM tracts can be used to form the connectivity networks that give comprehensive pictures of interactions between different brain regions. A WM connectivity network can be described mathematically as a graph consisting of (1) a collection of nodes, representing the ROIs and (2) a set of edges between nodes, describing the connections (e.g., fiber counts) between ROI pairs. The characteristics of a connectivity network can be described using metrics at three hierarchical levels: global, regional, and local.

The stability of connectivity networks is influenced by multiple factors, including field strength [19, 20], scanners [21], imaging acquisition parameters [22], and tractography parameters [23]. Zhan et al. [24] compared several tractography and feature extraction methods in relation to AD diagnostic accuracy. Among these factors, the choice of diffusion models is found to be the most influential. The most commonly used approach, namely, diffusion tensor imaging (DTI), is based on the Gaussian assumption of water diffusion. This approach works well in regions with unidirectional fiber bundles, but this model may fail in regions with fiber crossings, which may introduce tractography errors in these regions. To address this issue, advanced models for high angular resolution diffusion imaging (HARDI) were proposed to estimate orientation distribution functions (ODF) [25, 26] at each voxel. By detecting the peaks (i.e., local maxima) of the ODF, one can then infer the number of directions contained in each voxel.

In this study, we investigate the global, regional, and local changes of whole-brain connectivity networks in AD patients in comparison to healthy elderly subjects. DTI and HARDI models are used to construct two different sets of connectivity networks for comparison. Such a systematic network analysis

at multiple levels on AD, to our knowledge, has not been attempted previously.

## 2. Methods

*2.1. Participant Recruitment.* This study involved 26 patients who were diagnosed with probable AD at the Alzheimer’s Disease and Related Disorders Center (ADRDC) in the tertiary hospital of Shanghai Mental Health Center (SMHC) at Shanghai Jiao Tong University School of Medicine. 16 cognitively healthy elderly subjects from the community of Shanghai Chang Ning district were included as the normal control (NC) group. Subjects were enrolled via self-referral or referral from families or physicians. The study was conducted from May 2011 to May 2012 at ADRDC. The SMHC Institution’s Ethical Committee approved the consent form and the study protocol. The study was carried out in accordance with the Declaration of Helsinki. Informed consent was obtained from all subjects and/or their legal guardians.

The ages of the AD subjects enrolled ranged from 50s to 90s. Prior to enrollment, patients provided their medical history and were given physical and neurological examinations, laboratory tests, and both T1-weighted and fluid-attenuated inversion recovery (FLAIR) MRI scans. Enrollment criteria included (1) the National Institute of Neurological and Communicative Disorders and Stroke/Alzheimer’s Disease and Related Disorder Association (NINCDS/ADRDA) criteria for probable AD [27]; (2) the Diagnostic and Statistical Manual for Mental Disorders, 4th edition (DSM-IV) criteria for the Alzheimer’s dementia; (3) a Hachinski Ischemia Score less than 4; (4) the systolic blood pressure between 95 and 160 and the diastolic blood pressure between 60 and 95; (5) identification of a responsible and consistent caregiver; (6) absence of diabetes, renal impairment, significant systemic conditions, psychiatric disorders, seizures, or traumatic brain injuries that could compromise their cognitive or brain functions; (7) significant brain abnormalities on the patient’s T1-weighted MRI; (8) clinical score requirements. In the Chinese version of the Mini-Mental Status Exam (MMSE) [28], there are three cut-off thresholds for AD diagnosis according to education levels: (1) AD subjects who had not been educated exhibited MMSE scores  $<18$ ; (2) those with elementary school education exhibited MMSE scores  $<21$ ; (3) those with higher than middle school education exhibited MMSE scores  $<25$ . The Clinical Dementia Rating (CDR) scale [29] was equal or more than 1.

The NC group was cognitively functioning healthy individuals. The NC group did not have any history of cognitive decline, neurological disorders, or uncontrolled systemic medical disorders. Their CDR scales were equal to 0. All subjects in the study were required to have fewer than two lacunar ischemia strokes (of diameter  $<1$  cm) in the brain, as revealed by FLAIR.

The demography and clinical scores for the AD group and the NC group are listed in Table 1. No significant differences between the two groups were observed in age or education. The difference was observed in gender. However, the effects of gender, age, education level, and brain size would be regressed

TABLE 1: The demography and clinical scores of the subjects in the study. The  $p$  values are based on the two-sample  $t$ -tests except the gender. The gender ratio was examined by the Chi-squared test.

	NC ( $n = 16$ )	AD ( $n = 26$ )	$p$ value
Age (years)	70.1 $\pm$ 7.5	69.5 $\pm$ 7.1	0.81
Male/female	11/5	8/18	0.03
Education (years)	10.6 $\pm$ 3.2	10.4 $\pm$ 3.9	0.91
CDR	0.0 $\pm$ 0.0	2.0 $\pm$ 0.7	<0.001
MMSE	25.3 $\pm$ 3.6	15.2 $\pm$ 6.5	<0.001

out in our analysis. As expected, the group difference was observed in the MMSE ( $p < 0.001$ ) and CDR scores ( $p < 0.001$ ).

**2.2. MR Image Acquisition.** MRI images were scanned with a Siemens MAGNETOM VERIO 3 T scanner at SMHC. T1-weighted images were obtained with 128 sagittal slices using the 3D magnetization prepared rapid acquisition gradient echo (MPRAGE) sequence with the following parameters: TR = 2,530 ms, TE = 3.39 ms, flip angle = 7°, and spatial resolution =  $1 \times 1 \times 1.3 \text{ mm}^3$ , and the acquisition time was 8 minutes 7 seconds. The DWI images were acquired with 75 axial slices by using an echo planar imaging (EPI) sequence that covered the whole brain. The acquisition parameters were as follows: TR = 10,000 ms, TE = 91 ms, and spatial resolution =  $2 \times 2 \times 2 \text{ mm}^3$ . A total volume of 62 directions was acquired, where two volumes were without diffusion gradient ( $b = 0$ ) and the rest 60 volumes were with diffusion gradient of  $b = 1,000 \text{ s/mm}^2$ . The acquisition time was 5 minutes and 42 seconds.

**2.3. Image Preprocessing.** T1-weighted images were first resampled to be 1 mm isotropic, intensity inhomogeneity corrected [30], and skull stripped to remove nonbrain tissues [31]. The resulting images were then tissue segmented to separate GM, WM, and cerebrospinal fluid (CSF) with FSL FAST (<http://fsl.fmrib.ox.ac.uk/fsl/fslwiki/>). DWI images were skull stripped and then corrected for eddy-current induced distortion with FSL. FA and MD images were then extracted from DWI data after diffusion tensor fitting.

**2.4. Network Construction.** Whole-brain tractography was performed with both DTI and HARDI models. For DTI, the diffusion tensors were fitted to the data using a weighted-least-squares estimation algorithm and the eigenvector of the largest eigenvalue was taken as the principal diffusion direction [32]. Seed points were chosen as voxels with FA > 0.3. The maximum turning angle was set to 45° and tracking was stopped when FA < 0.2. The allowed fiber length was at minimum, 20 mm, and at maximum, 300 mm. For HARDI, ODFs were estimated with dictionary-based spherical deconvolution [26]. A maximum of three peaks were detected from the ODF at each voxel [26]. Four seeds were randomly sampled within each seed voxel. The criteria of fiber tracking were the same for both methods. The resulting

tractography was manually visualized and checked in ParaView (Kitware, <http://www.paraview.org/>).

The Automated Anatomical Labeling (AAL) template [33] is a widely used high-resolution T1-weighted brain parcellation based on a single adult subject, which includes 90 cortical and subcortical brain regions for the cerebrum. The names and abbreviations of these 90 ROIs are listed in Table 2. First, we nonlinearly registered the AAL template to each subject's segmented T1-weighted image using HAMMER [34]. Then, the T1-weighted image was rigidly aligned to the FA image. The original 90 ROIs of the AAL template were transferred to each individual's DWI space using the deformation fields and the affine transformation matrix generated during the registration step. These ROIs were used as nodes in the connectivity network for each subject.

Two ROIs were considered anatomically connected, if there were fibers traversing them. In the network, the edge, connecting the nodes representing these two ROIs, was defined as the number of fibers connecting them. Two ROIs were considered connected if there were no less than four fibers between them, which has been proven effective to reduce false-positive connections [35–37]. As a result, the WM connectivity network, represented by a symmetric  $90 \times 90$  matrix, was constructed for each subject. The network was weighted and undirected.

**2.5. Multilevel Network Measures.** Three hierarchical levels (global, regional, and local) of complex network measures were used to compare the measures of connectivity networks constructed in Section 2.4 between the AD group and the NC group. The measures were calculated with the GRETNAToolbox (<https://www.nitrc.org/projects/gretna/>). For a detailed review of those measures, please see [38].

**2.5.1. Global Measures.** Global and local network efficiencies are used to describe global and local characteristics of parallel information transfer in a network. Global network efficiency quantifies the exchange of information across the entire brain:

$$E_{\text{glob}} = \frac{1}{N(N-1)} \sum_{i=1}^N \sum_{j=1, j \neq i}^N \frac{1}{L_{ij}}, \quad (1)$$

where  $L_{ij}$  is the shortest absolute path length between node  $i$  and node  $j$ .  $N$  is the total number of nodes. Similarly, local network efficiency of node  $i$  is defined as

$$E_{\text{loc}}^i = \frac{1}{N_{G_i}(N_{G_i}-1)} \sum_{j=1}^{N_{G_i}} \sum_{k=1, k \neq j}^{N_{G_i}} \frac{1}{L_{jk}}, \quad (2)$$

where  $G_i$  is a subgraph comprising nodes directly connected to node  $i$ , and  $N_{G_i}$  is the node number of the subgraph  $G_i$ . Therefore, the average local network efficiency for the whole brain is  $E_{\text{loc}} = (1/N) \sum_{i=1}^N E_{\text{loc}}^i$ .

TABLE 2: Names and abbreviations of the 90 ROIs defined in the AAL template.

Index*	Region	Abbreviation
1, 2	Precentral gyrus	PreCG
3, 4	Superior frontal gyrus (dorsal)	SFGdor
5, 6	Orbitofrontal cortex (superior)	ORBsupb
7, 8	Middle frontal gyrus	MFG
9, 10	Orbitofrontal cortex (middle)	ORBmid
11, 12	Inferior frontal gyrus (opercular)	IFGoperc
13, 14	Inferior frontal gyrus (triangular)	IFGtriang
15, 16	Orbitofrontal cortex (inferior)	ORBinf
17, 18	Rolandic operculum	ROL
19, 20	Supplementary motor area	SMA
21, 22	Olfactory	OLF
23, 24	Superior frontal gyrus (medial)	SFGmed
25, 26	Orbitofrontal cortex (medial)	ORBmed
27, 28	Rectus gyrus	REC
29, 30	Insula	INS
31, 32	Anterior cingulate gyrus	ACG
33, 34	Middle cingulate gyrus	MCG
35, 36	Posterior cingulate gyrus	PCG
37, 38	Hippocampus	HIP
39, 40	Parahippocampal gyrus	PHG
41, 42	Amygdala	AMYG
43, 44	Calcarine	CAL
45, 46	Cuneus	CUN
47, 48	Lingual gyrus	LING
49, 50	Superior occipital gyrus	SOG
51, 52	Middle occipital gyrus	MOG
53, 54	Inferior occipital gyrus	IOG
55, 56	Fusiform gyrus	FFG
57, 58	Postcentral gyrus	PoCG
59, 60	Superior parietal gyrus	SPG
61, 62	Inferior parietal lobule	IPL
63, 64	Supramarginal gyrus	SMG
65, 66	Angular gyrus	ANG
67, 68	Precuneus	PCUN
69, 70	Paracentral lobule	PCL
71, 72	Caudate	CAU
73, 74	Putamen	PUT
75, 76	Pallidum	PAL
77, 78	Thalamus	THA
79, 80	Heschl gyrus	HES
81, 82	Superior temporal gyrus	STG
83, 84	Temporal pole (superior)	TPOsup
85, 86	Middle temporal gyrus	MTG
87, 88	Temporal pole (middle)	TPOmid
89, 90	Inferior temporal	ITG

\*The odd and even indices indicate the regions in the left and right hemispheres, respectively.

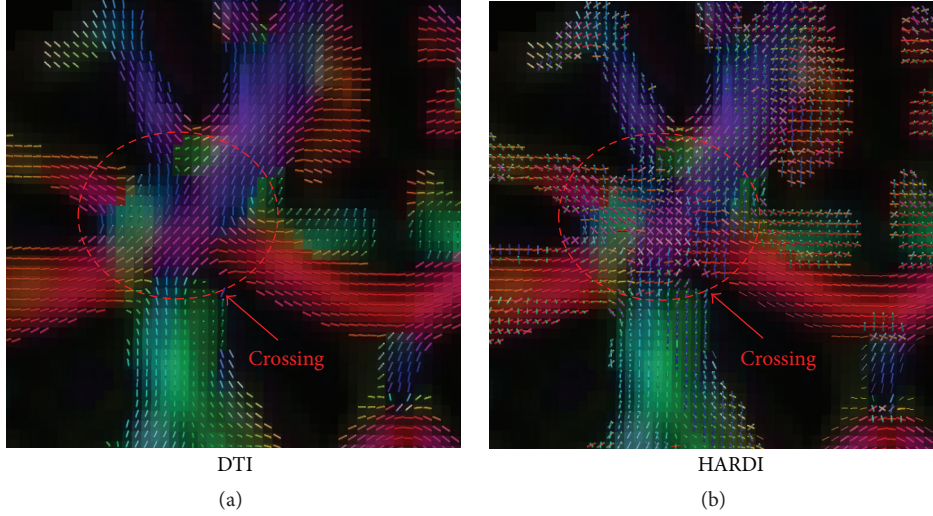


FIGURE 1: Directional glyphs at the intersection of the left corticospinal tract and the corpus callosum given by (a) the DTI method and (b) the HARDI method.

The global clustering coefficient gives an overall indication of clustering in a network. It is the average of absolute local clustering coefficients of all nodes:

$$C = \frac{1}{N} \sum_{i=1}^N C_i, \quad (3)$$

$$C_i = \frac{E_i}{K_i(K_i - 1)/2},$$

where  $C_i$  is the local clustering coefficient for node  $i$ ,  $E_i$  is the number of edges in the subgraph  $G_i$  of node  $i$ , and  $K_i$  denotes the number of nodes in  $G_i$ . In other words,  $C_i$  is the proportion of edges between the nodes within the neighborhood of node  $i$  divided by the number of edges that could possibly exist between them. In addition, the average shortest path length of the network is defined as

$$L = \frac{1}{N(N-1)} \sum_{i=1}^N \sum_{j=1, j \neq i}^N L_{ij}. \quad (4)$$

The human brain exhibits the “small-world” property characterized by dense local clustering between neighboring nodes and high global network efficiency with short path lengths due to the existence of relatively few long-range connections [39–41]. Mathematically, it can be represented by the ratio of the normalized global clustering coefficient  $\gamma = C^{\text{real}}/C^{\text{rand}}$  to the normalized shortest path length  $\lambda = L^{\text{real}}/L^{\text{rand}}$ , where  $C^{\text{rand}}$  and  $L^{\text{rand}}$  are the global clustering coefficient and the normalized shortest path length of a random network. A random network was simulated by iteratively rewiring 50% pairs of random edges of the existing brain network for 1,000 times. Then, small-worldness can be measured as  $\sigma = \gamma/\lambda$  [42] and it should be greater than 1 if the graph demonstrates the small-world property.

**2.5.2. Regional Measures.** The nodal efficiency was computed to represent the regional characteristics of a network. The nodal efficiency  $E_i$  is defined as

$$E_i = \frac{1}{N-1} \sum_{j=1, j \neq i}^N \frac{1}{L_{ij}}, \quad (5)$$

where  $L_{ij}$  is the shortest path length between node  $i$  and node  $j$ . Therefore,  $E_i$  measures the overall information flow between a given node  $i$  and the rest of the nodes in the network. The node  $i$  is defined as a hub if  $E_i$  is at least 1 standard deviation (SD) above the average nodal efficiency of the network.

**2.5.3. Local Measures.** The network edges, that is, the fiber counts between each pair of ROIs, were directly used to describe the local characteristics of a network.

**2.6. Statistical Analysis.** The nonparametric permutation test was used to evaluate statistical differences of brain network properties between the AD and NC groups. First, linear regression was performed on all the network measures at global, regional, and local levels (described in Section 2.5), respectively, with age, gender, level of education, and intracranial volume (ICV) as covariates. Then, after removing those factors on the measures, the regressed measures were permuted 5,000 times to assess the statistical significance of the differences [36]. The significance level was set as  $p < 0.05$ , with false discovery rate (FDR) [43] for multiple comparison correction. To compare the performance between the DTI and HARDI methods, the same analysis was performed to the networks constructed by each method, respectively.

### 3. Results

**3.1. DTI versus HARDI.** We compared the DTI and HARDI networks, in terms of their ability, to distinguish the AD group from the NC group. Figure 1 shows that HARDI

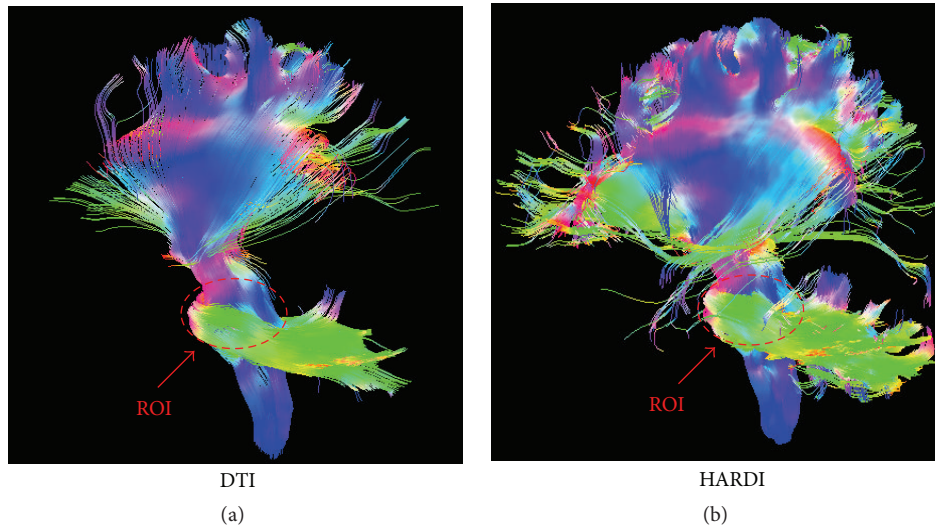


FIGURE 2: Tractography results based on a seed ROI at the brain stem with (a) the DTI method and (b) the HARDI method.

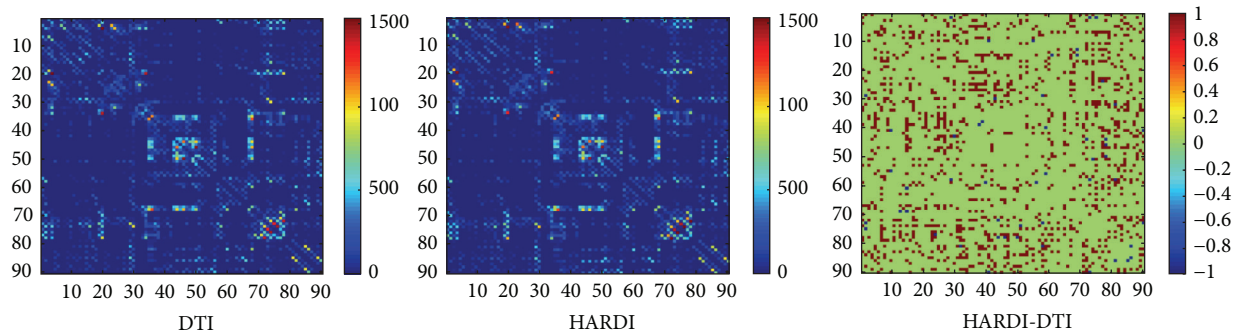


FIGURE 3: The  $90 \times 90$  connectivity matrices built with the DTI method and the HARDI method, respectively. The right panel shows the binary difference between the left two matrices for a selected subject, where the entries with +1 denote connections detected by HARDI but not DTI, and -1 for connections detected by DTI but not HARDI.

method can handle fiber crossings in the intersection between the left corticospinal tract and the corpus callosum. The DTI method, on the other hand, was not able to do so. Figure 2 shows the tractography results based on a seed ROI near the brain stem. The HARDI method was able to produce significantly more fibers than the DTI method.

Figure 3 shows the  $90 \times 90$  connectivity matrices ( $\geq 4$  fiber connections) with both DTI and HARDI methods from a randomly selected subject in our dataset. The binary difference between the two matrices is also shown, where the entries with +1 denote connections detected by HARDI but not DTI, and -1 for connections detected by DTI but not HARDI. For this selected subject, the meaningful connections ( $\geq 4$  fiber connections) account for 38% and 52% out of the total connections for DTI and HARDI, respectively. From the difference map in the right panel of Figure 3, it is obvious that more connections can be detected with HARDI compared to DTI.

**3.2. Global Characteristics.** Both the NC and the AD groups showed small-world organization ( $\sigma > 1$ ) in their networks.

The AD networks actually showed higher small-worldness than the NC networks did, in both DTI and HARDI cases ( $\sigma_{AD} > \sigma_{NC}$ ). In both cases, the AD group, when compared to the NC group, showed decreases in global efficiency and local efficiency but increases in the normalized shortest path length ( $\lambda$ ) and the normalized clustering coefficient ( $\gamma$ ). Also, all results given by the HARDI method were statistically significant ( $p < 0.05$ ), while most results by the DTI method were not, except global efficiency. Table 3 lists the values of these measures for the AD and NC groups by both the DTI and HARDI methods.

**3.3. Regional Characteristics.** An ROI is defined as a network hub, if its nodal efficiency is 1 SD greater than the mean nodal efficiency of the network. For the HARDI case, we identified 20 hub nodes in the NC group, including 6 association cortical regions, 13 paralimbic cortical regions, and 1 primary cortical region. Only 16 hub nodes were identified in the AD group, including 5 association regions and 11 paralimbic regions. In both groups, 12 ROIs were identified as hubs in common, including the bilateral superior frontal gyri,

TABLE 3: The comparison of the global connectivity characteristics between the AD and the NC groups with the DTI and HARDI models, respectively.

	$E_{\text{glob}}$	$E_{\text{loc}}$	$\gamma$	$\lambda$	$\sigma$
DTI					
AD	524 ± 93	674 ± 134	1.46 ± 0.18	1.20 ± 0.06	1.22 ± 0.11
NC	617 ± 114	748 ± 121	1.39 ± 0.12	1.16 ± 0.04	1.20 ± 0.07
Difference	-93	-74	0.07	0.03	0.02
$p$ value	<b>0.03</b>	0.12	0.12	0.07	0.20
HARDI					
AD	426 ± 100	578 ± 126	1.66 ± 0.24	1.27 ± 0.08	1.31 ± 0.16
NC	543 ± 134	674 ± 144	1.53 ± 0.19	1.22 ± 0.06	1.25 ± 0.11
Difference	-116	-95	0.14	0.05	0.06
$p$ value	<b>0.01</b>	<b>0.05</b>	<b>0.03</b>	<b>0.03</b>	<b>0.04</b>

dorsolateral (SFGdor), the bilateral supplementary motor areas (SMA), the bilateral median cingulate gyri (MCG), the bilateral precuneus (PCUN), the bilateral putamina (PUT), and the bilateral thalami (THA). In addition, 4 ROIs, such as the left insula (INS.L), the right caudate nucleus (CAU.R), and the bilateral pallida (PAL), were identified as the hubs in the AD group but not in the NC group. 8 ROIs, such as the right medial superior frontal gyrus (SFGmed.R), the bilateral posterior cingulate gyri (PCG), the right calcarine cortex (CAL.R), the right cuneus (CUN.R), the bilateral superior occipital gyri (SOG), and the left middle occipital gyrus (MOG.L), were identified as the hubs in the NC group but not in the AD group. For the DTI case, most of the hubs identified in the HARDI case were also detected. The AD group had the exact 16 hubs as in the HARDI case, while the NC group only had 19 hubs. The right calcarine cortex (CAL.R) and the left middle occipital gyrus (MOG.L) were only identified in the HARDI case for the NC group, while the left medial superior frontal gyrus (SFGmed.L) was only identified in the DTI case. The hub distributions in the AD and NC groups are shown in Figure 4 for both methods.

In both DTI and HARDI cases, when compared to the NC group, the AD group showed reduced nodal efficiency ( $p < 0.05$ , FDR corrected) in the bilateral superior occipital gyri (SOG), the right middle occipital gyrus (MOG.R), the right rectus gyrus (REC.R), the left posterior cingulate gyrus (PCG.L), the right parahippocampal gyrus (PHG.R), the right middle temporal pole (TPOMid.R), the right inferior occipital gyrus (IOG.R), the right fusiform gyrus (FFG.R), the right precuneus (PCUN.R), and the bilateral cuneus (CUN). Besides all of the regions shown above, the right posterior cingulate gyrus (PCG.R), the right calcarine cortex (CAL.R), and the left precuneus (PCUN.L) showed the significantly reduced nodal efficiency only in the HARDI case, while the left middle temporal pole (TPOMid.L) showed the reduced efficiency only in the DTI. The comparison between the ROIs that had the reduced efficiency in the two groups for the DTI and HARDI cases is shown in Figure 5.

**3.4. Local Characteristics.** We utilized the fiber counts between a pair of ROIs to measure the strength of their

connection. After performing the permutation test [36] on each connection, the axial and the sagittal views of those significantly different connections ( $p < 0.05$ ) between the AD group and the NC group, with the DTI and HARDI method, are illustrated in Figure 6. Additionally, the connectogram, a circular representation tool called Circos (<http://www.cpan.org/ports/>) [44], was used to demonstrate those connections with the two models in Figure 7. In both figures, the stronger connections (higher fiber counts between a pair of ROIs) in the AD group are shown in *blue*, and the weaker connections (lower fiber counts between a pair of ROIs) are in *red*. Particularly, the thicker the line in Figure 7, the greater the difference in the connection between the two groups. The identified differences in connections spread over the entire brain. A large portion of these differences was located in the limbic system and subcortical regions. It is obvious that the HARDI model was able to detect noticeably more pairs of different connections between the groups (30 pairs in HARDI versus 20 pairs in DTI). For example, the connections through the left supplementary motor area (SMA.L), the right lingual gyrus (LING.R), the left superior parietal gyrus (SPG.L), the bilateral thalami (THA), the left middle temporal gyrus (MTG.L), and the left hippocampus (HIP.L) were only shown in the HARDI case.

## 4. Discussion

This study investigates the impact of AD on the topological characteristics of the WM connectivity network at three hierarchical levels, global, regional, and local level, through tractography data reconstructed using DTI and HARDI methods, respectively. The main findings are as follows: (1) the global and average local network efficiency are reduced in AD, with increased shortest path length; (2) the number of regional hubs and nodal efficiency decreases in AD; (3) the local connections weaken in AD; (4) the HARDI method has an advantage over the DTI method in identifying more abnormal network characteristics at all the three levels.

At the global level, consistent with the previous studies [41, 45, 46], our results indicate that the WM connectivity networks of both AD and NC have the small-world topology.

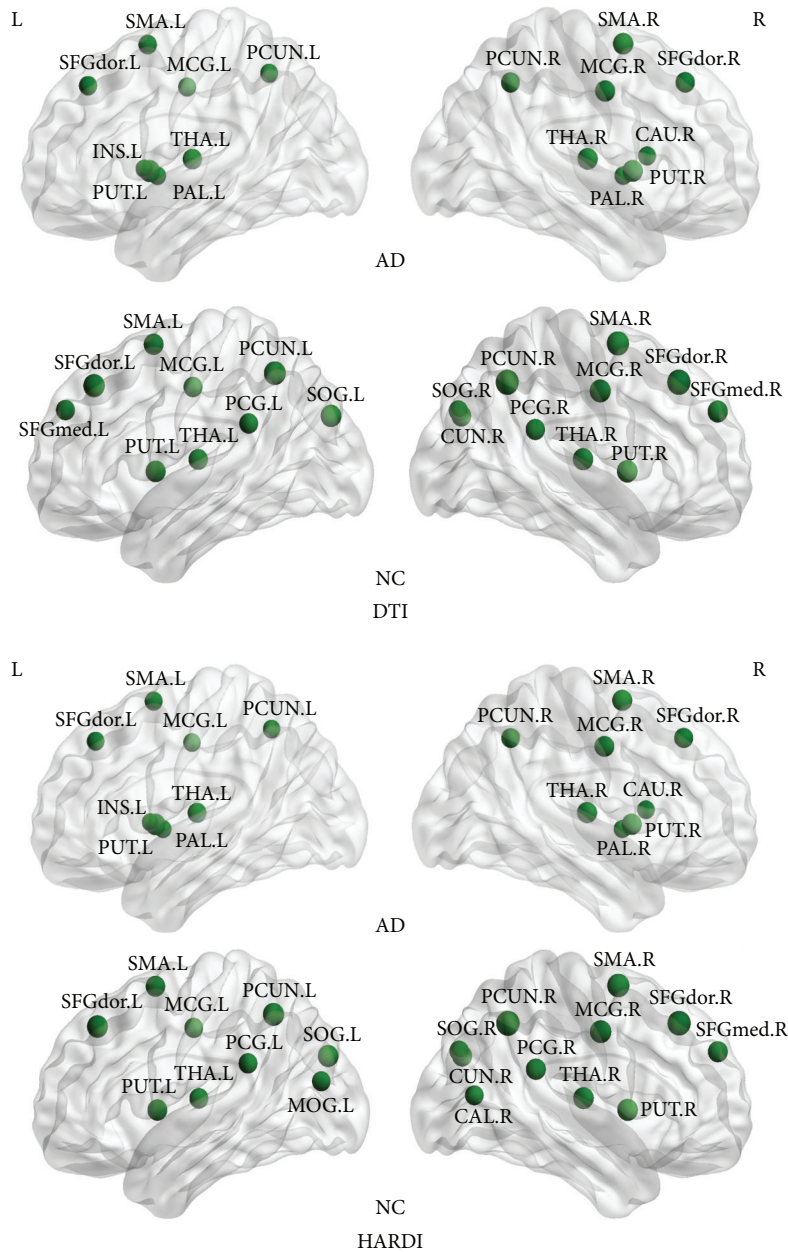


FIGURE 4: Hubs in the AD group and the NC group given by the DTI method and the HARDI method, respectively. Each sphere represents the center of an ROI. Refer to Table 2 for the label of each ROI.

Although the AD networks show a slightly elevated small-world attribute, most global measures are lower in AD, compared to those in NC. AD patients show significant decreases in global efficiency and average local efficiency, but increases in normalized shortest path length. Global efficiency and average local efficiency are known to reflect the overall ability of information transfer between different nodes in a network. They are comprehensive indices for the capability of parallel information processing. The reductions in those measures can be attributed to the degeneration of WM, which indicates that connections between cortical regions are abnormal. The less strength of connections between cortical regions is due

to the damaged WM integrity, resulting in longer pathways that connect different regions in the brain. The breakdown in the optimal brain balance between the local specialization and the global integration causes information processing to malfunction in AD. Similarly to previous studies [47], we have also found that the normalized weighted shortest path length increases in the AD group. Shortest path length ensures interregional effective communication, or prompt transfer of information between regions, which constitutes the basis of cognitive processes [48]. The WM damage can lead to an increase in shortest path length. Therefore, it is likely that, in people with AD, information may flash in a

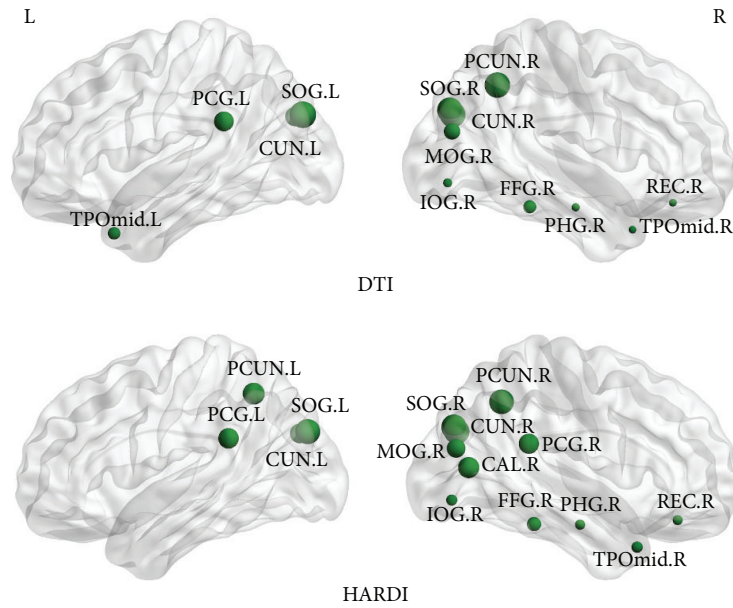


FIGURE 5: ROIs that have the reduced nodal efficiency in the AD group compared to the NC group ( $p < 0.05$ ), given by the DTI and HARDI methods, respectively. Each sphere represents the center of an ROI and its size is proportional to the nodal efficiency. Refer to Table 2 for the label of each ROI.

certain brain region but fail to transmit to other regions effectively to form stable memories. The normalized clustering coefficient is a ratio of local information transfer capability in a network to that of a random network. In AD, its increase reflects the reinforcement of information transfer capability. Likewise, previous studies have also found a greater clustering coefficient and a longer absolute path length in AD, which may indicate that the organization of the cortical network is least optimal in AD [49].

At the regional level, several hubs identified in NC are not shown in AD, such as precuneus (PCUN) and posterior cingulate gyrus (PCG). These two regions also demonstrate reduced connectivity in functional magnetic resonance imaging (fMRI) studies in patients with amnesic mild cognitive impairment (aMCI), a stage with high risk in developing AD [50], which may suggest that these two regions maintain pivotal roles in both structural and functional default mode networks in AD [51].

The AD networks also show decreased nodal efficiency in many cortical regions, mainly located in the bilateral cunei (CUN), the right precuneus (PCUN.R), the bilateral posterior cingulate gyri (PCG), the right temporal pole, middle (TPOmid.R), and the right parahippocampal gyrus (PHG.R). The cuneus (CUN), the precuneus (PCUN), and the posterior cingulate gyrus (PCG) are thought to be involved in the episodic memory information transmission and malfunction in AD [52]. Although the degeneration of the posterior cingulate gyrus was originally interpreted as not being a direct consequence of degeneration in the medial temporal lobe, recent studies have revealed that this area has atrophy and metabolic abnormalities in incipient AD [52–54]. In a study that examined the cingulum tract in AD, both the anterior and posterior regions were affected [55]. The posterior cingulate region is a key “hub” affected in AD. The

temporal pole, middle (TPOmid), and the parahippocampal gyrus (PHG) are involved in semantic memory processing and recognition [56] and show atrophy and neuronal loss in AD [57, 58]. Notably, the decreased efficiency in the temporal lobes was observed to be mainly located in the right hemisphere. Together, the reduced nodal efficiency suggests that possible WM degeneration in these brain regions may negatively affect information transmission and functional integration in AD patients.

At the local level, weaker connection (lower fiber counts) happens predominantly in the area of the bilateral precunei (PCUN), the right cuneus (CUN.R), the left middle temporal gyrus (MTG.L), and left hippocampal gyrus (HIP.L). These areas, which are mostly associated with linguistic integration, emotion, and semantic memory [56, 59], are affected in AD patients [57, 58]. It is worth noting that precuneus, cuneus, and temporal lobe also show reduced nodal efficiency at the regional level. In addition to the typically well-known affected regions in AD, the right amygdala (AMYG.R) and the right middle frontal gyrus (MFG.R) show weaker connections as well. These regions are the structures mostly involved in emotional processing, perceptions, psychological states, and behavioral responses [60]. Weaker connections can also be identified at the right thalamus (THA.R), which is known to have a significantly reduced volume in AD [61]. Interestingly, a few regions show increased local connection in the AD group than in the NC group, for example, the connection between the left insula (INS.L) and left inferior parietal lobule (IPL.L). It is possible that this may result from the compensation to weak connections in the neighboring regions.

Overall, the HARDI method outperforms the DTI method in terms of differentiating AD and NC at all three levels. At the global level, the HARDI method has more

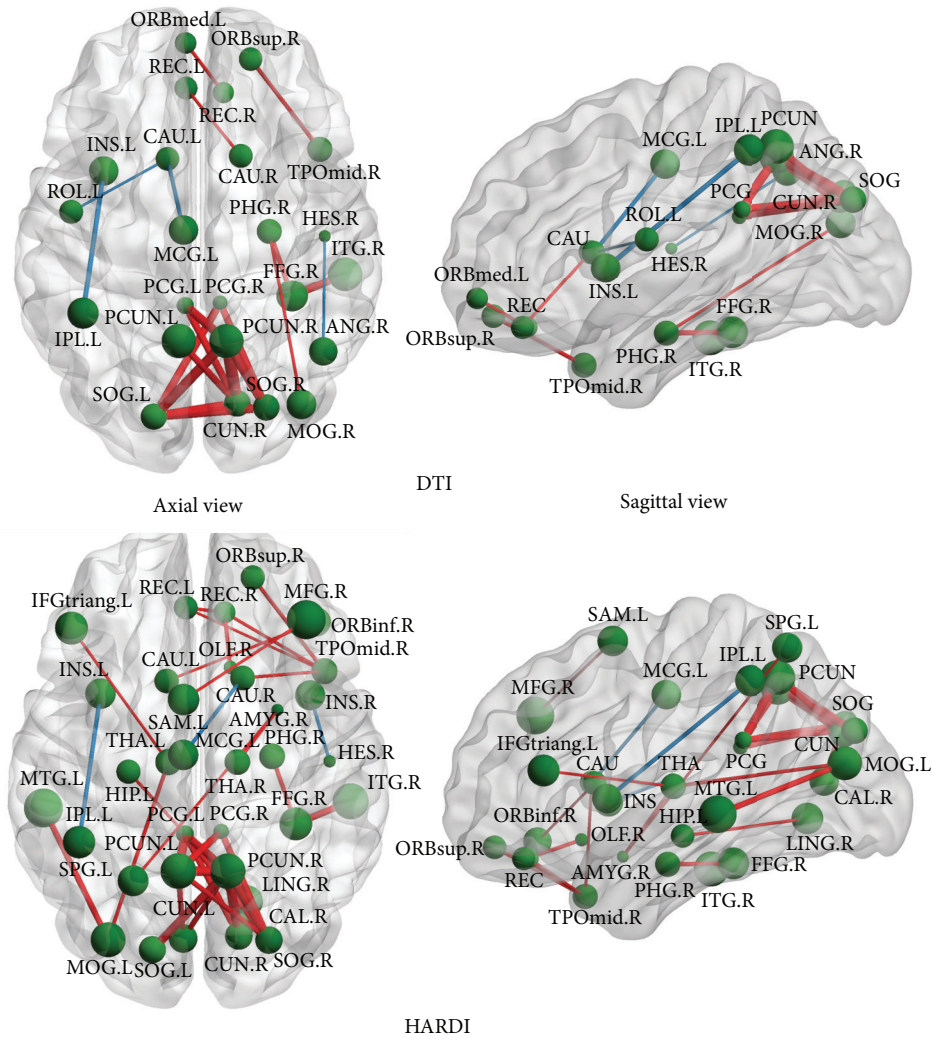


FIGURE 6: The axial and the sagittal views of the significantly different connections ( $p < 0.05$ ) based on the fiber counts between the AD group and the NC group given by the DTI and HARDI methods, respectively. The stronger connections (higher fiber counts between a pair of ROIs) in the AD group are shown in *blue*, while the weaker connections (lower fiber counts between a pair of ROIs) are in *red*. Refer to Table 2 for the label of each ROI.

statistical power in distinguishing the groups for all the measures, according to the  $p$  values in Table 3. The group differences of all the measures are statistically significant in the HARDI case, while most of them are not statistically significant in the DTI case. At the regional level, the HARDI method detects more regions with reduced nodal efficiency. These include the bilateral posterior cingulate gyri (PCG) and the bilateral precunei (PCUN), while the results of the DTI method only show the unilateral deficiency of these regions. The results from the HARDI method are more consistent with the pathology of AD, as the bilateral posterior cingulate gyri and precunei are both associated with memory processing and affected in AD [62, 63]. At the local level, the two methods show the greatest difference. The HARDI method is able to identify 50% more of the weaker connections in AD than the DTI method (30 pairs versus 20 pairs). This may be

because the HARDI method is able to find the correct tract directions at the fiber crossing regions and can find more connections in the NC group. Specifically, the left superior parietal gyrus (SPG.L), the right thalamus (THA.R), and the left middle temporal gyrus (MTG.L), especially the left hippocampus (HIP.L) and the left cuneus (CUN.L), are only found using the HARDI method. During the early onset of AD, the superior parietal gyrus and the middle temporal gyrus undergo neuronal loss [64]. Besides the neocortical atrophy, subcortical structures, such as the thalamus, also suffer atrophy and may contribute to cognitive decline and emotion disorder in AD [65].

Fiber count is one of the most commonly used measures in evaluating connectivity characteristics. For example, Dennis et al. [66] computed graph theory metrics based on the fiber count to track changes in both structural connectivity

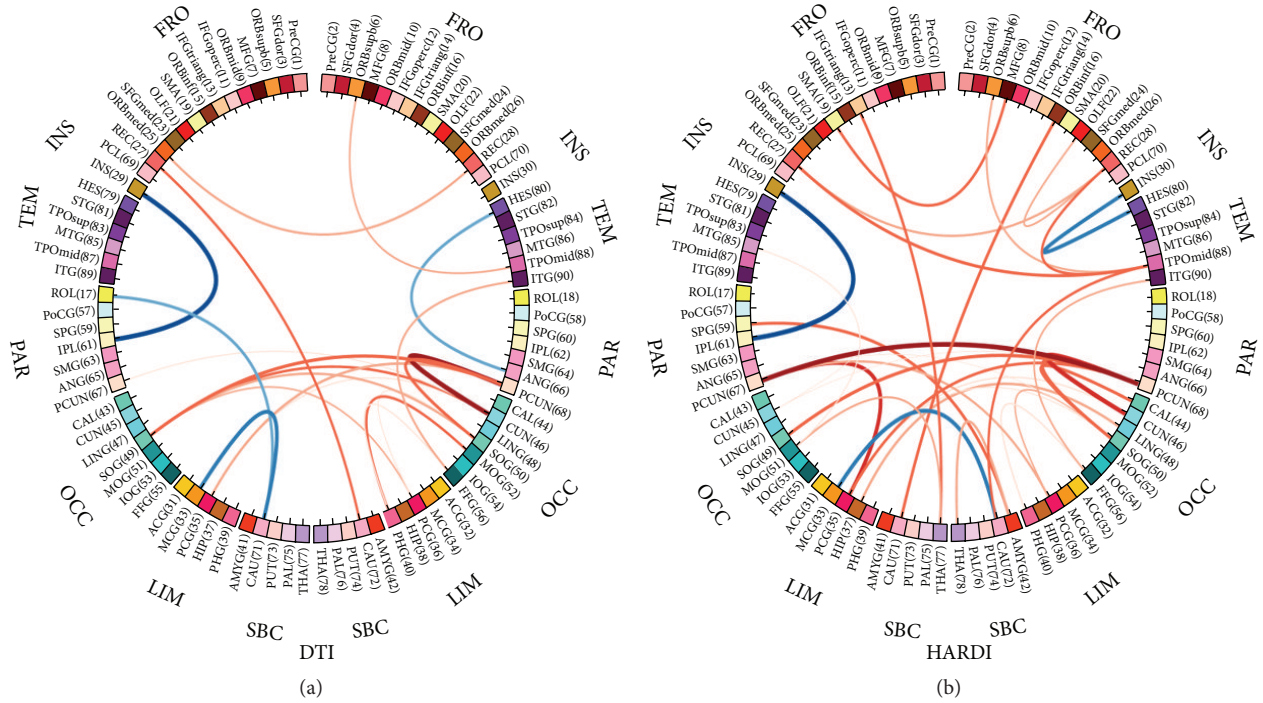


FIGURE 7: Connectograms showing significantly different connections ( $p < 0.05$ ) based on the fiber counts between the AD group and the NC group, given (a) the DTI method and (b) the HARDI method. The thickness of each line indicates the extent of the difference between the corresponding connections in the two groups. The stronger connections (higher fiber counts between a pair of ROIs) in the AD group are shown in blue, while the weaker connections (lower fiber counts between a pair of ROIs) are in red. Refer to Table 2 for the label of each ROI.

and network efficiency in young healthy individuals, while Zhan et al. [67] developed a machine learning framework to classify different stages of AD with fiber counts as features. However, sometimes, fiber count may not be a suitable feature in connectivity studies. For instance, in [68, 69], the networks constructed with the mean FA, MD, and fiber length provided better performance in identifying high-risk autistic infants than fiber count. Therefore, we will consider incorporating other network measures in our future work since they may provide additional insights into connectivity breakdown, especially for the case that the fiber count based networks cannot reveal the progression of AD.

The conventional statistical analysis on network properties is often performed in a univariate manner, that is, pairwise comparison between groups. This might overlook the interaction among sets of connections in group difference. On the other hand, instead of doing simple pairwise comparison, a classification framework is able to consider all individual connection features, as well as their relationships, for selecting the most discriminative features for classification [68–70]. Ensemble learning algorithm, such as random forest, is one of this type of classification algorithms that can be applied to identify discriminative connectivity patterns in a multivariate manner for AD or MCI classification. This will be our future work.

We do acknowledge that there are some limitations in this study. Firstly, the sample size of our study is quite small. In the future, more participants need to be recruited to increase the statistic power of the results. Secondly, the lack of gold

standard for regional parcellation makes the definition of ROI not very precise, especially on the boundary. Registration error may also play a role in this issue. Therefore, it may affect the accuracy in the analysis of connectivity networks [71, 72]. Thirdly, the underlying biological relationship between the network properties and the AD progression is currently unclear. Studying the intermediate stage, for example, MCI, may be beneficial for further understanding of the relationship [73, 74]. In the future work, we will include participants from this stage to perform a more comprehensive study on this topic.

### 5. Conclusion

In summary, we performed a systematic study on the WM connectivity comparison at three hierarchical levels (global, regional, and local) between the two groups: the AD group and the NC group. The analysis was conducted using tractography data generated using two diffusion models (DTI and HARDI) to evaluate the influence of tractography on the network analysis. Globally, both the AD group and the NC group demonstrate the small-world topology. However, many global measures, such as global efficiency, average local efficiency, and normalized shortest path length, were suboptimal in the AD group. Regionally, the AD group had the reduced number of hubs and significantly decreased nodal efficiency in the precuneus and the temporal lobe (the well-known atrophic regions in AD). Locally, weaker

connections exist in these regions, as well as regions in the limbic system and the subcortex, such as hippocampus and thalamus. The HARDI method outperforms the DTI method at all three levels since the advanced model in the HARDI method can more accurately reflect the underlying complex fiber configurations.

### Conflict of Interests

The authors declare that there is no conflict of interests regarding the publication of this paper.

### Authors' Contribution

Tao Wang and Feng Shi equally contributed to this paper.

### Acknowledgments

This work was partially supported by the National Natural Science Foundation of China (81201030, 61210001, 81571298, and 61473190), the China Ministry of Science and Technology (2009BAI77B03), the National Key Clinical Disciplines at Shanghai Mental Health Center (OMA-MH, 2011-873), the Shanghai Science and Technology Committee Grants (134119a2600, 14411965000), the Shanghai Jiao Tong University Technological Innovation Special Fund (YG2014MS39), the SHSMU-ION Research Center for Brain Disorders, and the Shanghai Jiao Tong University K. C. Wong Medical Fellowship Fund. This work was also supported in part by NIH Grants AG041721, EB006733, EB008374, and EB009634.

### References

- [1] I. McKeith and J. Cummings, "Behavioural changes and psychological symptoms in dementia disorders," *Lancet Neurology*, vol. 4, no. 11, pp. 735–742, 2005.
- [2] Alzheimer's association, "2014 Alzheimer's disease facts and figures," *Alzheimer's & Dementia*, vol. 10, no. 2, pp. e47–e92, 2014.
- [3] J. B. Toledo, J. Brettschneider, M. Grossman et al., "CSF biomarkers cutoffs: the importance of coincident neuropathological diseases," *Acta Neuropathologica*, vol. 124, no. 1, pp. 23–35, 2012.
- [4] P. Scheltens, M. Kuiper, E. Ch Wolters et al., "Atrophy of medial temporal lobes on MRI in 'probable' Alzheimer's disease and normal ageing: diagnostic value and neuropsychological correlates," *Journal of Neurology, Neurosurgery and Psychiatry*, vol. 55, no. 10, pp. 967–972, 1992.
- [5] C. R. Jack Jr., R. C. Petersen, Y. C. Xu et al., "Medial temporal atrophy on MRI in normal aging and very mild Alzheimer's disease," *Neurology*, vol. 49, no. 3, pp. 786–794, 1997.
- [6] G. B. Frisoni, C. Testa, A. Zorzan et al., "Detection of grey matter loss in mild Alzheimer's disease with voxel based morphometry," *Journal of Neurology Neurosurgery and Psychiatry*, vol. 73, no. 6, pp. 657–664, 2002.
- [7] G. B. Karas, E. J. Burton, S. A. R. B. Rombouts et al., "A comprehensive study of gray matter loss in patients with Alzheimer's disease using optimized voxel-based morphometry," *NeuroImage*, vol. 18, no. 4, pp. 895–907, 2003.
- [8] P. J. Basser, J. Mattiello, and D. LeBihan, "MR diffusion tensor spectroscopy and imaging," *Biophysical Journal*, vol. 66, no. 1, pp. 259–267, 1994.
- [9] S. Mori, B. J. Crain, V. P. Chacko, and P. C. M. Van Zijl, "Three-dimensional tracking of axonal projections in the brain by magnetic resonance imaging," *Annals of Neurology*, vol. 45, no. 2, pp. 265–269, 1999.
- [10] T. E. J. Behrens, M. W. Woolrich, M. Jenkinson et al., "Characterization and propagation of uncertainty in diffusion-weighted MR imaging," *Magnetic Resonance in Medicine*, vol. 50, no. 5, pp. 1077–1088, 2003.
- [11] S. M. Smith, H. Johansen-Berg, M. Jenkinson et al., "Acquisition and voxelwise analysis of multi-subject diffusion data with tract-based spatial statistics," *Nature Protocols*, vol. 2, no. 3, pp. 499–503, 2007.
- [12] Y. Jin, Y. Shi, L. Zhan et al., "Labeling white matter tracts in hardi by fusing multiple tract atlases with applications to genetics," in *Proceedings of the IEEE 10th International Symposium on Biomedical Imaging (ISBI '13)*, pp. 512–515, IEEE, San Francisco, Calif, USA, April 2013.
- [13] Y. Jin, Y. Shi, L. Zhan et al., "Automatic clustering of white matter fibers in brain diffusion mri with an application to genetics," *NeuroImage*, vol. 100, pp. 75–90, 2014.
- [14] A. W. Toga, K. A. Clark, P. M. Thompson, D. W. Shattuck, and J. D. Van Horn, "Mapping the human connectome," *Neurosurgery*, vol. 71, no. 1, pp. 1–5, 2012.
- [15] Y. Liu, G. Spulber, K. K. Lehtimäki et al., "Diffusion tensor imaging and tract-based spatial statistics in Alzheimer's disease and mild cognitive impairment," *Neurobiology of Aging*, vol. 32, no. 9, pp. 1558–1571, 2011.
- [16] Y. Jin, Y. Shi, L. Zhan, and P. M. Thompson, "Automated multi-atlas labeling of the fornix and its integrity in Alzheimer's disease," in *Proceedings of the IEEE International Symposium on Biomedical Imaging (ISBI '15)*, pp. 140–143, New York, NY, USA, April 2015.
- [17] J. Li, Y. Jin, Y. Shi et al., "Voxelwise spectral diffusional connectivity and its applications to Alzheimer's disease and intelligence prediction," in *Medical Image Computing and Computer-Assisted Intervention—MICCAI 2013*, vol. 8149 of *Lecture Notes in Computer Science*, pp. 655–662, Springer, 2013.
- [18] M. Daianu, N. Jahanshad, T. M. Nir et al., "Breakdown of brain connectivity between normal aging and Alzheimer's disease: a structural k-core network analysis," *Brain Connectivity*, vol. 3, no. 4, pp. 407–422, 2013.
- [19] E. L. Dennis, L. Zhan, N. Jahanshad et al., "Rich club analysis of structural brain connectivity at 7 Tesla versus 3 Teslas," in *Computational Diffusion MRI and Brain Connectivity*, Mathematics and Visualization, pp. 209–218, Springer, Basel, Switzerland, 2013.
- [20] L. Zhan, B. A. Mueller, N. Jahanshad et al., "Magnetic resonance field strength effects on diffusion measures and brain connectivity networks," *Brain Connectivity*, vol. 3, no. 1, pp. 72–86, 2013.
- [21] L. Zhan, N. Jahanshad, Y. Jin et al., "Understanding scanner upgrade effects on brain integrity & connectivity measures," in *Proceedings of the IEEE 11th International Symposium on Biomedical Imaging (ISBI '14)*, pp. 234–237, Beijing, China, May 2014.
- [22] L. Zhan, N. Jahanshad, D. B. Ennis et al., "Angular versus spatial resolution trade-offs for diffusion imaging under time constraints," *Human Brain Mapping*, vol. 34, no. 10, pp. 2688–2706, 2013.

- [23] E. L. Dennis, Y. Jin, C. Kernan et al., "White matter integrity in traumatic brain injury: effects of permissible fiber turning angle," in *Proceedings of the 12th IEEE International Symposium on Biomedical Imaging (ISBI '15)*, pp. 930–933, IEEE, New York, NY, USA, April 2015.
- [24] L. Zhan, J. Zhou, Y. Wang et al., "Comparison of nine tractography algorithms for detecting abnormal structural brain networks in Alzheimer's disease," *Frontiers in Aging Neuroscience*, vol. 7, article 48, 2015.
- [25] D. S. Tuch, "Q-ball imaging," *Magnetic Resonance in Medicine*, vol. 52, no. 6, pp. 1358–1372, 2004.
- [26] P.-T. Yap and D. Shen, "Spatial transformation of DWI data using non-negative sparse representation," *IEEE Transactions on Medical Imaging*, vol. 31, no. 11, pp. 2035–2049, 2012.
- [27] G. McKhann, D. Drachman, and M. Folstein, "Clinical diagnosis of Alzheimer's disease: report of the NINCDS-ADRDA work group under the auspices of Department of Health and Human Services Task Force on Alzheimer's disease," *Neurology*, vol. 34, no. 7, pp. 939–944, 1984.
- [28] R. Katzman, M. Zhang, Ouang-Ya-Qu et al., "A Chinese version of the mini-mental state examination; impact of illiteracy in a Shanghai dementia survey," *Journal of Clinical Epidemiology*, vol. 41, no. 10, pp. 971–978, 1988.
- [29] K. A. Schafer, R. E. Tractenberg, M. Sano et al., "Reliability of monitoring the clinical dementia rating in multicenter clinical trials," *Alzheimer Disease and Associated Disorders*, vol. 18, no. 4, pp. 219–222, 2004.
- [30] J. G. Sied, A. P. Zijdenbos, and A. C. Evans, "A nonparametric method for automatic correction of intensity nonuniformity in MRI data," *IEEE Transactions on Medical Imaging*, vol. 17, no. 1, pp. 87–97, 1998.
- [31] F. Shi, L. Wang, Y. Dai, J. H. Gilmore, W. Lin, and D. Shen, "LABEL: pediatric brain extraction using learning-based meta-algorithm," *NeuroImage*, vol. 62, no. 3, pp. 1975–1986, 2012.
- [32] A. Leemans, B. Jeurissen, J. Sijbers, and D. Jones, "Explore DTI: a graphical toolbox for processing, analyzing, and visualizing diffusion MR data," in *Proceedings of the Annual Meeting of International Society for Magnetic Resonance in Medicine (ISMRM '09)*, p. 3537, 2009.
- [33] N. Tzourio-Mazoyer, B. Landeau, D. Papathanassiou et al., "Automated anatomical labeling of activations in SPM using a macroscopic anatomical parcellation of the MNI MRI single-subject brain," *NeuroImage*, vol. 15, no. 1, pp. 273–289, 2002.
- [34] D. G. Shen and C. Davatzikos, "HAMMER: hierarchical attribute matching mechanism for elastic registration," *IEEE Transactions on Medical Imaging*, vol. 21, no. 11, pp. 1421–1439, 2002.
- [35] A. Zalesky, A. Fornito, M. L. Seal et al., "Disrupted axonal fiber connectivity in schizophrenia," *Biological Psychiatry*, vol. 69, no. 1, pp. 80–89, 2011.
- [36] F. Shi, P.-T. Yap, W. Gao, W. Lin, J. H. Gilmore, and D. Shen, "Altered structural connectivity in neonates at genetic risk for schizophrenia: a combined study using morphological and white matter networks," *NeuroImage*, vol. 62, no. 3, pp. 1622–1633, 2012.
- [37] N. Shu, Y. Liu, K. Li et al., "Diffusion tensor tractography reveals disrupted topological efficiency in white matter structural networks in multiple sclerosis," *Cerebral Cortex*, vol. 21, no. 11, pp. 2565–2577, 2011.
- [38] M. Rubinov, O. Sporns, C. van Leeuwen, and M. Breakspear, "Symbiotic relationship between brain structure and dynamics," *BMC Neuroscience*, vol. 10, article 55, 2009.
- [39] D. S. Bassett and E. Bullmore, "Small-world brain networks," *Neuroscientist*, vol. 12, no. 6, pp. 512–523, 2006.
- [40] O. Sporns and J. D. Zwi, "The small world of the cerebral cortex," *Neuroinformatics*, vol. 2, no. 2, pp. 145–162, 2004.
- [41] P. Hagmann, M. Kurant, X. Gigandet et al., "Mapping human whole-brain structural networks with diffusion MRI," *PLoS ONE*, vol. 2, no. 7, article e597, 2007.
- [42] D. J. Watts and S. H. Strogatz, "Collective dynamics of 'small-world' networks," *Nature*, vol. 393, no. 6684, pp. 440–442, 1998.
- [43] Y. Benjamini and Y. Hochberg, "Controlling the false discovery rate: a practical and powerful approach to multiple testing," *Journal of the Royal Statistical Society, Series B: Methodological*, vol. 57, no. 1, pp. 289–300, 1995.
- [44] M. Krzywinski, J. Schein, I. Birol et al., "Circos: an information aesthetic for comparative genomics," *Genome Research*, vol. 19, no. 9, pp. 1639–1645, 2009.
- [45] Y. Li, Y. Liu, J. Li et al., "Brain anatomical network and intelligence," *PLoS Computational Biology*, vol. 5, no. 5, Article ID e1000395, 2009.
- [46] N. Shu, Y. Liu, J. Li, Y. Li, C. Yu, and T. Jiang, "Altered anatomical network in early blindness revealed by diffusion tensor tractography," *PLoS ONE*, vol. 4, no. 9, Article ID e7228, 2009.
- [47] C.-Y. Lo, P.-N. Wang, K.-H. Chou, J. Wang, Y. He, and C.-P. Lin, "Diffusion tensor tractography reveals abnormal topological organization in structural cortical networks in Alzheimer's disease," *The Journal of Neuroscience*, vol. 30, no. 50, pp. 16876–16885, 2010.
- [48] V. Latora and M. Marchiori, "Efficient behavior of small-world networks," *Physical Review Letters*, vol. 87, no. 19, Article ID 198701, 2001.
- [49] Z. Yao, Y. Zhang, L. Lin et al., "Abnormal cortical networks in mild cognitive impairment and Alzheimer's disease," *PLoS Computational Biology*, vol. 6, no. 11, Article ID e1001006, 2010.
- [50] C. Sorg, V. Riedl, M. Mühlau et al., "Selective changes of resting-state networks in individuals at risk for Alzheimer's disease," *Proceedings of the National Academy of Sciences of the United States of America*, vol. 104, no. 47, pp. 18760–18765, 2007.
- [51] P. Fransson and G. Marrelec, "The precuneus/posterior cingulate cortex plays a pivotal role in the default mode network: evidence from a partial correlation network analysis," *NeuroImage*, vol. 42, no. 3, pp. 1178–1184, 2008.
- [52] T. Wang, S. Xiao, X. Li et al., "Using proton magnetic resonance spectroscopy to identify mild cognitive impairment," *International Psychogeriatrics*, vol. 24, no. 1, pp. 19–27, 2012.
- [53] S. J. Choi, K. O. Lim, I. Monteiro, and B. Reisberg, "Diffusion tensor imaging of frontal white matter microstructure in early Alzheimer's disease: a preliminary study," *Journal of Geriatric Psychiatry and Neurology*, vol. 18, no. 1, pp. 12–19, 2005.
- [54] M. Pievani, F. Agosta, E. Pagani et al., "Assessment of white matter tract damage in mild cognitive impairment and Alzheimer's disease," *Human Brain Mapping*, vol. 31, no. 12, pp. 1862–1875, 2010.
- [55] G. Catheline, O. Periot, M. Amirault et al., "Distinctive alterations of the cingulum bundle during aging and Alzheimer's disease," *Neurobiology of Aging*, vol. 31, no. 9, pp. 1582–1592, 2010.
- [56] I. R. Olson, A. Plotzker, and Y. Ezzyat, "The enigmatic temporal pole: a review of findings on social and emotional processing," *Brain*, vol. 130, no. 7, pp. 1718–1731, 2007.

- [57] S. E. Arnold, B. T. Hyman, and G. W. Van Hoesen, "Neuropathologic changes of the temporal pole in Alzheimer's disease and Pick's disease," *Archives of Neurology*, vol. 51, no. 2, pp. 145–150, 1994.
- [58] C. J. Galton, B. Gomez-Anson, N. Antoun et al., "Temporal lobe rating scale: application to Alzheimer's disease and frontotemporal dementia," *Journal of Neurology Neurosurgery and Psychiatry*, vol. 70, no. 2, pp. 165–173, 2001.
- [59] S. Dupont, "Investigating temporal pole function by functional imaging," *Epileptic Disorders*, vol. 4, supplement 1, pp. S17–S22, 2002.
- [60] R. N. Cardinal, J. A. Parkinson, J. Hall, and B. J. Everitt, "Emotion and motivation: the role of the amygdala, ventral striatum, and prefrontal cortex," *Neuroscience and Biobehavioral Reviews*, vol. 26, no. 3, pp. 321–352, 2002.
- [61] L. W. de Jong, K. van der Hiele, I. M. Veer et al., "Strongly reduced volumes of putamen and thalamus in Alzheimer's disease: an MRI Study," *Brain*, vol. 131, no. 12, pp. 3277–3285, 2008.
- [62] M. Boccia, M. Acierno, and L. Piccardi, "Neuroanatomy of Alzheimer's disease and late-life depression: a coordinate-based meta-analysis of MRI studies," *Journal of Alzheimer's Disease*, vol. 46, no. 4, pp. 963–970, 2015.
- [63] D. Wang, S. C. Hui, L. Shi et al., "Application of multimodal MR imaging on studying Alzheimer's disease: a survey," *Current Alzheimer Research*, vol. 10, no. 8, pp. 877–892, 2013.
- [64] H. Braak and E. Braak, "On areas of transition between entorhinal allocortex and temporal isocortex in the human brain. Normal morphology and lamina-specific pathology in Alzheimer's disease," *Acta Neuropathologica*, vol. 68, no. 4, pp. 325–332, 1985.
- [65] L. W. de Jong, K. van der Hiele, I. M. Veer et al., "Strongly reduced volumes of putamen and thalamus in Alzheimer's disease: an MRI study," *Brain*, vol. 131, no. 12, pp. 3277–3285, 2008.
- [66] E. L. Dennis, N. Jahanshad, K. L. McMahon et al., "Development of brain structural connectivity between ages 12 and 30: a 4-Tesla diffusion imaging study in 439 adolescents and adults," *NeuroImage*, vol. 64, pp. 671–684, 2013.
- [67] L. Zhan, Z. Nie, J. Ye et al., "Multiple stages classification of Alzheimer's disease based on structural brain networks using generalized low rank approximations (GLRAM)," in *Computational Diffusion MRI: MICCAI Workshop, Boston, MA, USA, September 2014*, Mathematics and Visualization, pp. 35–44, Springer, 2014.
- [68] Y. Jin, C.-Y. Wee, F. Shi et al., "Identification of infants at risk for autism using multi-parameter hierarchical white matter connectomes," in *Machine Learning in Medical Imaging*, vol. 9352 of *Lecture Notes in Computer Science*, pp. 170–177, Springer, Basel, Switzerland, 2015.
- [69] Y. Jin, C.-Y. Wee, F. Shi et al., "Identification of infants at high-risk for autism spectrum disorder using multiparameter multiscale white matter connectivity networks," *Human Brain Mapping*, vol. 36, no. 12, pp. 4880–4896, 2015.
- [70] L. Huang, Y. Gao, Y. Jin, K.-H. Thung, and D. Shen, "Soft-split sparse regression based random forest for predicting future clinical scores of Alzheimer's disease," in *Machine Learning in Medical Imaging*, vol. 9352 of *Lecture Notes in Computer Science*, pp. 246–254, Springer, Basel, Switzerland, 2015.
- [71] A. Zalesky, A. Fornito, I. H. Harding et al., "Whole-brain anatomical networks: does the choice of nodes matter?" *NeuroImage*, vol. 50, no. 3, pp. 970–983, 2010.
- [72] C.-Y. Wee, P.-T. Yap, D. Zhang, L. Wang, and D. G. Shen, "Group-constrained sparse fMRI connectivity modeling for mild cognitive impairment identification," *Brain Structure and Function*, vol. 219, no. 2, pp. 641–656, 2014.
- [73] T. C. Chua, W. Wen, M. J. Slavin, and P. S. Sachdev, "Diffusion tensor imaging in mild cognitive impairment and Alzheimer's disease: a review," *Current Opinion in Neurology*, vol. 21, no. 1, pp. 83–92, 2008.
- [74] G. T. Stebbins and C. M. Murphy, "Diffusion tensor imaging in Alzheimer's disease and mild cognitive impairment," *Behavioural Neurology*, vol. 21, no. 1-2, pp. 39–49, 2009.

## Research Article

# Node Detection Using High-Dimensional Fuzzy Parcellation Applied to the Insular Cortex

Ugo Vercelli,<sup>1,2,3</sup> Matteo Diano,<sup>1,2,3</sup> Tommaso Costa,<sup>1,2,3</sup> Andrea Nani,<sup>1,2,3</sup> Sergio Duca,<sup>1</sup> Giuliano Geminiani,<sup>1,3</sup> Alessandro Vercelli,<sup>4</sup> and Franco Cauda<sup>1,2,3</sup>

<sup>1</sup>GCS fMRI, Koelliker Hospital, Turin, Italy

<sup>2</sup>Functional Neuroimaging and Neural Complex System Group, Department of Psychology, University of Turin, Turin, Italy

<sup>3</sup>Department of Psychology, University of Turin, Turin, Italy

<sup>4</sup>Neuroscience Institute of the Cavalieri Ottolenghi Foundation and Department of Neuroscience, University of Turin, Turin, Italy

Correspondence should be addressed to Franco Cauda; [franco.cauda@unito.it](mailto:franco.cauda@unito.it)

Received 29 April 2015; Revised 29 June 2015; Accepted 6 July 2015

Academic Editor: Yong Liu

Copyright © 2016 Ugo Vercelli et al. This is an open access article distributed under the Creative Commons Attribution License, which permits unrestricted use, distribution, and reproduction in any medium, provided the original work is properly cited.

Several functional connectivity approaches require the definition of a set of regions of interest (ROIs) that act as network nodes. Different methods have been developed to define these nodes and to derive their functional and effective connections, most of which are rather complex. Here we aim to propose a relatively simple “one-step” border detection and ROI estimation procedure employing the fuzzy *c*-mean clustering algorithm. To test this procedure and to explore insular connectivity beyond the two/three-region model currently proposed in the literature, we parcellated the insular cortex of 20 healthy right-handed volunteers scanned in a resting state. By employing a high-dimensional functional connectivity-based clustering process, we confirmed the two patterns of connectivity previously described. This method revealed a complex pattern of functional connectivity where the two previously detected insular clusters are subdivided into several other networks, some of which are not commonly associated with the insular cortex, such as the default mode network and parts of the dorsal attentional network. Furthermore, the detection of nodes was reliable, as demonstrated by the confirmative analysis performed on a replication group of subjects.

## 1. Introduction

One powerful method for studying brain organization is the graph-theoretical approach [1]. Similar to other connectivity methods, such as seed-based functional connectivity and diffusion-tensor-imaging approaches, this method requires the definition of a set of regions of interest (ROIs) that act as network nodes [2]. Several techniques have been employed to functionally derive these nodes and their connections [3, 4]. The definition of such nodes often involves complicated functional connectivity estimation and border detection procedures [5]. Here, we suggest a relatively simple “one-step” border detection and ROI estimation procedure. In particular, we propose to take advantage of one of the characteristics of the fuzzy *c*-mean clustering algorithm [6]. This procedure allows a fixed percentage of voxels with a borderline pattern of connectivity to be nonunequivocally attributed. The further we move from the centre towards the border of a cluster,

the more the characteristics of the pattern of connectivity are intermixed with those of the neighbouring clusters (e.g., nonunequivocally determined). As was recently shown by Smith et al. [7], the maximization of spatial independence could lead to suboptimal detection of networks that share significant spatial overlaps. Our method maximizes the temporal independence because the criterion used in the clustering algorithm is the correlation between the time series of each voxel and the time series of the centre of each cluster.

Previous clustering studies [6, 8–10] performed the clustering procedure at subject level. Given the relative deficiency of time points (about 120–200 points in a six-minute run), this procedure has good reliability only for low-dimensional parcellation (e.g., with a limited number of clusters). In line with other investigations [2, 11, 12], we concatenated the time courses across all subjects to constitute a very big dataset that allowed us to obtain a higher clustering dimensionality. Far from representing a step backwards, this “fixed-effect”

approach permits good estimation of a common set of clusters (and thereby of nodes) for a given group of subjects. Subsequently, the between-subject variance was taken into consideration, so that each node’s functional connectivity pattern was evaluated at the subject level and summarized using a random-effect analysis. This method is very similar to the dual regression approach [13], according to which the independent component analysis (ICA) was first applied to the concatenated dataset.

To investigate how this node detection method performs with real data, we applied our procedure to the insular surface of 20 healthy subjects scanned in a resting state. A second dataset of 18 healthy volunteers was used for replication testing. We chose the insular surface because the insula is a complex and pivotal [14] brain area in which different inputs from the body and the external world are highly integrated [15]. This brain region has been parcellated by using different measures, such as resting-state functional connectivity [8, 10, 14], task-related functional connectivity [16, 17], and diffusion tensor imaging [18, 19], into two [8, 16, 20–23], or three [9, 10], or more clusters [4, 5, 17, 24], each of which has a unique pattern of connectivity. A recent paper by Kelly et al. [25] demonstrated a convergence between resting state, task-based functional connectivity, and anatomical coactivations at several different parcellation levels (from two to 12 clusters per side; with more than 12 clusters, reliability dropped by about 50%), thus supporting a common hierarchical structure within the insular cortex.

Given these premises, it would be of great interest to test this new node detection method in search of a resting-state functional parcellation of the insular surface. As an additional consideration, we suppose that high-dimensional clustering [11] can make it possible to demonstrate the existence of a more complex pattern with “echoes” [12] of several brain networks nested within the two main insular patterns previously reported.

## 2. Methods

**2.1. Main Group.** Main group consists of twenty healthy right-handed volunteers (10 females, with a mean age of  $32.6 \pm 11.2$ ). Replication group comprises eighteen healthy right-handed volunteers (nine females, with a mean age of  $25.3 \pm 4.2$ ). All subjects were free of neurological or psychiatric conditions, were not taking any medication known to alter brain activity, and had no history of drug or alcohol abuse. Handedness was ascertained with the Edinburgh Inventory [26]. We obtained written informed consent from every subject, in accordance with the Declaration of Helsinki. The study was approved by the institutional committee on ethical use of human subjects at the University of Turin.

**2.2. Task and Image Acquisition.** Images were acquired during a resting-state scan on a 1.5 Tesla INTERA scanner (Philips Medical Systems). Functional T2\* weighted images were acquired using echoplanar (EPI) sequences, with a repetition time (TR) of 2000 ms, an echo time (TE) of 50 ms, and a 90° flip angle. The acquisition matrix was  $64 \times 64$ , with a

200 mm field of view (FoV). A total of 200 volumes were acquired, with each volume consisting of 19 axial slices; slice thickness was 4.5 mm with a 0.5 mm gap, while in-plane resolution was 3.1 mm. Two scans were added at the beginning of functional scanning to achieve steady-state magnetization before acquiring the experimental data. A set of three-dimensional high-resolution T<sub>1</sub>-weighted structural images was acquired, using a fast field echo (FFE) sequence, with a 25 ms TR, an ultrashort TE, and a 30° flip angle. The acquisition matrix was  $256 \times 256$  and the FoV was 256 mm. The set consisted of 160 contiguous sagittal images covering the whole brain.

**2.3. Data Analysis.** Datasets were preprocessed and analysed using BrainVoyager QX software (Brain Innovation, Maastricht, The Netherlands).

Functional images were preprocessed to reduce artefacts as follows [27]: (i) slice scan time correction was performed using a sinc interpolation algorithm; (ii) 3D motion correction was applied using a trilinear interpolation algorithm according to which all volumes were spatially aligned to the first volume by rigid body transformations, and the roto-translation information was saved for subsequent elaborations; (iii) spatial smoothing was performed using a Gaussian kernel of 8 mm FWHM. Several nuisance covariations were regressed out from the time courses to control for the effects of physiological processes, such as fluctuations related to cardiac and respiratory cycles and motion [28–30]. Specifically, we included nine additional covariations from white matter (WM), global signal (GS) [31], and cerebrospinal fluid (CSF), as well as six motion parameters. Subsequently, time courses were temporally filtered in order to keep only frequencies between 0.008 and 0.08 Hz and normalized.

Following the preprocessing, we implemented some steps to improve intersubject analysis of the anatomical location of brain activations. For each subject the functional scans were coregistered with a relatively high-resolution structural scan. This coregistration was done using both the slice positioning as stored in the raw data’s headers and fine adjustments calculated comparing the intensity values of the data sets. After this we transformed each subject’s 3D structural data into Talairach space [32]. This was obtained by translating and rotating the cerebrum on the plain passing through the anterior and the posterior commissure; then, the borders of the cerebrum were identified. The coregistration matrix of anatomical and functional data consisted of the parameters of rotation and translation during the coregistration step and the parameters of Talairach normalization. Finally, by applying the anatomical-functional coregistration matrix we transformed into Talairach space the functional time course of each subject and created the volume time course.

We applied a fuzzy *c*-mean algorithm to the time courses of all the insular voxels and clustered these voxels on the basis of their temporal similarity. As is typical of fuzzy clustering techniques, a certain percentage of voxels can be nonunivocally attributed to the parcels. The percentage of nonunivocally attributed voxels (the fuzziness coefficient) is an arbitrary parameter. In line with other studies [33], we chose 20% of nonunivocally attributed voxels.

The fuzzy clustering technique parcels out a subset of  $N$  voxels in  $C$  “clusters” of activation [34]. Signal time courses of all voxels were  $z$ -standardized. We subsequently confronted the voxel’s time courses  $\mathbf{x}_n$  ( $n = 1 \cdots N$ ) with each other and derived a representative cluster of time courses (cluster centroids)  $\mathbf{v}_c$  ( $c = 1 \cdots C$ ). On the basis of this unsupervised method, and starting from the original fMRI time series, we got a predefined number of spatial modes, which were composed of a spatial map and an associated centroid time course. Accordingly, a voxel is assigned to a cluster with reference to the similarity (e.g., by correlation) of its time course to the cluster centroid. This similarity is determined in a fuzzy way, which means that a voxel is not uniquely assigned to one cluster (hard clustering) because the similarity is expressed by the “membership”  $u_{cn}$  of voxel  $n$  to cluster  $c$ .

Centroids  $\mathbf{v}_c$  and memberships  $u_{cn}$  are both updated in an iterative procedure [35], which terminates when successive iterations do not further change memberships. Cluster centres are determined via classical cluster-algorithm distance measures and are expressed as follows:

$$\sum_{c=1}^C u_{cn} = 1 \quad (1)$$

$$\mathbf{v}_c = \frac{\sum_{n=1}^N u_{cn}^m \mathbf{x}_n}{\sum_{n=1}^N u_{cn}^m} \quad (2)$$

$$u_{cn} = \frac{1}{\sum_{k=1}^C (d(\mathbf{x}_n, \mathbf{v}_c) / d(\mathbf{x}_n, \mathbf{v}_k))^{2/(m-2)}},$$

where  $d$  is the distance between a voxel and a cluster centre and  $m$  is the coefficient that determines the fuzziness of the procedure;  $m$  “tunes out” the noise in the data and lies between 1 (smallest fuzziness) and infinity. The most commonly used of the several distance measures of  $d$  are the Euclidean distance,  $d_E$ , and the Mahalanobis distance,  $d_M$  [36], which are defined as

$$\begin{aligned} d_E(\mathbf{x}_n, \mathbf{v}_c) &= \|\mathbf{x}_n - \mathbf{v}_c\|^2, \\ d_M(\mathbf{x}_n, \mathbf{v}_c) &= (\mathbf{x}_n - \mathbf{v}_c)^T \Sigma_c^{-1} (\mathbf{x}_n - \mathbf{v}_c). \end{aligned} \quad (3)$$

$\Sigma_c$  is the covariance matrix of cluster  $c$ . The Mahalanobis distance takes in the elliptical shape of the cluster (i.e., it weights the differences by the range of variability, described by  $\Sigma_c$ , in the direction of the voxel instead of treating all voxels  $\mathbf{x}_n$  equally when calculating the distance  $d$  to the cluster centre  $\mathbf{v}_c$ ). The Euclidean distance assumes a spherical shape, without taking into account the shape of clustering, which corresponds to a covariance matrix  $\Sigma_c$  with 1s on the main diagonal and 0s elsewhere.

Calculation starts from an initial set of membership values for the data set in the following matrix form:

$$U^{(0)} = \left(1 - \frac{\sqrt{2}}{2}\right)U + \frac{\sqrt{2}}{2}V \quad (4)$$

with  $U = 1/C$  and  $V$  a matrix of randomly chosen cluster centres with initial  $C = 2$ . Subsequently, the new centroids

and memberships are calculated using (2). When further iterations do not cause significant change to memberships and centroids, the procedure stops. With this procedure the following function is minimized:

$$\sigma_w^2 = \frac{1}{N} \sum_{n=1}^N \sum_{c=1}^C u_{cn}^m d(\mathbf{x}_n, \mathbf{v}_c). \quad (5)$$

This formula calculates the within-class variance over all clusters,  $\sigma_w^2$ . In other words, a user-defined threshold for change in  $\sigma_w^2$  is fixed when convergence is reached. The criterion of convergence is based on the first local optimum of (5) [37]. Each time series is transformed into its  $z$ -score in order to avoid a classification of the voxels on signal amplitude rather than on signal shape. Then, the principal component analysis (PCA) is performed to reduce data dimensionality. The number of PCA components was calculated to retain 95% of the variance.

Optimal number of clusters: The a priori definition of the number of clusters and the fuzziness coefficient is often debated in the literature [38]. Usually, the optimal number of classes is unknown in fuzzy clustering. A number of cluster-validity indices have been proposed to estimate the optimal number of clusters in an unsupervised manner (for a review see [39]). These indices aim to identify compact and well-separated clusters. In this study, we used the silhouette validation method [40], which consists in considering the silhouette coefficient of each element:

$$s_i = \frac{b_i - a_i}{\max(b_i, a_i)}, \quad (6)$$

where  $a_i$  is the average dissimilarity of the  $i$ -point to all points in the same cluster and  $b_i$  is the minimum of the average dissimilarity of the  $i$ -point to all points in the other cluster.

Unlike Cauda et al. [8], to perform the clustering procedure time courses were concatenated across all subjects; this step, as has been pointed out by others [2], makes it possible to obtain a higher clustering dimensionality (i.e., more clusters).

Due to the fuzziness coefficient employed, 20% of voxels were classified as nonunequivocal. We considered these voxels as border voxels, with a time course that showed transitional characteristics between contiguous clusters.

The final step of this procedure was to place a spherical ROI with a radius of 3 mm in the local maxima of each cluster (i.e., the area of maximal similarity between voxel time courses). See Figure 1 for a graphical representation of the method.

To investigate the specific pattern of connectivity of each cluster we employed a variant of the dual regression approach [13]. In brief, we performed a generalized linear model (GLM) including all the subject-specific time courses of all 12 right-insular spherical ROIs in a multiple regression analysis. This method resulted in a subject-specific time course relative to each ROI, while controlling for the variance explained by all the other ROIs [12]. Subject-specific patterns of functional connectivity relative to each ROI were then summarized at a group-level using a one-sample  $t$ -test.

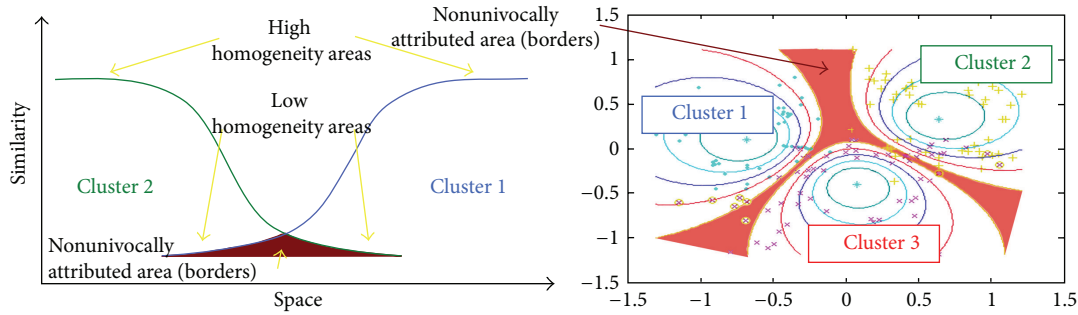


FIGURE 1: Infographic depicting the functioning of the method.

To confirm previous connectivity results [8], we also calculated the functional connectivity of the anterior and posterior insular clusters by grouping together the ROIs belonging to each cluster (see Figure 2(a)).

To validate our parcellation results we applied our method to a second dataset (replication group) and compared the results of the two datasets.

All maps were thresholded at  $p < 0.05$  and corrected for multiple comparisons using the false discovery rate (FDR).

### 3. Results

Our method was able to separate 12 clusters for each insula. This number turned out to be the preferred number of clusters after the application of the silhouette validation method [40]. The algorithm returned the borders of the functionally homogeneous areas; for each cluster a spherical ROI with a radius of 3 mm was placed in the area with the maximal homogeneity (see Figure 2(a)). These results were replicable. Indeed, as shown in Figure 2(c), all the ROIs were also found in the control group and the locations were almost overlapping in 17 out of 24 ROIs, while the other ROIs were displaced by only a few millimetres.

Our calculation of the functional connectivity of the ROIs belonging to anterior and posterior insular clusters confirmed the two patterns of connectivity described in a previous study [8]. The anterior pattern, which occupies the most anterior ventral part of the insular cortex, is characterized by a cingulate-frontoparietal connectivity that has often been related to salience detection. In turn, the posterior pattern, which occupies the posterior dorsal insula, principally shows a sensorimotor connectivity pattern. However, by considering all the 12 ROIs and including the ROI time courses in a multiple regression analysis [12], we discovered a much more intricate picture. With this method we demonstrated that these areas are connected to several other networks, such as the default mode network, the sensorimotor network, and parts of the dorsal attentional network.

### 4. Discussion

By focusing on resting-state data, this study has demonstrated that the proposed fuzzy clustering node detection approach is

able to perform simple yet reliable node detection and surface parcellation.

By virtue of the fuzzy clustering procedure, we successfully generated nodes, and the data obtained with this method were replicable with other datasets. This method allows a very simple one-step border detection procedure, taking advantage of the fact that the borders between areas with homologous functional connectivity are characterized by a temporal profile (i.e., time course) with mixed characteristics of time courses of contiguous regions. These time courses were therefore nonunivocally classified.

The fuzzy clustering procedure has proven to be replicable using a replication dataset. By varying the fuzziness coefficient it is possible to change the number of voxels that are attributed to borders, and as a consequence the homogeneity of the voxels pertaining to the univocally defined parcels. Furthermore, by applying a high-dimensional clustering procedure to the analysis of the functional connectivity of the insula, we were able to detect the connectivity patterns, or, as defined by Leech et al. [12], the “echoes” of the other neural networks that we hypothesized might constitute the hierarchical subparcellation of the aforementioned anterior and posterior patterns of connectivity: the ventral anterior cingulo-fronto-parietal “salience detection” network and the dorsal posterior sensorimotor network, respectively.

As has been previously reported [8, 16, 25, 33], there was some interhemispheric lateralization in the connectivity patterns of the insula. Indeed, the localization of the clusters in the right and the left insula was slightly different, especially in the posterior insula. These results were confirmed when we subdivided the ROIs on the basis of their involvement within the two anterior and posterior clusters. A possible explanation for this hemispheric asymmetry could involve some aspects of emotional and sympathetic processing; for example, the right insula is likely to respond more to sympathetic arousal, and the left insula to parasympathetic nervous functions [41, 42]. Furthermore, the anatomical connections of the anterior insula (AI) with areas pertaining to the ventral attentional network, in particular the temporoparietal junction (TPJ), have been shown to be lateralized on the right side [43]. This is coherent with the “fight or flight” function of the sympathetic system, which requires an evaluation of the potential danger of incoming stimuli.

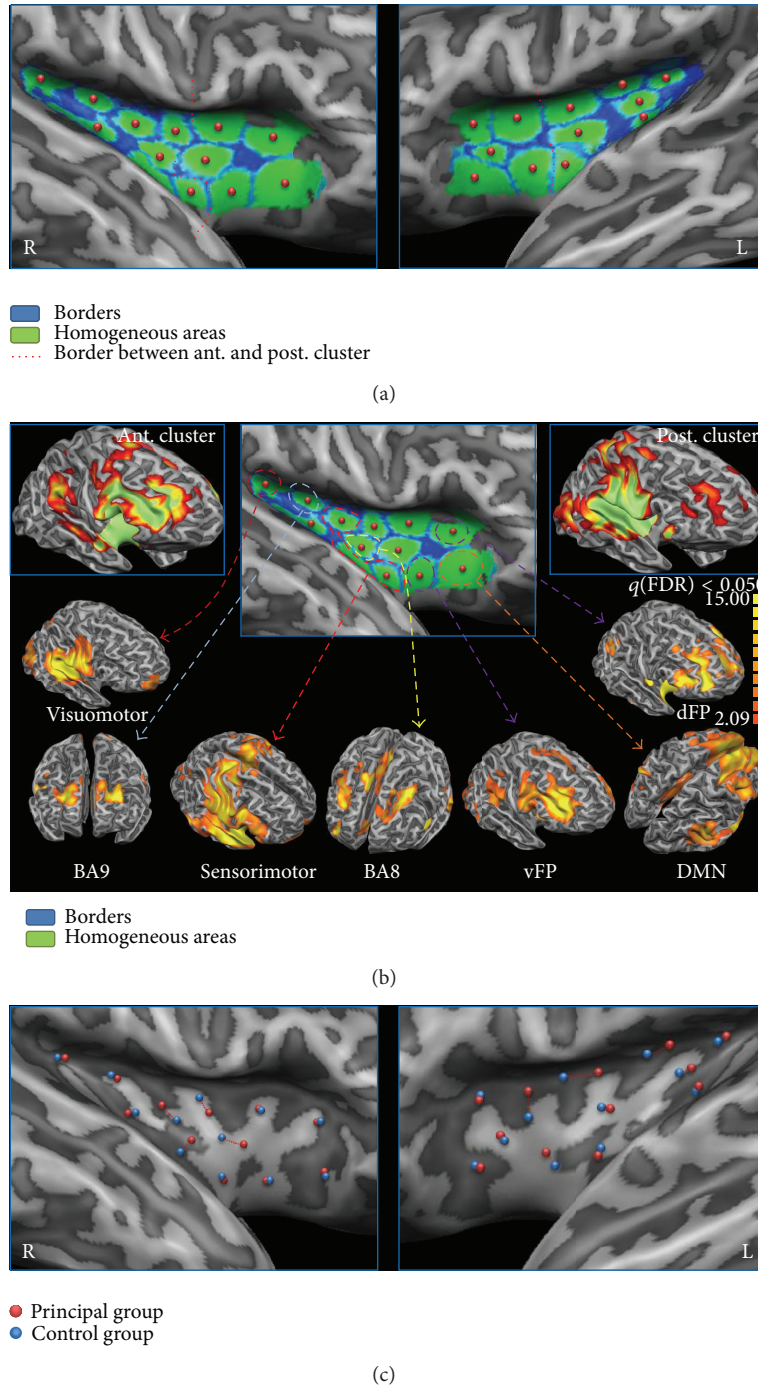


FIGURE 2: High-dimensional clusterization and node creation of the insular cortex. (a) High-dimensional insular clusterization. Homogeneous areas are shown in green and borders in blue. The dotted red line outlines the separation between anterior and posterior clusters as detected in our previous studies [8, 33]. (b) Upper panels: anterior- and posterior-cluster functional connectivity. (b) Lower panels: patterns of functional connectivity regressing out the common variance. (c) Reliability of node creation. Nodes calculated from the main group are shown in red, nodes calculated from the replication group in blue. If separated, paired nodes are shown by a dotted red line.

The posterior part of the insula is characterized by smaller clusters and less homogeneity than the anterior part. Accordingly, hemispheric asymmetry is also more evident in the posterior than in the AI. These findings support the idea that the posterior circuits have more heterogeneous connectivity

patterns, in line with Craig's hypothesis suggesting that the posterior insula is a sort of data collector linked to many different networks [15, 44]. As reported in recent studies [9, 25], this group of posterior clusters mainly exhibits a sensorimotor pattern of connectivity. Indeed, if we move

from the more posterior part of the insular surface towards the middle and anterior parts, the connectivity changes from visuomotor to prefrontal pathways (BA9), then to sensorimotor, and back again to prefrontal pathways (BA8) within the middle insular cortex. In fact, not only action and perception-related patterns but also some prefrontal patterns of connectivity are present within the posterior insula. This is probably due to the involvement of this area in a variety of different activities, such as pain, language, interoception, and sexuality, as has been recently reported [17, 25]. Overall, the posterior insula shows a more specific connectivity pattern than the AI, which, on the contrary, shows connections with networks related to the switch of attention between internal and external stimuli, such as the attentional and default mode networks. Thus, rather than being specific, this pattern suggests a general function that can be exploited in a variety of everyday activities. This has been confirmed by several papers that have shown how the AI is more aspecifically and massively activated in a broad series of different behavioural domains [8, 9, 17, 25]. In line with our data, these studies linked the activity of the AI with cognitive and emotional responses, an involvement that, together with saliency detection [45] and task switching [46], is almost ubiquitous.

Some authors [10, 14, 17, 47–49] have suggested a differentiation or a gradient of connectivity between the dorsal and ventral AI, a variance that, however, we failed to demonstrate in our previous papers. Different levels of parcellation determined by the various methods used to calculate the optimal number of clusters lead to a different picture of the insular cortex. This phenomenon is particularly evident in the results of the study by Kelly et al. [25], which compared insular parcellations with  $n = 2$  and  $n = 3$  clusters. In the parcellation with  $n = 3$  clusters the higher number of clusters made it possible to reveal an anterior ventral cluster that was not present with  $n = 2$ .

In the present paper the complex structure of the anterior insular cortex has been further clarified. We have validated the recent identification made by Touroutoglou et al. [50] of two dissociable frontoparietal patterns of functional connectivity, the dorsal and ventral AI, respectively (for a similar result see also [14]). These two networks (the dorsal one here referred to as dFP and the ventral one as vFP) probably subserve only two partially different functions. The dorsal network is likely to be more involved in the integration of top-down and bottom-up salient information, whereas the ventral network is likely to be more involved in aspects of emotional salience detection as well as the integration of bodily feelings [50]. These two large-scale networks exhibit a different pattern of connectivity: the dorsal network is more centred on dorsolateral and dorsomedial prefrontal cortices plus mid-dorsal cingulate cortices, whereas the ventral network is more linked to the anterior cingulate, ventral prefrontal cortices, and TPJ. Other authors have identified a network that is similar to the dorsal anterior cluster, or, rather, to a mix of the dorsal and ventral anterior insular clusters, for example, the frontoparietal control network [51], and the cingulo-opercular, ventral attentional [52, 53], and basal ganglia-fronto-insular [53] control networks [14, 46]. The two anterior insular frontoparietal networks show areas

of overlap and might have a shared variance that in some conditions makes these two components less easily separable.

Interestingly, a cluster placed in between and just anterior to these two areas shows connectivity with the default mode network. This cluster resides in a position that largely overlaps with the agranular area described by Marsel Mesulam and Mufson in 1982 [54]. This result seems to validate the hypothesis according to which the AI is placed in a pivotal brain site so as to continuously reallocate cerebral resources between internal and external focused networks [55, 56] and modulate the switch between goal-oriented attentional and default mode networks. This supposition would also explain the frequent activation of this brain area in so many different tasks.

## 5. Conclusions

The dFP and vFP patterns of connectivity, which further subdivide the anterior and posterior insular clusters, are probably overcome by the variance of two other main patterns, but when this variance is regressed out, a more complex picture emerges. This phenomenon can be explained by the hierarchical connectivity structure of the insular cortex, as has been suggested by some authors [16, 25]. The two clusters that were previously identified in our papers were here divided into a series of smaller parcels, a procedure in line with recent studies [18, 25, 57]. This is also in accordance with the suggested intrinsically hierarchical structure of this area [5, 24, 58], as hypothesized by Craig and Damasio [15, 41, 59].

In this study we were able to demonstrate that the detection of nodes using high-dimensional fuzzy  $c$ -mean parcellation is a simple, efficient, and reliable method. This indicates that the insula displays a potentially hierarchical structure, in which information coming from the environment and from the body is integrated and distributed to different areas of the brain. Although our study confirmed the two (or three) major insular subdivisions, a more in-depth investigation also showed that these areas can be further subdivided into smaller clusters, each characterized by its own pattern of connectivity that can be detected with appropriate techniques.

## Conflict of Interests

The authors declare that there is no conflict of interests regarding the publication of this paper.

## References

- [1] E. Bullmore and O. Sporns, “Complex brain networks: graph theoretical analysis of structural and functional systems,” *Nature Reviews Neuroscience*, vol. 10, no. 3, pp. 186–198, 2009.
- [2] S. M. Smith, K. L. Miller, G. Salimi-Khorshidi et al., “Network modelling methods for FMRI,” *NeuroImage*, vol. 54, no. 2, pp. 875–891, 2011.
- [3] S. M. Nelson, A. L. Cohen, J. D. Power et al., “A parcellation scheme for human left lateral parietal cortex,” *Neuron*, vol. 67, no. 1, pp. 156–170, 2010.
- [4] A. L. Cohen, D. A. Fair, N. U. F. Dosenbach et al., “Defining functional areas in individual human brains using resting

- functional connectivity MRI,” *NeuroImage*, vol. 41, no. 1, pp. 45–57, 2008.
- [5] B. T. T. Yeo, F. M. Krienen, J. Sepulcre et al., “The organization of the human cerebral cortex estimated by intrinsic functional connectivity,” *Journal of Neurophysiology*, vol. 106, no. 3, pp. 1125–1165, 2011.
  - [6] F. Cauda, G. Geminiani, F. D’Agata et al., “Functional connectivity of the posteromedial cortex,” *PLoS ONE*, vol. 5, no. 9, Article ID e13107, pp. 1–11, 2010.
  - [7] S. M. Smith, K. L. Miller, S. Moeller et al., “Temporally-independent functional modes of spontaneous brain activity,” *Proceedings of the National Academy of Sciences of the United States of America*, vol. 109, no. 8, pp. 3131–3136, 2012.
  - [8] F. Cauda, F. D’Agata, K. Sacco, S. Duca, G. Geminiani, and A. Vercelli, “Functional connectivity of the insula in the resting brain,” *NeuroImage*, vol. 55, no. 1, pp. 8–23, 2011.
  - [9] L. J. Chang, T. Yarkoni, M. W. Khaw, and A. G. Sanfey, “Decoding the role of the insula in human cognition: functional parcellation and large-scale reverse inference,” *Cerebral Cortex*, vol. 23, no. 3, pp. 739–749, 2013.
  - [10] B. Deen, N. B. Pitskel, and K. A. Pelphrey, “Three systems of insular functional connectivity identified with cluster analysis,” *Cerebral Cortex*, vol. 21, no. 7, pp. 1498–1506, 2011.
  - [11] V. Kiviniemi, T. Starck, J. Remes et al., “Functional segmentation of the brain cortex using high model order group PICA,” *Human Brain Mapping*, vol. 30, no. 12, pp. 3865–3886, 2009.
  - [12] R. Leech, R. Braga, and D. J. Sharp, “Echoes of the brain within the posterior cingulate cortex,” *The Journal of Neuroscience*, vol. 32, no. 1, pp. 215–222, 2012.
  - [13] X.-N. Zuo, C. Kelly, J. S. Adelstein, D. F. Klein, F. X. Castellanos, and M. P. Milham, “Reliable intrinsic connectivity networks: test-retest evaluation using ICA and dual regression approach,” *NeuroImage*, vol. 49, no. 3, pp. 2163–2177, 2010.
  - [14] S. M. Nelson, N. U. F. Dosenbach, A. L. Cohen, M. E. Wheeler, B. L. Schlaggar, and S. E. Petersen, “Role of the anterior insula in task-level control and focal attention,” *Brain structure & function*, vol. 214, no. 5-6, pp. 669–680, 2010.
  - [15] A. D. Craig, “How do you feel—now? The anterior insula and human awareness,” *Nature Reviews Neuroscience*, vol. 10, no. 1, pp. 59–70, 2009.
  - [16] F. Cauda, T. Costa, D. M. E. Torta et al., “Meta-analytic clustering of the insular cortex: characterizing the meta-analytic connectivity of the insula when involved in active tasks,” *NeuroImage*, vol. 62, no. 1, pp. 343–355, 2012.
  - [17] F. Kurth, K. Zilles, P. T. Fox, A. R. Laird, and S. B. Eickhoff, “A link between the systems: functional differentiation and integration within the human insula revealed by meta-analysis,” *Brain Structure & Function*, vol. 214, no. 5-6, pp. 519–534, 2010.
  - [18] L. Nanetti, L. Cerliani, V. Gazzola, R. Renken, and C. Keysers, “Group analyses of connectivity-based cortical parcellation using repeated k-means clustering,” *NeuroImage*, vol. 47, no. 4, pp. 1666–1677, 2009.
  - [19] L. Cerliani, R. M. Thomas, S. Jbabdi et al., “Probabilistic tractography recovers a rostrocaudal trajectory of connectivity variability in the human insular cortex,” *Human Brain Mapping*, vol. 33, no. 9, pp. 2005–2034, 2012.
  - [20] L. L. Cloutman, R. J. Binney, M. Drakesmith, G. J. M. Parker, and M. A. L. Ralph, “The variation of function across the human insula mirrors its patterns of structural connectivity: evidence from *in vivo* probabilistic tractography,” *NeuroImage*, vol. 59, no. 4, pp. 3514–3521, 2012.
  - [21] A. Jakab, P. P. Molnár, P. Bogner, M. Béres, and E. L. Berényi, “Connectivity-based parcellation reveals interhemispheric differences in the insula,” *Brain Topography*, vol. 25, no. 3, pp. 264–271, 2012.
  - [22] K. S. Taylor, D. A. Seminowicz, and K. D. Davis, “Two systems of resting state connectivity between the insula and cingulate cortex,” *Human Brain Mapping*, vol. 30, no. 9, pp. 2731–2745, 2009.
  - [23] S. Alcauter, W. Lin, J. Keith Smith, J. H. Gilmore, and W. Gao, “Consistent anterior-posterior segregation of the insula during the first 2 years of life,” *Cerebral Cortex*, vol. 25, no. 5, pp. 1176–1187, 2015.
  - [24] J. D. Power, A. L. Cohen, S. M. Nelson et al., “Functional network organization of the human brain,” *Neuron*, vol. 72, no. 4, pp. 665–678, 2011.
  - [25] C. Kelly, R. Toro, A. Di Martino et al., “A convergent functional architecture of the insula emerges across imaging modalities,” *NeuroImage*, vol. 61, no. 4, pp. 1129–1142, 2012.
  - [26] R. C. Oldfield, “The assessment and analysis of handedness: the Edinburgh inventory,” *Neuropsychologia*, vol. 9, no. 1, pp. 97–113, 1971.
  - [27] F. M. Miezin, L. Maccotta, J. M. Ollinger, S. E. Petersen, and R. L. Buckner, “Characterizing the hemodynamic response: effects of presentation rate, sampling procedure, and the possibility of ordering brain activity based on relative timing,” *NeuroImage*, vol. 11, no. 6, part 1, pp. 735–759, 2000.
  - [28] P. A. Bandettini and E. Bullmore, “Endogenous oscillations and networks in functional magnetic resonance imaging,” *Human Brain Mapping*, vol. 29, no. 7, pp. 737–739, 2008.
  - [29] R. M. Birn, K. Murphy, and P. A. Bandettini, “The effect of respiration variations on independent component analysis results of resting state functional connectivity,” *Human Brain Mapping*, vol. 29, no. 7, pp. 740–750, 2008.
  - [30] V. Napadow, R. Dhond, G. Conti, N. Makris, E. N. Brown, and R. Barbieri, “Brain correlates of autonomic modulation: combining heart rate variability with fMRI,” *NeuroImage*, vol. 42, no. 1, pp. 169–177, 2008.
  - [31] M. D. Fox, D. Zhang, A. Z. Snyder, and M. E. Raichle, “The global signal and observed anticorrelated resting state brain networks,” *Journal of Neurophysiology*, vol. 101, no. 6, pp. 3270–3283, 2009.
  - [32] J. Talairach and P. Tournoux, *Co-Planar Stereotaxic Atlas of the Human Brain: 3-Dimensional Proportional System: An Approach to Cerebral Imaging*, Thieme, 1988.
  - [33] F. Cauda, D. M. E. Torta, K. Sacco et al., “Functional anatomy of cortical areas characterized by von Economo neurons,” *Brain Structure and Function*, vol. 218, no. 1, pp. 1–20, 2013.
  - [34] J. Zadeh and L. Campan, “Age factors in the prognosis of cerebral trauma,” *Annales de l’Anesthesiologie Francaise*, vol. 18, no. 5-6, pp. 471–474, 1977.
  - [35] J. C. Bezdek, R. Ehrlich, and W. Full, “FCM: the fuzzy c-means clustering algorithm,” *Computers & Geosciences*, vol. 10, no. 2-3, pp. 191–203, 1984.
  - [36] P. C. Mahalanobis, “On the generalized distance in statistics,” *Proceedings of the National Institute of Sciences*, vol. 2, no. 1, pp. 49–55, 1936.
  - [37] J. C. Bezdek, *Pattern Recognition with Fuzzy Objective Function Algorithms*, Plenum Press, 1981.
  - [38] M. J. Fadili, S. Ruan, D. Bloyet, and B. Mazoyer, “On the number of clusters and the fuzziness index for unsupervised FCA application to BOLD fMRI time series,” *Medical Image Analysis*, vol. 5, no. 1, pp. 55–67, 2001.

- [39] W. Wang and Y. Zhang, "On fuzzy cluster validity indices," *Fuzzy Sets and Systems*, vol. 158, no. 19, pp. 2095–2117, 2007.
- [40] P. J. Rousseeuw, "Silhouettes—a graphical aid to the interpretation and validation of cluster analysis," *Journal of Computational and Applied Mathematics*, vol. 20, pp. 53–65, 1987.
- [41] A. D. Craig, "Forebrain emotional asymmetry: a neuroanatomical basis?" *Trends in Cognitive Sciences*, vol. 9, no. 12, pp. 566–571, 2005.
- [42] N. A. Harrison, M. A. Gray, P. J. Gianaros, and H. D. Critchley, "The embodiment of emotional feelings in the brain," *The Journal of Neuroscience*, vol. 30, no. 38, pp. 12878–12884, 2010.
- [43] A. Kucyi, M. Moayed, I. Weissman-Fogel, M. Hodaie, and K. D. Davis, "Hemispheric asymmetry in white matter connectivity of the temporoparietal junction with the insula and prefrontal cortex," *PLoS ONE*, vol. 7, no. 4, Article ID e35589, 2012.
- [44] A. D. B. Craig, "Significance of the insula for the evolution of human awareness of feelings from the body," *Annals of the New York Academy of Sciences*, vol. 1225, no. 1, pp. 72–82, 2011.
- [45] W. W. Seeley, V. Menon, A. F. Schatzberg et al., "Dissociable intrinsic connectivity networks for salience processing and executive control," *The Journal of Neuroscience*, vol. 27, no. 9, pp. 2349–2356, 2007.
- [46] N. U. F. Dosenbach, D. A. Fair, F. M. Miezin et al., "Distinct brain networks for adaptive and stable task control in humans," *Proceedings of the National Academy of Sciences of the United States of America*, vol. 104, no. 26, pp. 11073–11078, 2007.
- [47] I. Mutschler, B. Wieckhorst, S. Kowalevski et al., "Functional organization of the human anterior insular cortex," *Neuroscience Letters*, vol. 457, no. 2, pp. 66–70, 2009.
- [48] D. M. Small, "Taste representation in the human insula," *Brain Structure & Function*, vol. 214, no. 5-6, pp. 551–561, 2010.
- [49] T. D. Wager and L. Feldman Barrett, "From affect to control: functional specialization of the insula in motivation and regulation," *PsycEXTRA*, 2004, <http://www.columbia.edu/cu/psychology/tor/>.
- [50] A. Touroutoglou, M. Hollenbeck, B. C. Dickerson, and L. Feldman Barrett, "Dissociable large-scale networks anchored in the right anterior insula subserved affective experience and attention," *NeuroImage*, vol. 60, no. 4, pp. 1947–1958, 2012.
- [51] J. L. Vincent, I. Kahn, A. Z. Snyder, M. E. Raichle, and R. L. Buckner, "Evidence for a frontoparietal control system revealed by intrinsic functional connectivity," *Journal of Neurophysiology*, vol. 100, no. 6, pp. 3328–3342, 2008.
- [52] M. Corbetta, G. Patel, and G. L. Shulman, "The reorienting system of the human brain: from environment to theory of mind," *Neuron*, vol. 58, no. 3, pp. 306–324, 2008.
- [53] G. L. Shulman, S. V. Astafiev, D. Franke et al., "Interaction of Stimulus-driven reorienting and expectation in ventral and dorsal frontoparietal and basal Ganglia-cortical networks," *The Journal of Neuroscience*, vol. 29, no. 14, pp. 4392–4407, 2009.
- [54] M. Marsel Mesulam and E. J. Mufson, "Insula of the old world monkey. I. Architectonics in the insulo-orbito-temporal component of the paralimbic brain," *Journal of Comparative Neurology*, vol. 212, no. 1, pp. 1–22, 1982.
- [55] R. N. Spreng, W. D. Stevens, J. P. Chamberlain, A. W. Gilmore, and D. L. Schacter, "Default network activity, coupled with the frontoparietal control network, supports goal-directed cognition," *NeuroImage*, vol. 53, no. 1, pp. 303–317, 2010.
- [56] D. Sridharan, D. J. Levitin, and V. Menon, "A critical role for the right fronto-insular cortex in switching between central-executive and default-mode networks," *Proceedings of the National Academy of Sciences of the United States of America*, vol. 105, no. 34, pp. 12569–12574, 2008.
- [57] F. Kurth, S. B. Eickhoff, A. Schleicher, L. Hoemke, K. Zilles, and K. Amunts, "Cytoarchitecture and probabilistic maps of the human posterior insular cortex," *Cerebral Cortex*, vol. 20, no. 6, pp. 1448–1461, 2010.
- [58] G. Doucet, M. Naveau, L. Petit et al., "Brain activity at rest: a multiscale hierarchical functional organization," *Journal of Neurophysiology*, vol. 105, no. 6, pp. 2753–2763, 2011.
- [59] A. R. Damasio, *Descartes' Error: Emotion, Reason, and the Human Brain*, 2005.

## Research Article

# Abnormal Resting-State Functional Connectivity Strength in Mild Cognitive Impairment and Its Conversion to Alzheimer's Disease

Yuxia Li,<sup>1,2</sup> Xiaoni Wang,<sup>1</sup> Yongqiu Li,<sup>2</sup> Yu Sun,<sup>1</sup> Can Sheng,<sup>1</sup> Hongyan Li,<sup>1</sup>  
Xuanyu Li,<sup>1</sup> Yang Yu,<sup>1</sup> Guanqun Chen,<sup>1</sup> Xiaochen Hu,<sup>3</sup> Bin Jing,<sup>4</sup> Defeng Wang,<sup>5</sup>  
Kuncheng Li,<sup>6</sup> Frank Jessen,<sup>3</sup> Mingrui Xia,<sup>7</sup> and Ying Han<sup>1,8</sup>

<sup>1</sup>Department of Neurology, XuanWu Hospital of Capital Medical University, Beijing 100053, China

<sup>2</sup>Department of Neurology, Tangshan Gongren Hospital, Tangshan 063000, China

<sup>3</sup>Department of Psychiatry and Psychotherapy, University Hospital of Cologne, Kerpener Strasse 62, 50937 Cologne, Germany

<sup>4</sup>School of Biomedical Engineering, Capital Medical University, Beijing 100069, China

<sup>5</sup>Research Center for Medical Image Computing, Department of Imaging and Interventional Radiology, The Chinese University of Hong Kong, Shatin, New Territories 000852, Hong Kong

<sup>6</sup>Department of Radiology, XuanWu Hospital of Capital Medical University, Beijing 100053, China

<sup>7</sup>State Key Laboratory of Cognitive Neuroscience and Learning and IDG/McGovern Institute for Brain Research, Beijing Normal University, Beijing 100875, China

<sup>8</sup>Center of Alzheimer's Disease, Beijing Institute for Brain Disorders, Beijing 100053, China

Correspondence should be addressed to Mingrui Xia; [mxia@bnu.edu.cn](mailto:mxia@bnu.edu.cn) and Ying Han; [13621011941@163.com](mailto:13621011941@163.com)

Received 5 August 2015; Accepted 4 October 2015

Academic Editor: Feng Shi

Copyright © 2016 Yuxia Li et al. This is an open access article distributed under the Creative Commons Attribution License, which permits unrestricted use, distribution, and reproduction in any medium, provided the original work is properly cited.

Individuals diagnosed with mild cognitive impairment (MCI) are at high risk of transition to Alzheimer's disease (AD). However, little is known about functional characteristics of the conversion from MCI to AD. Resting-state functional magnetic resonance imaging was performed in 25 AD patients, 31 MCI patients, and 42 well-matched normal controls at baseline. Twenty-one of the 31 MCI patients converted to AD at approximately 24 months of follow-up. Functional connectivity strength (FCS) and seed-based functional connectivity analyses were used to assess the functional differences among the groups. Compared to controls, subjects with MCI and AD showed decreased FCS in the default-mode network and the occipital cortex. Importantly, the FCS of the left angular gyrus and middle occipital gyrus was significantly lower in MCI-converters as compared with MCI-nonconverters. Significantly decreased functional connectivity was found in MCI-converters compared to nonconverters between the left angular gyrus and bilateral inferior parietal lobules, dorsolateral prefrontal and lateral temporal cortices, and the left middle occipital gyrus and right middle occipital gyri. We demonstrated gradual but progressive functional changes during a median 2-year interval in patients converting from MCI to AD, which might serve as early indicators for the dysfunction and progression in the early stage of AD.

## 1. Introduction

Alzheimer's disease (AD), an irreversible neurodegenerative disease characterized by memory dysfunction, executive function decline, and multiple cognitive domain impairments, is one of the most financially costly diseases [1]. Since there is currently no effective treatment to stop or reverse the progression of AD, the research spotlight has turned to its

predementia stage, specifically termed amnesic mild cognitive impairment (aMCI). For individuals with MCI due to AD (called "aMCI" or MCI in this paper for short), the development of AD is a high risk factor that the rate of MCI conversion to AD reaches 10% to 15% annually [2]. Considering the urgent requirement for the identification of those MCI patients who are most likely to undergo rapid progression and conversion to AD, it is of great significance to investigate and

discover the potential biomarkers for the early identification of the dysfunction and progression in the early stage of AD.

Magnetic resonance imaging, a noninvasive, nonradiation means for the mapping of both structures and functions of the human brain, is a promising avenue to investigate the progressive brain changes from MCI to AD [3, 4]. Structurally, studies have consistently found that the gray matter atrophy originally starts at the medial temporal lobe, spreads along the midline of the cerebral cortex, and finally extends to the whole brain during the progress from MCI to AD [5–7]. Functionally, however, investigations have yielded limited functional biomarkers that predict the progression from MCI to AD, except the consistent identification of the changes of resting-state functional connectivity (RSFC) of the default-mode network (DMN) in AD [8, 9]. However, deficits in RSFC are not confined to the DMN in patients with MCI converting to AD [10]. Furthermore, it is not clear whether other brain regions participate in the conversion to AD.

Most previous studies have focused on the AD- or MCI-related functional connectivity changes of specific predefined regions of interest, such as posterior cingulate cortex and thalamus [11, 12]. Given the complex pathology and widespread functional abnormalities in AD and MCI, it would be of great interest to examine differences between MCI-converters (MCI-c) and MCI-nonconverters (MCI-nc) within a whole-brain range. Here, we used resting-state functional magnetic resonance imaging (R-fMRI) data and functional connectivity strength (FCS), computed as the sum of connections between a given voxel and all other voxels [13–15], to detect the functional differences among AD, MCI, and normal controls and especially between MCI patients who converted to AD (MCI-c) and MCI-nc. We sought to determine (1) whether there exists an AD-related progressive abnormality pattern on the whole-brain functional connectivity strength in MCI patients and (2) if so whether these changes are different between MCI-c and MCI-nc groups and are related to their clinical behaviors.

## 2. Materials and Methods

**2.1. Participants.** The study was approved by the Research Ethics Review Board of XuanWu Hospital (ClinicalTrials.gov Identifier: NCT02353845). A total of 98 right-handed subjects were recruited in the study including 25 AD patients, 31 MCI patients, and 42 well-matched cognitive normal controls. All AD and MCI patients were recruited at the memory clinic of the Neurology Department, XuanWu Hospital, Capital Medical University, Beijing, China. Control subjects were recruited from the local community via broadcast and advertisements. Diagnoses of MCI due to AD were made by experienced neurologists using Petersen's criteria [16]. The diagnosis of AD fulfilled the published diagnostic criteria [17]. Controls were screened as described in the *Structured Interview for DSM-IV Nonpatient Edition* [18] to confirm the life-long absence of psychiatric and neurological illness. Inclusion criteria for MCI due to AD included the following: (1) memory complaint, preferably confirmed by an informant; (2) objective memory impairment, (cutoff points of Mini-Mental State Examination (MMSE) score [19]: 19 (no formal education),

22 (1 to 6 years of education), and 26 (7 or more years of education); cutoff points of Montreal Cognitive Assessment (MoCA) [20]: 13 (no formal education), 19 (1 to 6 years of education), and 24 (7 or more years of education); cutoff point of auditory verbal learning test- (AVLT-) delayed recall [21]: 6); (3) no or minimal impairment of daily life activities; (4) a Clinical Dementia Rating (CDR) [22] score of 0.5; (5) being free from dementia according to the *Diagnostic and Statistical Manual of Mental Disorders, Fourth Edition*, revised (DSM-IV-R) [18]; (6) hippocampal atrophy confirmed by structural MRI; and (7) the Han nationality, right-handed (the Edinburgh handedness scale score [23] >40 points). The exclusion criteria applied to all subjects with contraindications for MRI; also excluded were those with histories of stroke, psychiatric disease, neurological disorder, alcohol or drug abuse, and systemic disease such as severe anemia, thyroid dysfunction, syphilis, or Acquired Immune Deficiency Syndrome. All subjects underwent a standardized clinical and neuropsychological evaluation, including the MMSE, MoCA, clock drawing test (CDT), AVLT, activities of daily living scale, Hachinski Ischemic Scaling, Hamilton Depression Scale, and CDR. Second, the quality of the whole-brain resting-state functional MRI images was inspected by an experienced neuroradiologist. Third, after a mean follow-up period of 24 months (ranging from 11 months to 48 months), subjects again underwent the entire clinical and neuropsychological assessment. All subjects underwent a follow-up review of approximately 24 months, and according to the diagnosis in the follow-up stage, MCI subjects were divided into converters to AD (MCI-c,  $n = 21$ ) and nonconverters (MCI-nc,  $n = 10$ ).

**2.2. Image Acquisition.** All participants were scanned within a single session on a 3.0T Trio Siemens scanner at XuanWu Hospital, Capital Medical University. Resting-state functional images were collected using an echo-planar imaging sequence with the following parameters: repetition time (TR) = 2000 ms, echo time (TE) = 40 ms, flip angle (FA) = 90°, number of slices = 28, slice thickness = 4 mm, gap = 1 mm, voxel size = 4 × 4 × 4 mm<sup>3</sup>, and matrix = 64 × 64. Participants were asked to lie quietly in the scanner with their eyes closed during data acquisition. Each scan lasted for 478 s. For registration purposes, high-resolution anatomical images were acquired using a 3D magnetization-prepared rapid gradient echo (MPRAGE) T1-weighted sequence with the following parameters: TR = 1900 ms, TE = 2.2 ms, inversion time (TI) = 900 ms, FA = 9°, number of slices = 176, slice thickness = 1 mm, voxel size = 1 × 1 × 1 mm<sup>3</sup>, and matrix = 256 × 256.

### 2.3. Data Analysis

**2.3.1. Image Preprocessing.** Image preprocessing was performed by using SPM8 (<http://www.fil.ion.ucl.ac.uk/spm/>) and Data Processing Assistant for R-fMRI [24]. The preprocessing procedures were performed including removal of the first 10 volumes, slice timing, and head motion correction. All data used in this study satisfied the criteria of spatial movement in any direction < 3 mm or 3° and the subjects demonstrated no

significant group differences in the head motion parameters (i.e., three translation and three rotation parameters). To normalize the fMRI data spatially, the T1-weighted images were firstly registered to the mean functional data, and the resulting aligned T1 data set was segmented and transformed into MNI space using the DARTEL toolbox [25] and a group template was generated. Next, the motion-corrected functional volumes were specially normalized to the group template using the transfer parameter estimated by DARTEL segmentation and resampled to 3 mm isotropic voxels. Further, the functional images were spatially smoothed with a 4 mm Gaussian kernel. The linear detrend and temporal band-pass filtering (0.01–0.08 Hz) was performed to reduce the influences of low-frequency drift and high-frequency physiological noise. Finally, several nuisance signals were regressed out from the data, including the six motion parameters, the global, the white matter, and the cerebrospinal fluid signals.

**2.3.2. Whole-Brain Functional Connectivity Strength.** To perform the whole-brain RSFC analysis, Pearson’s correlations between the time courses of any pairs of voxels were first computed, resulting in a whole-brain connectivity matrix for each participant. This procedure was limited within a gray matter (GM) mask, which was generated by thresholding (cutoff = 0.2) the mean map of all GM maps involving all subjects without cerebellum. These individual correlation matrices were then transformed as a  $z$ -score matrix by using Fisher’s  $r$ -to- $z$  transformation to improve normality. We computed the FCS as the sum of the connections between a given voxel and all other GM voxels. This computation was conservatively restricted to connections with a correlation coefficient above 0.2, which could eliminate the weak correlations possibly arising from noise.

**2.3.3. Seed-Based Functional Connectivity.** To examine the detailed RSFC differences between MCI-c and MCI-nc, we performed seed-based connectivity analyses, using the clusters showing significant between-group difference on FCS as the seeds (i.e., left angular gyrus and middle occipital gyrus). Briefly, the mean time course within each seed was extracted by averaging the time courses of all the voxels belonging to the seed. Subsequently, the mean time course was further used to compute correlation coefficients with the time courses of all GM voxels. Notably, the computation was constrained within a custom GM mask that was made by thresholding (a probability threshold of 0.2) the GM probability map obtained in DARTEL segmentation. The resulting correlation coefficients were then converted to  $z$ -scores using Fisher’s  $r$ -to- $z$  transform to improve normality. For each MCI patient, we obtained two  $z$ -score maps indicative of the intrinsic RSFC patterns of the two seeds (i.e., left angular gyrus and middle occipital gyrus) based on the previous results of the group difference on FCS. Notably, given the ambiguous biological interpretations of negative functional connections, the statistical analysis for RSFC was restricted to positive connections.

**2.3.4. Statistical Analysis.** A one-way analysis of covariance (ANCOVA) was performed to determine the main effect of

groups on FCS, with age and gender as covariates, followed by two-sample  $t$ -tests *post hoc* analyses. The result for ANCOVA was thresholded at  $P < 0.05$  with a cluster size of  $1350 \text{ mm}^3$ , corresponding to a corrected  $P < 0.05$ . The two-sample  $t$ -tests *post hoc* analyses were performed within the regions showing significant group effects, and the threshold was set at  $P < 0.05$  with a cluster size of  $324 \text{ mm}^3$ , corresponding to a corrected  $P < 0.05$ . Furthermore, in the AD pathology-related group, to determine the difference between MCI-c and MCI-nc, we performed a two-sample  $t$ -test on FCS maps of the MCI-c and MCI-nc within the regions showing significant differences of AD against controls. The significant level was set at  $P < 0.05$  with cluster size of  $216 \text{ mm}^3$ , corresponding to a corrected  $P < 0.05$ . All the cluster sizes were determined by Monte Carlo simulations [26] using the REST AlphaSim utility [27].

The two-sample  $t$ -tests were performed on the RSFC maps for each seed, with age and gender as covariates. The significant level was set at  $P < 0.05$  with a cluster size of  $1350 \text{ mm}^3$ , corresponding to a corrected  $P < 0.05$ . The analysis mask was generated by selecting the voxels that showed significant positive RSFC in any of the two groups. To investigate the relationship between FCS and cognitive behavior, we performed general linear model analysis (dependent variable: FCS; independent variable: clinical variables, including MMSE, MoCA, AVLT-immediate recall, AVLT-delayed recall, and AVLT-delayed recognition) in the combined AD and MCI group with age and gender treated as covariates within the regions showing group effect. The statistical threshold was set to  $P < 0.05$  with a cluster size of  $324 \text{ mm}^3$ , which corresponded to a corrected  $P < 0.05$ .

**2.3.5. Discriminate Analysis.** To assess whether the discovered differences of FCS and RSFC between MCI-c and MCI-nc could serve as the features to identify MCI-c patients from MCI-nc patients, we used support vector machine (SVM) as classifier to distinguish patients of the two groups. The features were selected as the values of voxels showing significant between-group differences, including the FCS and the whole-brain functional connectivity of the left angular gyrus and middle occipital gyrus. The leave-one-out cross-validation (LOOCV) was then used to estimate the performance of our classifier. In LOOCV, each sample was designated as the test sample, while the remaining samples were used to train the classifier. Accuracy, sensitivity, and specificity can be defined on the basis of prediction results of LOOCV to quantify the performance of the classifier:

$$\begin{aligned} \text{accuracy} &= \frac{\text{TP} + \text{TN}}{\text{TP} + \text{FN} + \text{TN} + \text{FP}}, \\ \text{sensitivity} &= \frac{\text{TP}}{\text{TP} + \text{FN}}, \\ \text{specificity} &= \frac{\text{TN}}{\text{TN} + \text{FP}}, \end{aligned} \quad (1)$$

where TP, FN, TN, and FP denoted the number of MCI-c patients correctly predicted, the number of MCI-c patients

TABLE 1: Demographics and clinical characteristics of the participants.

	AD ( $n = 25$ )	MCI ( $n = 31$ )	Control ( $n = 42$ )	$F$ or $\chi^2$ value	$P$ value
Age (years)	51–88 (69.4 $\pm$ 11.1)	50–82 (67.9 $\pm$ 9.5)	51–79 (65.6 $\pm$ 7.1)	$F_{(2,95)} = 1.52$	0.22 <sup>a</sup>
Gender (M/F)	9/16	14/17	15/27	$\chi^2_{(2)} = 1.52$	0.67 <sup>b</sup>
Education years	0–17 (8.3 $\pm$ 5.4)	0–21 (10.1 $\pm$ 5)	0–18 (11.1 $\pm$ 4.9)	$F_{(2,95)} = 2.4$	0.10 <sup>a</sup>
MMSE	6–24 (16.8 $\pm$ 4.7)	17–29 (23.5 $\pm$ 2.9)	20–30 (28.0 $\pm$ 2.3)	$F_{(2,95)} = 93.04$	<0.0001 <sup>a</sup>
MoCA <sup>c</sup>	5–22 (12.8 $\pm$ 4.8)	9–24 (18.3 $\pm$ 3.9)	19–30 (26.0 $\pm$ 2.8)	$F_{(2,73)} = 81.32$	<0.0001 <sup>a</sup>
CDT <sup>d</sup>	0–3 (1.7 $\pm$ 1.1)	0–3 (1.8 $\pm$ 0.8)	1–3 (2.9 $\pm$ 0.4)	$F_{(2,87)} = 23.39$	<0.0001 <sup>a</sup>
AVLT-I	0–5.7 (3.6 $\pm$ 1.5)	2–7 (4.6 $\pm$ 1.3)	6–14.7 (9.3 $\pm$ 2.1)	$F_{(2,95)} = 108.87$	<0.0001 <sup>a</sup>
AVLT-D	0–4 (0.6 $\pm$ 1.1)	0–7 (2.7 $\pm$ 2.2)	4–15 (10.4 $\pm$ 3.0)	$F_{(2,95)} = 159.79$	<0.0001 <sup>a</sup>
AVLT-R	–2–8 (3.4 $\pm$ 3.1)	–3–13 (7.1 $\pm$ 3.9)	7–15 (12.4 $\pm$ 2.1)	$F_{(2,95)} = 72.48$	<0.0001 <sup>a</sup>

Data are presented as the range of minimum–maximum (mean  $\pm$  SD).

AD, Alzheimer’s disease; MCI, mild cognitive impairment; MMSE, Mini-Mental State Examination; MoCA, Montreal Cognitive Assessment; CDT, clock drawing test; AVLT-I, auditory verbal learning test–immediate recall; AVLT-D, auditory verbal learning test–delayed recall; AVLT-R, auditory verbal learning test–recognition; MCI-c, mild cognitive impairment converter; MCI-nc, mild cognitive impairment nonconverter.

<sup>a</sup>The  $P$  value was obtained by one-way ANOVA.

<sup>b</sup>The  $P$  value was obtained by two-tailed Pearson chi-square test.

<sup>c</sup>MoCA included 24 AD patients, 22 MCI patients and 30 controls.

<sup>d</sup>CDT included 23 AD patients, 29 MCI patients and 38 controls.

classified as MCI-nc patients, the number of MCI-nc patients correctly predicted, and the number of MCI-nc patients classified as MCI-c patients, respectively.

**2.3.6. Validations.** Given that the results of the FCS analysis might be influenced by several methodological choices (e.g., correlation threshold, head motion, and removal of global signal), we conducted the following procedures and re-compared the FCS within left angular gyrus and middle occipital gyrus between the two MCI groups. (i) Change of correlation thresholds. In the initial analysis, a correlation coefficient threshold of 0.2 was used during the FCS analysis. To determine whether the FCS results depend on the selection of correlation thresholds, the other two different correlation thresholds (i.e., 0.1 and 0.3) were used to recompute the FCS maps. There resultant FCS maps were then used to perform the statistical analyses, respectively. (ii) Include the head motion parameter into statistical analysis. The influences of head motion on RSFC have been reported by several studies recently [28–30]. Although we observed no significant differences between any pairs of the groups in the maximum movements at each direction, we cautiously evaluated the head motion effects on our results by calculating the frame-wise displacement (FD) of our data [30] and further compared the group difference by adding FD as an additional nuisance covariate. (iii) Do not use global signal regression (GSR). Whether the global mean signal should be removed is currently still debatable in the preprocessing procedure of the R-fMRI images. Some studies suggested that the global signal should be removed [31], as it was confounded with physiological noise [32], whereas several other studies [33, 34] indicated that the GSR could introduce negative correlations and therefore alter the intrinsic architecture of the brain network. To examine whether the process of GSR changes our results, the data was reanalyzed without using GSR in the preprocessing steps.

### 3. Results

**3.1. Demographics and Neuropsychological Tests.** Clinical and demographic data for the 98 participants are presented in Tables 1 and 2. Some of these data were used previously to detect functional brain abnormalities in MCI patients [35, 36]. There were no significant differences among MCI, AD, or controls with respect to age ( $P = 0.22$ ), gender ( $P = 0.67$ ), and years of education ( $P = 0.10$ ). However, the clinical variables, including the MMSE, MoCA, CDT, AVLT-immediate recall (AVLT-I), AVLT-delayed recall (AVLT-D), and AVLT-delayed recognition (AVLT-R), differed significantly among the three groups ( $P < 0.0001$  for all comparisons), with an ascending order of AD, MCI, and controls. Furthermore, there were no significant differences between MCI-c and MCI-nc groups in age, gender, years of education, or any of the clinical or neuropsychological variables ( $P > 0.12$  for all comparisons). However, after a mean follow-up period of 24 months, the MMSE and AVLT-I were significantly lower in the MCI-c group than in the MCI-nc group (both  $P$  values < 0.02), and the AVLT-D, AVLT-R, and MoCA were marginally lower in the MCI-c group (all  $P$  values < 0.1).

**3.2. Whole-Brain Functional Connectivity Strength.** The spatial patterns of FCS were remarkably similar across the MCI, AD, and control groups by visual inspection, in spite of different strengths. Regions with high FCS were mostly located in the DMN (mainly involving the medial prefrontal cortex, precuneus, posterior cingulate cortex, and inferior parietal lobule), anterior insula, sensorimotor, and visual cortices (Figure 1(a)). The FCS patterns were similar to those observed in previous studies [13–15].

Significant group differences of FCS among the MCI, AD, and control groups were observed in bilateral precuneus/posterior cingulate cortices (PCu/PCC), bilateral parahippocampal cortices, bilateral angular gyri, right temporal pole, left

TABLE 2: Demographics and clinical characteristics of MCI-c and MCI-nc patients.

	MCI-c ( $n = 21$ )	MCI-nc ( $n = 10$ )	$T$ or $\chi^2$ value	$P$ value
Baseline				
Age (years)	50–82 ( $68.6 \pm 9.3$ )	50–78 ( $66.5 \pm 10.4$ )	$T_{(29)} = 0.57$	0.57 <sup>b</sup>
Gender (M/F)	11/10	3/7	$\chi^2_{(1)} = 4.19$	0.24 <sup>a</sup>
Education years	4–20 ( $10.5 \pm 4.6$ )	0–21 ( $9.2 \pm 5.9$ )	$T_{(29)} = 0.66$	0.52 <sup>b</sup>
MMSE	17–28 ( $23.5 \pm 2.9$ )	17–29 ( $23.6 \pm 3.2$ )	$T_{(29)} = -0.07$	0.95 <sup>b</sup>
MoCA <sup>c</sup>	9–24 ( $18.1 \pm 3.7$ )	10–24 ( $18.7 \pm 4.5$ )	$T_{(20)} = -0.36$	0.73 <sup>b</sup>
CDT <sup>d</sup>	0–3 ( $1.7 \pm 0.9$ )	1–3 ( $2.0 \pm 0.7$ )	$T_{(27)} = -0.79$	0.44 <sup>b</sup>
AVLT-I	2–6.7 ( $4.4 \pm 1.2$ )	3–7 ( $4.9 \pm 1.4$ )	$T_{(29)} = -0.96$	0.34 <sup>b</sup>
AVLT-D	0–6 ( $2.3 \pm 1.9$ )	0–7 ( $3.6 \pm 2.6$ )	$T_{(29)} = -1.60$	0.12 <sup>b</sup>
AVLT-R	–3–13 ( $6.6 \pm 4.2$ )	1–12 ( $8.1 \pm 3.1$ )	$T_{(29)} = -0.99$	0.33 <sup>b</sup>
Follow-up <sup>e</sup>				
MMSE	9–28 ( $20.0 \pm 4.2$ )	21–29 ( $24.4 \pm 2.9$ )	$T_{(24)} = -2.59$	0.02 <sup>b</sup>
MoCA	4–22 ( $15.8 \pm 4.3$ )	12–24 ( $19.0 \pm 4.0$ )	$T_{(24)} = -1.69$	0.10 <sup>b</sup>
CDT	0–3 ( $1.7 \pm 0.9$ )	1–3 ( $2.1 \pm 0.7$ )	$T_{(24)} = -1.23$	0.23 <sup>b</sup>
AVLT-I	0.7–6 ( $4.1 \pm 1.3$ )	3.7–7.3 ( $5.5 \pm 1.3$ )	$T_{(24)} = -2.44$	0.02 <sup>b</sup>
AVLT-D	0–8 ( $1.7 \pm 2.3$ )	0–6 ( $3.4 \pm 2.0$ )	$T_{(24)} = -1.99$	0.06 <sup>b</sup>
AVLT-R	0–13 ( $6.1 \pm 3.8$ )	4–10 ( $8.3 \pm 2.1$ )	$T_{(24)} = -1.76$	0.09 <sup>b</sup>

Data are presented as the range of minimum–maximum (mean  $\pm$  SD).

MCI, mild cognitive impairment; MMSE, Mini-Mental State Examination; MoCA, Montreal Cognitive Assessment; CDT, clock drawing test; AVLT-I, auditory verbal learning test-immediate recall; AVLT-D, auditory verbal learning test-delayed recall; AVLT-R, auditory verbal learning test-recognition; MCI-c, mild cognitive impairment converter; MCI-nc, mild cognitive impairment nonconverter.

<sup>a</sup>The  $P$  value was obtained by two-tailed Pearson chi-square test.

<sup>b</sup>The  $P$  value was obtained by two-sample two-tailed  $t$ -test.

<sup>c</sup>MoCA included 15 MCI-c and 7 MCI-nc patients.

<sup>d</sup>CDT included 19 MCI-c and 10 MCI-nc patients.

<sup>e</sup>The follow-up clinical scores included 17 MCI-c and 7 MCI-nc patients.

TABLE 3: Clusters showing significant group effects on FCS.

Number	Brain regions	Brodmann area	Cluster size ( $\text{mm}^3$ )	Peak MNI coordinate			Max $F$ score
				$x$	$y$	$z$	
1	R ITG/FG/HIP/PHG	20/37/28	12,582	51	–27	–27	11.19
2	L FG/HIP	20/38	9,153	–30	–42	–24	10.78
3	R TPOmid	38	2,376	54	–6	–15	8.62
4	L ORBsup	11	7,668	–3	12	–18	11.71
5	B LING	18	6,183	–18	–60	–6	8.75
6	L MOG	19	1,701	–45	–72	6	8.30
7	B PCC/PCu/CUN	31/7/19	12,339	–3	–51	21	9.52
8	R ANG	39	1,863	39	–63	42	13.09
9	L ANG	39	2,241	–54	–57	36	7.49
10	L SFG	6	2,349	–18	9	60	10.83

Significance level:  $P < 0.05$ ; voxel size  $>1350 \text{ mm}^3$ ; AlphaSim corrected  $P < 0.05$ .

B, bilateral; L, left; R, right; ITG, inferior temporal gyrus; FG, frontal gyrus; HIP, hippocampus; PHG, parahippocampal gyrus; TPOmid, middle temporopolar; ORB sup, superior orbitofrontal cortex; LING, lingual gyri; MOG, middle occipital gyrus; PCC, posterior cingulate cortices; PCu, precuneus; ANG, angular gyri; SFG, superior frontal gyrus; CUN, cuneus.

superior frontal gyrus, left orbitofrontal cortex, bilateral lingual gyri, and left middle occipital gyrus (Figure 1(b), Table 3). The *post hoc* analysis revealed that (i) the MCI showed decreased FCS in bilateral PCu/PCC, bilateral lingual gyri, and left middle occipital gyrus, as compared to controls (Figure 1(b)); (ii) the AD group exhibited lower FCS than controls in bilateral PCu/PCC, bilateral angular gyri, bilateral

lingual gyri, and left middle occipital gyrus, but greater FCS in bilateral parahippocampal cortices, right temporal pole, left superior frontal gyrus, and left orbitofrontal cortex (Figure 1(b)); and (iii) the AD group had significantly lower FCS in bilateral angular gyri but higher FCS in bilateral parahippocampal cortices, right temporal pole, left superior frontal gyrus, and left orbitofrontal cortex than the MCI group

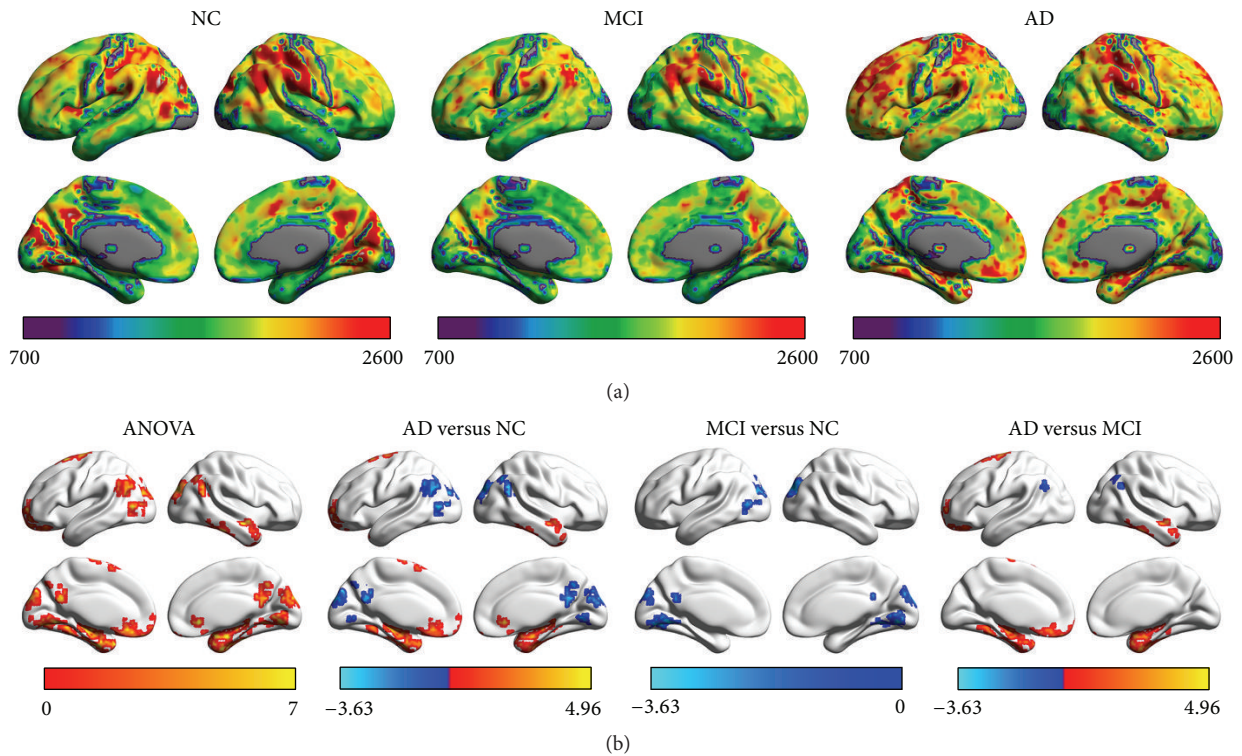


FIGURE 1: The FCS in AD, MCI, and control groups. (a) The images show the mean FCS in AD, MCI, and control groups. The color bar at the bottom of each picture represents the FCS value for each group. (b) The images demonstrated the significant differences among the three groups and within each pair of the groups at baseline. The color bar at the bottom of each picture represents either  $F$  values for ANOVA or  $T$  values for *post hoc t*-tests.

(Figure 1(b)). In the comparison between MCI-c and MCI-nc, the FCS of the left angular gyrus and middle occipital gyrus were significantly lower in the MCI-c group (Figure 2).

**3.3. Seed-Based Functional Connectivity.** To examine the detailed difference in RSFC of the left angular gyrus and middle occipital gyrus, we generated whole-brain RSFC maps of each region in the two MCI groups. The spatial patterns of the whole-brain RSFC for each seed region were similar across the two groups. The left angular gyrus was functionally connected with the default-mode regions, including the PCu/PCC, medial prefrontal cortex, inferior parietal lobule (IPL), dorsolateral prefrontal cortex (dlPFC), and lateral temporal cortex, whereas the left middle occipital gyrus exhibited RSFC with the sensorimotor and visual cortices. Between-group comparisons revealed that the MCI-c patients had significantly decreased RSFC between the left angular gyrus and bilateral IPL, dlPFC and lateral temporal cortices, and the left middle occipital gyrus and right central sulci and right middle occipital gyrus, as compared to the MCI-nc group (Figure 3).

**3.4. Discriminate Analysis.** The SVM method achieved a classification accuracy of 80.6%, with sensitivity of 70.0% and specificity of 85.7% in distinguishing MCI-c patients from

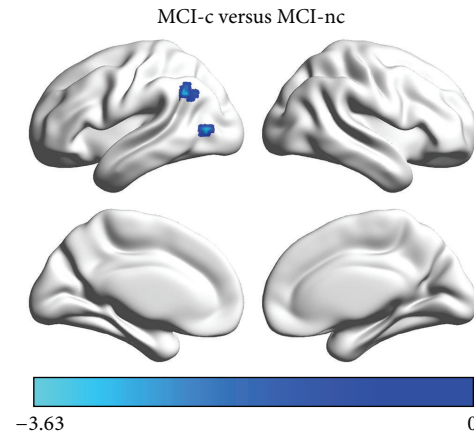


FIGURE 2: The FCS differences between MCI-c and MCI-nc groups. The FCS of the left angular gyrus and middle occipital gyrus were significantly lower in the MCI-c group compared with the MCI-nc group. The color bar represents the  $T$  values for the two-sample *t*-test between MCI-c and MCI-nc groups.

MCI-nc patients, suggesting the potential capacity of the functional metrics left angular gyrus and middle occipital gyrus in predicting converting from MCI to AD.

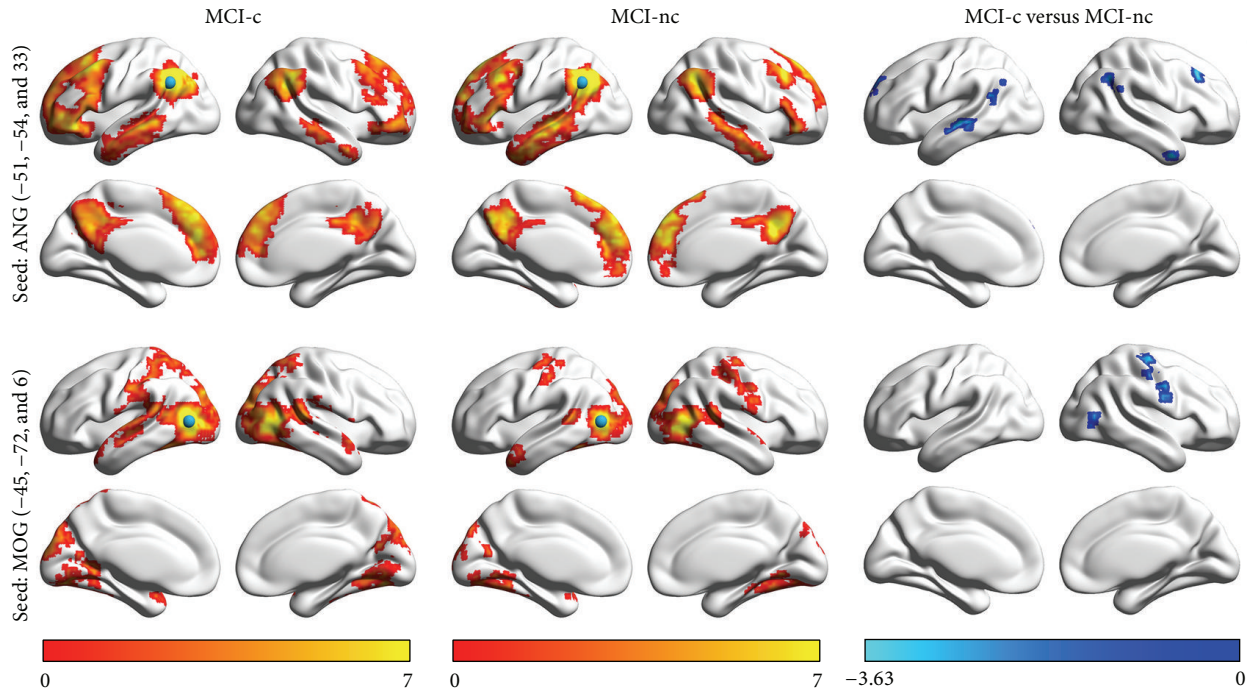


FIGURE 3: The seed-based RSFC analysis between MCI-c and MCI-nc. The left and middle column present the within group RSFC pattern for the left angular gyrus and the left middle occipital gyrus. Between-group comparison on the right column revealed that comparing to MCI-nc group the MCI-c group had significantly decreased functional connectivity between the left angular gyrus and bilateral dlPFC and lateral temporal cortices and between the left middle occipital gyrus and right central sulci and right middle occipital gyrus. The color bars at the bottom represent the  $T$  value for either the one-sample  $t$ -test or two-sample  $t$ -test.

**3.5. Correlations between Functional Connectivity Strength and Neuropsychological Variables.** Significant positive correlation was found between FCS of the left angular gyrus and MMSE. The FCS of the medial temporal cortices was significantly negatively correlated with all the clinical and neuropsychological variables. Additionally, significant negative correlations were observed between the FCS of left dorsal frontal and right lateral temporal cortices and MMSE, MoCA and AVLT-I, and the FCS of ventral genu anterior cingulate cortex and MMSE, MoCA, AVLT-I, and AVLT-D (Figure 4).

**3.6. Validations.** We found that the differences on FCS in the left angular gyrus and middle occipital gyrus between two MCI subgroups were quite stable across different process procedures. The FCS in these two regions remained significantly lower value in MCI-c group under different network correlation thresholds (for threshold 0.1: angular gyrus,  $t = -3.73$ ,  $P = 0.00094$ ; middle occipital gyrus,  $t = -3.12$ ,  $P = 0.0044$ ; for threshold 0.3:  $t = -3.81$ ,  $P = 0.00077$ ; middle occipital gyrus,  $t = 3.14$ ,  $P = 0.0042$ ). There are no significant group differences in the movement parameter FD ( $P = 0.6$ ). FCS differences were unchanged after adding FD as an additional covariate to the reanalysis (angular gyrus,  $t = 3.81$ ,  $P = 0.00085$ ; middle occipital gyrus,  $t = 3.05$ ,  $P = 0.0053$ ). However, these group differences could not be identified in case the global signal was retained ( $P > 0.88$  for all comparisons) in the preprocessing, suggesting that the pathological differences might be buried into systematic and physiological noise.

## 4. Discussion

The present longitudinal study was designed to use R-fMRI for the identification of valuable imaging markers in patients with MCI and AD for predicting conversion from MCI to AD dementia in a mean follow-up of two years. We demonstrated that (i) the MCI group showed decreased FCS in the default-mode regions and occipital cortex, as compared to normal controls at baseline; however, the AD group exhibited simultaneously lower and higher FCS than the MCI and NC group; (ii) the FCS of the left angular gyrus and middle occipital gyrus was significantly lower in the MCI-c group than MCI-nc group. Finally, FCS of several brain regions correlated with clinical and neuropsychological scores.

**4.1. Features of Functional Connectivity Strength in Subjects with AD and MCI.** AD is considered as a disconnection syndrome, and as previous studies showed, AD patients have abnormal RSFC between several brain regions, especially within the DMN [37, 38]. Here, the use of FCS method confirmed progressive functional changes in the DMN from MCI to AD. Our study extended previous finding into MCI patients and provided additional evidence of the progressive features of brain function in subjects with MCI who develop AD.

We observed that patients with MCI and AD showed decreased FCS in the DMN (including bilateral PCu/PCC) and occipital cortex as compared to controls, in line with previous studies [9, 37–41]. At the early stage of AD, the declines

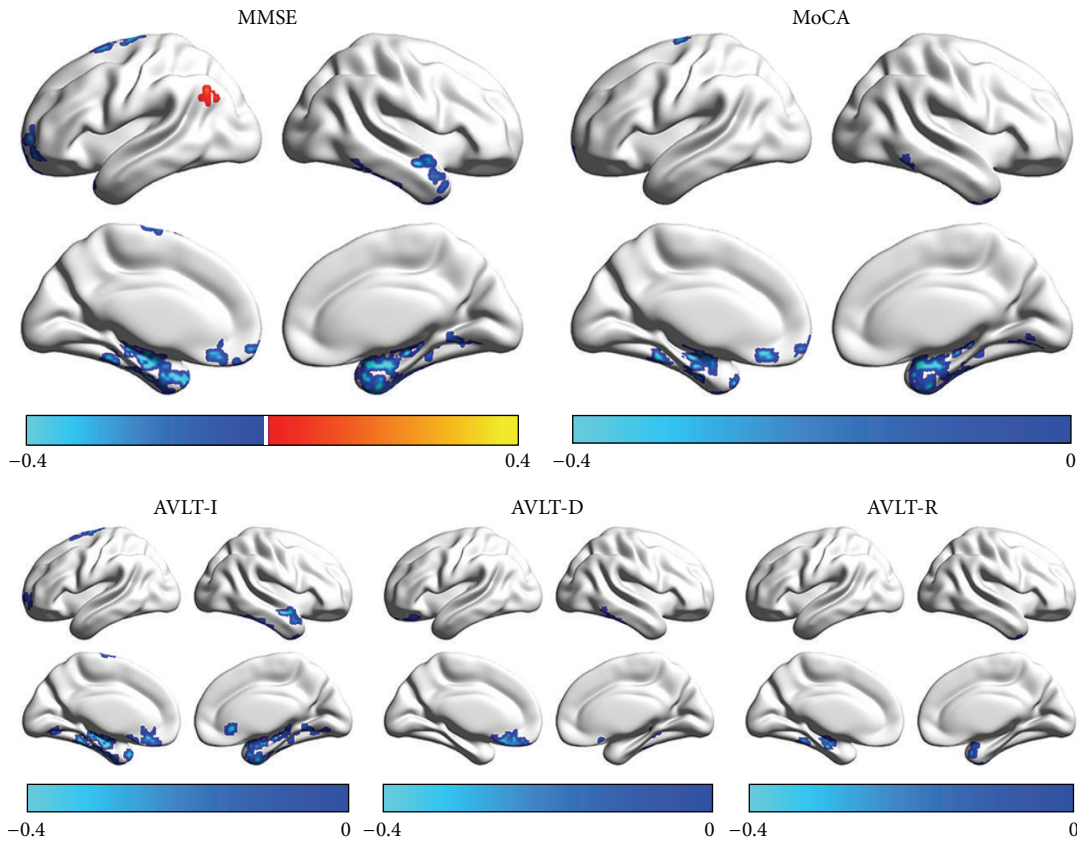


FIGURE 4: The correlation between FCS and neuropsychological scores in patients. The color bar represents the  $r$  value. AVLT-I, auditory verbal learning test-immediate recall; AVLT-D, auditory verbal learning test-delayed recall; AVLT-R, auditory verbal learning test-recognition; MMSE, Mini-Mental State Examination; MoCA, Montreal Cognitive Assessment.

of episodic memory of the patients have been associated with the structural and functional defects in the DMN, which might be due to their underlying accumulations of beta-amyloid plaques [42] and decreased metabolic activity [43]. Studies reported that the decline of RSFC was related to the low neuropsychological assessment scores and to higher conversion rates from MCI to AD [9] or to AD progression [44]. Furthermore, the current study also validated the results of our previous research denoting impairment in the DMN of patients with AD and MCI [35, 36, 45]. Beyond these findings, the occipital cortex (including bilateral lingual gyri and left middle occipital gyrus) manifested decreases of FCS in patients with AD and even MCI. The lingual gyrus and middle occipital gyrus are located in the visual network and are associated with the processing of visual memory and visuospatial function [46, 47]. Our results provided the potential brain bases for the impaired multiple cognitive domains in MCI and AD, which is in consistency with previous study showing the decline of functional connectivity of the occipital cortex in AD and MCI patients [48].

Other than the brain regions cited above, the bilateral angular gyri manifested reductions in FCS in bearers of AD rather than those with MCI, which is consistent with several previous studies [49, 50]. The angular gyrus is an important

brain region of the inferior parietal lobule in the DMN, and its impairments are highly correlated with damage of multiple cognitive domains to identify direction and presence of alexia, agraphia, and dyscalculia in AD patients [51]. A recent study showed decreased RSFC between the left angular gyrus and right thalamus and such an alteration of the thalamo-DMN circuit was also linked to the disease severity in AD and MCI patients [49]. Specifically, in the current study, FCS of the left angular gyrus was positively related to MMSE of patients, suggesting that FCS of the left angular gyri may be a potential imaging marker for monitoring disease progression.

Comparing with MCI patients, AD exhibited increased FCS mainly involving the frontal lobe (including left superior frontal gyrus and orbitofrontal cortex) and temporal lobe (including bilateral parahippocampal cortices and right temporal pole). A notable finding in this study was significant negative correlations between the FCS of left dlPFC, ventral genu anterior cingulate cortex, right lateral temporal cortices, and neuropsychological scores such as MMSE, MoCA, and AVLT-I. A possible mechanistic explanation for these increased FCS could be the compensation mechanism [48, 52, 53] that acts to counterbalance regional deficits in function [54]. Compensatory mechanisms accompany the impairments seen during the interval when a patient with

MCI progresses to AD [11]. A study utilizing single photon emission computed tomography demonstrated the compensation mechanism in the medial temporal lobe in AD with the phenomenon of high perfusion in the neocortex along with hypoperfusion [55]. Besides, synaptic loss was related to the cognitive decline in AD and compensation mechanisms via maintaining the activity levels of neural circuits that could otherwise reduce the impairment of cognitive function induced by synaptic loss [56]. Here, the observation of the increases of FCS in AD rather than in MCI patients suggests that AD patients could utilize additional brain connectivity for cognitive functions, presumably as a compensatory mechanism for cognitive decline.

**4.2. The Diversity of Functional Connectivity between MCI-c and MCI-nc.** Compared to the MCI-nc group, the MCI-c patients had significantly decreased RSFC between the left angular gyrus and bilateral IPL, dlPFC and lateral temporal cortices, and the left middle occipital gyrus and right central sulci and right middle occipital gyrus. IPL (including the angular gyrus and supramarginal gyrus) and dlPFC were the key component in the DMN, and many previous studies have suggested that the lesion in IPL was closely related to AD, especially in MCI [49, 57, 58]. Interestingly, this result explained the reductions of FCS in the bilateral angular gyri in AD rather than in MCI in the current study, which suggested that the decline of FCS in the angular gyrus in MCI-c group may predict a more serious disease closer to AD dementia. Furthermore, several previous studies found decreased RSFC in the dlPFC in early AD, which involves in a series of cognitive functions, including working memory, decision making, and executive controls [38, 59].

Studies have consistently identified structural and metabolic abnormality in the lateral temporal cortex during stage of AD and MCI [60–62]: Li and colleagues found significant reductions in gray matter volume of the left lateral superior temporal gyrus in patients with MCI [62], suggesting that the lateral temporal lobe was impaired in the early stage of MCI. Additionally, we revealed the decline of RSFC of the occipital cortex (middle occipital gyrus) in MCI-c group, compared to MCI-nc. It should be noted that the abnormality in the occipital cortex has gained less attention than the DMN regions in previous studies in MCI developing to AD [8, 9]. Activity and functional connectivity of the occipital lobe are highly associated with visual hallucination [63], visual memory [46], and visuospatial function [47]. Therefore, the functional impairments of occipital cortex could suggest the probable multiple cognitive domains damage, especially the visual cognitive declines in patients converting to AD. Interestingly, a recent study on atrophy patterns of various phenotypes of AD showed the atrophy in the visual network to be dominant in the AD phenotype with posterior cortical atrophy [64]. A more refined differential diagnosis of various AD phenotypes in the future is necessary to delineate the probable relationship between decreased FCS in occipital cortex and specific functional impairment in AD. In summary, the functional alterations of DMN and visual cortex demonstrated imaging impairments in the conversion from MCI to

AD and might provide potential biomarkers for predicting MCI progression.

**4.3. Further Considerations.** Several limitations of the present study require further considerations. First, the clinical criteria for the recruitment of MCI did not classify different subtypes of aMCI patients (single or multiple domain impairment), which introduces the clinical heterogeneity of our data set. Future studies could focus on the differences and conversation of different types of MCI to better characterize the pathology of aMCI. Second, in the present longitudinal study, the conversion rate from MCI to AD was relatively high (33.87% annually), which might be because these patients came to the clinic with obvious memory symptoms at a late stage of MCI. Future studies aiming at the longitudinal database with larger sample size including early MCI and even preclinical stage of AD with multimodal imaging and biophysical data (e.g., Alzheimer's Disease Neuroimaging Initiative (ADNI) database) are of great importance to investigate the progression of AD. Third, the MCI-nonconverters in the current study were just stable in the follow-up stage (about two years) and whether they would convert to AD in the future remains unknown. Therefore, we planned to continue to track these patients to observe the dynamic changes and delineate the progressing trajectory on brain changes during the AD progression. Fourth, we noticed that the FCS differences between MCI-c and MCI-nc could not be identified in case the global signal was retained in the preprocessing. Recent studies have demonstrated raised variability of global signal in schizophrenia but not bipolar illness, suggesting the potential specific association between brain disorders and global signal [65]. Future studies focusing on the global signal in AD could further reveal the deep relationship between the pathology of AD and physiological signals. Finally, the current study was concentrated on the R-fMRI functional connectivity of the whole brain. Further studies that simultaneously combine the R-fMRI, diffusion tensor MRI, and other biophysical data would reveal structural and biological substrates underlying these functional deficits in AD and MCI.

## 5. Conclusions

In conclusion, we demonstrated gradual but progressive functional changes during median 2-year interval in patients converting from MCI to AD, which might serve as early indicators for the dysfunction and progression in the early stage of AD.

## Conflict of Interests

The authors declare that there is no conflict of interests regarding the publication of this paper.

## Acknowledgments

This paper was supported by National Natural Science Foundation of China (Grant nos. 31371007, 81430037, 30970823, and 81401479), Beijing Municipal Science & Technology

Commission (Grant no. Z131100006813022), and National Key Department of Neurology funded by Chinese Health and Family Planning Committee.

## References

- [1] B. Dubois, H. H. Feldman, C. Jacova et al., “Advancing research diagnostic criteria for Alzheimer’s disease: the IWG-2 criteria,” *The Lancet Neurology*, vol. 13, no. 6, pp. 614–629, 2014.
- [2] R. C. Petersen, R. Doody, A. Kurz et al., “Current concepts in mild cognitive impairment,” *Archives of Neurology*, vol. 58, no. 12, pp. 1985–1992, 2001.
- [3] N. Fayed, P. J. Modrego, G. R. Salinas, and J. Gazulla, “Magnetic resonance imaging based clinical research in Alzheimer’s disease,” *Journal of Alzheimer’s Disease*, vol. 31, supplement 3, pp. S5–S18, 2012.
- [4] M. P. Wattjes, “Structural MRI,” *International Psychogeriatrics/IPA*, vol. 23, supplement 2, pp. S13–S24, 2011.
- [5] L. G. Apostolova, L. Mosconi, P. M. Thompson et al., “Subregional hippocampal atrophy predicts Alzheimer’s dementia in the cognitively normal,” *Neurobiology of Aging*, vol. 31, no. 7, pp. 1077–1088, 2010.
- [6] F. Bai, C. Xie, D. R. Watson et al., “Aberrant hippocampal sub-region networks associated with the classifications of aMCI subjects: a longitudinal resting-state study,” *PLoS ONE*, vol. 6, no. 12, Article ID e29288, 2011.
- [7] S. F. Eskildsen, P. Coupé, V. S. Fonov, J. C. Pruessner, and D. L. Collins, “Structural imaging biomarkers of Alzheimer’s disease: predicting disease progression,” *Neurobiology of Aging*, vol. 36, supplement 1, pp. S23–S31, 2015.
- [8] F. Bai, D. R. Watson, Y. Shi et al., “Specifically progressive deficits of brain functional marker in amnesic type mild cognitive impairment,” *PLoS ONE*, vol. 6, no. 9, Article ID e24271, 2011.
- [9] M. A. A. Binnewijzend, M. M. Schoonheim, E. Sanz-Arigitia et al., “Resting-state fMRI changes in Alzheimer’s disease and mild cognitive impairment,” *Neurobiology of Aging*, vol. 33, no. 9, pp. 2018–2028, 2012.
- [10] O. Dipasquale, L. Griffanti, M. Clerici, R. Nemni, G. Baselli, and F. Baglio, “High-dimensional ica analysis detects within-network functional connectivity damage of default-mode and sensory-motor networks in alzheimer’s disease,” *Frontiers in Human Neuroscience*, vol. 9, article 43, 2015.
- [11] Z. Wang, P. Liang, X. Jia et al., “The baseline and longitudinal changes of PCC connectivity in mild cognitive impairment: a combined structure and resting-state fMRI study,” *PLoS ONE*, vol. 7, no. 5, Article ID e36838, 2012.
- [12] Z. Wang, X. Jia, P. Liang et al., “Changes in thalamus connectivity in mild cognitive impairment: evidence from resting state fMRI,” *European Journal of Radiology*, vol. 81, no. 2, pp. 277–285, 2012.
- [13] Z. Dai, C. Yan, K. Li et al., “Identifying and mapping connectivity patterns of brain network hubs in Alzheimer’s disease,” *Cerebral Cortex*, vol. 25, no. 10, pp. 3723–3742, 2015.
- [14] X. Liang, Q. Zou, Y. He, and Y. Yang, “Coupling of functional connectivity and regional cerebral blood flow reveals a physiological basis for network hubs of the human brain,” *Proceedings of the National Academy of Sciences of the United States of America*, vol. 110, no. 5, pp. 1929–1934, 2013.
- [15] R. L. Buckner, J. Sepulcre, T. Talukdar et al., “Cortical hubs revealed by intrinsic functional connectivity: mapping, assessment of stability, and relation to Alzheimer’s disease,” *The Journal of Neuroscience*, vol. 29, no. 6, pp. 1860–1873, 2009.
- [16] R. C. Petersen, “Mild cognitive impairment as a diagnostic entity,” *Journal of Internal Medicine*, vol. 256, no. 3, pp. 183–194, 2004.
- [17] B. Dubois, H. H. Feldman, C. Jacova et al., “Research criteria for the diagnosis of Alzheimer’s disease: revising the NINCDS-ADRDA criteria,” *The Lancet Neurology*, vol. 6, no. 8, pp. 734–746, 2007.
- [18] American Psychiatric Association, *Diagnostic and Statistical Manual of Mental Disorders*, American Psychiatric Press, Washington, DC, USA, 4th edition, 1994.
- [19] Z. Zhenxin, H. Xia, L. Hui, and et al., “The mini-mental state examination in the Chinese residents population aged 55 years and over in the urban and rural areas of Beijing,” *Chinese Journal of Neurology*, vol. 32, no. 3, pp. 149–153, 1999.
- [20] J. Lu, D. Li, F. Li et al., “Montreal cognitive assessment in detecting cognitive impairment in Chinese elderly individuals: a population-based study,” *Journal of Geriatric Psychiatry and Neurology*, vol. 24, no. 4, pp. 184–190, 2011.
- [21] D. C. Delis, J. H. Kramer, E. Kaplan, and B. A. Ober, *California Verbal Learning Test: Adult Version Manual*, The Psychological Corporation, San Antonio, Tex, USA, 1987.
- [22] J. C. Morris, “The Clinical Dementia Rating (CDR): current version and scoring rules,” *Neurology*, vol. 43, no. 11, pp. 2412–2414, 1993.
- [23] R. C. Oldfield, “The assessment and analysis of handedness: the Edinburgh inventory,” *Neuropsychologia*, vol. 9, no. 1, pp. 97–113, 1971.
- [24] Y. Chao-Gan and Z. Yu-Feng, “DPARSE: a MATLAB toolbox for “pipeline” data analysis of resting-state fMRI,” *Frontiers in System Neuroscience*, vol. 4, article 13, 2010.
- [25] J. Ashburner, “A fast diffeomorphic image registration algorithm,” *NeuroImage*, vol. 38, no. 1, pp. 95–113, 2007.
- [26] A. Ledberg, S. Åkerman, and P. E. Roland, “Estimation of the probabilities of 3D clusters in functional brain images,” *NeuroImage*, vol. 8, no. 2, pp. 113–128, 1998.
- [27] X.-W. Song, Z.-Y. Dong, X.-Y. Long et al., “REST: a toolkit for resting-state functional magnetic resonance imaging data processing,” *PLoS ONE*, vol. 6, no. 9, Article ID e25031, 2011.
- [28] L.-L. Zeng, D. Wang, M. D. Fox et al., “Neurobiological basis of head motion in brain imaging,” *Proceedings of the National Academy of Sciences of the United States of America*, vol. 111, no. 16, pp. 6058–6062, 2014.
- [29] K. R. A. van Dijk, M. R. Sabuncu, and R. L. Buckner, “The influence of head motion on intrinsic functional connectivity MRI,” *NeuroImage*, vol. 59, no. 1, pp. 431–438, 2012.
- [30] J. D. Power, K. A. Barnes, A. Z. Snyder, B. L. Schlaggar, and S. E. Petersen, “Spurious but systematic correlations in functional connectivity MRI networks arise from subject motion,” *NeuroImage*, vol. 59, no. 3, pp. 2142–2154, 2012.
- [31] M. D. Fox, D. Zhang, A. Z. Snyder, and M. E. Raichle, “The global signal and observed anticorrelated resting state brain networks,” *Journal of Neurophysiology*, vol. 101, no. 6, pp. 3270–3283, 2009.
- [32] R. M. Birn, J. B. Diamond, M. A. Smith, and P. A. Bandettini, “Separating respiratory-variation-related fluctuations from

- neuronal-activity-related fluctuations in fMRI," *NeuroImage*, vol. 31, no. 4, pp. 1536–1548, 2006.
- [33] A. Weissenbacher, C. Kasess, F. Gerstl, R. Lanzenberger, E. Moser, and C. Windischberger, "Correlations and anticorrelations in resting-state functional connectivity MRI: a quantitative comparison of preprocessing strategies," *NeuroImage*, vol. 47, no. 4, pp. 1408–1416, 2009.
- [34] K. Murphy, R. M. Birn, D. A. Handwerker, T. B. Jones, and P. A. Bandettini, "The impact of global signal regression on resting state correlations: are anti-correlated networks introduced?" *NeuroImage*, vol. 44, no. 3, pp. 893–905, 2009.
- [35] Y. Han, J. Wang, Z. Zhao et al., "Frequency-dependent changes in the amplitude of low-frequency fluctuations in amnesic mild cognitive impairment: a resting-state fMRI study," *NeuroImage*, vol. 55, no. 1, pp. 287–295, 2011.
- [36] J. Wang, X. Zuo, Z. Dai et al., "Disrupted functional brain connectome in individuals at risk for Alzheimer's disease," *Biological Psychiatry*, vol. 73, no. 5, pp. 472–481, 2013.
- [37] P.-J. Toussaint, S. Maiz, D. Coynel et al., "Characteristics of the default mode functional connectivity in normal ageing and Alzheimer's disease using resting state fMRI with a combined approach of entropy-based and graph theoretical measurements," *NeuroImage*, vol. 101, pp. 778–786, 2014.
- [38] N. Gour, O. Felician, M. Didic et al., "Functional connectivity changes differ in early and late-onset Alzheimer's disease," *Human Brain Mapping*, vol. 35, no. 7, pp. 2978–2994, 2014.
- [39] J. Cha, H. J. Jo, H. J. Kim et al., "Functional alteration patterns of default mode networks: comparisons of normal aging, amnesic mild cognitive impairment and Alzheimer's disease," *The European Journal of Neuroscience*, vol. 37, no. 12, pp. 1916–1924, 2013.
- [40] J. Persson, S. Pudas, L.-G. Nilsson, and L. Nyberg, "Longitudinal assessment of default-mode brain function in aging," *Neurobiology of Aging*, vol. 35, no. 9, pp. 2107–2117, 2014.
- [41] C. Sorg, V. Riedel, M. Mühlau et al., "Selective changes of resting-state networks in individuals at risk for Alzheimer's disease," *Proceedings of the National Academy of Sciences of the United States of America*, vol. 104, no. 47, pp. 18760–18765, 2007.
- [42] M. A. Mintun, G. N. Larossa, Y. I. Sheline et al., "[<sup>11</sup>C]PIB in a nondemented population: potential antecedent marker of Alzheimer disease," *Neurology*, vol. 67, no. 3, pp. 446–452, 2006.
- [43] H. Matsuda, "Cerebral blood flow and metabolic abnormalities in Alzheimer's disease," *Annals of Nuclear Medicine*, vol. 15, no. 2, pp. 85–92, 2001.
- [44] J. S. Damoiseaux, K. E. Prater, B. L. Miller, and M. D. Greicius, "Functional connectivity tracks clinical deterioration in Alzheimer's disease," *Neurobiology of Aging*, vol. 33, no. 4, pp. 828.e19–828.e30, 2012.
- [45] Z. Hu, C. Sheng, Y. Sun et al., "Structural and resting state functional MRI characteristics of patients at high risk for Alzheimer's disease," *Chinese Journal of Neurology*, vol. 47, no. 12, pp. 824–830, 2014.
- [46] P. M. Bays and M. Husain, "Dynamic shifts of limited working memory resources in human vision," *Science*, vol. 321, no. 5890, pp. 851–854, 2008.
- [47] M. Weiler, A. Fukuda, L. H. P. Massabki et al., "Default mode, executive function, and language functional connectivity networks are compromised in mild Alzheimer's disease," *Current Alzheimer Research*, vol. 11, no. 3, pp. 274–282, 2014.
- [48] S. Cai, L. Huang, J. Zou et al., "Changes in thalamic connectivity in the early and late stages of amnesic mild cognitive impairment: a resting-state functional magnetic resonance study from ADNI," *PLoS ONE*, vol. 10, no. 2, Article ID e0115573, 2015.
- [49] B. Zhou, Y. Liu, Z. Zhang et al., "Impaired functional connectivity of the thalamus in Alzheimer's disease and mild cognitive impairment: a resting-state fMRI study," *Current Alzheimer Research*, vol. 10, no. 7, pp. 754–766, 2013.
- [50] M. Ewers, P. S. Insel, Y. Stern, M. W. Weiner, and The Alzheimer's Disease Neuroimaging Initiative, "Cognitive reserve associated with FDG-PET in preclinical Alzheimer disease," *Neurology*, vol. 80, no. 13, pp. 1194–1201, 2013.
- [51] K. Motomura, M. Fujii, S. Maesawa, S. Kuramitsu, A. Natsume, and T. Wakabayashi, "Association of dorsal inferior frontooccipital fasciculus fibers in the deep parietal lobe with both reading and writing processes: a brain mapping study," *Journal of Neurosurgery*, vol. 121, no. 1, pp. 142–148, 2014.
- [52] Z. Wang, M. Xia, Z. Dai et al., "Differentially disrupted functional connectivity of the subregions of the inferior parietal lobule in Alzheimer's disease," *Brain Structure and Function*, vol. 220, no. 2, pp. 745–762, 2015.
- [53] H. I. L. Jacobs, M. P. J. Van Boxtel, A. Heinecke et al., "Functional integration of parietal lobe activity in early Alzheimer disease," *Neurology*, vol. 78, no. 5, pp. 352–360, 2012.
- [54] F. Bai, W. Liao, D. R. Watson et al., "Abnormal whole-brain functional connection in amnesic mild cognitive impairment patients," *Behavioural Brain Research*, vol. 216, no. 2, pp. 666–672, 2011.
- [55] A. Caroli, C. Geroldi, F. Nobili et al., "Functional compensation in incipient Alzheimer's disease," *Neurobiology of Aging*, vol. 31, no. 3, pp. 387–397, 2010.
- [56] K. Abuhassan, D. Coyle, A. Belatreche, and L. Maguire, "Compensating for synaptic loss in Alzheimer's disease," *Journal of Computational Neuroscience*, vol. 36, no. 1, pp. 19–37, 2014.
- [57] A. Tramutola, J. C. Triplett, F. Di Domenico et al., "Alteration of mTOR signaling occurs early in the progression of Alzheimer disease (AD): analysis of brain from subjects with pre-clinical AD, amnesic mild cognitive impairment and late-stage AD," *Journal of Neurochemistry*, vol. 133, no. 5, pp. 739–749, 2015.
- [58] K.-I. Yamashita, Y. Taniwaki, H. Utsunomiya, and T. Taniwaki, "Cerebral blood flow reduction associated with orientation for time in amnesic mild cognitive impairment and Alzheimer disease patients," *Journal of Neuroimaging*, vol. 24, no. 6, pp. 590–594, 2014.
- [59] H.-Y. Zhang, S.-J. Wang, J. Xing et al., "Detection of PCC functional connectivity characteristics in resting-state fMRI in mild Alzheimer's disease," *Behavioural Brain Research*, vol. 197, no. 1, pp. 103–108, 2009.
- [60] L. G. Apostolova, C. A. Steiner, G. G. Akopyan et al., "Three-dimensional gray matter atrophy mapping in mild cognitive impairment and mild Alzheimer disease," *Archives of Neurology*, vol. 64, no. 10, pp. 1489–1495, 2007.
- [61] R. Ossenkoppele, N. Tolboom, J. C. Foster-Dingley et al., "Longitudinal imaging of Alzheimer pathology using [<sup>11</sup>C]PIB, [<sup>18</sup>F]FDDNP and [<sup>18</sup>F]FDG PET," *European Journal of Nuclear Medicine and Molecular Imaging*, vol. 39, no. 6, pp. 990–1000, 2012.
- [62] S. Li, X. Yuan, F. Pu et al., "Abnormal changes of multidimensional surface features using multivariate pattern classification

in amnesic mild cognitive impairment patients,” *The Journal of Neuroscience*, vol. 34, no. 32, pp. 10541–10553, 2014.

- [63] S.-H. Lin, C.-Y. Yu, and M.-C. Pai, “The occipital white matter lesions in Alzheimer’s disease patients with visual hallucinations,” *Clinical Imaging*, vol. 30, no. 6, pp. 388–393, 2006.
- [64] R. Ossenkoppele, B. I. Cohn-Sheehy, R. La Joie et al., “Atrophy patterns in early clinical stages across distinct phenotypes of Alzheimer’s disease,” *Human Brain Mapping*, 2015.
- [65] G. J. Yang, J. D. Murray, G. Repovs et al., “Altered global brain signal in schizophrenia,” *Proceedings of the National Academy of Sciences of the United States of America*, vol. 111, no. 20, pp. 7438–7443, 2014.

## Research Article

# The Exercising Brain: Changes in Functional Connectivity Induced by an Integrated Multimodal Cognitive and Whole-Body Coordination Training

Traute Demirakca, Vita Cardinale, Sven Dehn, Matthias Ruf, and Gabriele Ende

*Department of Neuroimaging, Central Institute of Mental Health, Medical Faculty Mannheim, Heidelberg University, J5, 68159 Mannheim, Germany*

Correspondence should be addressed to Traute Demirakca; [traute.demirakca@zi-mannheim.de](mailto:traute.demirakca@zi-mannheim.de)

Received 3 July 2015; Revised 7 September 2015; Accepted 8 September 2015

Academic Editor: Feng Shi

Copyright © 2016 Traute Demirakca et al. This is an open access article distributed under the Creative Commons Attribution License, which permits unrestricted use, distribution, and reproduction in any medium, provided the original work is properly cited.

This study investigated the impact of “life kinetik” training on brain plasticity in terms of an increased functional connectivity during resting-state functional magnetic resonance imaging (rs-fMRI). The training is an integrated multimodal training that combines motor and cognitive aspects and challenges the brain by introducing new and unfamiliar coordinative tasks. Twenty-one subjects completed at least 11 one-hour-per-week “life kinetik” training sessions in 13 weeks as well as before and after rs-fMRI scans. Additionally, 11 control subjects with 2 rs-fMRI scans were included. The CONN toolbox was used to conduct several seed-to-voxel analyses. We searched for functional connectivity increases between brain regions expected to be involved in the exercises. Connections to brain regions representing parts of the default mode network, such as medial frontal cortex and posterior cingulate cortex, did not change. Significant connectivity alterations occurred between the visual cortex and parts of the superior parietal area (BA7). Premotor area and cingulate gyrus were also affected. We can conclude that the constant challenge of unfamiliar combinations of coordination tasks, combined with visual perception and working memory demands, seems to induce brain plasticity expressed in enhanced connectivity strength of brain regions due to coactivation.

## 1. Introduction

Already in 1949 Hebb proposed that simultaneous neuronal firing stimulates synaptic plasticity [1]. Later several studies found evidence for experience-dependent neurogenesis in the hippocampi of adult mice (for a review see [2]). Today there is accumulating evidence that also the human brain continues to be shaped by experience throughout adulthood [3–5]. These adaptive changes have been shown to take place on structural as well as functional level [6–9].

A practicable approach to study experience-dependent plasticity in humans is to investigate longitudinal changes in brain structure or function following exposure to training. Recently, a number of studies have been published that investigated the effect of training on the functional architecture of the brain by resting-state fMRI (rs-fMRI) (for a review see [9, 10]). Resting-state functional connectivity is

commonly defined as temporal correlations of spontaneous, low frequency fluctuations of the BOLD signal between brain areas during rest due to common history of coactivation. As such, it allows a task-independent assessment of training-related changes in brain function [11–14].

Training studies can roughly be subdivided into motor and cognitive interventions. Motor training varied from joystick tracking tasks [15], chopstick handling [16], finger tapping [17], and force-field learning [18] to whole-body balancing [19] and aerobic fitness training [20]. Training duration varied from 11 minutes [15] to several weeks or months [20]. In the cognitive domain training comprised working memory training [21, 22], multitasking [23], and logical reasoning [24] and duration varied from 4 weeks to 3 months.

Newer approaches used also video-gaming [25] and fMRI based neurofeedback [26, 27].

Within the motor domain, several research groups investigated different kinds of motor skills training with varying duration, intensity, and complexity. Overall, changes in intrinsic functional connectivity were located in sensorimotor and cerebellar areas. In these areas both intrinsic functional connectivity increases [15, 17–19] and decreases [16–19] have been found; decreases were rather associated with cerebellar regions [16, 18]. In the studies conducted by Taubert et al. [19] and Ma et al. [17] intrinsic functional connectivity decreased back to baseline whereas decreases were found by the groups of Yoo et al. [16] and Vahdat et al. [18]; there, the intrinsic functional connectivity after the training was reduced compared to before the intervention.

In the cognitive domain, training rather affected intrinsic functional connectivity between frontal and parietal areas [21, 22, 24]. However, the precise location of training-related change in intrinsic functional connectivity differs between studies. Regarding the variety of changes found by different research groups, the training effects seem to be rather specific to the content of the training, the duration, the intensity, and the timing of the resting-state quantification. However, the studies mentioned before show that changes in intrinsic functional connectivity can reliably be induced by training, that is, experience, across a variety of domains.

The majority of published intervention studies investigated the effect of unimodal training. Within the field of healthy aging research the question rises if combined interventions might be more successful than unimodal interventions (for a review see [28]). Also in the context of studies investigating effects of physical exercise on neuroplasticity and cognition it is suggested that adding cognitive training might enhance the beneficial effect of physical training (for a review see [29]). Yet, there are only few studies that focus on the effect of combined interventions. To our knowledge, there are only two studies exploring the effect of a multimodal training using neuroimaging techniques [30, 31]. In both studies, physical and cognitive training were performed apart from each other. In Li et al.'s study older adults took part in tai chi exercises at one time and memory training and supportive group counselling on another time. They found increased resting-state connectivity between the medial prefrontal cortex and the medial temporal lobe. In Holzschneider et al.'s study participants engaged in cycling sessions and additional spatial memory training sessions. However, only task-based fMRI changes were quantified. After combined training, changes in brain activation and changes in cardiovascular fitness correlated positively in the medial frontal gyrus and the cuneus.

Here, we investigated the effect of combined whole-body motor coordination training with integrated cognitive exercises in healthy adults. Lutz and colleagues (“life kinetik”: <http://www.lifekinetik.de/>) developed a multimodal training that combines coordinative, cognitive, and visual tasks in a way that the physical exercise is performed while participants are cognitively challenged at the same time. The training consists of combinations of motor activity and cognitive challenges and the training of visual perception, especially the perception of the peripheral visual field. Moving limbs in different unusual combinations, catching, and throwing

objects, thus training the visual perception and limb-eye coordination, is a basic characteristic of the training. Moreover, the training tasks are not practiced to perfection but are modified after a few minutes or whenever the performance reaches about 60%. In addition to the avoidance of boredom and frustration, this is supposed to stimulate the brain to constantly adapt to new unfamiliar challenges. Our motivation was to test a training concept that is flexible and interesting for the participants and includes cognitive and motor elements. Although the “life kinetik” training was originally designed to train the coordination of athletes (soccer players, skiers) the difficulty of the task can easily be adapted to the capabilities of patient populations.

Based on the assumption that spontaneous activity reflects the history of coactivation within a local brain network or between brain regions [26, 32] we expect increases in resting-state connectivity of those brain regions probably involved in the exercises and tasks.

The *thalamus* is a subcortical brain area processing and integrating neocortical inputs and outputs [33]. Its connections seem to decrease with age [34] and diminished in mild cognitive impairment (MCI) and Alzheimer’s disease (AD) [35, 36]. It serves as a “switchboard of information” or relay station for sensory information. As the training includes unusual pattern of motoric activity in combination with cognitive task, we expect the connectivity of the thalamus to increase.

All the exercises and tasks involve some motor action; hence we expect changes in the *primary motor area* (BA4, M1) and the *premotor area* (BA6) because not only the execution but also the constant alertness to perform an action is involved in the task. In particular the connectivity to the right motor areas may be increased because the exercises include a considerable amount of movement of the left limbs, which is challenging for the right handed participants.

The *cerebellum* is highly involved in motor activity and learning and the functional connections reflect the connections of the cortex [37, 38] so we can expect some changes in its connectivity as well.

The *frontal eye field* (FEF), a brain region responsible for eye movement and gaze control, is known to be altered in the course of learning to handle moving objects [39–41], which is also part of the exercise, except that this is not trained to perfection like in juggling.

The whole *visual cortex* is additionally challenged by the attempt to train the peripheral vision and the manipulation of different moving objects and due to the possibility of assigning the requested action via a visual stimulus (specific gesture of the trainer or colours). So the primary as well as the secondary visual cortices (BA17, BA18, and BA19) are expected to change their connection to other brain regions.

Each exercise or task consists of chains of movements, which alternate randomly. The prompt to change is frequently given by a verbal command. Hence, we expect an increased connectivity between *auditory areas* (primary and secondary BA41 and BA42) and other brain regions especially the motor and premotor area and as a result of repeated coactivation.

The functional connectivity from and to the *dorsolateral prefrontal cortex* (DLPFC) may be increased because

the working memory is involved in linking the action or movement to the assigned command or prompt. The *anterior cingulate cortex* (ACC) is also expected to be involved as a region needed for error detection and impulse control and might accordingly change the connection to other brain regions.

## 2. Methods

**2.1. Participants.** 32 right handed subjects with no history of psychiatric or neurological illness were included in the study. 21 individuals (12 females, mean age 48 ( $\pm 9$ ) years) participated in eleven or twelve of the 13 “life kinetik” training sessions (1 hour per week). The other 11 subjects (7 females, mean age 49 ( $\pm 8$ ) years) were interested in the training but were not able to attend due to their time schedule but completed two MRI scans.

The study was approved by the Ethics Committee of the Medical Faculty Mannheim, University of Heidelberg, and performed in accordance with the Declaration of Helsinki.

**2.2. Training Description.** “Life kinetik” training pursues the goal to combine motor coordination exercises with cognitive training with an emphasis on working memory. The motor coordination exercises can involve multiple limbs at the same time. Additionally, most of the time one or more pieces of sports equipment (e.g., ball, racket, juggling balls, and scarves) are used which have to be thrown, caught, bounced, or similarly manipulated. The cognitive aspect comes into play by assigning distinct motor tasks to different visual or auditory cues (symbols/key words). For example, a red flag might indicate bouncing a ball with the left hand while a blue flag indicates throwing and catching a ball with the right hand. The same movement-cue coupling can be done with semantic categories, for example, city names, animals, or trees. These pairs of motor task and specific cue have to be memorized during one training session. The randomization of cues is self-evident. Within one training session (1 hour per week) approximately 6 different types of exercises have been performed either in groups, in pairs, or by oneself.

An essential aspect of this combined training is that the exercises are not trained until automatized. As soon as participant’s performance reaches about 60% correct trials the task demands are changed and new combinations of symbols and movements are introduced. The focus on novelty is supposed to constantly challenge the participants. Moreover, cross talk of the hemispheres is fostered by including movements where limbs purposefully cross the sagittal midline (e.g., to catch a ball arriving at the left side of the body with the right hand).

In total, there were 13 training sessions of 1 hour per week of which our participants followed at least 11; that is, the minimal training duration was 11 hours across a period of 13 weeks.

**2.3. Data Acquisition.** Functional and anatomical data were acquired from each participant within 2 weeks before the start of the first training session and within 2 weeks after the last training session on a 3 Tesla MRI Scanner (Magnetom Trio with TIM technology, Siemens Medical Service, Erlangen,

Germany) equipped with a 32-channel head coil. 200 rs-fMRI images were acquired with gradient echo T2\*-weighted echo-planar-imaging sequence (TE = 28 ms, TR = 1.79 s, FOV = 192 mm  $\times$  192 mm, matrix size = 64  $\times$  64, and total duration is 6 min). A volume comprised 34 slices in AC-PC orientation with a thickness of 3 mm and slice gap of 1 mm. Participants’ heads were lightly restrained using soft pads to prevent head movement. Subjects were instructed to look at the fixation cross and keep their eyes open.

A T1-weighted anatomical image was also recorded (TE = 3.03 ms, TR = 2.3 s, 192 slices and FOV = 256 mm  $\times$  256 mm, matrix size is 256  $\times$  256, and slice thickness is 1 mm).

**2.4. Data Preprocessing.** Data were preprocessed and analyzed using SPM12 (The Wellcome Department of Cognitive Neurology, London, UK, <http://www.fil.ion.ucl.ac.uk/spm/software/spm12/>). All functional images were slice-time corrected and realigned to the first volume using a six-parameter rigid body transformation. Threshold for exclusion due to excessive motion was set to 3 mm. The movement was not more than 1.5 mm in each subject, so no one had to be removed.

The anatomical image and functional images were coregistered for the corresponding time-point. Segmented gray matter and white matter images of all participants were used to construct a study specific template using DARTEL [42]. The template was normalized to MNI space and all images, anatomical and functional, were normalized to this template using the according flow fields. The smoothing kernel for the functional images was 8 mm and 2 mm for the anatomical image.

**2.5. Connectivity Analysis.** Functional connectivity analyses were carried out using the CONN-fMRI functional connectivity toolbox v14 [43] (<http://www.nitrc.org/projects/conn>). The modest test-retest reliability of the rs-fMRI seems attributable to remaining noise after preprocessing, adding nonneural correlation to the BOLD signal [44]. Removing the noise is a possibility to increase the reliability of rs-fMRI data. Several preprocessing steps have been proposed [44] to achieve this.

One major point is reducing the noise via the anatomical CompCor approach. This method extracts principal components (5 each) from WM and CSF time series. WM and CSF voxels are identified via a segmentation of the anatomical images. These components are added as confounds in the denoising step of the CONN toolbox [43, 45]. The six head motion parameters derived from spatial motion correction were also added as confounds. We did not perform global signal regression as the discussion about the impact is still ongoing [44, 46] and it is not available on the CONN toolbox.

As recommended band-pass filtering was performed with a frequency window of 0.01 to 0.1 Hz. This preprocessing step was found to increase the retest reliability [44].

Seed-to-voxel and ROI-to-ROI functional connectivity maps were created for each participant. The ROI-to-ROI analysis was used to identify possible differences between trainees and control subjects at pretraining and to verify that brain networks of control subjects did not change over time.

For this analysis we used all the provided Brodmann areas. The mean BOLD time series was computed across all voxels within each ROI. Bivariate-correlation analyses were used to determine the linear association of the BOLD time series between each pair of sources and a Fisher Z transformation was applied.

Individual seed-to-voxel and ROI-to-ROI maps were entered into a second-level analysis.

A within group ROI-to-ROI analysis for the control group tested the stability of the connectivity over time. A between groups ROI-to-ROI analysis verified the lack of differences between the two groups for the first measurement.

Seed-to-voxel analyses were used for two purposes. First we used the posterior cingulate and the medial prefrontal cortex as seed region and verified the occurrence of the default mode network in each group and to both time-points. This seems necessary due to the different size of the two groups.

The second seed-to-voxel analysis was used to examine differences in connectivity changes in a  $2 \times 2$  factorial analysis with time by training interaction (group \* time; contrast  $-1 +1 +1 -1$ ). Age and sex were entered as covariates of no interest in the analysis [47]. The threshold for significant changes was set to  $p = 0.05$  whole brain cluster level FWE corrected with a cluster building threshold of  $p = 0.001$  uncorrected on voxel level. As we expected an increase in training participants due to coactivation and no change in control subjects we verified the direction of changes with two post hoc paired sample  $t$ -tests for the trainee and the control group separately for each significant seed-to-voxel cluster. This step was chosen to assure that the significant results were not caused by between-subject variance. The other reason for this approach was the different sample size of the two groups. We report significant results due to three criteria: (a) significant time by group interaction, (b) significant increase within the training group, and (c) no significant decrease in the control group.

For display purposes the cluster building threshold for the result-figure was set to 0.002 uncorrected on voxel level.

**2.6. Regions of Interest.** As we could not investigate task related activity for the exercises and it is somewhat arbitrary and prone to bias to create a region of interest out of a single coordinate and an according sphere, we used the provided ROIs that are based on the Brodmann areas according to the WFU PickAtlas (<http://fmri.wfubmc.edu/software/PickAtlas>). We used all existing areas as ROIs, in order to get a complete picture of possible changes within the control group. Some ROIs are not provided by the toolbox (e.g., thalamus, cerebellum, and FEF); here we created ROI using the masks provided by WFU PickAtlas of the according brain region.

### 3. Results

ROI-to-ROI analysis for the rs-fMRI at the first time-point showed no differences between trainees and controls. The default network could be shown with the medial prefrontal cortex as seed in both groups and both time-points.

The impact of the training was analyzed by a  $2 \times 2$  ANOVA (group and time) with age and sex as covariates

of no interest. All seed regions with significant positive connectivity changes in trainees and no significant decreases in controls are listed in Table 1.

The training involved a great amount of motor activity and the motor region was one of the hypothesized regions changing their connectivity strength. The increase occurred only for the *left motor region*. The left primary motor area (BA4, M1) showed increased connectivity to parts of the visual cortex (Figure 1(a), red) and the somatosensory association area (BA7, Figure 1(a), red). The right primary motor cortex showed no changes to any other brain region. The connectivity strength of the whole *premotor areas* (BA6) as seed to other cortical regions did not change.

The primary *sensorimotor cortices* (BA1, BA2, and BA3) as part of the sensorimotor network showed few changes in connectivity strength. Only the spontaneous fluctuations of the left BA1 showed higher correlation to parts of the associative visual cortex (BA19, Figure 1(a), cyan) and parts of the parietal cortex (BA7, Figure 1(a), cyan). Connectivity from BA2 or BA3 did not change.

The functional coupling within the visual network changed for the *primary sensory areas* (BA17) of the right hemisphere. This ROI increased in functional connectivity to the ventral ACC (BA24, Figure 1(b), violet) and parts of the right premotor cortex (BA6, Figure 1(c), violet). The connection to the left premotor cortex (Figure 1(c), blue) was increased for the right *secondary visual cortices* (BA18). The connection increase to the ventral ACC (midcingulate; Figure 1(b), violet and blue) of the visual areas was overlapping. Different areas of the visual cortex show changes in functional coupling to the same premotor region and the cingulate cortex.

The functional connectivity strength between the *primary auditory cortex* (BA41) as part of the auditory network and the right cerebellum (areas VIII and IX) increased with the training as well as the connection to the somatosensory association cortex (BA7, Figure 1(d), green and red). This connectivity change was interhemispheric and overlapping. The connections of the *secondary auditory cortex* (BA42) to the parietal cortex (BA7, Figure 1(d), violet and blue) changed as well, partly overlapping with the increased connectivity of the primary auditory cortex. Connections from the auditory to the visual cortex did also increase (Figures 1(d) and 1(e), blue and green).

The *left FEF* but not the right FEF showed connectivity changes to several clusters in the visual cortex (Figure 1(f), blue) and the ventral ACC (Figure 1(f), blue).

The connectivity between the *right dorsolateral prefrontal cortex* and the right supramarginal gyrus (Figure 1(f), red) increased. The ACC (BA24) showed no increase in connectivity. A more posterior part of the *cingulate gyrus* showed an increased functional connectivity to the right anterior frontal cortex and partially of the dorsolateral prefrontal cortex (BA10 and BA9, Figure 1(f), violet).

The characteristic regions of the default mode network, *medial prefrontal cortex*, *lateral parietal cortex*, *posterior cingulate*, and *superior frontal cortex*, showed no change in connectivity after the training.

TABLE 1: Seed-to-voxel results of  $2 \times 2$  ANOVA ( $f1 < f2$ ; trainees > controls), age and sex as covariates, cluster building threshold  $p = 0.001$  uncorrected, cluster threshold  $p = 0.05$  FWE corrected, post hoc test increase in trainees, and no decrease in controls.

Figure/colour	Seed	Seed hemisphere	Result region	BA	Result hemisphere	x	y	z	k	Cluster p-FWE	Cluster p-unc	Peak p-FWE	Peak p-unc
<i>Motor area</i>													
(a)/red	BA4/MI	Left	Somatosensory association cortex	BA7	Left	-30	-48	52	83	0.04605	0.00103	0.373	0.000002
(a)/red	BA4/MI	Left	Somatosensory association cortex	BA7	Right	26	-44	48	99	0.01981	0.00044	0.982	0.000035
(a)/red	BA4/MI	Left	Associative visual cortex	BA19	Right	38	-78	-4	258	0.00002	0	0.791	0.000011
<i>Sensory-motor area</i>													
(a)/cyan	BA1	Left	Associative visual cortex	BA19	Right	40	-82	8	137	0.00354	0.00008	0.869	0.000015
(a)/cyan	BA1	Left	Somatosensory association cortex	BA7	Right	30	-42	50	126	0.0059	0.00013	0.987	0.00004
<i>Visual area</i>													
(b)/violet	Primary visual cortex BA17	Right	Ventral ACC	BA24	Left	-8	4	38	81	0.04406	0.00095	0.477	0.000003
(c)/violet	Primary visual cortex BA17	Right	Premotor cortex	BA6	Right	22	-8	66	133	0.00294	6.2E-05	0.844	0.000012
(b)/blue	Secondary visual cortex BA18	Right	Secondary visual cortex	BA18	Left	-14	-82	2	329	1E-06	0	0.005	0
(b)/blue	Secondary visual cortex BA18	Right	Dorsal posterior cingulate cortex	BA31	Right	14	-66	20	85	0.03536	0.00076	0.223	0.000001
(b)/blue	Secondary visual cortex BA18	Right	Ventral ACC	BA24	Left	-6	12	40	97	0.01841	0.00039	0.718	0.000008
(c)/blue	Secondary visual cortex BA18	Right	Premotor cortex	BA6	Left	-20	-2	60	96	0.01942	0.00041	0.923	0.000019
<i>Auditory area</i>													
(e)/green	Primary auditory cortex BA41	Left	Cerebellum	Cerebellum (8 & 9)	Right	20	-34	-46	163	0.00073	1.5E-05	0.003	0
(e)/green	Primary auditory cortex BA41	Right	Somatosensory association cortex & associative visual cortex	BA7 & BA19	Right	36	-78	12	874	0	0	0.007	0
(d)/green	Primary auditory cortex BA41	Right	Somatosensory association cortex	BA7	Left	-26	-54	40	218	4.8E-05	1E-06	0.951	0.000022
(d)/red	Primary auditory cortex BA41	Left	Somatosensory association cortex	BA7	Right	14	-66	52	200	0.00014	3E-06	0.933	0.00002
(d)/red	Primary auditory cortex BA41	Left	Somatosensory association cortex	BA7	Left	-10	-70	52	131	0.00327	6.9E-05	0.932	0.00002
(d)/violet	Secondary auditory cortex BA42	Right	Somatosensory association cortex	BA7	Right	22	-64	54	76	0.04641	0.00094	0.864	0.000012
(d)/violet	Secondary auditory cortex BA42	Right	Somatosensory association cortex	BA7	Left	-20	-58	40	131	0.00225	4.4E-05	0.583	0.000004
(d)/blue	Secondary auditory cortex BA42	Left	Somatosensory association cortex	BA7	Right	34	-50	48	130	0.00319	6.6E-05	0.568	0.000004
(e)/blue	Secondary auditory cortex BA42	Left	Secondary visual cortex	BA18	Midline	0	-92	0	140	0.00196	4.1E-05	0.983	0.000033
<i>Frontal cortex</i>													
(f)/red	Dorsolateral prefrontal cortex (BA9)	Right	Supramarginal gyrus	BA40	Right	64	-18	24	192	0.00026	6E-06	0.737	0.000008
(f)/blue	Frontal eye field/superior frontal	Left	Ventral ACC	BA24	Right	8	-12	38	110	0.00696	0.00014	0.563	0.000004
(f)/blue	Frontal eye field/superior frontal	Left	Secondary visual cortex	BA18	Right	36	-90	6	397	0	0	0.577	0.000004
(f)/blue	Frontal eye field/superior frontal	Left	Secondary visual cortex	BA18	Left	-24	-96	14	193	0.00012	2E-06	0.771	0.000009
(f)/violet	Midcingulate gyrus	Right	Anterior prefrontal cortex & dorsolateral prefrontal cortex	BA10 & BA9	Right	6	66	18	100	0.01336	0.00027	0.934	0.000019

BA = Brodmann area, x, y, and z = MNI coordinates, k = cluster size, and (a)-(f) = parts of Figure 1.

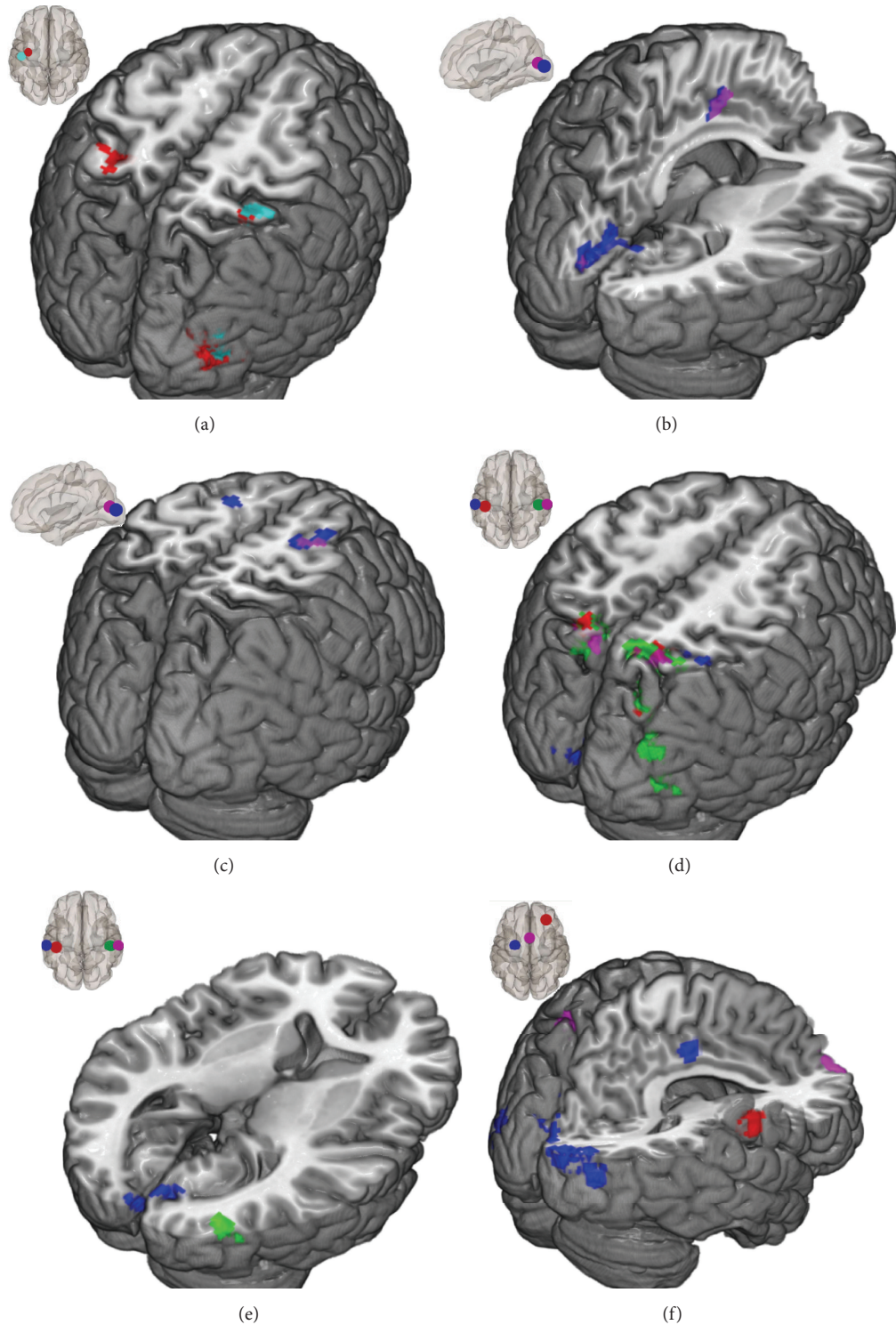


FIGURE 1: Greater connectivity increases in trainees compared to controls subjects; seed regions are represented in the small brain images; seeds determine the colour of the result region: (a) BA4 left: red and BA1 left: cyan; (b) and (c) visual cortex: BA17 right: violet and BA18 right: blue; (d) and (e) auditory cortex: BA41 right: green, BA41 left: red, BA42 right: violet, and BA42 left: blue; (f) dorsolateral prefrontal cortex: right: red, FEF left: blue, and midcingulate cortex: violet.

#### 4. Discussion

This study is the first to investigate the impact of an integrated multimodal training on functional brain connectivity. The training combines physical and cognitive exercises and does not aim at automating but focuses on novelty. For this purpose we compared the changes of the resting-state intrinsic functional connectivity of a group of subjects attending the first standard training course of “life kinetik” with the rs-fMRI changes of a control sample. The training offers a great variety of exercises and can easily be adapted to clinical populations. We found a considerable amount of changes in resting-state functional connectivity in the training group. The connections within the default mode network, the most prominent resting-state network, did not change.

The changes in functional connectivity mirror the activation during the training and some increases in correlation occur in regions that are known to be a key region in cognitive deficits, ageing or mental illness.

Connectivity increases of the motor region were assumed to be the most probable ones. In particular the connections from the right motor and premotor cortex, responsible for the left part of the body, were expected to strengthen. The training involved a great amount of motor activity and all participants were right handed, thus being forced to coordinate their left hand, arm, and leg. An increase of the connectivity for the whole region was only visible for the left primary motor area. The connection to parts of the somatosensory association area changed as well as to the visual cortex. The involvement of motor areas in brain plasticity has been corroborated in several studies. Musicians, for example, who have a long history of motoric training showed increased resting-state connectivity in motor areas and multisensory cortices compared to a control group [48]. This is in contrast to other studies that found a decrease in connectivity accompanied with cumulative performance increase after initial “beginners” increase of connectivity [17]. As the “life kinetik” training focuses on the novelty of the exercises a decrease of connectivity was not expected.

Various seed regions in the visual cortex showed an increased connectivity with parts of the premotor cortex, almost overlapping (see Figure 1(c)). A great number of the training tasks consisted of throwing and catching different and, in some cases, relative small objects. The most comparable task used in other studies was juggling training where an impact of training intensity was found [49]. Low intensity training resulted in increases in functional connectivity in the motor network, whereas the high intensity juggling training group showed decreased functional connectivity. The results suggest that different training regimes are associated with distinct patterns of brain change [50]. Our training on the other hand was much less intensive than the low intensity juggling training which consisted of 15 min per day and furthermore, as already mentioned, “life kinetik” training is not directed to perfection.

The cerebellum is mapped to the association areas of the cerebrum [37] so that we expected some changes in connectivity, which we found but less pronounced than

expected. In contrast to the analysis of Buckner et al. [37] who found that the primary sensory cortices were not represented in the cerebellum, we found a change in the correlation of time courses in the primary auditory cortex and the cerebellum. Maybe this is an effect of the verbal prompts during the exercises, which indicated different movements.

The visual cortex is also diversified. Some subregions responsible for the retention of visual-motion information [51] were shown to change their structure during motor training. Not structural but functional changes occur in our sample of trainees in contrast to the control sample.

The brain region with the most prominent connectivity changes was the secondary somatosensory association cortex (BA7). Several parts of BA7 exhibited connectivity increases with other regions. Mainly the auditory cortices change their relation to parts of BA7 (Figure 1(d)). These clusters are all overlapping irrespective of the according seed region. Also distinct from these regions are the clusters changing the connections to the motor cortex (Figure 1(b), red) and the sensorimotor cortex. This result seems to corroborate the findings of the diversification of the parietal cortex [52, 53]. Grasping and visuospatial tasks activated different parts of the parietal cortex [53], overlapping with the regions that showed changes during “life kinetik” training (Figures 1(a) and 1(d)).

The functional connectivity between the left FEF as seed region and clusters in the visual cortex and the ventral ACC increased, but not with the dorsal attention network. The FEF is responsible for eye movement and surely active during throwing and catching of objects. The change of connectivity between FEF and visual cortex might be an indication for a combined activation of these regions due to the increased visual attention during the training.

Regions of the frontal cortex involved in working memory processes and error processing showed few connectivity increases. The ACC showed, in contrast to our hypothesis, no changes in connectivity to other brain regions. The ventral part of the cingulate cortex showed increased connectivity to the anterior prefrontal cortex, to the FEF, and to the visual cortex. The left dorsolateral prefrontal cortex (BA9) on the other hand showed an increased connectivity to the right supramarginal gyrus (BA40).

Given the specific property of the training, the connectivity changes seem reasonable. Prompts for the movements and tasks are given by verbal or visual cues. The cue has to be translated to an action, in most cases movements or manipulation of objects. Parts of the premotor regions showed increased connections to visual areas. These regions were not distinct but overlapping thus indicating the importance of these regions for preparing the action and also for the object manipulation [54].

The question is why the auditory areas predominantly showed increased functional connectivity to the somatosensory areas (BA7) but not to the premotor area. Attention is one important aspect of the training in combination with working memory. One major effort for the trainees is to remember the according movement to the prompt. But this did not result in the expected changes in connectivity of the dorsolateral prefrontal cortex.

The functional connection of the thalamus to the right inferior frontal gyrus and insula increased in trainees but also decreased in controls. This makes the interpretation difficult. The thalamus is a region with multiple connections [33, 55, 56]. The strength of the thalamocortical connection has been reported to predict the performance in motor learning [57], to change with age [34], and to be diminished in MCI and AD [35, 36], and a disruption of the thalamus-cortex relation has severe implications on mental health [58–60].

Proper or optimal function of BA7 seems to be an indication for a cognitive reserve, preventing dementia symptoms [61]. Switching attention is an important part of the training; regions that are activated in such a task are part of the parietal cortex as well as premotor areas and the dorsolateral PFC [62] but the relation between these regions and especially the change in relation have not yet been investigated.

With our study we could show that the applied “life kinetik” training changes the connectivity strength between several brain regions. There is a lot of evidence for brain plasticity even in the adult and aging brain. Basic research has shown that different aspects of the brain can be shaped by various types of training and tasks. Resting-state connectivity seems to be relatively stable [63], but disturbed in psychiatric disorders [64], changing with age [65, 66], and changeable by activity [26]. Intrinsic connectivity is shown to be an indicator for efficiency [67] and positively correlated with cognitive performance [68, 69] and intelligence [70].

The data on the direction of changes or alterations in terms of increase or decrease are inconsistent. It is not generally known which direction is more beneficial. This most likely depends on many functional aspects the connectivity is supporting. For example, patients with major depression show an increased functional connectivity [71] whereas schizophrenia seems to be accompanied by decreased functional connectivity [60].

The functional connectivity of the motor cortex, for example, is increasing with age but different relations to performance were reported. One study interpreted the positive relation of connectivity and performance as a protection against decline [66]. The second study found the increase in connectivity with age accompanied by poorer performance [65]. This contradicting consequence of connectivity increase with regard to performance demonstrates that an intervention leading to enhanced connectivity between brain areas might not necessarily help attenuate age related decline.

The tasks and types of training used in different studies to investigate the change of brain networks are somewhat arbitrary, varying from perception tasks according to robot-hand movements to juggling or transcranial electrical or magnetic stimulation. Most training concepts do not have the potential to serve as a training method or therapy approach for psychiatric patients or elderly individuals.

Exceptions are various types of motor training like juggling [50], video games [25], aerobic training [72], or the quadrato-motor training [73] which are all aimed at perfecting the task without varying the task.

Our motivation was to look for a training that includes motor and cognitive exercises and has the potential to be stimulating for a patient population.

**4.1. Limitations.** Test-retest reliability is a not yet completely resolved issue in fMRI studies [74–77]. Few studies addressed this issue for rs-fMRI but retest reliability was found to be robust [44, 78]. Improvement can be made via the inclusion of several preprocessing steps [44]. This enhances the intersession retest reliability to 0.81. We addressed this issue by including preprocessing steps that are known to reduce noise [44, 79, 80]. We carefully screened the control group for changes and reported only results with a significant post hoc test.

A second limitation for our results is the whole sample size as well as the difference in the size of the trainee and control group. We tried to address this issue by verifying the occurrence of the default mode network that did not change in control subjects despite the small sample size.

The impact of the training intensity is unknown. The actual program consisted of 1-hour training per week. Further studies should investigate the effect of shorter but more frequent training sessions.

The subject group participating in the training showed an increase in resting-state functional connectivity but the impact on task performance is unknown and could not be monitored due to the nature of the training. A next step would be to find suitable motor and cognitive test tasks to quantify an improvement following “life kinetik” training.

Further investigations should include an active control group (practicing either motor performance or cognitive tasks or training a limited number of tasks to perfection) to show the benefit of the combined training compared to its isolated parts. Furthermore, we will investigate the impact of the training on cognitive performance and memory, preferably in a group of impaired subjects.

Since it is not possible to measure the brain activity during the training, we only could assume which brain regions are activated. This study was planned as a pilot study to show that the training is able to change brain connectivity. We assume that our subjects show “normal” resting-state networks. In a patient group the connectivity increases may depend on the underlying alteration of the according network.

## Disclosure

The results were presented at the OHBM meeting 2015 in Honolulu.

## Conflict of Interests

The author and the coauthors declare that there is no conflict of interests regarding the publication of this paper.

## Acknowledgments

The authors thank Inanc Karaca and Laura Uhrig for providing the training sessions and Gunilla Oberthür and Julia van Eijk for the support with the MR scan. This study was funded by the DFG through Center Grant SFB636, project Z03.

## References

- [1] D. O. Hebb, *The Organization of Behavior: A Neuropsychological Theory*, Psychology Press, New York, NY, USA, 1949.
- [2] G. Kempermann, H. G. Kuhn, and F. H. Gage, "More hippocampal neurons in adult mice living in an enriched environment," *Nature*, vol. 386, no. 6624, pp. 493–495, 1997.
- [3] C. S. Green and D. Bavelier, "Exercising your brain: a review of human brain plasticity and training-induced learning," *Psychology and Aging*, vol. 23, no. 4, pp. 692–701, 2008.
- [4] D. Bavelier, D. M. Levi, R. W. Li, Y. Dan, and T. K. Hensch, "Removing brakes on adult brain plasticity: from molecular to behavioral interventions," *Journal of Neuroscience*, vol. 30, no. 45, pp. 14964–14971, 2010.
- [5] A. Gutches, "Plasticity of the aging brain: new directions in cognitive neuroscience," *Science*, vol. 346, no. 6209, pp. 579–582, 2014.
- [6] R. J. Zatorre, R. D. Fields, and H. Johansen-Berg, "Plasticity in gray and white: neuroimaging changes in brain structure during learning," *Nature Neuroscience*, vol. 15, no. 4, pp. 528–536, 2012.
- [7] A. May, "Experience-dependent structural plasticity in the adult human brain," *Trends in Cognitive Sciences*, vol. 15, no. 10, pp. 475–482, 2011.
- [8] M. Spolidoro, A. Sale, N. Berardi, and L. Maffei, "Plasticity in the adult brain: lessons from the visual system," *Experimental Brain Research*, vol. 192, no. 3, pp. 335–341, 2009.
- [9] B. Guerra-Carrillo, A. P. MacKey, and S. A. Bunge, "Resting-state fMRI: a window into human brain plasticity," *Neuroscientist*, vol. 20, no. 5, pp. 522–533, 2014.
- [10] C. Kelly and F. X. Castellanos, "Strengthening connections: functional connectivity and brain plasticity," *Neuropsychology Review*, vol. 24, no. 1, pp. 63–76, 2014.
- [11] B. Biswal, F. Z. Yetkin, V. M. Haughton, and J. S. Hyde, "Functional connectivity in the motor cortex of resting human brain using echo-planar MRI," *Magnetic Resonance in Medicine*, vol. 34, no. 4, pp. 537–541, 1995.
- [12] M. J. Lowe, "The emergence of doing 'nothing' as a viable paradigm design," *NeuroImage*, vol. 62, no. 2, pp. 1146–1151, 2012.
- [13] A. Z. Snyder and M. E. Raichle, "A brief history of the resting state: the Washington University perspective," *NeuroImage*, vol. 62, no. 2, pp. 902–910, 2012.
- [14] M. D. Fox and M. E. Raichle, "Spontaneous fluctuations in brain activity observed with functional magnetic resonance imaging," *Nature Reviews Neuroscience*, vol. 8, no. 9, pp. 700–711, 2007.
- [15] N. B. Albert, E. M. Robertson, and R. C. Miall, "The resting human brain and motor learning," *Current Biology*, vol. 19, no. 12, pp. 1023–1027, 2009.
- [16] K. Yoo, W. S. Sohn, and Y. Jeong, "Tool-use practice induces changes in intrinsic functional connectivity of parietal areas," *Frontiers in Human Neuroscience*, vol. 7, article 49, 2013.
- [17] L. Ma, S. Narayana, D. A. Robin, P. T. Fox, and J. Xiong, "Changes occur in resting state network of motor system during 4 weeks of motor skill learning," *NeuroImage*, vol. 58, no. 1, pp. 226–233, 2011.
- [18] S. Vahdat, M. Darainy, T. E. Milner, and D. J. Ostry, "Functionally specific changes in resting-state sensorimotor networks after motor learning," *Journal of Neuroscience*, vol. 31, no. 47, pp. 16907–16915, 2011.
- [19] M. Taubert, G. Lohmann, D. S. Margulies, A. Villringer, and P. Ragert, "Long-term effects of motor training on resting-state networks and underlying brain structure," *NeuroImage*, vol. 57, no. 4, pp. 1492–1498, 2011.
- [20] M. W. Voss, R. S. Prakash, K. I. Erickson et al., "Plasticity of brain networks in a randomized intervention trial of exercise training in older adults," *Frontiers in Aging Neuroscience*, vol. 2, article 32, 2010.
- [21] H. Takeuchi, Y. Taki, R. Nouchi et al., "Effects of working memory training on functional connectivity and cerebral blood flow during rest," *Cortex*, vol. 49, no. 8, pp. 2106–2125, 2013.
- [22] D. D. Jolles, M. A. van Buchem, E. A. Crone, and S. A. R. B. Rombouts, "Functional brain connectivity at rest changes after working memory training," *Human Brain Mapping*, vol. 34, no. 2, pp. 396–406, 2013.
- [23] H. Takeuchi, Y. Taki, R. Nouchi et al., "Effects of multitasking-training on gray matter structure and resting state neural mechanisms," *Human Brain Mapping*, vol. 35, no. 8, pp. 3646–3660, 2014.
- [24] A. P. Mackey, A. T. M. Singley, and S. A. Bunge, "Intensive reasoning training alters patterns of brain connectivity at rest," *Journal of Neuroscience*, vol. 33, no. 11, pp. 4796–4803, 2013.
- [25] K. Martínez, A. B. Solana, M. Burgaleta et al., "Changes in resting-state functionally connected parietofrontal networks after videogame practice," *Human Brain Mapping*, vol. 34, no. 12, pp. 3143–3157, 2013.
- [26] T. Harmelech, S. Preminger, E. Wertman, and R. Malach, "The day-after effect: long term, hebbian-like restructuring of resting-state fMRI patterns induced by a single epoch of cortical activation," *Journal of Neuroscience*, vol. 33, no. 22, pp. 9488–9497, 2013.
- [27] F. Megumi, A. Yamashita, M. Kawato, and H. Imazumi, "Functional MRI neurofeedback training on connectivity between two regions induces long-lasting changes in intrinsic functional network," *Frontiers in Human Neuroscience*, vol. 9, article 160, 2015.
- [28] E. Kraft, "Cognitive function, physical activity, and aging: possible biological links and implications for multimodal interventions," *Aging, Neuropsychology, and Cognition*, vol. 19, no. 1-2, pp. 248–263, 2012.
- [29] K. Hötting and B. Röder, "Beneficial effects of physical exercise on neuroplasticity and cognition," *Neuroscience and Biobehavioral Reviews*, vol. 37, no. 9, pp. 2243–2257, 2013.
- [30] R. Li, X. Zhu, S. Yin et al., "Multimodal intervention in older adults improves resting-state functional connectivity between the medial prefrontal cortex and medial temporal lobe," *Frontiers in Aging Neuroscience*, vol. 6, article 39, 2014.
- [31] K. Holzschneider, T. Wolbers, B. Röder, and K. Hötting, "Cardiovascular fitness modulates brain activation associated with spatial learning," *NeuroImage*, vol. 59, no. 3, pp. 3003–3014, 2012.
- [32] C. M. Lewis, A. Baldassarre, G. Committeri, G. L. Romani, and M. Corbetta, "Learning sculpts the spontaneous activity of the resting human brain," *Proceedings of the National Academy of Sciences of the United States of America*, vol. 106, no. 41, pp. 17558–17563, 2009.
- [33] T. E. J. Behrens, H. Johansen-Berg, M. W. Woolrich et al., "Non-invasive mapping of connections between human thalamus and cortex using diffusion imaging," *Nature Neuroscience*, vol. 6, no. 7, pp. 750–757, 2003.
- [34] R. Fama and E. V. Sullivan, "Thalamic structures and associated cognitive functions: relations with age and aging," *Neuroscience & Biobehavioral Reviews*, vol. 54, pp. 29–37, 2015.
- [35] B. Zhou, Y. Liu, Z. Zhang et al., "Impaired functional connectivity of the thalamus in Alzheimer's disease and mild cognitive

- impairment: a resting-state fMRI study,” *Current Alzheimer Research*, vol. 10, no. 7, pp. 754–766, 2013.
- [36] Z. Wang, X. Jia, P. Liang et al., “Changes in thalamus connectivity in mild cognitive impairment: evidence from resting state fMRI,” *European Journal of Radiology*, vol. 81, no. 2, pp. 277–285, 2012.
- [37] R. L. Buckner, F. M. Krienen, A. Castellanos, J. C. Diaz, and B. T. Thomas Yeo, “The organization of the human cerebellum estimated by intrinsic functional connectivity,” *Journal of Neurophysiology*, vol. 106, no. 5, pp. 2322–2345, 2011.
- [38] J. X. O’Reilly, C. F. Beckmann, V. Tomassini, N. Ramnani, and H. Johansen-Berg, “Distinct and overlapping functional zones in the cerebellum defined by resting state functional connectivity,” *Cerebral Cortex*, vol. 20, no. 4, pp. 953–965, 2010.
- [39] J. Pa, S. Dutt, J. B. Mirsky et al., “The functional oculomotor network and saccadic cognitive control in healthy elders,” *NeuroImage*, vol. 95, pp. 61–68, 2014.
- [40] R. M. Hutchison, J. P. Gallivan, J. C. Culham, J. S. Gati, R. S. Menon, and S. Everling, “Functional connectivity of the frontal eye fields in humans and macaque monkeys investigated with resting-state fMRI,” *Journal of Neurophysiology*, vol. 107, no. 9, pp. 2463–2474, 2012.
- [41] E. J. Anderson, D. K. Jones, R. L. O’Gorman, A. Leemans, M. Catani, and M. Husain, “Cortical network for gaze control in humans revealed using multimodal MRI,” *Cerebral Cortex*, vol. 22, no. 4, pp. 765–775, 2012.
- [42] J. Ashburner, “A fast diffeomorphic image registration algorithm,” *NeuroImage*, vol. 38, no. 1, pp. 95–113, 2007.
- [43] S. Whitfield-Gabrieli and A. Nieto-Castanon, “Conn: a functional connectivity toolbox for correlated and anticorrelated brain networks,” *Brain Connectivity*, vol. 2, no. 3, pp. 125–141, 2012.
- [44] W. R. Shirer, H. Jiang, C. M. Price, B. Ng, and M. D. Greicius, “Optimization of rs-fMRI pre-processing for enhanced signal-noise separation, test-retest reliability, and group discrimination,” *NeuroImage*, vol. 117, pp. 67–79, 2015.
- [45] Y. Behzadi, K. Restom, J. Liau, and T. T. Liu, “A component based noise correction method (CompCor) for BOLD and perfusion based fMRI,” *NeuroImage*, vol. 37, no. 1, pp. 90–101, 2007.
- [46] Z. Qing, Z. Dong, S. Li, Y. Zang, and D. Liu, “Global signal regression has complex effects on regional homogeneity of resting state fMRI signal,” *Magnetic Resonance Imaging*, 2015.
- [47] O. Agcaoglu, R. Miller, A. R. Mayer, K. Hugdahl, and V. D. Calhoun, “Lateralization of resting state networks and relationship to age and gender,” *NeuroImage*, vol. 104, pp. 310–325, 2015.
- [48] C. Luo, Z.-W. Guo, Y.-X. Lai et al., “Musical training induces functional plasticity in perceptual and motor networks: insights from resting-state fMRI,” *PLoS ONE*, vol. 7, no. 5, Article ID e36568, 2012.
- [49] C. Sampaio-Baptista, A. A. Khrapitchev, S. Foxley et al., “Motor skill learning induces changes in white matter microstructure and myelination,” *Journal of Neuroscience*, vol. 33, no. 50, pp. 19499–19503, 2013.
- [50] C. Sampaio-Baptista, N. Filippini, C. J. Stagg, J. Near, J. Scholz, and H. Johansen-Berg, “Changes in functional connectivity and GABA levels with long-term motor learning,” *NeuroImage*, vol. 106, pp. 15–20, 2015.
- [51] B. Draganski, C. Gaser, V. Busch, G. Schuierer, U. Bogdahn, and A. May, “Neuroplasticity: changes in grey matter induced by training,” *Nature*, vol. 427, no. 6972, pp. 311–312, 2004.
- [52] J. C. Culham and N. G. Kanwisher, “Neuroimaging of cognitive functions in human parietal cortex,” *Current Opinion in Neurobiology*, vol. 11, no. 2, pp. 157–163, 2001.
- [53] O. Simon, J.-F. Mangin, L. Cohen, D. Le Bihan, and S. Dehaene, “Topographical layout of hand, eye, calculation, and language-related areas in the human parietal lobe,” *Neuron*, vol. 33, no. 3, pp. 475–487, 2002.
- [54] A. Bartels and S. Zeki, “Brain dynamics during natural viewing conditions—a new guide for mapping connectivity in vivo,” *NeuroImage*, vol. 24, no. 2, pp. 339–349, 2005.
- [55] M.-T. Herrero, C. Barcia, and J. M. Navarro, “Functional anatomy of thalamus and basal ganglia,” *Child’s Nervous System*, vol. 18, no. 8, pp. 386–404, 2002.
- [56] L. Hearne, L. Cocchi, A. Zalesky, and J. B. Mattingley, “Interactions between default mode and control networks as a function of increasing cognitive reasoning complexity,” *Human Brain Mapping*, vol. 36, no. 7, pp. 2719–2731, 2015.
- [57] L. Bonzano, E. Palmaro, R. Teodorescu, L. Fleysher, M. Inglese, and M. Bove, “Functional connectivity in the resting-state motor networks influences the kinematic processes during motor sequence learning,” *European Journal of Neuroscience*, vol. 41, no. 2, pp. 243–253, 2015.
- [58] N. C. Andreasen, “The role of the thalamus in schizophrenia,” *Canadian Journal of Psychiatry*, vol. 42, no. 1, pp. 27–33, 1997.
- [59] J. D. Schmahmann and D. N. Pandya, “Disconnection syndromes of basal ganglia, thalamus, and cerebrotectal systems,” *Cortex*, vol. 44, no. 8, pp. 1037–1066, 2008.
- [60] H. S. Wang, C. Rau, Y. Li, Y. Chen, and R. Yu, “Disrupted thalamic resting-state functional networks in schizophrenia,” *Frontiers in Behavioral Neuroscience*, vol. 9, article 45, 2015.
- [61] C. Solé-Padullés, D. Bartrés-Faz, C. Junqué et al., “Brain structure and function related to cognitive reserve variables in normal aging, mild cognitive impairment and Alzheimer’s disease,” *Neurobiology of Aging*, vol. 30, no. 7, pp. 1114–1124, 2009.
- [62] C.-Y. C. Sylvester, T. D. Wager, S. C. Lacey et al., “Switching attention and resolving interference: fMRI measures of executive functions,” *Neuropsychologia*, vol. 41, no. 3, pp. 357–370, 2003.
- [63] M. E. Raichle, “The restless brain: how intrinsic activity organizes brain function,” *Philosophical Transactions of the Royal Society of London Series B: Biological Sciences*, vol. 370, no. 1668, 2015.
- [64] D. Zhang and M. E. Raichle, “Disease and the brain’s dark energy,” *Nature Reviews Neurology*, vol. 6, no. 1, pp. 15–28, 2010.
- [65] E. Solesio-Jofre, L. Serbruyns, D. G. Woolley, D. Mantini, I. A. M. Beets, and S. P. Swinnen, “Aging effects on the resting state motor network and interlimb coordination,” *Human Brain Mapping*, vol. 35, no. 8, pp. 3945–3961, 2014.
- [66] R. Seidler, B. Erdeniz, V. Koppelmans, S. Hirsiger, S. Méritat, and L. Jäncke, “Associations between age, motor function, and resting state sensorimotor network connectivity in healthy older adults,” *NeuroImage*, vol. 108, pp. 47–59, 2015.
- [67] O. Ajilore, M. Lamar, and A. Kumar, “Association of brain network efficiency with aging, depression, and cognition,” *The American Journal of Geriatric Psychiatry*, vol. 22, no. 2, pp. 102–110, 2014.
- [68] Z. Zheng, X. Zhu, S. Yin et al., “Combined cognitive-psychological-physical intervention induces reorganization of intrinsic functional brain architecture in older adults,” *Neural Plasticity*, vol. 2015, Article ID 713104, 11 pages, 2015.

- [69] A. Lampit, H. Hallock, C. Suo, S. L. Naismith, and M. Valenzuela, "Cognitive training-induced short-term functional and long-term structural plastic change is related to gains in global cognition in healthy older adults: a pilot study," *Frontiers in Aging Neuroscience*, vol. 7, article 014, 2015.
- [70] M. W. Cole, T. Yarkoni, G. Repovš, A. Anticevic, and T. S. Braver, "Global connectivity of prefrontal cortex predicts cognitive control and intelligence," *The Journal of Neuroscience*, vol. 32, no. 26, pp. 8988–8999, 2012.
- [71] Y. I. Sheline, J. L. Price, Z. Yan, and M. A. Mintun, "Resting-state functional MRI in depression unmasks increased connectivity between networks via the dorsal nexus," *Proceedings of the National Academy of Sciences of the United States of America*, vol. 107, no. 24, pp. 11020–11025, 2010.
- [72] M. W. Voss, K. I. Erickson, R. S. Prakash et al., "Functional connectivity: a source of variance in the association between cardiorespiratory fitness and cognition?" *Neuropsychologia*, vol. 48, no. 5, pp. 1394–1406, 2010.
- [73] T. D. Ben-Soussan, A. Berkovich-Ohana, J. Glicksohn, and A. Goldstein, "A suspended act: increased reflectivity and gender-dependent electrophysiological change following Quadrato Motor Training," *Frontiers in Psychology*, vol. 5, article 55, 2014.
- [74] C. M. Bennett and M. B. Miller, "How reliable are the results from functional magnetic resonance imaging?" *Annals of the New York Academy of Sciences*, vol. 1191, pp. 133–155, 2010.
- [75] K. J. Gorgolewski, A. J. Storkey, M. E. Bastin, I. Whittle, and C. Pernet, "Single subject fMRI test-retest reliability metrics and confounding factors," *NeuroImage*, vol. 69, pp. 231–243, 2013.
- [76] R. Maitra, S. R. Roys, and R. P. Gullapalli, "Test-retest reliability estimation of functional MRI data," *Magnetic Resonance in Medicine*, vol. 48, no. 1, pp. 62–70, 2002.
- [77] M. Raemaekers, S. du Plessis, N. F. Ramsey, J. M. H. Weusten, and M. Vink, "Test-retest variability underlying fMRI measurements," *NeuroImage*, vol. 60, no. 1, pp. 717–727, 2012.
- [78] Z. Shehzad, A. M. C. Kelly, P. T. Reiss et al., "The resting brain: unconstrained yet reliable," *Cerebral Cortex*, vol. 19, no. 10, pp. 2209–2229, 2009.
- [79] K. Murphy, R. M. Birn, and P. A. Bandettini, "Resting-state fMRI confounds and cleanup," *NeuroImage*, vol. 80, pp. 349–359, 2013.
- [80] X.-N. Zuo and X.-X. Xing, "Test-retest reliabilities of resting-state FMRI measurements in human brain functional connectomics: a systems neuroscience perspective," *Neuroscience and Biobehavioral Reviews C*, vol. 45, pp. 100–118, 2014.

## Research Article

# Compensation through Functional Hyperconnectivity: A Longitudinal Connectome Assessment of Mild Traumatic Brain Injury

Armin Iraj, <sup>1</sup> Hanbo Chen, <sup>2</sup> Natalie Wiseman, <sup>3</sup> Robert D. Welch, <sup>4</sup> Brian J. O'Neil, <sup>4</sup>  
E. Mark Haacke, <sup>1,5</sup> Tianming Liu, <sup>2</sup> and Zhifeng Kou <sup>1,5</sup>

<sup>1</sup>Department of Biomedical Engineering, Wayne State University, Detroit, MI, USA

<sup>2</sup>Department of Computer Science, The University of Georgia, Athens, GA, USA

<sup>3</sup>Department of Psychiatry and Behavioral Neurosciences, Wayne State University, Detroit, MI, USA

<sup>4</sup>Department of Emergency Medicine, Wayne State University, Detroit, MI, USA

<sup>5</sup>Department of Radiology, Wayne State University, Detroit, MI, USA

Correspondence should be addressed to Tianming Liu; [tianming.liu@gmail.com](mailto:tianming.liu@gmail.com) and Zhifeng Kou; [zhifeng\\_kou@wayne.edu](mailto:zhifeng_kou@wayne.edu)

Received 7 May 2015; Revised 7 August 2015; Accepted 11 August 2015

Academic Editor: Shuyu Li

Copyright © 2016 Armin Iraj et al. This is an open access article distributed under the Creative Commons Attribution License, which permits unrestricted use, distribution, and reproduction in any medium, provided the original work is properly cited.

Mild traumatic brain injury (mTBI) is a major public health concern. Functional MRI has reported alterations in several brain networks following mTBI. However, the connectome-scale brain network changes are still unknown. In this study, sixteen mTBI patients were prospectively recruited from an emergency department and followed up at 4–6 weeks after injury. Twenty-four healthy controls were also scanned twice with the same time interval. Three hundred fifty-eight brain landmarks that preserve structural and functional correspondence of brain networks across individuals were used to investigate longitudinal brain connectivity. Network-based statistic (NBS) analysis did not find significant difference in the group-by-time interaction and time effects. However, 258 functional pairs show group differences in which mTBI patients have higher functional connectivity. Meta-analysis showed that “Action” and “Cognition” are the most affected functional domains. Categorization of connectomic signatures using multiview group-wise cluster analysis identified two patterns of functional hyperconnectivity among mTBI patients: (I) between the posterior cingulate cortex and the association areas of the brain and (II) between the occipital and the frontal lobes of the brain. Our results demonstrate that brain concussion renders connectome-scale brain network connectivity changes, and the brain tends to be hyperactivated to compensate the pathophysiological disturbances.

## 1. Introduction

Mild traumatic brain injury (mTBI) represents a major public health burden with an annual incidence of over 1.2 million people in the USA [1–3]. Despite normal findings in clinical imaging such as computed tomography (CT) and structural magnetic resonance imaging (MRI) for the majority of mTBI patients, mTBI can cause emotional, physical, and cognitive symptoms that significantly impact the patients' quality of life and cost the nation \$16.7 billion each year [4–6]. TBI in general can be thought of as a disorder of network disconnection [7]. Similar clinical presentations are observed in diverse range of insult and injury despite different origins

and locations of impact. Therefore, evaluating the outcome of injury in specific brain regions is confusing, and it provides a distorted view of brain functional disruption [8]. This situation is more significant in mild TBI than in severe and moderate TBI because there is usually no significant structural damage at mild TBI, indicating that this may account for a greater portion of the problem in mTBI than in moderate or severe TBI [9].

In light of heterogeneous locations of injury, use of large-scale approaches can provide a better understanding of brain function and improve neuropsychological understanding of the sequela of mTBI. Furthermore, mapping the topography of the brain functional connectivity alterations

at a macrolevel can elucidate the role of brain plasticity. It has been reported that brain injury induces not only structural damage, which could be detected by diffusion tensor imaging (DTI), but also functional disturbances and compensation, which are considered a neural plastic effect [10–13]. In adults, brain plasticity still takes place, especially at a large scale, which is known as adult plasticity [9, 14, 15]. In general, brain plasticity can be defined as the capacity of the brain to change its structural or functional connectivity and organization during a short or long period of time [16, 17]. In adult plasticity, according to the Hebbian theory, coincident neuronal firing leads to wiring together [18]. At the same time, brain functional connectivity is measured using the temporal dependency of neural activity [19]. Therefore, it has been suggested that functional connectivity (FC) of the brain during the resting state is linked to the brain plasticity [20], which has been confirmed by showing a strong correlation between brain plasticity and resting-state FC (rs-FC) changes [21, 22].

Accumulating evidences demonstrate brain plasticity after brain injury. Zhou et al. [20] studied brain plasticity using rs-FC after partial and complete callosotomy groups, in which disrupted functional connectivity was restored at day 28 in the partial callosotomy group through the remaining interhemispheric axonal pathways. Additionally, intrahemispheric functional connectivity was increased in both partial and complete callosotomy, representing plasticity in brain FC and adaptation after injury [20]. Nakamura et al. [23] examined neural plasticity in a longitudinal study during recovery period of TBI using graph theory, which revealed that overall functional connectivity strength is higher at three months after injury as compared with what is observed in healthy adults; however, functional connectivity decreases and approaches that of the healthy subjects sample after six months after injury. These findings indicate that overall functional connectivity increases to compensate the effect of injury after TBI [23]. Therefore, the study of neuroplasticity can provide a new angle to inspect the neurological origins of brain alterations after injury, especially at a large scale, and provide new insights into the pathophysiological substrates of cognitive and behavioral alterations [7, 24]. However, to date, the field is still short of investigation on connectome-scale brain network alterations and compensatory effects after TBI. Moreover, the impacts of brain alterations over time in connectome-scale brain networks during brain recovery are still unknown [11]. We hypothesize that mTBI induces brain network disturbances and also the consequent compensatory effects at the connectome-scale network level. Our objective is to investigate the connectome-scale brain network changes after mTBI and recovery and potential brain plasticity.

Resting-state functional MRI (rsfMRI) constitutes an ideal way to evaluate brain functional connectivity and changes in brain functional connectivity at a connectome scale which can contribute to a better understanding of plasticity and the brain's attempts to compensate for injury [7–9]. Brain functional connectivity can be measured using statistical relationships between the blood-oxygen-level dependent (BOLD) signals of brain regions, which reflects the prior history of coactivation between brain regions [25].

The large-scale rs-FC is an ideal way to evaluate brain functional connectivity on a connectome scale at a macrolevel, which can be used to investigate brain plasticity and serve as an index of the efficacy of healing [8]. rsfMRI provides unique insights into brain plasticity at the macrolevel, which can provide a better understanding of brain disorders such as TBI and consequently guide proper rehabilitation plan [11].

In the evaluation of connectome-scale brain networks, one technical challenge is to define the network nodes or regions of interest (ROIs). The network nodes serve as structural and functional substrates for network analysis. Several approaches are available in the field with remarkable progress. However, they also suffer different limitations from different perspectives, particularly at a large scale, when the network is at very fine level. Any mismatch will result in the cross talk of a network to its neighbors. Zhu et al. previously identified 358 regions of interest (ROIs), known as dense individualized common connectivity based cortical landmarks (DICCCOLs), distributed across the brain. The location of each DICCCOL is identified based on the white matter fiber connection profile obtained from diffusion MRI (dMRI). Each DICCCOL preserves similar structural and functional properties across individuals [26]. Since each DICCCOL preserves consistent structural connection patterns, according to the connective fingerprint concept, its functional role should be similar across subjects [27]. In addition to reproducibility and consistency, DICCCOL analysis has been shown to be powerful in identifying connectivity signatures (disrupted connectivity) in affected brains [28]. After localizing DICCCOLs across an individual's brain, the time series related to each DICCCOL is derived from the BOLD rsfMRI signal of the gray matter area in the 5 mm neighborhood of each DICCCOL. The functional connectivity of an individual's brain at a large scale is assessed by measuring temporal Pearson correlation between each pair of the time series allocated to the DICCCOLs. Our goal is to use the DICCCOL framework to define the functional network nodes at a large scale and further assess the effect of brain injury on mTBI patients over time.

## 2. Materials and Methods

**2.1. Data Acquisition.** Patient eligibility was based on the mTBI definition by the American Congress of Rehabilitation Medicine, 1993, with the following inclusion criteria: patients aged 18 or older with an initial Glasgow Coma Scale (GCS) score of 13–15 in the ED with any loss of consciousness less than 30 minutes or any posttraumatic amnesia less than 24 hours, or recorded change of mental status (confused, disoriented, or dazed). In the acute stage (first scan), patients were scanned at 82.64/17 hours (average/median) after injury, and the second scan was acquired at 4–6 weeks after injury (subacute stage). For healthy subjects, two scans were acquired with a 4–6-week interval in between. rsfMRI and dMRI data were acquired on a 3-Tesla Siemens Verio scanner with a 32-channel radiofrequency head-only coil. Demographic characteristics are presented in Table 1. dMRI data has been already used and analyzed for another study. Thus, dMRI has only been used to identify the locations of

TABLE 1: Demographic characteristics of healthy controls and patients.

Characteristic	Control subjects ( $n = 24$ )	mTBI patients ( $n = 16$ )
Gender		
Male	20	10
Female	4	6
Age (years)		
Mean $\pm$ SD	28.00 $\pm$ 7.55	34.52 $\pm$ 13.85
Median/range	26/(19~50)	30/(19~63)
Race		
African American	2	11
White	15	3
Others	7	2
Cause of injury		
Motorcycle accident	—	1
Bicycle accident	—	1
Motor vehicle accident	—	5
Struck by vehicle	—	2
Assault	—	4
Fall	—	3
Time between injury and 1st scan (hours)		
Mean $\pm$ SD	—	82.64 $\pm$ 121.90
Median/range	—	17/(3~446)
Time between 2 scans (days)		
Mean $\pm$ SD	84.60 $\pm$ 55.48	42.68 $\pm$ 17.48
Median/range	70/(22~225)	36/(26~89)
Glasgow Coma Scale		
Mean $\pm$ SD	—	14.92 $\pm$ 0.28
Range	—	(14~15)

DICCCOLs in this study. dMRI data was acquired using a gradient echo EPI sequence with  $b = 0/1000 \text{ s/mm}^2$  in 30 diffusion gradients directions with the following parameters: TR (repetition time) = 13300 ms, TE (echo time) = 124 ms, slice thickness = 2 mm, pixel spacing size =  $1.333 \times 1.333 \text{ mm}$ , matrix size =  $192 \times 192$ , flip angle =  $90^\circ$ , and number of averages (NEX) = 2. For rsfMRI data, gradient echo EPI sequence with following imaging parameters has been performed: pixel spacing size =  $3.125 \times 3.125 \text{ mm}$ , slice thickness = 3.5 mm, slice gap = 0.595 mm, matrix size =  $64 \times 64$ , TR/TE = 2000/30 ms, flip angle =  $90^\circ$ , 240 volumes for whole-brain coverage, and NEX = 1. During rsfMRI scans, subjects were instructed to keep their eyes closed and not to think about anything specific. In addition, T1, T2, fluid attenuated inversion recovery (FLAIR), and susceptibility weighted imaging (SWI) were also acquired. The total data acquisition protocol took about 40 minutes.

**2.2. Data Analysis.** A series of steps were taken to analyze the data: (1) localizing DICCCOL nodes of each subject using

the DICCCOL framework and computing FC between the time series of each pair of DICCCOLs; (2) performing a longitudinal statistical analysis using mixed  $2 \times 2$  design analysis of variance (ANOVA) and network-based statistic (NBS) analyses to determine the connectomic signatures; (3) determining the functional roles of the connectomic signatures using meta-analysis; and (4) performing multiview group-wise cluster analysis to determine involved FC clusters and the interrelationships of the connectomic signatures.

**2.2.1. Localizing DICCCOLs and Computing FC Matrix for Each Subject.** In the connectomic study, one essential step is to identify the locations of ROIs across the brain that preserve consistent structural and functional connections across individuals. DICCCOLs are a set of brain landmarks with similar structural and functional connectivity across individuals obtained by identifying the consistent white matter (WM) fiber connection profile across subjects. This has been done using the tool available to download at <http://dicccol.cs.uga.edu/>. Identifying the locations of DICCCOLs on the brain of an individual can be summarized in the following steps (see Figure 1): (1) deterministic tractography of whole brain was performed (Figure 1(a)). As a result, we were able to identify the WM fiber connection profile of each location of the brain. (2) Extraction of the transformation matrix was performed for the coregistering of the brain of an individual subject to the brain template (Figure 1(b)). (3) Application of the transformation matrix was carried out to transfer the individual surface and fiber bundles to the template space for prediction (Figure 1(c)). As a result, the initial location of DICCCOLs on the individual's brain was obtained. (4) Searching the local neighborhood (6 mm radius) of the initial location of each DICCCOL was conducted to find the optimized location of that DICCCOL. For this purpose, similarity between the WM fiber connection profile in the template and all local neighborhoods was measured. The neighborhood with the maximum similarity of the WM fiber connection profile with the WM fiber connection profile of the DICCCOL on the template was selected as the optimized location of the DICCCOL (Figure 1(d)). This was performed to identify optimized locations of all DICCCOLs on each individual's brain (Figure 1(e)). DICCCOL landmarks have been shown to be highly reproducible across individuals [28]. At the same time, according to the connectomic fingerprint concept, each brain's cytoarchitectonic area has a unique set of extrinsic inputs and outputs that largely determines the functions that each brain area performs [27]. The close relationships between structural connection patterns and brain functions have extensively been reported [29–31]. Since each DICCCOL preserves consistent structural connection patterns, its functional role should be similar across subjects. The intrinsic functional role of each DICCCOL has been already extensively examined and validated [28, 32]. On the other hand, although function-based ROIs are helpful for wide range of studies, they seem to not be an appropriate choice for connectome studies, which require fine identification of ROI locations, because the accuracy of ROIs locations in function-based ROIs can be compromised by several

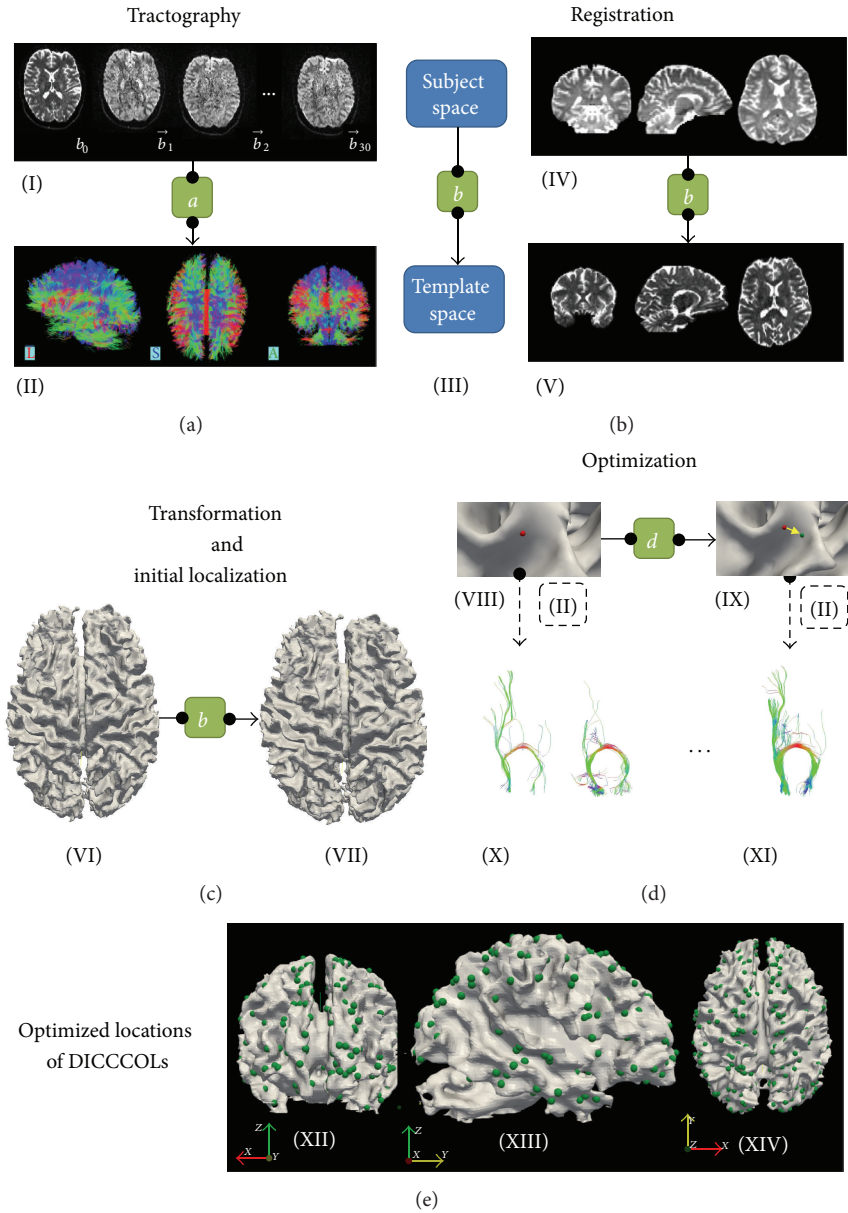


FIGURE 1: Pipeline for identifying the locations of DICCCOLs on the brain of an individual. (a) Fiber tracking and tractography of the whole brain was performed via MedINRIA (<http://med.inria.fr/>). Box “ $a$ ” presents the preprocessing steps (including brain extraction, motion correction, and eddy current correction) and deterministic tractography. (a)(I) shows diffusion data of an individual brain at  $b_0$  and some different gradient directions, and (a)(II) shows the result of tractography in 3D space in the sagittal, axial, and coronal views. (b) The transformation matrix to transfer coordinates from the subject space to the template space was obtained by registering the brain of an individual subject to the brain template. (b)(III) shows the schematic of this procedure in which box  $b$  represents the transformation matrix. (b)(IV) and (b)(V) show the coronal, axial, and sagittal views of individual and template’s brains, respectively. (c) Transformation and identification of the initial location of DICCCOLs. The transformation matrix ( $b$ ) is applied to transfer the individual surface and fiber bundles to the template space for prediction. As a result, the initial location of DICCCOLs on the individual’s brain is obtained. (c)(VI) is the surface of an individual in the subject space, and (c)(VII) is the surface of the same individual, which is transferred to the template space. The initial location of DICCCOLs on an individual’s brain was obtained by overlaying the location of DICCCOLs of the template on the transformed surface of the individual. (d) The schematic procedure of optimization in which the local neighborhood (6 mm radius) was searched in order to identify the location where the profile of connected fiber has the most similarity with the WM fiber connection profile of the DICCCOL on the template. (d)(VIII) shows the initial location of a DICCCOL, obtained from the previous step. Using the information of deterministic tractography ((a)(II)), the connected fiber at this initial location was extracted ((d)(X)). Next, the similarity between the connected fibers at this location and the connected WM fiber on the template was measured. The same procedure took place for all local neighborhoods, and the location with maximum similarity of the connected WM fibers was identified as the optimized location of the DICCCOL. Box  $d$  represents the optimization procedure. (d)(IX) shows the initial and optimized locations of a DICCCOL in red and green, respectively. (d)(X) and (d)(XI) show the connected fibers at the initial and optimized locations of the DICCCOL, respectively. (e) represents the optimized locations of all DICCCOLs on an individual’s brain. (e)(XII), (e)(XIII), and (e)(XIV) show the coronal, sagittal, and axial views in 3D space, respectively.

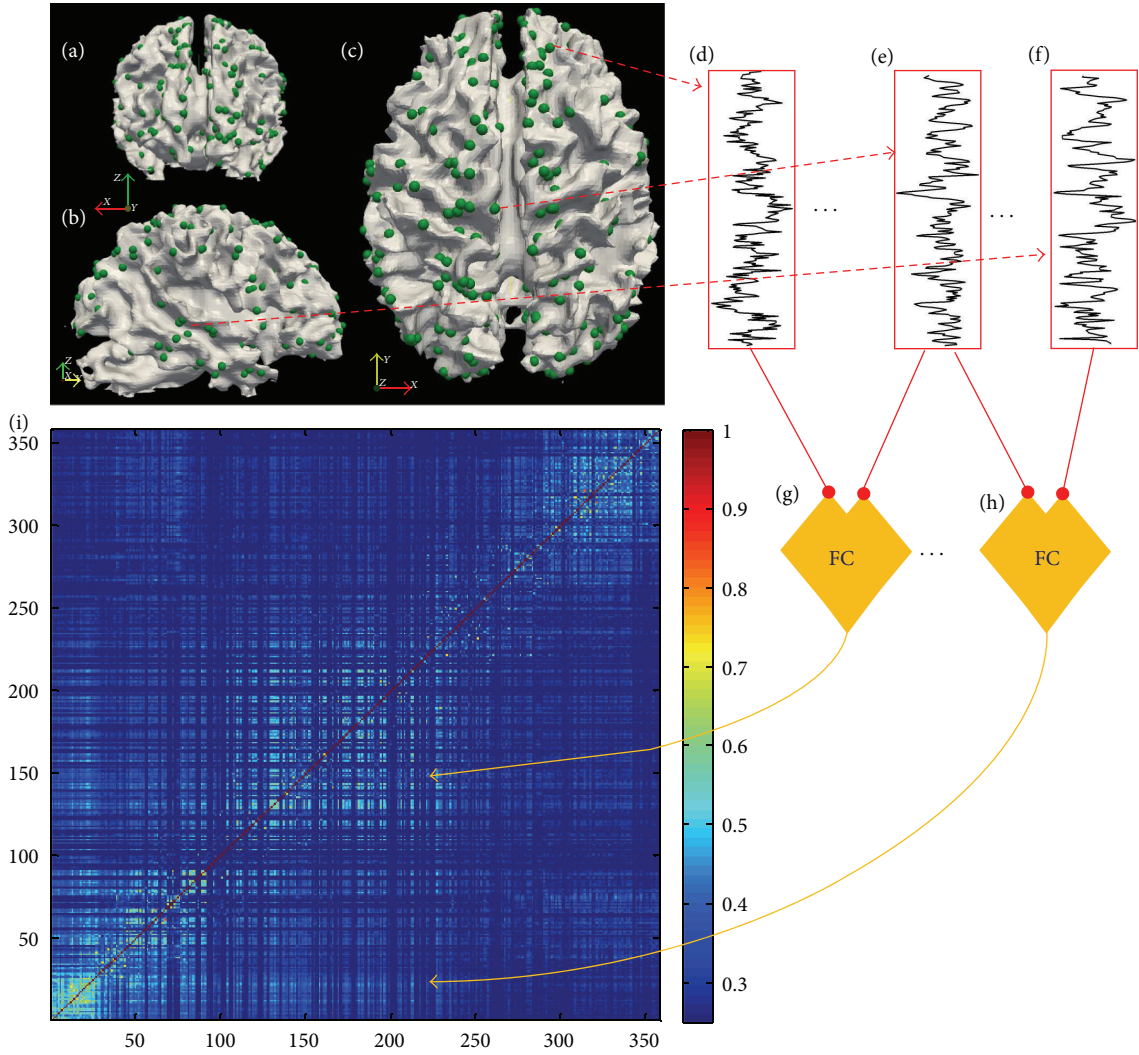


FIGURE 2: Functional connectivity (FC) was measured across the brain using the DICCCOL framework. (a), (b), and (c) show the optimized locations of DICCCOLs across the brain in the coronal, sagittal, and axial views, respectively. (d), (e), and (f) represent the time series allocated to three DICCCOLs obtained from the rsfMRI data of the gray matter of the 5 mm neighborhood of each DICCCOL. The Pearson correlation was calculated between time series of 358 DICCCOLs in order to obtain the FC of the brain at large scale. (g) and (h) show two examples of FC measurement, and (i) is a symmetric affinity matrix, which represents FC at a connectomic level.

factors such as normalization and spatial smoothing [30]. Therefore, the DICCCOL framework was applied to identify the corresponding ROIs across individuals for FC analysis.

For FC analysis of the rsfMRI data using FSL, pre-processing included brain extraction, motion correction, slice-time correction, spatial smoothing (FWHM = 5 mm), temporal whitening, grand mean removal, and temporal high-pass filtering [33]. The time series allocated to each DICCCOL was derived from the gray matter area in the 5 mm neighborhood of that DICCCOL. FC between each pair of DICCCOLs was obtained by measuring temporal Pearson correlations between the time series allocated to each DICCCOL. Therefore, a symmetric affinity matrix with 64261 unique features was obtained to represent functional connectivity of the brain at a connectomic level (Figure 2).

**2.2.2. Network-Based Statistical (NBS) Analysis.** Neuroimaging studies suggest that networks compose cognitive and

functional domains of the brain. At the same time, the networks for different cognitive and functional domains can overlap with each other [34]. To fully investigate the disrupted cognitive and functional domains of the brain, meta-analysis and multiview group-wise clustering approaches were applied. For the statistical longitudinal analysis, a mixed  $2 \times 2$  design ANOVA was used to identify connectomic signatures. Independent variables were group (controls versus patients) and time (acute versus subacute). NBS is a validated method which was originally developed for connectomic studies to perform nonparametric statistical analysis on large-scale pairs of connections [35]. While the false discovery rate (FDR) is sensitive to detecting an independent, isolated connected pair regardless of its affiliation (or conjunction) with other connected pairs, NBS improves power to detect a nexus that includes multiple affiliated connected pairs [35]. In other words, NBS, while controlling the family-wise error

rate (FWER), implements rejection of a null hypothesis at the network level. NBS, intuitively, includes the following steps:

- (a) Performing a statistical test on each connected pair independently. NBS, like other common neuroimaging software packages, uses the general linear model (GLM) as the statistical test. The output of this step is a set of connected pairs that are the potential candidates to be connectomic signatures (connected pairs which are statistically different between two groups).
- (b) Identifying any possible connectivity structure from connected pairs which were selected at the previous step.
- (c) Calculating a FWER-corrected  $p$  value for a connectivity structure with size of  $K$  using permutation testing. Specifically, for each permutation, connectivity structures were identified and the maximal component size was obtained. Then,  $p$  value for any observed connectivity structure with size of  $K$  can be calculated based on the possibility of having maximal connectivity structure size  $> K$  in  $M$  permutation.

NBS parameters, including the uncorrected threshold value, were chosen as follows according to previous published literature [36–39]: threshold = 3.5, permutation = 5000, component size = extent, and  $p$  value = 0.05. For statistical longitudinal analysis, a mixed  $2 \times 2$  design ANOVA has been used to identify connectomic signatures. Independent variables are group (controls versus patients) and time (acute versus subacute). If the interaction effect was not significant, we investigated the group and time effects. Otherwise, we investigated each simple effect. In other words, if the interaction effect was significant, we used a two-sample unpaired  $t$ -test to compare two groups and a two-sample paired  $t$ -test to investigate each group over time.

**2.2.3. Categorizing Connectomic Signatures Using Meta-Analysis.** BrainMap (<http://www.nitrc.org/projects/brain-map/>) is an online database of published neuroimaging literature, which can be used to identify the function of brain regions based on previous reported data from well-credited labs [40]. Yuan et al. used the BrainMap software to identify the possible functional roles for each DICCCOL using meta-analysis [32]. Using the BrainMap database, we can categorize the DICCCOLs involved in connectomic signatures into five general functional categories, including “Action,” “Perception,” “Cognition,” “Interoception,” and “Emotion,” and these five categories can be further divided into 53 subcategories. At the same time, the strength of functional connectivity between two DICCCOLs can be part of the strength of functional connectivity between their corresponding networks. For instance, if DICCCOL “A” was identified as “Cognition” and DICCCOL “B” was identified as “Emotion,” then we can interpret that the strength of functional connectivity between “A” and “B” is related to the strength of functional connectivity between “Cognition” and “Emotion.” Therefore, by categorizing the DICCCOLs

involved in connectomic signatures to these functional categories, we can have better understanding of brain functional and cognitive interactions at large scale.

**2.2.4. Multiview Group-Wise Cluster Analysis.** Multiview group-wise clustering has been applied to the DICCCOL system to extract the substrate brain functional clusters as previously described by Chen et al. [41]. A cluster is defined as a set of DICCCOLs that have stronger inner functional connectivity with each other rather than with the DICCCOLs of other clusters. If we consider the DICCCOL system to be a graph representation of the brain, the DICCCOLs can be considered to be the nodes of the graph, and functional connectivities between DICCCOLs are the edges of the graph. For each subject, the functional connectivity matrix of the brain was extracted and considered to be one “view” for the clustering approach. The group-wise clustering method was applied to categorize common clusters across individuals. Briefly, in this clustering method, the clusters were obtained by projecting each view on the others to derive consistent functional clusters across brain functional connectivity of individuals [41]. After identifying the brain functional clusters, the connectomic signatures of mTBI were categorized into these identified clusters to reveal possible patterns in functional connectivity alterations of the brain after injury.

### 3. Results

Statistical analysis (Section 2.2.2) was performed on the brain functional connectivity, which was obtained from 24 healthy subjects and 16 mTBI patients at two time points. No statistically significant difference was found in the interaction effect ( $p$  value = 0.05). The time effect did not show any significant difference ( $p$  value = 0.05), either. However, in our NBS analysis, which only considers the interconnected network clusters, we identified a group effect on 258 FC pairs that were significantly affected in mTBI patients (Figure 3). All of these affected FC pairs (i.e., connectomic signatures) showed increased functional connectivity in the patient group.

In order to have a better understanding of changes in brain function after mTBI, meta-analysis was performed. The affected functional connectivity was categorized into five major brain functional domains: “Action,” “Perception,” “Cognition,” “Interoception,” and “Emotion.” We have observed that “Action” and “Cognition” are more involved in altered functional connectivity after mTBI, especially the interaction between “Action” and “Cognition” networks, which has been affected the most (Figure 4). Further investigation of the roles of DICCCOLs which were evaluated in greater detail using 53 subcategories reveals that the interactions between “Execution” (from the “Action” category) and “Attention” (from the “Cognition” category) and between “Execution” (from “Action” category), and “Working Memory” (from “Cognition” category) were affected the most (Figure 4).

Due to the nature of mTBI and the prevalence of diffuse axonal injury (DAI) pathology in TBI patients, the brain functional response is expected to be seen throughout the

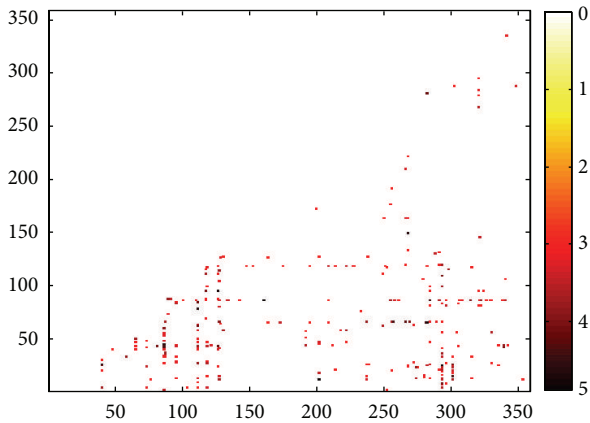


FIGURE 3:  $T$ -values from the longitudinal statistical analysis using a mixed design ANOVA and NBS on the 258 FC pairs which are significantly stronger in the patient group. Since the FC matrices are symmetric, only the lower half was used for the statistical analysis.

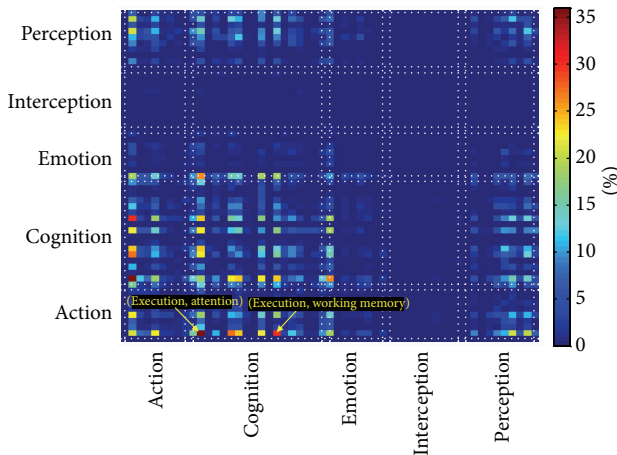


FIGURE 4: Categorization of altered functional connectivity in mTBI. The color-bar indicates percent change. The results show that the “Action” and “Cognition” networks have been disrupted the most. Further functional analysis using the 53 subcategories shows that interaction between “Execution” (from the “Action” category) and “Attention” (from the “Cognition” category) and between “Execution” (from the “Action” category) and “Working Memory” (from the “Cognition” category) has been affected the most (yellow arrow). This is consistent with published literature on Attention, Working Memory, and executive function deficits in mTBI patients.

brain rather than only in certain restricted regions (see Figure 5). One aim of this study was to discover possible existing patterns among the connectomic signatures after mTBI. For this purpose, we first categorized DICCCOLs into similar clusters based on their rsfMRI time series similarity using a multiview group-wise clustering approach. Using the multiview group-wise clustering approach on all data (a combination of two time points and two groups), we have identified eight functional connectivity clusters (Figure 6). The estimated clusters are similar to the result of our previous work obtained in young healthy subjects

[41]. After identifying the corresponding cluster for each DICCCOL, the connectomic signatures were categorized based on the DICCCOLs’ clustering information. Results demonstrated that cluster number 1, specifically the posterior cingulate cortex (PCC) portion of it, is the most involved cluster in functional connectivity alterations after mTBI (Figure 7). Interestingly, among all 258 connectomic signatures, 253 (98%) are involved in between-clusters interactions (Figure 7). Further investigation reveals two general patterns among the affected interactions: (I) an increase in functional connectivity between the PCC (from cluster number 1) and the association areas of the brain such as the associative visual cortex, supplementary motor cortex, and the somatosensory association cortex (from clusters numbers 4, 5, and 8), see Figures 8(a)–8(c); and (II) functional hyperconnectivity between the occipital lobe of the brain from cluster number 3 and the frontal lobe area from cluster number 8 (Figure 8(d)).

#### 4. Discussion

Our work demonstrates that (a) mTBI affects brain functional connectivity changes at a connectome scale, which is consistent with the published data on diffuse axonal injury pathology [10, 42]. The brain functional connectivity changes at a large scale after mTBI emphasize the necessity of applying connectome-scale study to have a better understanding of brain function and its network substrates of mTBI sequela; (b) there is functional hyperconnectivity across the brain, which can be interpreted as the brain’s attempts at large scale to compensate for injury, as has been observed in previous studies [20, 23]; (c) the most affected neurocognitive domains are executive function, attention, and working memory, in line with reported neurocognitive profiles of mTBI patients [43, 44], of which attention and working memory domains are also shown to be particularly susceptible to plasticity in noninjured brains [15, 22, 45, 46]; and (d) the cluster analysis of brain functional connectivity alterations demonstrates two general compensatory patterns: (1) hyperconnectivity between the PCC and the association areas of the brain and (2) increase in frontal-occipital functional connectivity. This study represents a systematic investigation of large-scale brain functional connectivity at resting state in response to mTBI. The results are well consistent with current findings and assumptions of mTBI and validate our hypothesis regarding brain compensation after injury through increasing functional connectivity at a connectome scale, as discussed below.

*Large-Scale Approaches.* Assessment of large-scale brain connectivity is required to properly investigate the brain connectivity alterations after mTBI. Alteration in one connection can directly or indirectly alter other brain connections [7]. The brain is a complex hyperconnected nexus, and any alteration in a brain connection due to mTBI causes a domino effect, which affects other structural or functional connections of the brain. In this situation, the outcome of the brain after injury is not limited to the location and the origin of the injury, and changes in brain functional connectivity are not limited to certain local regions near the site of injury

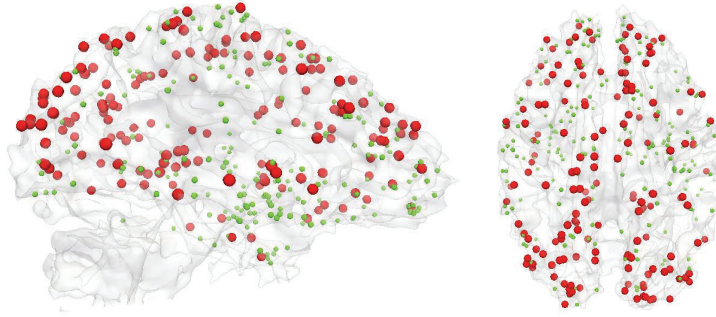


FIGURE 5: Visualization of location of DICCCOLs involved in affected functional connectivity signatures (red sphere) and the remaining DICCCOLs (green sphere) on cortical surface.

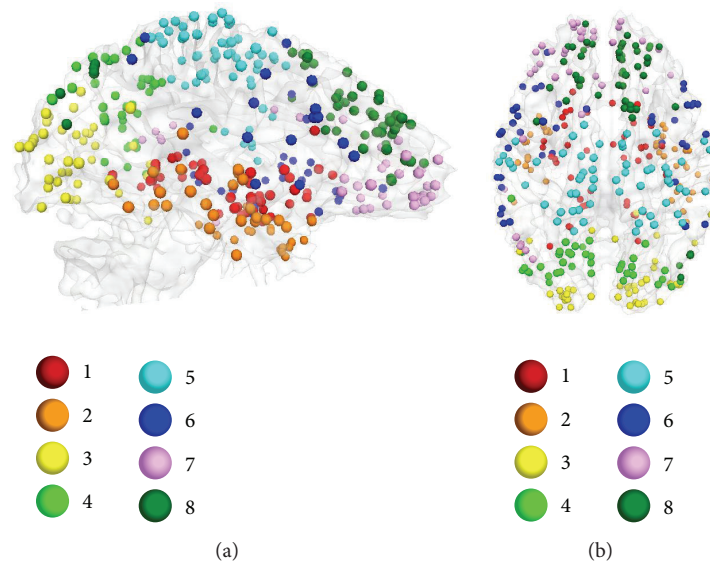


FIGURE 6: Eight functional connectivity clusters as results of using a multiview group-wise clustering. Eight functional clusters were identified in different colored bubbles.

and could be distributed across the brain [11, 13, 47–51], as we already know structural changes like diffuse axonal injury (DAI) to be a common result of mTBI [10, 42, 52]. At the same time, large-scale brain connectivity analyses such as connectome-scale approaches are more sensitive to alterations that are less apparent in gross structure (i.e., white matter integrity and DAI), because large-scale approaches consider each region's integration into the global unit rather than as an independent entity. In light of this, large-scale approaches can provide a better understanding of brain alterations and uncover the role of brain alterations at the macrolevel even in the absence of obvious structural damages [9, 14]. However, to date, most of the brain functional imaging investigations focus on a single or a limited number of brain regions or networks instead of assessing the brain networks at a connectome scale [11, 47, 48, 51], and there is still a lack of investigation into large-scale brain functional connectivity changes after mTBI. Our work supported our hypothesis that mTBI does induce large-scale brain network changes. This is well consistent with the published literature about DAI

pathology, which reports multifocal lesions across the brain. It also offers new insights from in vivo imaging perspective.

*Functional Hyperconnectivity as Compensation.* It has been reported that most mTBI patients suffer reversible brain injury or transient pathophysiological disturbances. After injury, the brain initiates its natural response by cellular repair mechanisms, which leads to recovery, and the brain's compensation through plasticity and modification of brain functional connectivity is a secondary response. Lastly, the brain could experience anatomical plasticity to compensate for the effect of injury [53, 54]. Several studies have shown increases in functional connectivity or hyperconnectivity after different severities of TBI and physical disruption as common brain response [23, 55–57]. Hyperconnectivity was observed mostly in highly connected regions of the brain [55], such as brain regions involved in executive functions and working memory, and central hubs of main brain networks such as the PCC and medial frontal cortex in the default mode network; the dorsolateral prefrontal cortex and parietal cortex in the executive control network; and/or anterior

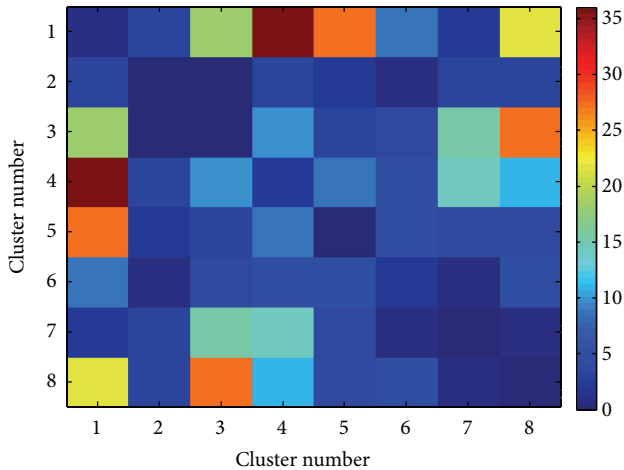


FIGURE 7: Categorizing the disturbed functional connectivity, which has been obtained using longitudinal statistical analysis by a mixed design ANOVA and NBS, into eight functional connectivity clusters that have been obtained using the multiview group-wise clustering method. Results show that some clusters (especially cluster number 1) are more involved in functional connectivity alteration after mTBI. The color-bar indicates number of involved connectomic signatures.

insula in the salience network [53, 55, 58, 59]. Our analysis of whole-brain large-scale networks demonstrates an overall increased functional connectivity in mTBI patients as a brain compensatory response to mTBI. This is consistent with the published literature on separate brain networks [11, 47, 48, 51]. It is of note that our results do not indicate that there was no hypoconnectivity among mTBI group. Our analysis reveals hypoconnectivity in several connections among mTBI patients. However, none of them were detected by the NBS analysis, which only detects disrupted functional connectivity pairs at the network level and does not detect changes if a pair is isolated or not well interconnected with other disrupted pairs in a network. In our data, hypoconnectivity pairs seem to not be well connected enough to survive the NBS analysis.

**Affected Neurocognitive Domains.** After mTBI, the constellation of clinical and neurocognitive symptoms significantly affects mTBI patients' quality of life. The detection of neural network substrates of these neurocognitive presentations may help attending physicians order a proper neurorehabilitation program for the patients. Symptoms in several neurocognitive domains have been widely reported in mTBI patients, including attention [56, 60], memory [23, 53, 61–68], processing speed [56], and execution [53, 69]. Among them, attention [56, 60], working memory [23, 56, 61–66], and execution [53, 69] are the most widely reported. Executive function deficits have also been reported in chronic mTBI patients and predicted by DTI data [70]. We hypothesized that the brain functional connectivity alterations should be involved in similar functional and cognitive domains. Categorizing the connectomic signatures using meta-analysis intriguingly validated our hypothesis. The results demonstrate that, among functional and cognitive domains, the

interaction between “execution and attention” and “execution and working memory” has been affected the most, which is consistent with the reported patients' symptoms in these neurocognitive domains. Our results further show that the DICCCOLs involved in “action” and “cognition” domains have been involved in brain functional connectivity alterations. This includes the intranetwork connectivity (the connectivity of the DICCCOLs within a cognitive domain) or between-network connectivity (the connectivity between “action” and “cognition” domains). Our study provides the foundation for understanding the changes in functional domains occurring after mTBI, which are similar to changes seen in moderate and severe TBI in adults [56].

**Brain Compensatory Patterns.** It has been well reported that the frontal, temporal, and occipital lobes are susceptible to focal contusions due to the direct impact of brain soft tissue onto the rigid inner table of the frontal, occipital, and temporal bones [10, 42]. At the same time, several TBI studies show alterations in functional connectivity of highly connected regions of the brain, specifically the PCC, as a central hub of the brain [11–13, 47, 71]. The multiview group-wise cluster analysis was used to identify the prevalent compensatory pattern of the brain functional connectivity. The results illustrate brain functional connectivity alteration in the expected regions. The PCC demonstrates an increase in functional connectivity with different brain regions including Brodmann area 8 (BA8) of the frontal cortex, the supplementary motor area (BA6), the somatosensory association cortex (BA7), the dorsolateral prefrontal cortex (BA9), the associative visual cortex (BA19), and the anterior cingulate cortex (BA32). Moreover, functional connectivity between the frontal and occipital lobes as two susceptible regions was observed.

**Limitation and Future Work.** One limitation of this study is the small number of subjects in comparison with the great number of networks and connectivity features, which easily makes the statistical analysis underpowered. A larger sample size and acquiring data at the chronic stage are required to increase the power of statistical analysis and the chance of finding a significant difference. Though we used the NBS approach, a relatively larger number of subjects are indispensable for future investigation to draw a more solid conclusion. Since there is no ground truth of the connectome-scale network alterations, another independent dataset will be necessary in future, as a reproducibility study to cross-validate the findings in the current study.

Another issue is the recovery effect after mTBI. It is expected to see FC recovery in mTBI patients over time. Therefore, assuming similar FC values for a healthy subject and changes in FC for mTBI patient over time, the interaction effect is highly expected. However, our  $2 \times 2$  design ANOVA does not show statistical significant difference between the two time points of patient group. Although we did not observe a *statistically significant* interaction effect, our analysis shows a trend of recovery in FC of mTBI. Overall functional connectivity of mTBI patients shows a slow trend of approaching the functional connectivity patterns of the

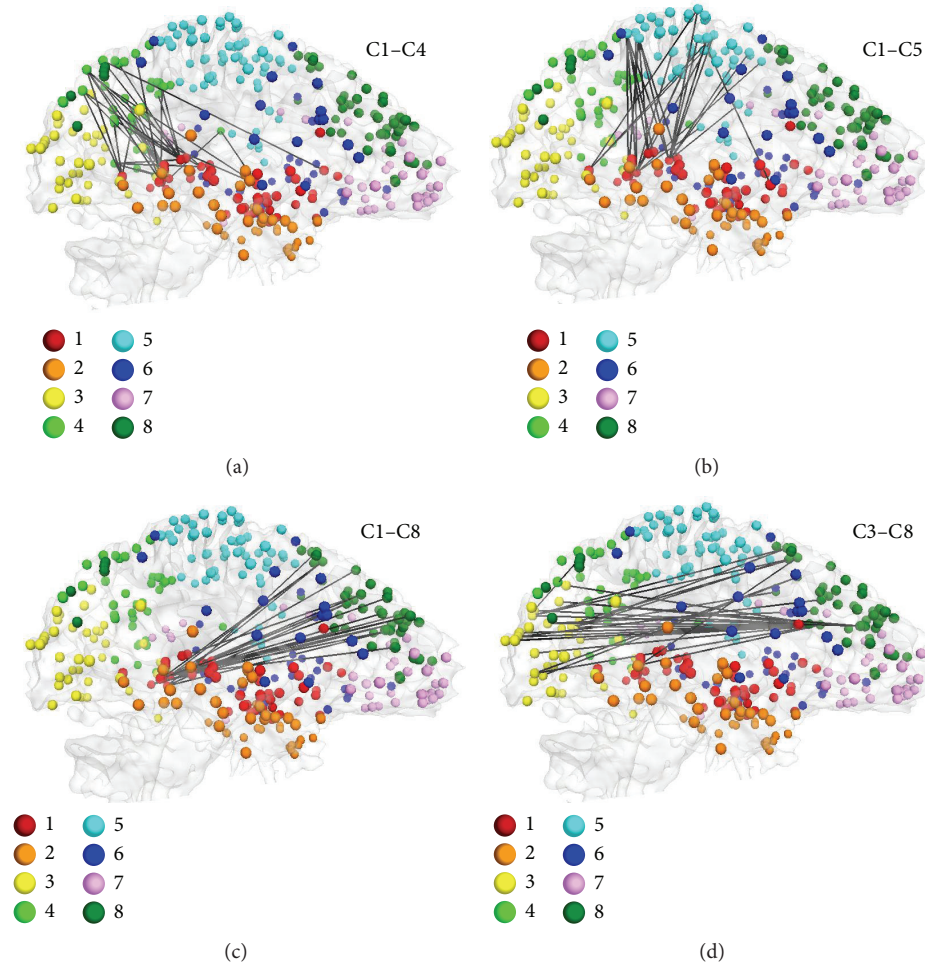


FIGURE 8: Categorization of affected functional connectivity using the multiview cluster-wise cluster method. (a)–(c) show the connectomic signatures involved in the interaction between cluster number 1 (C1) and clusters numbers 4 (C4), 5 (C5), and 8 (C8), respectively. These interactions represented the important role of the PCC as the central hub of the brain and its interactions with association brain areas as compensatory effects after brain injury. (d) reveals the interaction between the occipital lobe, cluster number 3 (C3), and the frontal lobe, cluster number 8 (C8).

healthy subjects over time. Increasing the number of time points would significantly improve a repeated measure data analysis method; thus another data acquisition at the chronic stage is required to evaluate it. It is possible to observe a statistically significant interaction effect if the time gap between the acquisitions was more than 4–6 weeks, allowing for more time to recover and therefore a larger effect size which statistical analysis might have been able to capture. For instance, Nakamura et al. [23] revealed that the overall functional connectivity strength is higher at three months after TBI but that functional connectivity decreases and approaches that of the healthy subjects sample after six months after injury. Moreover, using a larger sample can improve the power of statistical analysis and the chance of finding a significant difference. Furthermore, to apply the current work to clinical management of mTBI patients, the predictive value of the current imaging-based network analysis for mTBI patients' functional and neurocognitive symptoms over long-term recovery is yet to be determined.

This could be done by correlating the network-based findings with the patients' chronic neurocognitive and functional assessment, which should also be performed in longitudinal framework.

## 5. Conclusion

In summary, our prospective longitudinal study of mTBI patients at the acute and subacute stages demonstrates functional hyperconnectivity of the brain at a connectome scale. The most affected neurocognitive domains are executive function, attention, and working memory, which is in line with reported neurocognitive profiles of mTBI patients. Furthermore, despite the functional connectivity alterations distributed throughout the whole brain, the cluster analysis reveals two general functional connectivity compensation patterns among mTBI patients, between the PCC and the association areas of the brain and between the occipital and the frontal lobes of the brain.

## Conflict of Interests

The authors declare that there is no conflict of interests regarding the publication of this paper.

## Acknowledgments

This study is supported by the Department of Defense (Award no. W81XWH-11-1-0493) and International Society for Magnetic Resonance in Medicine (ISMRM) Seed Grant Award. The first author (Armin Iraj) would also like to sincerely acknowledge Drs. Anthony and Joyce Danielski Kales Endowed Scholars Award which significantly helped to accomplish this work.

## References

- [1] T. Kay, "Neuropsychological treatment of mild traumatic brain injury," *Journal of Head Trauma Rehabilitation*, vol. 8, no. 3, pp. 74–85, 1993.
- [2] M. E. Shenton, H. M. Hamoda, J. S. Schneiderman et al., "A review of magnetic resonance imaging and diffusion tensor imaging findings in mild traumatic brain injury," *Brain Imaging and Behavior*, vol. 6, no. 2, pp. 137–192, 2012.
- [3] J. J. Bruns Jr. and A. S. Jagoda, "Mild traumatic brain injury," *Mount Sinai Journal of Medicine*, vol. 76, no. 2, pp. 129–137, 2009.
- [4] CDC, *Report to Congress on Mild Traumatic Brain Injury in the United States: Steps to Prevent a Serious Public Health Problem*, Centers for Disease Control and Prevention, National Center for Injury Prevention and Control, Atlanta, Ga, USA, 2003.
- [5] J. J. Bazarian, J. McClung, M. N. Shah, Y. T. Cheng, W. Flesher, and J. Kraus, "Mild traumatic brain injury in the United States, 1998–2000," *Brain Injury*, vol. 19, no. 2, pp. 85–91, 2005.
- [6] R. Ruff, "Two decades of advances in understanding of mild traumatic brain injury," *The Journal of Head Trauma Rehabilitation*, vol. 20, no. 1, pp. 5–18, 2005.
- [7] C. R. Gillebert and D. Mantini, "Functional connectivity in the normal and injured brain," *The Neuroscientist*, vol. 19, no. 5, pp. 509–522, 2013.
- [8] C. Kelly and F. X. Castellanos, "Strengthening connections: functional connectivity and brain plasticity," *Neuropsychology Review*, vol. 24, no. 1, pp. 63–76, 2014.
- [9] A. R. Carter, G. L. Shulman, and M. Corbetta, "Why use a connectivity-based approach to study stroke and recovery of function?" *NeuroImage*, vol. 62, no. 4, pp. 2271–2280, 2012.
- [10] Z. Kou and P. J. VandeVord, "Traumatic white matter injury and glial activation: from basic science to clinics," *Glia*, vol. 62, no. 11, pp. 1831–1855, 2014.
- [11] Z. Kou and A. Iraj, "Imaging brain plasticity after trauma," *Neural Regeneration Research*, vol. 9, no. 7, pp. 693–700, 2014.
- [12] A. R. Mayer, J. M. Ling, E. A. Allen, S. D. Klimaj, R. A. Yeo, and F. M. Hanlon, "Static and dynamic intrinsic connectivity following mild traumatic brain injury," *Journal of Neurotrauma*, vol. 32, no. 14, pp. 1046–1055, 2015.
- [13] A. R. Mayer, M. V. Mannell, J. Ling, C. Gasparovic, and R. A. Yeo, "Functional connectivity in mild traumatic brain injury," *Human Brain Mapping*, vol. 32, no. 11, pp. 1825–1835, 2011.
- [14] A. R. Carter, S. V. Astafiev, C. E. Lang et al., "Resting interhemispheric functional magnetic resonance imaging connectivity predicts performance after stroke," *Annals of Neurology*, vol. 67, no. 3, pp. 365–375, 2010.
- [15] B. Guerra-Carrillo, A. P. MacKey, and S. A. Bunge, "Resting-state fMRI: a window into human brain plasticity," *The Neuroscientist*, vol. 20, no. 5, pp. 522–533, 2014.
- [16] C. Y. Wan and G. Schlaug, "Music making as a tool for promoting brain plasticity across the life span," *The Neuroscientist*, vol. 16, no. 5, pp. 566–577, 2010.
- [17] H. U. Voss and N. D. Schiff, "MRI of neuronal network structure, function, and plasticity," *Progress in Brain Research*, vol. 175, pp. 483–496, 2009.
- [18] D. O. Hebb, *The Organization of Behavior: A Neuropsychological Theory*, Psychology Press, 2005.
- [19] K. J. Friston, C. D. Frith, P. F. Liddle, and R. S. J. Frackowiak, "Functional connectivity: the principal-component analysis of large (PET) data sets," *Journal of Cerebral Blood Flow and Metabolism*, vol. 13, pp. 5–14, 1993.
- [20] I. Y. Zhou, Y.-X. Liang, R. W. Chan et al., "Brain resting-state functional MRI connectivity: morphological foundation and plasticity," *NeuroImage*, vol. 84, pp. 1–10, 2014.
- [21] M. Taubert, G. Lohmann, D. S. Margulies, A. Villringer, and P. Ragert, "Long-term effects of motor training on resting-state networks and underlying brain structure," *NeuroImage*, vol. 57, no. 4, pp. 1492–1498, 2011.
- [22] A. P. Mackey, A. T. M. Singley, and S. A. Bunge, "Intensive reasoning training alters patterns of brain connectivity at rest," *The Journal of Neuroscience*, vol. 33, no. 11, pp. 4796–4803, 2013.
- [23] T. Nakamura, F. G. Hillary, and B. B. Biswal, "Resting network plasticity following brain injury," *PLoS ONE*, vol. 4, no. 12, Article ID e8220, 2009.
- [24] M. Merzenich, M. Nahum, and T. van Vleet, *Changing Brains: Applying Brain Plasticity to Advance and Recover Human Ability*, Elsevier, 2013.
- [25] R. L. Buckner and J. L. Vincent, "Unrest at rest: default activity and spontaneous network correlations," *NeuroImage*, vol. 37, no. 4, pp. 1091–1096, 2007.
- [26] D. Zhu, K. Li, L. Guo et al., "DICCCOL: dense individualized and common connectivity-based cortical landmarks," *Cerebral Cortex*, vol. 23, no. 4, pp. 786–800, 2013.
- [27] R. E. Passingham, K. E. Stephan, and R. Kötter, "The anatomical basis of functional localization in the cortex," *Nature Reviews Neuroscience*, vol. 3, no. 8, pp. 606–616, 2002.
- [28] D. Zhu, K. Li, D. P. Terry et al., "Connectome-scale assessments of structural and functional connectivity in MCI," *Human Brain Mapping*, vol. 35, no. 7, pp. 2911–2923, 2014.
- [29] C. J. Honey, O. Sporns, L. Cammoun et al., "Predicting human resting-state functional connectivity from structural connectivity," *Proceedings of the National Academy of Sciences of the United States of America*, vol. 106, no. 6, pp. 2035–2040, 2009.
- [30] K. Li, L. Guo, C. Faraco et al., "Individualized ROI optimization via maximization of group-wise consistency of structural and functional profiles," *Advances in Neural Information Processing Systems*, vol. 23, pp. 1369–1377, 2010.
- [31] A. Messé, D. Rudrauf, A. Giron, and G. Marrelec, "Predicting functional connectivity from structural connectivity via computational models using MRI: an extensive comparison study," *NeuroImage*, vol. 111, pp. 65–75, 2015.
- [32] Y. Yuan, X. Jiang, D. Zhu et al., "Meta-analysis of functional roles of DICCCOLs," *Neuroinformatics*, vol. 11, no. 1, pp. 47–63, 2013.
- [33] M. Jenkinson, C. F. Beckmann, T. E. J. Behrens, M. W. Woolrich, and S. M. Smith, "FSL," *NeuroImage*, vol. 62, no. 2, pp. 782–790, 2012.

- [34] J. Lv, X. Jiang, X. Li et al., "Holistic atlases of functional networks and interactions reveal reciprocal organizational architecture of cortical function," *IEEE Transactions on Biomedical Engineering*, vol. 62, no. 4, pp. 1120–1131, 2015.
- [35] A. Zalesky, A. Fornito, and E. T. Bullmore, "Network-based statistic: identifying differences in brain networks," *NeuroImage*, vol. 53, no. 4, pp. 1197–1207, 2010.
- [36] F. M. Krienen, B. T. T. Yeo, and R. L. Buckner, "Reconfigurable task-dependent functional coupling modes cluster around a core functional architecture," *Philosophical Transactions of the Royal Society B: Biological Sciences*, vol. 369, no. 1653, Article ID 20130526, 2014.
- [37] E. S. Finn, X. Shen, J. M. Holahan et al., "Disruption of functional networks in dyslexia: a whole-brain, data-driven analysis of connectivity," *Biological Psychiatry*, vol. 76, no. 5, pp. 397–404, 2014.
- [38] M. S. Korgaonkar, A. Fornito, L. M. Williams, and S. M. Grieve, "Abnormal structural networks characterize major depressive disorder: a connectome analysis," *Biological Psychiatry*, vol. 76, no. 7, pp. 567–574, 2014.
- [39] D. L. Harrington, M. Rubinov, S. Durgerian et al., "Network topology and functional connectivity disturbances precede the onset of Huntington's disease," *Brain*, vol. 138, no. 8, pp. 2332–2346, 2015.
- [40] A. R. Laird, S. B. Eickhoff, F. Kurth et al., "ALE meta-analysis workflows via the BrainMap database: progress towards a probabilistic functional brain atlas," *Frontiers in Neuroinformatics*, vol. 3, article 23, 2009.
- [41] H. Chen, K. Li, D. Zhu et al., "Inferring group-wise consistent multimodal brain networks via multi-view spectral clustering," *IEEE Transactions on Medical Imaging*, vol. 32, no. 9, pp. 1576–1586, 2013.
- [42] Z. Kou, Z. Wu, K. A. Tong et al., "The role of advanced MR imaging findings as biomarkers of traumatic brain injury," *The Journal of Head Trauma Rehabilitation*, vol. 25, no. 4, pp. 267–282, 2010.
- [43] R. S. Naunheim, D. Matero, and R. Fucetola, "Assessment of patients with mild concussion in the emergency department," *The Journal of Head Trauma Rehabilitation*, vol. 23, no. 2, pp. 116–122, 2008.
- [44] K. Bergman and E. Bay, "Mild traumatic brain injury/Concussion: a review for ED nurses," *Journal of Emergency Nursing*, vol. 36, no. 3, pp. 221–230, 2010.
- [45] A. P. Mackey, K. J. Whitaker, and S. A. Bunge, "Experience-dependent plasticity in white matter microstructure: reasoning training alters structural connectivity," *Frontiers in Neuroanatomy*, vol. 6, article 32, 2012.
- [46] B. S. McEwen and J. H. Morrison, "The brain on stress: vulnerability and plasticity of the prefrontal cortex over the life course," *Neuron*, vol. 79, no. 1, pp. 16–29, 2013.
- [47] M. C. Stevens, D. Lovejoy, J. Kim, H. Oakes, I. Kureshi, and S. T. Witt, "Multiple resting state network functional connectivity abnormalities in mild traumatic brain injury," *Brain Imaging and Behavior*, vol. 6, no. 2, pp. 293–318, 2012.
- [48] L. Tang, Y. Ge, D. K. Sodickson et al., "Thalamic resting-state functional networks: disruption in patients with mild traumatic brain injury," *Radiology*, vol. 260, no. 3, pp. 831–840, 2011.
- [49] S. N. Niogi and P. Mukherjee, "Diffusion tensor imaging of mild traumatic brain injury," *Journal of Head Trauma Rehabilitation*, vol. 25, no. 4, pp. 241–255, 2010.
- [50] A. Messé, S. Caplain, G. Paradot et al., "Diffusion tensor imaging and white matter lesions at the subacute stage in mild traumatic brain injury with persistent neurobehavioral impairment," *Human Brain Mapping*, vol. 32, no. 6, pp. 999–1011, 2011.
- [51] A. Iraj, R. R. Benson, R. D. Welch et al., "Resting state functional connectivity in mild traumatic brain injury at the acute stage: independent component and seed-based analyses," *Journal of Neurotrauma*, vol. 32, no. 14, pp. 1031–1045, 2015.
- [52] S. N. Niogi and P. Mukherjee, "Diffusion tensor imaging of mild traumatic brain injury," *The Journal of Head Trauma Rehabilitation*, vol. 25, no. 4, pp. 241–255, 2010.
- [53] A. K. Barbey, A. Belli, A. Logan, R. Rubin, M. Zamroziewicz, and J. T. Operskalski, "Network topology and dynamics in traumatic brain injury," *Current Opinion in Behavioral Sciences*, vol. 4, pp. 92–102, 2015.
- [54] T. Wieloch and K. Nikolich, "Mechanisms of neural plasticity following brain injury," *Current Opinion in Neurobiology*, vol. 16, no. 3, pp. 258–264, 2006.
- [55] F. G. Hillary, S. M. Rajtmajer, C. A. Roman et al., "The rich get richer: brain injury elicits hyperconnectivity in core subnetworks," *PLoS ONE*, vol. 9, Article ID e104021, 2014.
- [56] F. G. Hillary, J. D. Medaglia, K. Gates et al., "Examining working memory task acquisition in a disrupted neural network," *Brain*, vol. 134, no. 5, pp. 1555–1570, 2011.
- [57] A. S. Pandit, P. Expert, R. Lambiotte et al., "Traumatic brain injury impairs small-world topology," *Neurology*, vol. 80, no. 20, pp. 1826–1833, 2013.
- [58] V. Bonnelle, T. E. Ham, R. Leech et al., "Salience network integrity predicts default mode network function after traumatic brain injury," *Proceedings of the National Academy of Sciences of the United States of America*, vol. 109, no. 12, pp. 4690–4695, 2012.
- [59] D. J. Sharp, G. Scott, and R. Leech, "Network dysfunction after traumatic brain injury," *Nature Reviews Neurology*, vol. 10, no. 3, pp. 156–166, 2014.
- [60] M. Maruishi, M. Miyatani, T. Nakao, and H. Muranaka, "Compensatory cortical activation during performance of an attention task by patients with diffuse axonal injury: a functional magnetic resonance imaging study," *Journal of Neurology, Neurosurgery and Psychiatry*, vol. 78, no. 2, pp. 168–173, 2007.
- [61] C. Christodoulou, J. DeLuca, J. H. Ricker et al., "Functional magnetic resonance imaging of working memory impairment after traumatic brain injury," *Journal of Neurology Neurosurgery and Psychiatry*, vol. 71, no. 2, pp. 161–168, 2001.
- [62] M. R. Newsome, R. S. Scheibel, J. L. Steinberg et al., "Working memory brain activation following severe traumatic brain injury," *Cortex*, vol. 43, no. 1, pp. 95–111, 2007.
- [63] W. M. Perlstein, M. A. Cole, J. A. Demery et al., "Parametric manipulation of working memory load in traumatic brain injury: behavioral and neural correlates," *Journal of the International Neuropsychological Society*, vol. 10, no. 5, pp. 724–741, 2004.
- [64] R. Sánchez-Carrión, P. V. Gómez, C. Junqué et al., "Frontal hypoactivation on functional magnetic resonance imaging in working memory after severe diffuse traumatic brain injury," *Journal of Neurotrauma*, vol. 25, no. 5, pp. 479–494, 2008.
- [65] R. S. Scheibel, M. R. Newsome, J. L. Steinberg et al., "Altered brain activation during cognitive control in patients with moderate to severe traumatic brain injury," *Neurorehabilitation and Neural Repair*, vol. 21, no. 1, pp. 36–45, 2007.

- [66] T. W. McAllister, L. A. Flashman, B. C. McDonald, and A. J. Saykin, "Mechanisms of working memory dysfunction after mild and moderate TBI: evidence from functional MRI and neurogenetics," *Journal of Neurotrauma*, vol. 23, no. 10, pp. 1450–1467, 2006.
- [67] B. Levine, R. Cabeza, A. R. McIntosh, S. E. Black, C. L. Grady, and D. T. Stuss, "Functional reorganisation of memory after traumatic brain injury: a study with  $H_2^{15}O$  positron emission tomography," *Journal of Neurology, Neurosurgery & Psychiatry*, vol. 73, no. 2, pp. 173–181, 2002.
- [68] J. H. Ricker, R.-A. Müller, R. D. Zafonte, K. M. Black, S. R. Millis, and H. Chugani, "Verbal recall and recognition following traumatic brain injury: a [O-15]-water positron emission tomography study," *Journal of Clinical and Experimental Neuropsychology*, vol. 23, no. 2, pp. 196–206, 2001.
- [69] G. R. Turner and B. Levine, "Augmented neural activity during executive control processing following diffuse axonal injury," *Neurology*, vol. 71, no. 11, pp. 812–818, 2008.
- [70] M. L. Lipton, E. Gulko, M. E. Zimmerman et al., "Diffusion-tensor imaging implicates prefrontal axonal injury in executive function impairment following very mild traumatic brain injury," *Radiology*, vol. 252, no. 3, pp. 816–824, 2009.
- [71] A. Iraj, E. Davoodi-Bojd, H. Soltanian-Zadeh, G. A. Hossein-Zadeh, and Q. Jiang, "Diffusion kurtosis imaging discriminates patients with white matter lesions from healthy subjects," in *Proceedings of the Annual International Conference of the IEEE Engineering in Medicine and Biology Society (EMBC '11)*, pp. 2796–2799, IEEE, Boston, Mass, USA, August-September 2011.

## Research Article

# Functional Reorganizations of Brain Network in Prelingually Deaf Adolescents

Wenjing Li,<sup>1,2,3</sup> Jianhong Li,<sup>4</sup> Jieqiong Wang,<sup>2</sup> Peng Zhou,<sup>2</sup> Zhenchang Wang,<sup>5</sup>  
Junfang Xian,<sup>4</sup> and Huiguang He<sup>2</sup>

<sup>1</sup>College of Electronic Information and Control Engineering, Beijing University of Technology, Beijing 100124, China

<sup>2</sup>State Key Laboratory of Management and Control for Complex Systems, Institute of Automation, Chinese Academy of Sciences, Beijing 100190, China

<sup>3</sup>Beijing Key Laboratory of Computational Intelligence and Intelligent System, Beijing 100124, China

<sup>4</sup>Department of Radiology, Beijing Tongren Hospital, Capital Medical University, Beijing 100730, China

<sup>5</sup>Department of Radiology, Beijing Friendship Hospital, Capital Medical University, Beijing 100050, China

Correspondence should be addressed to Junfang Xian; [cjr.xianjunfang@vip.163.com](mailto:cjr.xianjunfang@vip.163.com) and Huiguang He; [huiguang.he@ia.ac.cn](mailto:huiguang.he@ia.ac.cn)

Received 5 June 2015; Accepted 22 July 2015

Academic Editor: Feng Shi

Copyright © 2016 Wenjing Li et al. This is an open access article distributed under the Creative Commons Attribution License, which permits unrestricted use, distribution, and reproduction in any medium, provided the original work is properly cited.

Previous neuroimaging studies suggested structural or functional brain reorganizations occurred in prelingually deaf subjects. However, little is known about the reorganizations of brain network architectures in prelingually deaf adolescents. The present study aims to investigate alterations of whole-brain functional network using resting-state fMRI and graph theory analysis. We recruited 16 prelingually deaf adolescents (10~18 years) and 16 normal controls matched in age and gender. Brain networks were constructed from mean time courses of 90 regions. Widely distributed network was observed in deaf subjects, with increased connectivity between the limbic system and regions involved in visual and language processing, suggesting reinforcement of the processing for the visual and verbal information in deaf adolescents. Decreased connectivity was detected between the visual regions and language regions possibly due to inferior reading or speaking skills in deaf subjects. Using graph theory analysis, we demonstrated small-worldness property did not change in prelingually deaf adolescents relative to normal controls. However, compared with healthy adolescents, eight regions involved in visual, language, and auditory processing were identified as hubs only present in prelingually deaf adolescents. These findings revealed reorganization of brain functional networks occurred in prelingually deaf adolescents to adapt to deficient auditory input.

## 1. Introduction

Prelingual deafness is the hearing loss that occurs at birth or before the onset of speech. Due to the deprivation of auditory inputs, brain plasticity has been reported by numerous neuroimaging studies. “Cross-modal plasticity” has been suggested in deaf subjects, which is represented by the phenomenon that the auditory cortex can be activated when deaf subjects perform various tasks, such as speech [1, 2] and visual tasks [3, 4]. Many morphological studies did not find structural changes in the primary auditory cortex [5–8], indicating the atrophy of the auditory cortex due to hearing loss could be compensated by the use of this cortex for other stimuli. However, brain regions involved in visual

and speech processing have been found to change in deaf subjects [7, 8], indicating that the sensory systems for vision and speech might participate in the tasks which are supposed to activate the auditory system in healthy controls. Therefore, we speculated that the cooperative manner for different brain regions would be altered in prelingually deaf subjects when dealing with a complex task.

The human brain is a highly complex system with synchronized neural activity from different brain regions. The concept of “connectome” was first proposed by Sporns et al. in 2005 [9], which represents the human brain as an interconnected network. Functional brain network refers to a pattern of statistical dependencies between distinct brain regions. The network architecture identified by the analysis

of functional connectivity could be an effective pattern to present the cooperative manner for brain regions, and it reflects the potential anatomical connections between brain regions as well. To further quantitatively measure the brain network, network topological properties could be evaluated at both global and regional levels using graph theory, which becomes a promising tool for analyzing brain networks in recent years [10–21]. Small-worldness, a concept that originated from social network, quantifies the effectiveness of information transferring within networks and has been successfully used to characterize brain networks [14–16]. Besides, nodal topological parameters based on graph theory analysis are used to illustrate the properties for nodes which are defined as brain regions, identifying the role of specific regions in transferring information. It has been demonstrated that these measures of brain network are sensitive to aging [17, 18] as well as various neuropsychiatric diseases, such as schizophrenia [16, 19] and Alzheimer’s disease [20, 21]. Therefore, investigation of brain network properties provides a new insight into brain reorganization and is critical to understand the working mechanism of brains with hearing loss.

Recently, a few studies have emerged to investigate the structural or functional connectivity between brain regions in deaf subjects. Kim et al. [22] examined morphological brain network in deaf adults using tissue density on MRI and analyzed the network properties using graph theory and network filtration. They found altered morphological network in prelingually deaf adults compared to normal controls but not in postlingually deaf adults, concluding that auditory experience could affect the morphology of brain networks in deaf adults. Besides, Li et al. [23] employed resting-state fMRI to investigate the effect of deafness on the intra- and interregional synchronization of different parts of superior temporal sulcus and revealed that the intrinsic function of these different parts are distinctly impacted by deafness. However, these previous studies focused on alterations in grown adult brains of deaf subjects but not developing brain. Adolescence is an important transitional stage for brain development, in which brain’s structure and function are in developmental changes to accommodate to external environment. Therefore, adolescents with prelingual deafness are supposed to go through a different pattern of brain reorganization to adapt to the silent world relative to normal adolescents, which is supported by one of our previous studies [24] using structural MRI to investigate grey matter connectivity within and between auditory, language, and visual systems in deaf adolescents. To the best of our knowledge, the whole-brain functional network and its properties have not been investigated in prelingually deaf adolescents yet.

We hypothesized the architectures or properties of brain network would change in prelingually deaf adolescents. In the present study, we used resting-state fMRI and graph theory analysis to investigate alterations of whole-brain functional networks in prelingually deaf adolescents. Functional brain network was constructed based on mean time series extracted from 90 brain regions. Functional connectivity patterns were studied in deaf and control groups, respectively, and compared between two groups. The global network

TABLE 1: Biographical information of two groups.

	Normal controls	Deaf adolescents
Number	15	15
Male/female	8/7	8/7
Mean age (years)	14.81	14.32
Standard deviation (SD) age (years)	2.07	2.24
Age range (years)	10~18	10~18

property of small-worldness was evaluated in each group and group differences were investigated as well. Besides, nodal topological parameters were calculated and brain hubs were identified for deaf and control groups, respectively. Nodal properties were finally compared in all the hubs between prelingually deaf adolescents and normal controls.

## 2. Materials and Methods

**2.1. Subjects.** In this study, we recruited 16 prelingually deaf adolescents and 16 normal controls with matched age ( $p = 0.815$ ) and gender (Chi-Squared  $p = 1.0$ ), which were the same as the data used in our previous studies [7, 8, 24]. All prelingually deaf adolescents suffered from severe sensorineural hearing loss after the birth and had a mean pure tone audiometry average air conduction threshold greater than 90 dB of hearing loss for the better ear and no single frequency better than 45 dB of hearing loss between 500 and 4000 Hz. All deaf subjects wore hearing aids and learnt Chinese sign language. Furthermore, all subjects had neither history of central nervous system disease nor significant head trauma. All subjects underwent an identical resting-state fMRI paradigm. The data from one prelingually deaf adolescent and one normal control were discarded due to excessive head movement during scanning. Therefore, 15 deaf subjects (age  $14.32 \pm 2.24$  years, 10~18 years; 8 males) and 15 normal controls (age  $14.81 \pm 2.07$  years, 10~18 years; 8 males) remained, and these two groups were still matched in age ( $p = 0.769$ ) and gender (Chi-Squared  $p = 1.0$ ). Detailed biographical information of all subjects is shown in Table 1. This project was approved by the Committee at Beijing Tongren Hospital, and all subjects and their parents gave written informed consent before inclusion.

**2.2. Data Acquisition.** Resting-state fMRI data were collected from all subjects on a 3-Tesla MR imaging scanner (GE Medical System, Milwaukee, WI, USA) with an eight-channel phased-array head coil. To acquire resting-state fMRI data, all subjects lay on their backs and were instructed explicitly to keep their eyes closed and not to think of anything in particular. Foam padding was used to limit head motion and reduce scanner noises. The scanning parameters were as follows: repetition time (TR) = 2000 ms, echo time (TE) = 30 ms, field of view (FOV) =  $24 \times 24$  cm<sup>2</sup>, matrix size =  $64 \times 64$ , slice thickness = 5 mm, and flip angle = 90°, yielding 28 axial slices with in-plane resolution of  $3.75 \times 3.75$  cm<sup>2</sup>. The fMRI scanning lasted 400 s and 200 volumes were obtained for each subject.

Furthermore, high-resolution T1-weighted structural brain images were collected for structural reference using a 3D SPGR sequence (TR = 9 ms, TE = 3.5 ms, inversion time (TI) = 450 ms, FOV =  $24 \times 24 \text{ cm}^2$ , matrix size =  $256 \times 256$ , slice thickness = 1 mm, and flip angle =  $13^\circ$ , yielding 196 sagittal slices with in-plane resolution of  $0.9375 \times 0.9375 \text{ cm}^2$ ).

**2.3. Data Preprocessing.** The preprocessing steps were performed using the Statistical Parametric Mapping (SPM8, <http://www.fil.ion.ucl.ac.uk/spm>, Wellcome Department of Cognitive Neurology, London, UK, 2008) on a Matlab 7.9 platform (MathWorks, Natick, MA, USA). The first 10 volumes of the resting-state fMRI data were discarded because of the initial transient effects and the adaption of the subjects to the environment. The remaining 190 time points were corrected for within-scan acquisition time differences between slices and realigned to the first image for head movement correction, resulting in 3 translational and 3 rotational parameters. The subjects with excessive head movement (translation > 2 mm and rotation degree >  $3^\circ$ ) were thus excluded. Subsequently, the functional scans were spatially normalized to a standard space (Montreal Neurological Institute, MNI) using the normalization parameters from T1 image with high resolution to structural T1 template in MNI space and resampled to  $3 \times 3 \times 3 \text{ mm}^3$ . The images were then smoothed with a 6 mm full width at half maximum (FWHM) isotropic Gaussian kernel. After that, the preprocessed images were linearly drifted and passed through a band-pass filter (0.01–0.08 Hz) to remove the effects of low frequency drift and physiological high frequency respiratory and cardiac noise. We regressed out six parameters of head movement as well as mean signals of the whole brain, white matter, and cerebral spinal fluid.

**2.4. Network Construction.** The functional images were parcellated into 90 brain regions (45 regions for each hemisphere) based on Automated Anatomical Labelling (AAL) template (see Table 2). To construct the whole-brain network, time courses were first extracted from all voxels within each ROI and averaged. Then, Pearson’s correlation coefficient was calculated between pairs of regions throughout the whole brain, resulting in a  $90 \times 90$  correlation matrix. Larger correlation coefficients indicate more synchronized time courses between the corresponding pairs of regions, implying stronger functional connectivity between these two regions.

**2.5. Graph Theory Analysis.** Brain network properties were analyzed using graph theory based on the correlation matrix, in which 90 ROIs and their connections were considered as nodes and edges, respectively. The correlation matrix was binarized by a given threshold, resulting in a sparse matrix. We adjusted the threshold and obtained a series of connectivity matrices with different sparsities. Using graph theory analysis, we characterized the global topological properties of brain functional networks using the parameters of small-worldness ( $\sigma$ ), which was defined as [25]

$$\sigma = \frac{\gamma}{\lambda} = \frac{C_p^{\text{real}}/C_p^{\text{rand}}}{L_p^{\text{real}}/L_p^{\text{rand}}}, \quad (1)$$

TABLE 2: Regions of interest (ROI) defined in AAL template.

Region name	Abbr.	Labels	
		L	R
Precentral gyrus	PreCG	1	2
Superior frontal gyrus, dorsolateral	SFGdor	3	4
Superior frontal gyrus, orbital	SFGorb	5	6
Middle frontal gyrus	MFG	7	8
Middle frontal gyrus, orbital	MFGorb	9	10
Inferior frontal gyrus, opercular	IFGoper	11	12
Inferior frontal gyrus, triangular	IFGtri	13	14
Inferior frontal gyrus, orbital	IFGorb	15	16
Rolandic operculum	ROL	17	18
Supplementary motor area	SMA	19	20
Olfactory cortex	OLF	21	22
Superior frontal gyrus, medial	SFGmed	23	24
Superior frontal gyrus, medial orbital	SFGmorb	25	26
Gyrus rectus	REG	27	28
Insula	INS	29	30
Anterior cingulate gyrus	ACG	31	32
Median cingulate gyrus	MCG	33	34
Posterior cingulate gyrus	PCG	35	36
Hippocampus	HIP	37	38
Parahippocampal gyrus	PHIP	39	40
Amygdala	AMYG	41	42
Calcarine fissure	CAL	43	44
Cuneus	CUN	45	46
Lingual gyrus	LING	47	48
Superior occipital gyrus	SOG	49	50
Middle occipital gyrus	MOG	51	52
Inferior occipital gyrus	IOG	53	54
Fusiform gyrus	FG	55	56
Postcentral gyrus	PoCG	57	58
Superior parietal gyrus	SPG	59	60
Inferior parietal gyrus	IPG	61	62
Supramarginal gyrus	SMG	63	64
Angular gyrus	ANG	65	66
Precuneus	PCNU	67	68
Paracentral lobule	PCL	69	70
Caudate	CAU	71	72
Putamen	PUT	73	74
Pallidum	PAL	75	76
Thalamus	THA	77	78
Heschl gyrus	HES	79	80
Superior temporal gyrus	STG	81	82
Superior temporal gyrus, temporal pole	STGp	83	84
Middle temporal gyrus	MTG	85	86
Middle temporal gyrus, temporal pole	MTGp	87	88
Inferior temporal gyrus	ITG	89	90

where  $\gamma$  and  $\lambda$  are normalized clustering coefficient and normalized path length, respectively. The normalized clustering coefficient is the ratio of clustering coefficient of a real

network  $C_p^{\text{real}}$  to that of a random network  $C_p^{\text{rand}}$ , and the normalized path length is defined as the ratio of characteristic path length of a real network  $L_p^{\text{real}}$  to that of a random network  $L_p^{\text{rand}}$ .

Here, clustering coefficient  $C_p$  is a measure of the degree to which nodes in a network cluster together and is defined as

$$C_p = \frac{1}{n} \sum_{i=1}^n \frac{2E_i}{D_{\text{nod}}(i)(D_{\text{nod}}(i) - 1)}, \quad (2)$$

where  $D_{\text{nod}}(i)$  is the degree of the node  $i$ , which is defined in the following part of this section,  $E_i$  is the total number of edges connecting the node  $i$  with the nodes which are the nearest neighbors to the node  $i$ , and  $N$  is the number of nodes in the network.

Characteristic path length  $L_p$  is the average shortest path length between two nodes over all pairs of nodes and is defined as

$$L_p = \frac{\sum_i \sum_j L_{ij}}{n(n-1)}, \quad (3)$$

where  $n$  is the number of nodes in the network and  $L_{ij}$  is the shortest path length between nodes  $i$  and  $j$ .

A network is said to have the property of small-worldness if it satisfies  $\lambda \approx 1$  and  $\gamma \gg 1$  or  $\sigma = \gamma/\lambda \gg 1$ .

It has been demonstrated that the sparsity of 12% is close to an optimal threshold at which most informative network edges are retained and disconnections between nodes are rare [26, 27]. Therefore, we chose 12% as the sparsity threshold for analysis of nodal topological properties, including betweenness centrality, nodal degree, and nodal efficiency, which are defined as follows.

(1) *Betweenness Centrality*. Betweenness centrality  $C_b$  is a measure of the number of times that a node is along the shortest path between other two nodes, reflecting the importance of the individual node in the overall network structure. It is computed as follows:

$$C_b = \sum_{s \neq i \neq t \in N} \frac{\delta_{st}(i)}{\delta_{st}}, \quad (4)$$

where  $N$  is the set of all nodes in the network,  $\delta_{st}$  is the total number of shortest paths from node  $s$  to node  $t$ , and  $\delta_{st}(i)$  is the number of the paths that pass through the node  $i$ .

(2) *Nodal Degree*. Nodal degree of the node  $i$  ( $D_{\text{nod}}(i)$ ) in a network is the number of connections linking the node with all other nodes and is defined as

$$D_{\text{nod}}(i) = \sum_{j \in N} a_{ij}, \quad (5)$$

where  $N$  is the set of all nodes in the network and  $a_{ij}$  is the connection status between node  $i$  and node  $j$  ( $a_{ij} = 1$  when the connection exists, and  $a_{ij} = 0$  otherwise).

(3) *Nodal Efficiency*. Nodal efficiency of the node  $i$  ( $E_{\text{nod}}(i)$ ) is the mean of the inverse shortest path length from node  $i$  to all other nodes and is defined as

$$E_{\text{nod}}(i) = \frac{1}{n} \sum_{j \neq i} \frac{1}{L_{ij}}, \quad (6)$$

where  $n$  is the number of nodes in the network and  $L_{ij}$  is the shortest path length between nodes  $i$  and  $j$ .

## 2.6. Statistical Analysis

*2.6.1. Analysis of Whole-Brain Functional Connectivity*. When constructing whole-brain network using resting-state fMRI, the correlation matrix characterized the brain functional connectivity pattern for each subject. To identify significant connectivity pattern in each group, one-sample  $t$ -test was performed to find significantly positive correlation in deaf group and normal controls, respectively, indicating significant connections between pairs of regions throughout the whole brain. To compare differences of connectivity patterns between groups, Fisher's  $R$ -to- $Z$  transformation was first performed and then two-sample  $t$ -test was conducted on the correlation matrices between prelingually deaf adolescents and normal controls. These statistical results were corrected for multiple comparisons using partial Bonferroni correction which considers the correlation between the dependent variables. This correction method was implemented using the Simple Interactive Statistical Analysis Bonferroni tool (<http://www.quantitativeskills.com/sisa/calculations/bonfer.htm>), which optimally balanced Type-I and Type-II errors. When performing one-sample  $t$ -test, the mean correlation coefficient between all variables in the matrix was 0.2236 in control group and 0.2274 in deaf group, leading to an equivalent corrected  $p$  of  $7.94e - 5$  for control group and  $8.63e - 5$  for deaf group (number of tests =  $90 * 89/2 = 4005$ ), respectively. For analysis of group differences, the mean correlation coefficient between pairs of variables for all subjects was 0.1624, resulting in an equivalent corrected  $p$  of  $4.83e - 5$ .

*2.6.2. Analysis of Network Topological Properties*. To present the properties of brain functional network for each group, the property of small-worldness was analyzed at different sparsities (from 10% to 45%) for prelingually deaf adolescents and normal controls, respectively. Then, two-sample  $t$ -test was performed between two groups to figure out the group differences.

As described above, we chose 12% as the sparsity threshold for analysis of nodal topological properties. First, the mean betweenness centrality, mean nodal degree, and mean nodal efficiency were calculated for each node in deaf and normal groups, respectively. Then, we ranked them among all the nodes with the highest score (90) for the highest betweenness centrality, nodal degree, and nodal efficiency, respectively, and the scores for each measure were summed up for each node. The top 20% nodes (18 out of 90 nodes) with high scores were identified as hub nodes in each group. The three nodal topological parameters were then compared

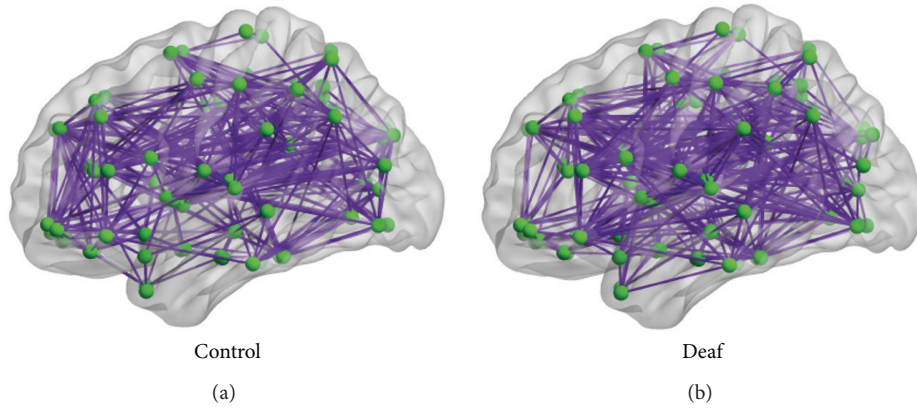


FIGURE 1: 3D views of functional connectivity patterns in normal controls (a) and prelingually deaf adolescents (b).

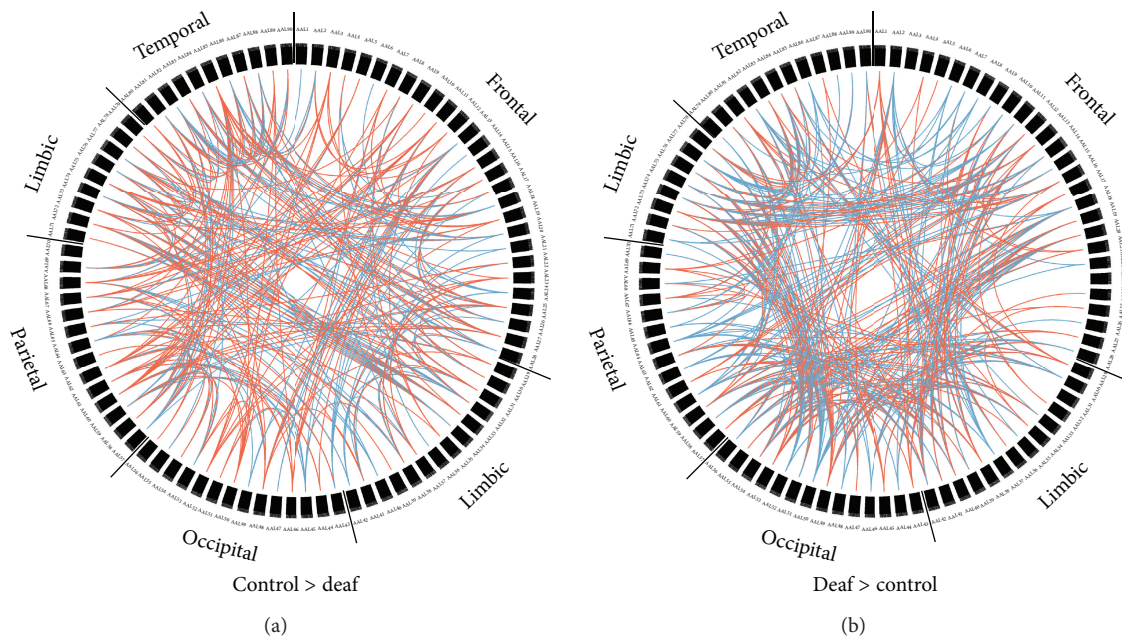


FIGURE 2: Group differences of brain functional connectivity between prelingually deaf adolescents and normal controls (uncorrected,  $p < 0.05$ ). (a) represents stronger functional connectivity in normal controls, while (b) shows stronger connectivity in prelingually deaf subjects. The red color indicates unilateral connections, and the blue color indicates bilateral connections.

between two groups for the hubs using two-sample  $t$ -test and the results were corrected for multiple comparisons using partial Bonferroni correction as well.

### 3. Results

**3.1. Whole-Brain Functional Connectivity Pattern.** Using one-sample  $t$ -test, significant functional connectivity was detected for both prelingually deaf adolescents and normal controls after partial Bonferroni correction (as shown in Figure 1). The 3D view in Figure 1 was visualized with the BrainNet Viewer (<http://www.nitrc.org/projects/bnv>) [28]. The figure shows functional connectivity was widely distributed throughout the whole brain in both groups.

To identify group differences of functional connectivity throughout the whole brain, connectivity matrices were

compared between two groups. Figure 2 shows the group differences before correction for multiple comparisons. From the figure, we can see that prelingually deaf adolescents show weaker connectivity between the regions within the temporal lobe, but stronger connectivity between regions in the occipital lobe and regions in the limbic system and temporal lobe. After partial Bonferroni correction, prelingually deaf adolescents showed significantly increased functional connectivity between the right superior gyrus (SPG) and right insula (INS) and between the left middle temporal gyrus (MTG) and right posterior cingulate gyrus (PCG) when compared with normal controls (see Figure 3). Besides, significantly decreased connectivity was found in deaf group between the right SPG and left middle frontal gyrus (orbital part, MFGorb) and between the right postcentral gyrus (PoCG) and left inferior frontal gyrus (opercular part, IFGoper).

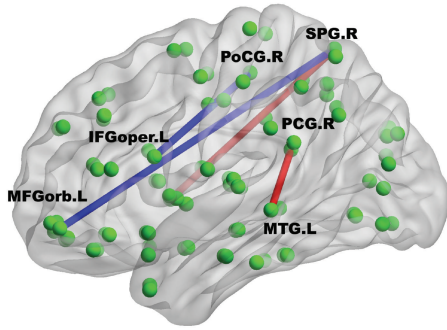


FIGURE 3: The 3D view for group differences after correction for multiple comparisons. While the warm color represents stronger connectivity in prelingually deaf adolescents compared to normal controls, the cold color suggests weaker connectivity.

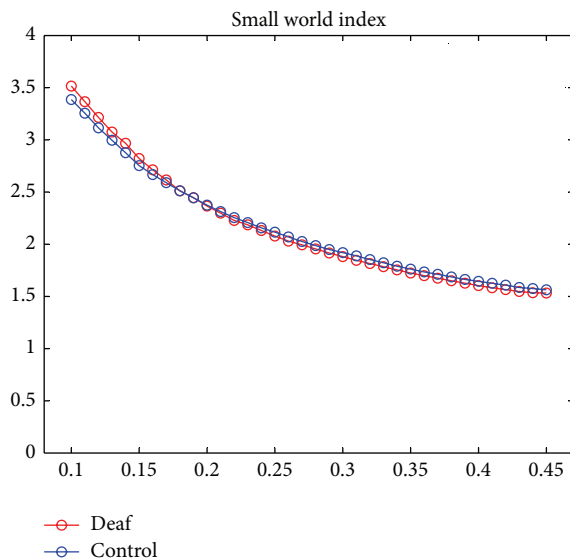


FIGURE 4: Small world index  $\sigma$  across sparsities from 10% to 45% with an interval of 1% in prelingually deaf adolescents (red color) and normal controls (blue color). Both of the two groups present the property of small-worldness since  $\sigma \gg 1$ .

**3.2. Properties of Brain Functional Network.** Small-worldness  $\sigma$  of brain functional network was measured at different sparsity (from 10% to 45% with an interval of 1%) in deaf group and control group, respectively. As shown in Figure 4, we found  $\sigma \gg 1$  across all the sparsities in both groups, indicating that the network has the property of small-worldness. We did not find significant differences of the small world index between prelingually deaf adolescents and normal controls.

Besides the global network property, the regional topological properties, including betweenness centrality, nodal degree, and nodal efficiency, were calculated in each ROI. Figure 5 shows the mean values for these regional properties in control and deaf groups.

**3.3. Hubs of Brain Network.** The hub in the network is supposed to have relatively high betweenness centrality,

nodal degree, and nodal efficiency. Based on the method described in Section 2, we identified 18 regions out of 90 ROIs as the hubs in each group at the sparsity of 12% since a network with this sparsity tends to retain the edges with most information and ensure disconnection is rare. As shown in Figure 6 and Table 3, ten brain regions, including the right rolandic operculum (ROL), left gyrus rectus (REG), bilateral calcarine fissure (CAL), right lingual gyrus (LING), left putamen (PUT), right pallidum (PAL), bilateral Heschl gyrus (HES), and right superior temporal gyrus (STG), were the hubs in both deaf and control groups. Besides, the middle and superior frontal gyri and cuneus (CUN) were hubs in deaf group but not in control group, while the right precentral gyrus (PreCG), bilateral hippocampus (HIPPP), and supramarginal gyrus (SMG) were hubs only in control group.

**3.4. Group Differences of Topological Parameters for Hubs.** There were a total of 26 brain regions identified as hubs either in deaf or in control groups. The nodal topological parameters, including betweenness centrality, nodal degree, and nodal efficiency, were compared for these nodes between prelingually deaf adolescents and normal controls. Significant differences did not survive after correction for multiple comparisons. However, we found trends for group differences, as listed in Table 3. Betweenness centrality is higher in the left superior frontal gyrus (orbital part, SFGorb) ( $p = 0.0204$ , not corrected) and is lower in the left ROL ( $p = 0.0480$ ), SMG ( $p = 0.0251$ ), and PAL ( $p = 0.0221$ ) in deaf group relative to control group. Besides, prelingually deaf adolescents have higher nodal degree in the left middle frontal gyrus (orbital part, MFGorb) ( $p = 0.0484$ ) and left superior frontal gyrus (medial part, SFGmed) ( $p = 0.0302$ ) and lower nodal efficiency in the left ROL ( $p = 0.0367$ ), left hippocampus ( $p = 0.0442$ ), and left pallidum ( $p = 0.0015$ ).

## 4. Discussions

The present study employed resting-state fMRI and graph theory analysis to investigate changes of brain functional network in prelingually deaf adolescents. Functional connectivity was widely distributed in both deaf and control groups, and significant differences were found for connections between the right SPG and right insula, the left MTG and right PCG, the right SPG and left MFGorb, and the right PoCG and left IFGoper. The whole-brain network has the property of small-worldness in both prelingually deaf adolescents and normal controls. Ten regions were identified as the hubs in both groups. While the middle and superior frontal gyri and CUN were the hubs that emerged only in deaf group, the right PreCG, bilateral HIPPP, and SMG were hubs only in control group. These findings provide new evidence for brain reorganization in prelingually deaf adolescents and could help to understand the working mechanism in the period of brain development after hearing loss.

In prelingually deaf adolescents, functional connectivity was widely distributed as observed in normal controls but differed in the connectivity pattern. Significantly increased

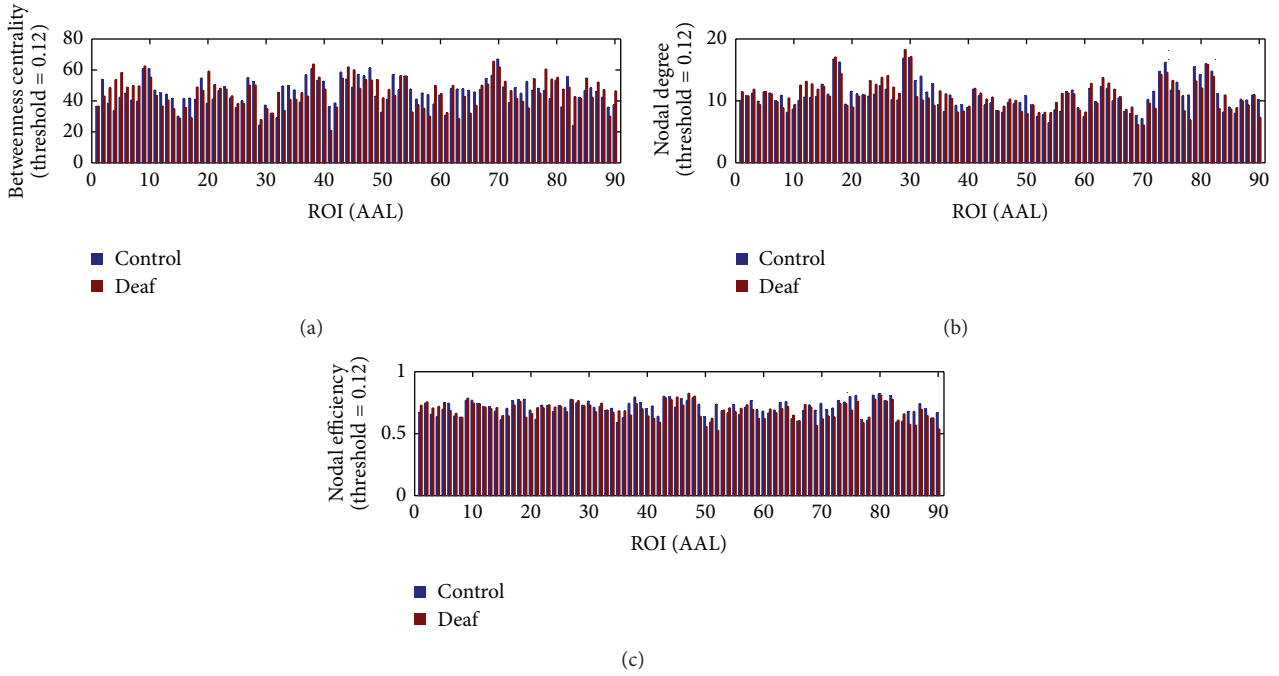


FIGURE 5: Bar plots for the average value for regional topological properties of 90 ROIs, including betweenness centrality (a), nodal degree (b), and nodal efficiency (c), in control and deaf groups. The blue color indicates the control group, and the red color represents the deaf group.

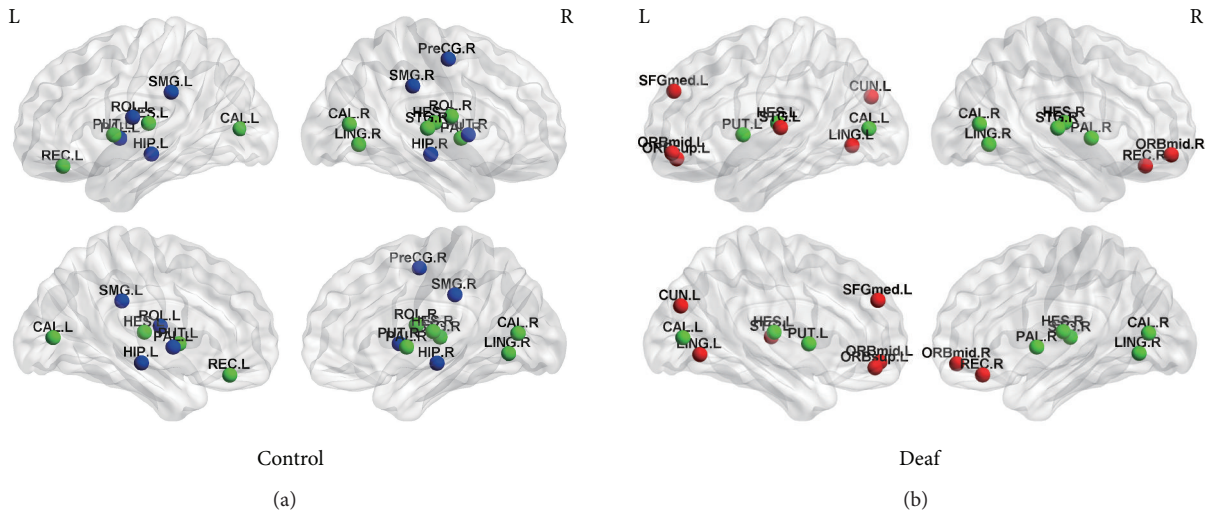


FIGURE 6: Hubs for brain functional networks in control (a) and deaf (b) groups. The hubs identified in both groups are shown in green color. While the hubs for the control group only are present with blue color, the hubs for the deaf group only are shown in red color.

connectivity was detected between the right SPG and right insula and between the left MTG and right PCG. The insula and PCG are in limbic system, which are thought to play an important role in recruiting relevant brain regions for sensory information processing [29]. The SPG is supposed to receive considerable visual input and is involved in visual-spatial relations [30]. Besides, the MTG has been reported to be one of the critical nodes in the brain’s language network, which can access word meaning while reading [31]. Therefore,

our findings of increased connectivity between these regions suggest that the limbic system in prelingually deaf adolescents could reinforce the processing of the visual and verbal information due to the deprivation of auditory sensory processing. Additionally, we found decreased functional connectivity between the right SPG and left MFGorb and between the right PoCG and left IFGoper. Evidence suggests that the left MFG is the specific brain region for Chinese reading [32], and the left IFG is extremely important for language

TABLE 3: Group differences of nodal topological parameters in hubs (not corrected).

Brain region	Hubs		BC		ND		NE	
	Deaf	Control	D > C	D < C	D > C	D < C	D > C	D < C
PreCG.R	nonhub	hub	ns	ns	ns	ns	ns	Ns
SFGorb.L	hub	nonhub	0.0204	ns	ns	ns	ns	Ns
MFGorb.L	hub	nonhub	ns	ns	0.0484	ns	ns	Ns
MFGorb.R	hub	nonhub	ns	ns	ns	ns	ns	Ns
ROL.L	nonhub	hub	ns	0.0480	ns	ns	ns	0.0367
ROL.R	hub	hub	ns	ns	ns	ns	ns	Ns
SFGmed.L	hub	nonhub	ns	ns	0.0302	ns	ns	Ns
REG.L	hub	hub	ns	ns	ns	ns	ns	Ns
REG.R	hub	nonhub	ns	ns	ns	ns	ns	Ns
HIPL	nonhub	hub	ns	ns	ns	ns	ns	0.0442
HIPR	nonhub	hub	ns	ns	ns	ns	ns	Ns
CALL	hub	hub	ns	ns	ns	ns	ns	Ns
CALR	hub	hub	ns	ns	ns	ns	ns	Ns
LING.L	hub	nonhub	ns	ns	ns	ns	ns	Ns
LING.R	hub	hub	ns	ns	ns	ns	ns	Ns
SMG.L	nonhub	hub	ns	0.0251	ns	ns	ns	Ns
SMG.R	nonhub	hub	ns	ns	ns	ns	ns	Ns
CUN.L	hub	nonhub	ns	ns	ns	ns	ns	Ns
PUT.L	hub	hub	ns	ns	ns	ns	ns	Ns
PUT.R	nonhub	hub	ns	ns	ns	ns	ns	Ns
PAL.L	nonhub	hub	ns	0.0221	ns	ns	ns	0.0015
PAL.R	hub	hub	ns	ns	ns	ns	ns	Ns
HES.L	hub	hub	ns	ns	ns	ns	ns	Ns
HES.R	hub	hub	ns	ns	ns	ns	ns	Ns
STG.L	hub	nonhub	ns	ns	ns	Ns	ns	Ns
STG.R	hub	hub	ns	ns	ns	Ns	ns	Ns

D > C: deaf > control; D < C: deaf < control; ns: not significant.

comprehension and production [33]. The decreased connectivity might be caused by the inferior skills of reading or speaking observed in most of the deaf subjects [34, 35].

Although it is not significant, we found a trend of significance for group differences in functional connectivity pattern. Connectivity between the regions within the temporal lobe was found to be weaker in prelingually deaf adolescents, indicating that the auditory cortex are less activated to auditory stimuli. In contrast, stronger connectivity was observed between regions in the occipital lobe and regions in the temporal lobe, which were identified as primary visual and auditory cortices, respectively. This result is consistent with one of our findings in the previous study [23], which detected significantly stronger structural connections between visual and auditory systems in prelingually deaf adolescents.

Using graph theory analysis, whole-brain network holds the property of small-worldness in both prelingually deaf adolescents and normal controls. The small world index was almost the same across all the sparsities from 10% to 45% (with an interval of 1%) between the two groups (see Figure 3). This result suggests that the effectiveness of information transferring of the brain network was not affected even without auditory inputs in prelingually deaf adolescents.

In the brain network, hubs are regions playing an important role in facilitating communication among parallel, distributed brain networks [36]. Eighteen hubs were identified in each group. In control group, the hubs included the right PreCG, bilateral ROL, left REG, bilateral HIPR, bilateral CAL, right LING, bilateral PUT, bilateral PAL, bilateral HES, and right STG. Compared with healthy adolescents, middle and superior frontal gyri, left LING, left CUN, left STG, and right REG were hubs only observed in prelingually deaf adolescents. Evidences show that the STG is the primary auditory cortex and is involved in phonological processing for speech perception and production as well [37, 38]. Although not activated by auditory stimuli, auditory regions could be activated by other stimuli [1–4] as stated in Section 1. Therefore, auditory regions might become a brain hub connecting with other brain regions. In the hubs of deaf subjects, the LING and CUN are associated with visual processing [39, 40]. To adapt to deficient auditory input, prelingually deaf adolescents could rely critically on vision to interact with the external environment. Our findings of the hubs in LING and CUN suggest the improvement of visual performance in deaf adolescents, supporting cross-modal changes in visual processing. Of note, deaf subjects recruited in the present study learn Chinese Sign Language (CSL). It has

been demonstrated that the middle and superior frontal gyri can be activated during observing and imitating CSL [41]. We speculated that the hubs of MFG and SFG only observed in prelingually deaf subjects might be caused by the use of CSL. All the above changes indicate brain reorganizations after hearing loss in prelingually deaf adolescents.

There are still some limitations in the present study. First, the sample size is relatively small. We recruited 16 prelingually deaf adolescents and 16 normal controls, and 15 subjects remained for each group after removing subjects with excessive head movement. More subjects will be scanned in further studies. Second, the effects of clinical parameters, such as the information for the use of sign language and hearing aids, were not analyzed in the present study, which will be taken into consideration in future.

## 5. Conclusions

The present study employed resting-state fMRI and graph theory to investigate alterations of brain functional network in prelingually deaf adolescents compared to normal controls. Functional connectivity was widely distributed in prelingually deaf adolescents. Increased connectivity was significantly found between the limbic system and visual and language-related regions, suggesting reinforcement of the processing for the visual and verbal information in deaf adolescents. Decreased connectivity was detected between the visual regions and language regions possibly due to inferior reading or speaking skills in deaf subjects. Graph theory analysis revealed that brain functional network holds small-worldness in both prelingually deaf adolescents and normal controls. Compared with healthy adolescents, middle and superior frontal gyri, left LING, left CUN, left STG, and right REG were hubs only observed in prelingually deaf adolescents. These hubs were involved in visual, language, and auditory processing, reflecting brain reorganization to adapt to deficient auditory input.

## Conflict of Interests

The authors declare that there is no conflict of interests regarding the publication of this paper.

## Authors' Contribution

Wenjing Li and Jianhong Li contributed equally to this paper.

## Acknowledgments

This work is supported by 863 Project (2013AA013803), the National Natural Science Foundation of China (NSFC) (no. 81271557, no. 61271151, and no. 61228103), Youth Innovation Promotion Association CAS, the Beijing Postdoctoral Research Foundation (no. 2014ZZ-8), the Project Funded by China Postdoctoral Science Foundation (no. 2015M570911), and the Basic Research Foundation Project of Beijing University of Technology. The authors thank all the subjects and

their families for the time and effort they dedicate to the authors' research.

## References

- [1] M. MacSweeney, R. Campbell, G. A. Calvert et al., "Dispersed activation in the left temporal cortex for speech-reading in congenitally deaf people," *Proceedings of the Royal Society B: Biological Sciences*, vol. 268, no. 1466, pp. 451–457, 2001.
- [2] H. Yoshida, Y. Kanda, H. Takahashi, I. Miyamoto, and K. Chiba, "Observation of cortical activity during speech stimulation in prelingually deafened adults with cochlear implantation by positron emission tomography-computed tomography," *Annals of Otology, Rhinology and Laryngology*, vol. 120, no. 8, pp. 499–504, 2011.
- [3] I. Fine, E. M. Finney, G. M. Boynton, and K. R. Dobkins, "Comparing the effects of auditory deprivation and sign language within the auditory and visual cortex," *Journal of Cognitive Neuroscience*, vol. 17, no. 10, pp. 1621–1637, 2005.
- [4] R. S. Dewey and D. E. Hartley, "Cortical cross-modal plasticity following deafness measured using functional near-infrared spectroscopy," *Hearing Research*, vol. 325, pp. 55–63, 2015.
- [5] K. Emmorey, J. S. Allen, J. Bruss, N. Schenker, and H. Damasio, "A morphometric analysis of auditory brain regions in congenitally deaf adults," *Proceedings of the National Academy of Sciences of the United States of America*, vol. 100, no. 17, pp. 10049–10054, 2003.
- [6] D. K. Shibata, "Differences in brain structure in deaf persons on MR imaging studied with voxel-based morphometry," *American Journal of Neuroradiology*, vol. 28, no. 2, pp. 243–249, 2007.
- [7] J. Li, W. Li, J. Xian et al., "Cortical thickness analysis and optimized voxel-based morphometry in children and adolescents with prelingually profound sensorineural hearing loss," *Brain Research*, vol. 1430, pp. 35–42, 2012.
- [8] W. Li, J. Li, J. Xian et al., "Alterations of grey matter asymmetries in adolescents with prelingual deafness: a combined VBM and cortical thickness analysis," *Restorative Neurology and Neuroscience*, vol. 31, no. 1, pp. 1–17, 2013.
- [9] O. Sporns, G. Tononi, and R. Kötter, "The human connectome: a structural description of the human brain," *PLoS Computational Biology*, vol. 1, no. 4, article e42, 2005.
- [10] O. Sporns, "From simple graphs to the connectome: networks in neuroimaging," *NeuroImage*, vol. 62, no. 2, pp. 881–886, 2012.
- [11] T. Nakamura, F. G. Hillary, and B. B. Biswal, "Resting network plasticity following brain injury," *PLoS ONE*, vol. 4, no. 12, Article ID e8220, 2009.
- [12] E. Bullmore and O. Sporns, "Complex brain networks: graph theoretical analysis of structural and functional systems," *Nature Reviews Neuroscience*, vol. 10, no. 3, pp. 186–198, 2009.
- [13] Y. He and A. Evans, "Graph theoretical modeling of brain connectivity," *Current Opinion in Neurology*, vol. 23, no. 4, pp. 341–350, 2010.
- [14] D. S. Bassett and E. Bullmore, "Small-world brain networks," *Neuroscientist*, vol. 12, no. 6, pp. 512–523, 2006.
- [15] J. Wang, L. Wang, Y. Zang et al., "Parcellation-dependent small-world brain functional networks: a resting-state fmri study," *Human Brain Mapping*, vol. 30, no. 5, pp. 1511–1523, 2009.
- [16] Y. Liu, M. Liang, Y. Zhou et al., "Disrupted small-world networks in schizophrenia," *Brain*, vol. 131, no. 4, pp. 945–961, 2008.

- [17] K. Wu, Y. Taki, K. Sato, H. Qi, R. Kawashima, and H. Fukuda, "A longitudinal study of structural brain network changes with normal aging," *Frontiers in Human Neuroscience*, vol. 7, no. 3, article 113, 2013.
- [18] Z. Liu, L. Ke, H. Liu, W. Huang, and Z. Hu, "Changes in topological organization of functional PET brain network with normal aging," *PLoS ONE*, vol. 9, no. 2, Article ID e88690, 2014.
- [19] M. P. van den Heuvel, R. C. W. Mandl, C. J. Stam, R. S. Kahn, and H. E. Hulshoff Pol, "Aberrant frontal and temporal complex network structure in schizophrenia: a graph theoretical analysis," *Journal of Neuroscience*, vol. 30, no. 47, pp. 15915–15926, 2010.
- [20] E. J. Sanz-Arigita, M. M. Schoonheim, J. S. Damoiseaux et al., "Loss of 'small-world' networks in Alzheimer's disease: graph analysis of fMRI resting-state functional connectivity," *PLoS ONE*, vol. 5, no. 11, Article ID e13788, 2010.
- [21] B. M. Tijms, A. M. Wink, W. de Haan et al., "Alzheimer's disease: connecting findings from graph theoretical studies of brain networks," *Neurobiology of Aging*, vol. 34, no. 8, pp. 2023–2036, 2013.
- [22] E. Kim, H. Kang, H. Lee et al., "Morphological brain network assessed using graph theory and network filtration in deaf adults," *Hearing Research*, vol. 315, pp. 88–98, 2014.
- [23] Y. Li, J. R. Booth, D. Peng et al., "Altered intra- and inter-regional synchronization of superior temporal cortex in deaf people," *Cerebral Cortex*, vol. 23, no. 8, pp. 1988–1996, 2013.
- [24] W. Li, J. Li, Z. Wang et al., "Grey matter connectivity within and between auditory, language and visual systems in prelingually deaf adolescents," *Restorative Neurology and Neuroscience*, vol. 33, no. 3, pp. 279–290, 2015.
- [25] D. J. Watts and S. H. Strogatz, "Collective dynamics of 'small-world' networks," *Nature*, vol. 393, no. 6684, pp. 440–442, 1998.
- [26] A. Lord, D. Horn, M. Breakspear, and M. Walter, "Changes in community structure of resting state functional connectivity in unipolar depression," *PLoS ONE*, vol. 7, no. 8, Article ID e41282, 2012.
- [27] M. Rubinov, S. A. Knock, C. J. Stam et al., "Small-world properties of nonlinear brain activity in schizophrenia," *Human Brain Mapping*, vol. 30, no. 2, pp. 403–416, 2009.
- [28] M. Xia, J. Wang, and Y. He, "BrainNet viewer: a network visualization tool for human brain connectomics," *PLoS ONE*, vol. 8, no. 7, Article ID e68910, 2013.
- [29] T. P. White, V. Joseph, S. T. Francis, and P. F. Liddle, "Aberrant salience network (bilateral insula and anterior cingulate cortex) connectivity during information processing in schizophrenia," *Schizophrenia Research*, vol. 123, no. 2-3, pp. 105–115, 2010.
- [30] M. Corbetta, G. L. Shulman, F. M. Miezin, and S. E. Petersen, "Superior parietal cortex activation during spatial attention shifts and visual feature conjunction," *Science*, vol. 270, no. 5237, pp. 802–805, 1995.
- [31] D. J. Acheson and P. Hagoort, "Stimulating the brain's language network: syntactic ambiguity resolution after TMS to the inferior frontal gyrus and middle temporal gyrus," *Journal of Cognitive Neuroscience*, vol. 25, no. 10, pp. 1664–1677, 2013.
- [32] L. H. Tan, H.-L. Liu, C. A. Perfetti, J. A. Spinks, P. T. Fox, and J.-H. Gao, "The neural system underlying Chinese logograph reading," *NeuroImage*, vol. 13, no. 5, pp. 836–846, 2001.
- [33] S. G. Costafreda, C. H. Y. Fu, L. Lee, B. Everitt, M. J. Brammer, and A. S. David, "A systematic review and quantitative appraisal of fMRI studies of verbal fluency: role of the left inferior frontal gyrus," *Human Brain Mapping*, vol. 27, no. 10, pp. 799–810, 2006.
- [34] I. Parasnis, V. J. Samar, and G. P. Berent, "Deaf adults without attention deficit hyperactivity disorder display reduced perceptual sensitivity and elevated impulsivity on the Test of Variables of Attention (T.O.V.A.)," *Journal of Speech, Language, and Hearing Research*, vol. 46, no. 5, pp. 1166–1183, 2003.
- [35] R. Hollingsworth, A. K. Ludlow, A. Wilkins, R. Calver, and P. M. Allen, "Visual performance and ocular abnormalities in deaf children and young adults: a literature review," *Acta Ophthalmologica*, vol. 92, no. 4, pp. 305–310, 2014.
- [36] K. Hwang, M. N. Hallquist, and B. Luna, "The development of hub architecture in the human functional brain network," *Cerebral Cortex*, vol. 23, no. 10, pp. 2380–2393, 2013.
- [37] M. A. Howard, I. O. Volkov, R. Mirsky et al., "Auditory cortex on the human posterior superior temporal gyrus," *Journal of Comparative Neurology*, vol. 416, no. 1, pp. 79–92, 1999.
- [38] B. R. Buchsbaum, G. Hickok, and C. Humphries, "Role of left posterior superior temporal gyrus in phonological processing for speech perception and production," *Cognitive Science*, vol. 25, no. 5, pp. 663–678, 2001.
- [39] A. Mechelli, G. W. Humphreys, K. Mayall, A. Olson, and C. J. Price, "Differential effects of word length and visual contrast in the fusiform and lingual gyri during reading," *Proceedings of the Royal Society B: Biological Sciences*, vol. 267, no. 1455, pp. 1909–1913, 2000.
- [40] S. Vanni, T. Tanskanen, M. Seppä, K. Uutela, and R. Hari, "Coinciding early activation of the human primary visual cortex and anteromedial cuneus," *Proceedings of the National Academy of Sciences of the United States of America*, vol. 98, no. 5, pp. 2776–2780, 2001.
- [41] Q. Li, S. Xia, and F. Zhao, "An FMRI picture study of Chinese sign language in functional cortex of prelingual deaf signers use computer," *Communications in Computer and Information Science*, vol. 158, pp. 348–355, 2011.

## Research Article

# Closely Spaced MEG Source Localization and Functional Connectivity Analysis Using a New Prewhitening Invariance of Noise Space Algorithm

Junpeng Zhang,<sup>1,2</sup> Yuan Cui,<sup>3</sup> Lihua Deng,<sup>1</sup> Ling He,<sup>1</sup> Junran Zhang,<sup>1</sup> Jing Zhang,<sup>1</sup> Qun Zhou,<sup>1</sup> Qi Liu,<sup>1</sup> and Zhiguo Zhang<sup>2</sup>

<sup>1</sup>Department of Medical Information Engineering, School of Electrical Engineering and Information, Sichuan University, Chengdu 610065, China

<sup>2</sup>School of Chemical and Biomedical Engineering, School of Electrical and Electronic Engineering, Nanyang Technological University, Singapore 639798

<sup>3</sup>School of Humanities and Information Management, Chengdu Medical College, Chengdu 610083, China

Correspondence should be addressed to Junpeng Zhang; [junpeng.zhang@gmail.com](mailto:junpeng.zhang@gmail.com), Qi Liu; [liuqi@scu.edu.cn](mailto:liuqi@scu.edu.cn), and Zhiguo Zhang; [zgzhang@ntu.edu.sg](mailto:zgzhang@ntu.edu.sg)

Received 4 June 2015; Revised 13 August 2015; Accepted 18 August 2015

Academic Editor: Xiaobo Li

Copyright © 2016 Junpeng Zhang et al. This is an open access article distributed under the Creative Commons Attribution License, which permits unrestricted use, distribution, and reproduction in any medium, provided the original work is properly cited.

This paper proposed a prewhitening invariance of noise space (PW-INN) as a new magnetoencephalography (MEG) source analysis method, which is particularly suitable for localizing closely spaced and highly correlated cortical sources under real MEG noise. Conventional source localization methods, such as sLORETA and beamformer, cannot distinguish closely spaced cortical sources, especially under strong intersource correlation. Our previous work proposed an invariance of noise space (INN) method to resolve closely spaced sources, but its performance is seriously degraded under correlated noise between MEG sensors. The proposed PW-INN method largely mitigates the adverse influence of correlated MEG noise by projecting MEG data to a new space defined by the orthogonal complement of dominant eigenvectors of correlated MEG noise. Simulation results showed that PW-INN is superior to INN, sLORETA, and beamformer in terms of localization accuracy for closely spaced and highly correlated sources. Lastly, source connectivity between closely spaced sources can be satisfactorily constructed from source time courses estimated by PW-INN but not from results of other conventional methods. Therefore, the proposed PW-INN method is a promising MEG source analysis to provide a high spatial-temporal characterization of cortical activity and connectivity, which is crucial for basic and clinical research of neural plasticity.

## 1. Introduction

Magnetoencephalography (MEG) is becoming a more and more popular brain imaging tool for exploring brain dynamics and interactions because of its millisecond temporal precision and high spatial resolution [1]. Particularly, the high temporal-spatial resolution of MEG enables tracking of dynamic neuronal interactions, which is crucial to study neural plasticity [2–5]. For example, surgical resection is a necessary operation for serious brain tumors-II gliomas, and it is important to precisely localize resection regions to optimize the benefit/risk ratio of the surgery. The variability of normal

anatomy and the functional reorganization due to cerebral plasticity phenomena make classic anatomic boundaries insufficient for predicting associated function. The emerging technology of individual brain mapping and functional connectivity (FC) can individually generate a functional map and facilitate localization of functional boundaries, which will greatly increase the accuracy in surgical resection (for a review, see [4]). Also, Tarapore et al. suggested that MEG-based FC was a better predictor of long-term postoperative morbidity than intraoperative electrical stimulation [6]. In such a case, neural plasticity plays an important role in postoperative brain tissue and function development and FC

can provide reliable indicators of neural plasticity related to postoperative neural development. In addition, the study of MEG-based FC is useful for understanding the short-term plasticity associated with sleep and memory. For example, generators of the oscillatory regime and FC underlying early and late synchrony may help understand the role of sleep spindles in brain plasticity [7].

Generally, MEG-based brain connectivity analysis can be conducted at two levels: sensor level and source level. Interpretation of sensor-level connectivity is not straightforward, as it suffers from a low spatial resolution and is severely corrupted by effects of field spread [8]. To overcome the limitation of sensor-level connectivity analysis, it is more desired to estimate connectivity among cortical sources. Source-level connectivity analysis generally comprises two steps: source localization and connectivity analysis [9]. Firstly, the locations of MEG sources and their time courses will be estimated using a spatiotemporal source model from scalp waveforms to mitigate the intrinsic volume conduction (field spread) effect. Second, connectivity measures (such as correlation and phase synchronization) will be estimated from time courses of cortical sources. Therefore, correct estimates of source locations and their time courses are the prerequisites of source-level connectivity analysis.

Many source localization methods, such as the linear constraint minimum variance (LCMV) beamformer [10, 11], and sLORETA (standardized low resolution brain electromagnetic tomography) [12] have been widely used to identify source locations from MEG and to reconstruct time courses in source space. However, these classical source localization methods have difficulty in resolving sources with strong connectivity (i.e., source time courses are highly correlated), especially when underlying sources are closely spaced. As shown in [8], previous work have already attempted to resolve correlated sources, such as [13, 14]. However, the distance between sources is generally randomly set in simulations of these papers. A close distance between two sources will add the difficulty in sources localization, because two sources have very similar lead field. Apparently, inaccurate results of source localization will lead to distorted reconstruction of source time courses and then will adversely affect sequential source connectivity analysis. In our previous paper, a new source localization method, invariance of noise space (INN) [15], has been proposed for MEG source localization. Based on the fact that modulations of source strengths only change the variance in signal subspace but do not change that in noise subspace, the INN method can provide more accurate results than conventional source localization methods, such as LCMV beamformer and MUSIC. In particular, INN has better performance in dealing with sources with strong interaction, even in the case that multiple sources are close to each other [15]. However, the simulation study in [15] only tested the performance of INN under simulated Gaussian noise and it is still not clear whether the INN method can work well under real-world MEG noise. Actually, MEG noise has different properties with Gaussian noise. Real MEG noise, as a kind of spatially correlated noise, is a combination of SQUID (superconducting quantum interference device) noise and interference generated by both environmental and

biomagnetic sources of no interest. While a Gaussian model may be adequate for describing SQUID noise, the interference will necessarily be correlated across MEG sensors and will not exhibit a flat frequency spectrum as white noise does. Therefore, it is necessary to examine the effectiveness of the INN method in source localization and subsequent source connectivity analysis in a real noise environment. More importantly, correlated noise usually deteriorates performance of source localization, so it is desirable to further improve the INN method to make it robust under real-world correlated noise.

In this study, we first intensively investigate the performance of INN in identifying sources, under the condition of simulated white noise as well as real spontaneous MEG noise. We particularly focus on the cases where sources are closely spaced and highly correlated. Further, to alleviate the effect of the correlated noise on localization performance of INN, we proposed a new prewhitening INN (PW-INN) method, which can suppress correlated noise by projecting MEG data to a new space defined by the orthogonal complement of dominant eigenvectors of correlated MEG noise. Next, based on identified source locations using PW-INN, source time courses can be derived using the classical least squares method. Finally, we used phase synchronization (PS) to measure the FC between source time courses estimated using PW-INN. For comparison, the classical LCMV beamformer and sLORETA are also tested on simulated MEG data in terms of their performance in identification of source locations, reconstruction of source time courses, and inference of source connectivity.

## 2. Methods and Materials

### 2.1. Methods

*2.1.1. Problem Formulation.* The MEG data  $\mathbf{Y}(t)$  generated by current dipole sources can be modeled as

$$\mathbf{Y}(t) = \mathbf{A}\mathbf{X}(t) + \mathbf{n}(t), \quad (1)$$

where  $\mathbf{A}$  is the gain matrix relating the measured signals to the dipole amplitudes, rows of  $\mathbf{X}(t)$  are the time courses of the current dipoles, and  $\mathbf{n}(t)$  is additive noise.

Assuming that  $\mathbf{n}(t)$  is uncorrelated across the channels, that the variance of the noise on each channel is  $\sigma^2$ , and that the signal and noise are uncorrelated, the correlation matrix of the MEG data is

$$\mathbf{R} = \langle \mathbf{Y}(t)\mathbf{Y}(t)^T \rangle = \mathbf{A}\mathbf{P}\mathbf{A}^T + \sigma^2\mathbf{I}, \quad (2)$$

where  $\mathbf{P} = \langle \mathbf{X}(t)\mathbf{X}(t)^T \rangle$ . Based on this assumption of uncorrelated noise, many source localization methods have been developed. However, this assumption does not hold true for real MEG signals. In the following, we will first introduce classical source localization methods, LCMV beamformer and sLORETA, and then develop a new source localization method to deal with real-world correlated noise.

*2.1.2. Beamformer.* Beamformers, as adaptive spatial filters, pass the signal from desirable locations while blocking signals

from other locations. The source activity  $\mathbf{s}(\theta, t)$  at location  $\theta$  and time  $t$  is estimated by a simple linear operation,

$$\mathbf{s}(\theta, t) = \mathbf{W}(\theta)^T \mathbf{Y}(t), \quad (3)$$

where  $\mathbf{W}(\theta)$  is a column vector consisting of a set of spatial filter weights. In an LCMV beamformer,  $\mathbf{W}(\theta)$  minimizes the variance of the filter output:

$$\begin{aligned} \min_{\mathbf{w}} \quad & \mathbf{W}(\theta)^T \mathbf{R} \mathbf{W}(\theta) \\ \text{subject to} \quad & \mathbf{W}(\theta)^T \mathbf{a}(\theta) = 1, \end{aligned} \quad (4)$$

where  $\mathbf{a}(\theta)$  indicates the gain matrix at location  $\theta$ . The solution of this constrained optimization problem [10, 11] is

$$\mathbf{W}(\theta) = \mathbf{R}^{-1} \mathbf{a}(\theta) [\mathbf{a}(\theta)^T \mathbf{R}^{-1} \mathbf{a}(\theta)]^{-1}. \quad (5)$$

Mapping the filter output as a function of location generates functional (pseudo) image. In this study, we use a vector LCMV beamformer described in previous studies [10, 11].

**2.1.3. sLORETA.** The sLORETA [12] is based on Minimum Norm Estimation (MNE) [16] and it standardizes the source distribution estimated from MNE by the variance of each estimated dipole source. The solution of MNE at location  $\theta$  and time  $t$  can be written as

$$\mathbf{s}(\theta, t)_{\text{MNE}} = \mathbf{A}^T (\mathbf{A}^T \mathbf{A} + \beta \mathbf{I})^{-1} \mathbf{Y}(\theta, t), \quad (6)$$

where  $\beta > 0$  is a scalar regularization parameter to be chosen allowing inversion of the matrix in parenthesis (Tikhonov regularization) and  $\mathbf{I}$  is the identity matrix. In order to obtain sLORETA solution,  $\mathbf{s}(\theta, t)_{\text{MNE}}$  is normalized by its estimated variance  $\sigma$  assuming independence of source activity, defined as  $\sigma = \mathbf{A}^T (\mathbf{A}^T \mathbf{A} + \beta \mathbf{I})^{-1} \mathbf{A}$ . Then, the sLORETA solution at source grid points  $\theta$  at time  $t$  is

$$\mathbf{s}(\theta, t)_{\text{sLORETA}} = \mathbf{s}(\theta, t)_{\text{MNE}}^T \sigma_{\theta}^{-1} \mathbf{s}(\theta, t)_{\text{MNE}}. \quad (7)$$

**2.1.4. INN.** In [15], we developed a new INN method, which is based on the assumption that the noise subspace of a multidimensional signal is invariant with respect to the strengths of the sources. Let us define a matrix  $\mathbf{D}^{\theta}$  as

$$\mathbf{D}^{\theta} = \mathbf{R} + h \mathbf{a}(\theta) \mathbf{a}(\theta)^T, \quad (8)$$

where  $\mathbf{R}$  is the data correlation matrix of (2),  $\mathbf{a}(\theta)$  is the lead field matrix generated by a unit source at location  $\theta$ , and  $h$  is a positive constant scalar. The cost function of INN is

$$J(\theta) = \frac{1}{\sum_{i=p+1}^K (\mu_i^{\theta} - \lambda_i)}, \quad (9)$$

where  $\lambda_i$  is ordered singular values of  $\mathbf{R}$ ,  $\mu_i^{\theta}$  is the ordered singular values of  $\mathbf{D}(\theta)$ ,  $p$  indicates the number of sources, and  $K$  indicates the number of rows or columns of  $\mathbf{D}(\theta)$ . As (9) implies, if one probe source is exactly placed at one of tentative source locations, only the variance of signal space

of  $\mathbf{D}^{\theta}$  will increase and the noise space keeps unchanged. As a result, the cost function  $J(\theta)$  will generate a peak since the denominator in (8) is approximately equal to zero. On the other hand, if one probe source is placed at locations other than true source locations, the noise space of  $\mathbf{D}^{\theta}$  will correspondingly change. Then,  $J(\theta)$  will obtain a small value since the values of the denominator in (8) will deviate from zero. The values of the cost function  $J(\theta)$  can be used as imaging indices to generate pseudoimages, and the peaks of  $J(\theta)$  could be regarded as the locations of the sources.

**2.1.5. Prewhitening INN (PW-INN).** LCMV beamformer, sLORETA, and INN are all based on the assumption of uncorrelated noise, which is actually not true for real MEG signals. Generally, MEG noise is correlated between MEG channels. Denoting the additive correlated noise as  $\mathbf{n}_c(t)$ , then (1) becomes

$$\mathbf{Y}(t) = \mathbf{A} \mathbf{X}(t) + \mathbf{n}_c(t). \quad (10)$$

By singular value decomposition of the noise covariance matrix  $\mathbf{R}_c = \langle \mathbf{n}_c(t) \mathbf{n}_c(t)^T \rangle$ , we obtain  $M$  dominant left eigenvectors,  $\mathbf{S}_i$ ,  $i = 1, \dots, M$ . Here, the first  $M$  eigenvectors, accounting for most of total noise variance (e.g., 90%), were chosen to construct a matrix  $[\mathbf{S}_1, \mathbf{S}_2, \dots, \mathbf{S}_M]$ . The orthogonal complement matrix of  $[\mathbf{S}_1, \mathbf{S}_2, \dots, \mathbf{S}_M]$ , indicated by  $\mathbf{P}$ , can be calculated according to

$$\mathbf{P} = \mathbf{I} - (\mathbf{S}_1 \mathbf{S}_1^T + \mathbf{S}_2 \mathbf{S}_2^T + \dots + \mathbf{S}_M \mathbf{S}_M^T). \quad (11)$$

Multiplying  $\mathbf{P}$  to two sides of (1), we get

$$\mathbf{P} \mathbf{Y}(t) = \mathbf{P} \mathbf{A} \mathbf{X}(t) + \mathbf{P} \mathbf{n}_c(t). \quad (12)$$

It is straightforward that  $\mathbf{n}_c(t)$  can be decomposed into

$$\mathbf{n}_c(t) \approx \mathbf{S}_1 \mathbf{V}_1^T + \mathbf{S}_2 \mathbf{V}_2^T + \dots + \mathbf{S}_M \mathbf{V}_M^T, \quad (13)$$

where  $\mathbf{V}_i$ ,  $i = 1, \dots, M$ , indicates the components along the directions  $\mathbf{S}_i$ ,  $i = 1, \dots, M$ , respectively. By multiplying (11) and (13), we can readily get  $\mathbf{P} \mathbf{n}_c(t) \approx 0$ . That is, by projecting correlated signals to the space defined by  $\mathbf{P}$ , the second term of the right side of (12) almost disappears. Then, the conventional INN method can be well applied to the projected MEG data (i.e.,  $\mathbf{P} \mathbf{Y}(t)$ ) and projected lead field  $\mathbf{P} \mathbf{a}(\theta)$ . By this means, the new PW-INN method can largely suppress correlated noise to overcome the limitation of INN in presence of real-world correlated noise. Once source locations are identified using PW-INN, source time courses can easily be derived using the least squares method [17].

## 2.2. Simulations

**2.2.1. Model Configuration and Parameter Definition.** In the simulations, the single layer sphere head model was adapted. The sensor array comprised 272 magnetometers arranged in an array on a sphere with 100 mm radius. The average distance between sensors was 22 mm. Our coordinate system is defined in Figure 1(a) and the whole brain was completely encompassed by the sphere, as shown in Figure 1(b), and thus

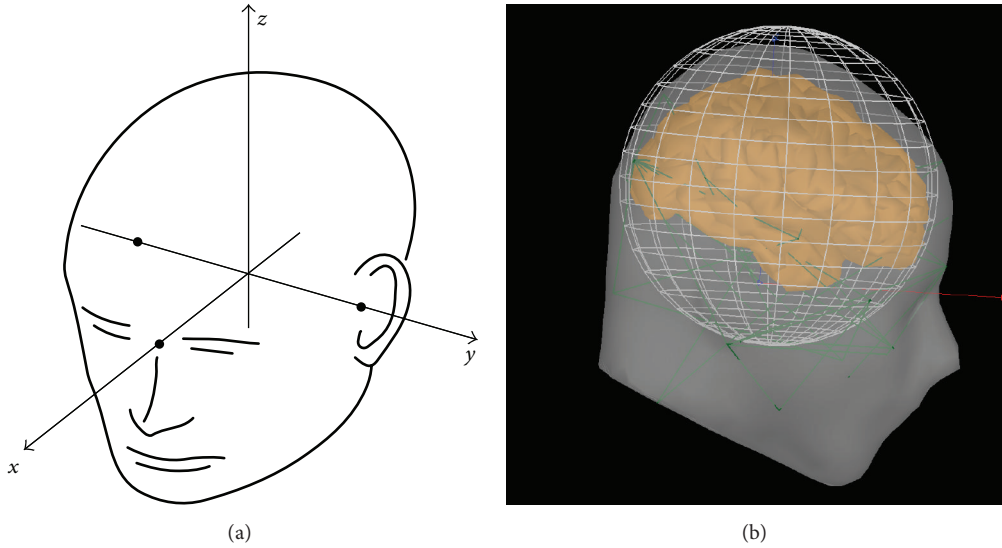


FIGURE 1: Simulation settings. (a) Coordinate system used in the simulation settings. The  $x$ -axis of the head coordinate system passes through the two periauricular points with positive direction to the right. The  $y$ -axis passes through the nasion and is normal to the axis. The  $z$ -axis points up according to the right-hand rule and is normal to the  $xy$  plane. (b) Illustration of the head model, where the whole brain was completely encompassed by the sphere.

the brain volume was well modeled. The brain volume was partitioned into about 17,000 grid points and the distance between neighboring grid points is 5 mm. Volume source space was used in this study and the lead field was calculated using NUTMEG [18, 19]. The signal-to-noise ratio (SNR) was defined as the ratio of the Frobenius norm of the data matrix to that of the noise matrix. Two types of noise were employed in simulations: white noise and real spontaneous MEG recordings. The spontaneous MEG data used as simulated noise were collected from a passive pure-tone listening task and extracted from a prestimulus period. MEG data were acquired with a 275-channel whole-head MEG device from CTF Systems. The sampling frequency was set at 1200 Hz. The selected prestimulus MEG data included samples at 120 time points from  $-100$  ms to 0 ms (stimulus onset). Prestimulus MEG trials from one subject were used as real MEG noise and added to simulated MEG signal. In PW-INN, the prestimulus MEG data used to construct the projection matrix are randomly selected from trials of the same subject that are different from those trials used to simulate real MEG noise. Correlation coefficient ( $r^2$ ) was used to measure the degree of linear correlation between two source time courses.

**2.2.2. Resolvability of Closely Spaced Sources.** We first tested how correlation and SNR modulate localization accuracy of source localization methods. Two equally strong sources were simulated: dipole 1 was located at  $(-5, 45, 40)$  mm with orientation  $(-0.6, -0.1, -0.7)$  and dipole 2 was at  $(5, 45, 40)$  mm with orientation  $(-0.9, 0.2, -0.3)$ . These two sources were close to each other and intersource distance was 10 mm. The locations of these two dipoles were illustrated in Figure 2. The time courses of the two sources were both 10 Hz sine functions with a duration of 100 ms but with different phases. Note that we only simulate evoked neural activities at sources

and do not include induced activities in our simulation. The sampling frequency of the simulated waveforms was 1200 Hz. The correlation coefficient ( $r^2$ ) between the two sources was set to 1, 0.99, 0.97, 0.95, 0.9, 0.8, 0.7, 0.5, 0.3, or 0 by adjusting the phase difference between the time courses. Uncorrelated white Gaussian noise or real MEG noise was added to all data points scaled such that SNR was 10, 12, 14, 16, 18, 20, or 30. For each condition (a specific combination of SNR, noise type, and  $r^2$ ), 100 trials of simulated evoked MEG responses were generated and the noise superimposed to each trial was either independently generated (for white noise) or randomly selected from available prestimulus MEG trials. All data analyses were performed using in-house MATLAB code.

**2.2.3. Reconstruction of Source Time Courses and FC Analysis.** In this simulation, the simulated sources were configured almost the same way as in Section 2.2.2. We tested the performance of different source localization methods in reconstruction of source time courses and FC analysis under two stimulation cases. In Case 1, the phase difference between two sources is set to 18 degrees and intersource correlation coefficient is 0.95. In Case 2, the phase difference is set to 90 degrees and the intersource correlation coefficient is 0. After source localization, the time courses of identified sources were also reconstructed. Instead of plotting the reconstructed source time courses in three orientations ( $xyz$ -axes), in our results we only showed the norm of source time courses, which is called collective time courses (CTC).

Next, FC analysis was performed on reconstructed source time courses. Only sources with energy larger than 90% of the highest energy of the cost function were retained for subsequent FC analysis, and their time courses were reconstructed. A 6 Hz–14 Hz bandpass filter was applied on source time courses and then the phases of these filtered

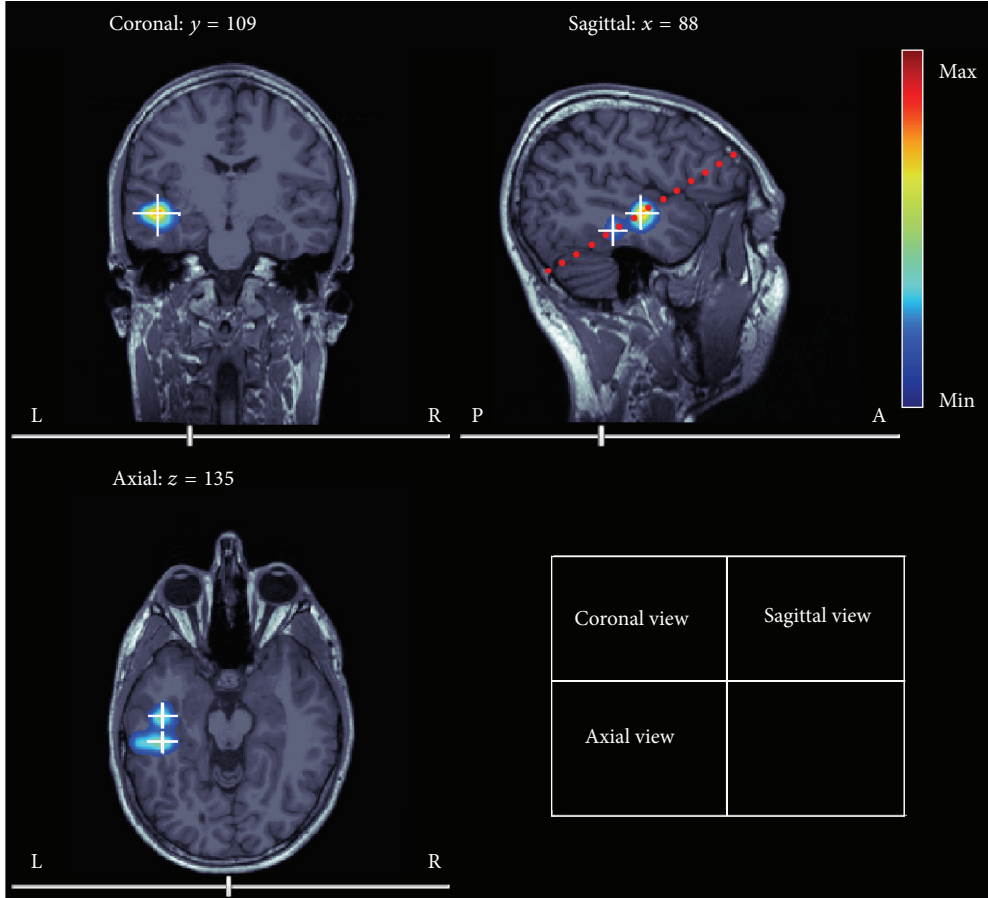


FIGURE 2: True source locations overlaid on T1 anatomical images. Two closely spaced simulated sources (indicated by white crosses) are located at  $(-5, 45, 40)$  mm and  $(5, 45, 40)$  mm, respectively. PW-INN-based source imaging result (obtained in the condition: real MEG noise; SNR = 18;  $r^2 = 0$ ) was also shown as color-coded spatial patterns, where the color denotes the imaging index from (9). The dotted red line in the sagittal view indicates the plane of  $z = 40$  mm.

source time courses were extracted by Hilbert transformation for the subsequent FC analysis. Phase synchronization (PS) [20, 21] is used to measure the FC between reconstructed CTC at two source regions, because PS can effectively detect correlation between two signals even if they have phase difference [21]. PS is calculated as

$$\text{PS}(l, m) = \left| \left\langle e^{i(\Phi_l(t) - \Phi_m(t))} \right\rangle \right|, \quad (14)$$

where  $\Phi_l(t)$  and  $\Phi_m(t)$  indicate the phases of the signals  $l$  and  $m$  at time  $t$ , respectively. A thresholding procedure was further applied on FC values to retain 10% strongest FC among all possible pairs of FC for a better visualization effect [21, 22].

### 3. Results

**3.1. Source Imaging.** Figures 3(a) and 3(b) compare the performances of different source imaging methods under white noise and real MEG noise, respectively, when SNR = 18 dB. It can be clearly seen from Figure 3 that, regardless of which type of noise (white or real MEG) was added, (1) sLORETA cannot resolve these two closely spaced sources even if they are not correlated; (2) the performance of beamformer in

resolving two closely spaced sources is decreased rapidly with the increase of correlation, and when  $r^2 \geq 0.7$  beamformer merged two sources into one equivalent source; (3) INN and PW-INN can still well resolve two sources even if correlation coefficient is as high as 0.97; (4) when  $r^2 = 1$ , which rarely happens in reality, all methods failed to resolve sources. By further comparing Figure 3(a) (under white noise) and Figure 3(b) (under real MEG noise), we can see that (1) real MEG noise increased the difficulty in resolving closely spaced sources for all methods; (2) PW-INN outperformed INN when two sources are highly correlated ( $r^2 = 0.99$ ) only under real MEG noise. The source imaging results of PW-INN are also overlaid on anatomical images in Figure 2. The better performance of PW-INN over INN can be explained by Figure 4, which shows the spatial correlation between real MEG noise of different sensors before and after prewhitening. It can be clearly seen that MEG noise exhibited very strong spatial correlation, but the spatial correlation can be greatly lowered by the prewhitening operation. For example, the sum of absolute values of nondiagonal elements in the correlation matrix, which represents the overall degree of cross-sensor correlation, before prewhitening is 1.6 times larger than that after prewhitening.

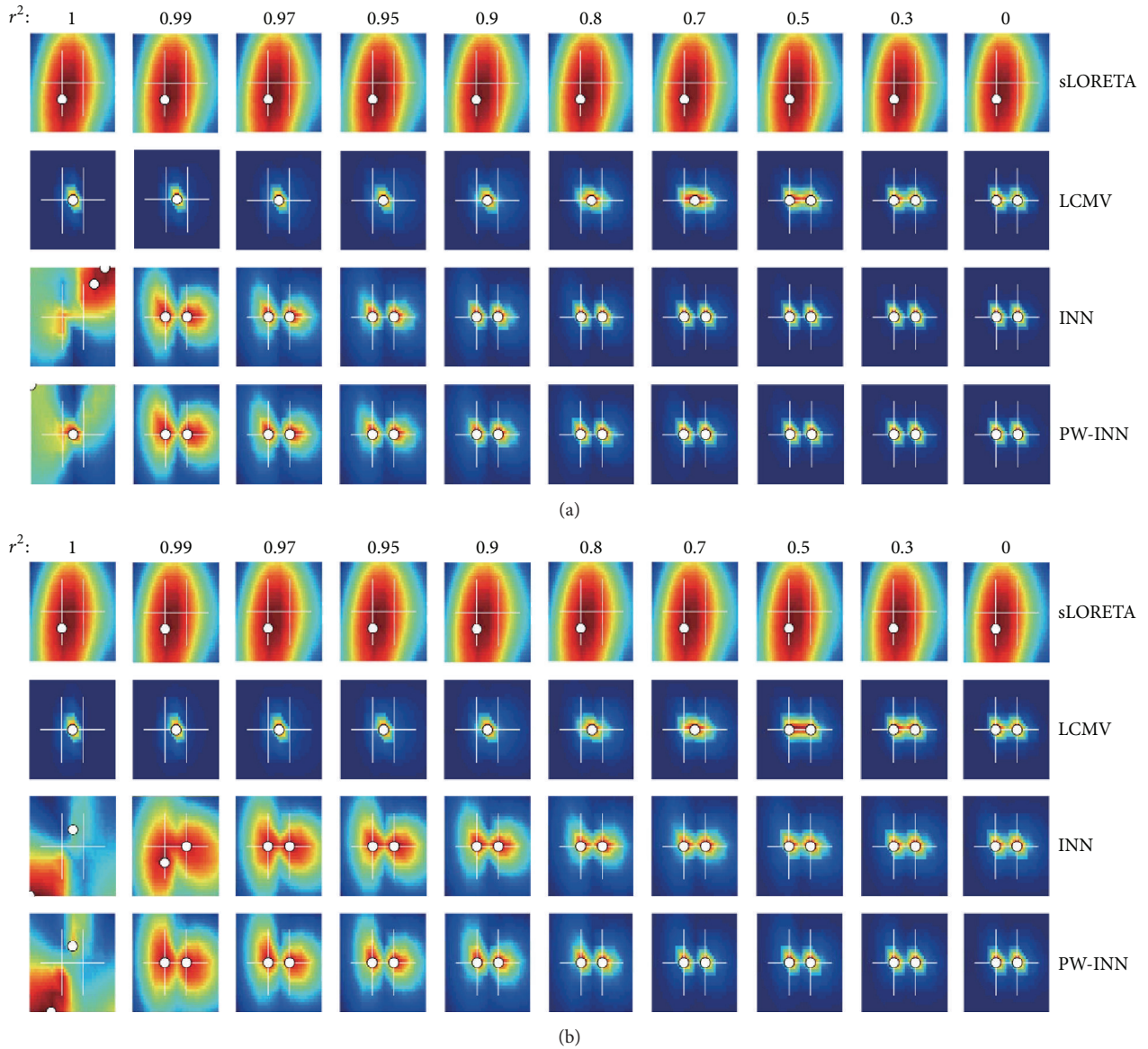


FIGURE 3: Performance comparison between sLORETA, LCMV beamformer, INN, and PW-INN in resolving closely spaced sources in presence of white noise (a) or real MEG noise (b). SNR is set to 18. Correlation coefficient ( $r^2$ ) varied from 1 to 0. From leftmost column to rightmost,  $r^2$  is sequentially set to 1, 0.99, 0.97, 0.95, 0.9, 0.8, 0.7, 0.5, 0.3, and 0. White crosses indicate true source locations and white dots indicate estimated source locations. All results are obtained by averaging 100 independent trials.

We also compared these source imaging methods under various levels of noise (SNR = [10, 12, 14, 16, 18, 20, or 30]). In general, as SNR increased, all methods can resolve these two closely spaced sources with higher accuracy. The performance difference between different methods under other SNR values is similar to the observation under a SNR of 18 dB. Due to page limitation, we only showed the results under SNR = 18 dB in Figure 3. It should also be noted that the prewhitening operation adopted by PW-INN is also used for sLORETA and beamformer, but we did not display the results here because prewhitening did not significantly improve the performance of sLORETA or beamformer.

**3.2. Reconstruction of Source Time Courses.** Figure 5 showed the source imaging results and the corresponding source time courses estimated using sLORETA, beamformer, and PW-INN, respectively, when there was no correlation between two simulated sources ( $r^2 = 0$ ) and real MEG noise of 18 dB is added. For comparison, all time courses in Figure 5 were normalized by the corresponding maximum values. The results of INN are not included here for comparison, because the previous section has shown that the new PW-INN method has better or at least comparable performance than INN. It can be clearly seen from Figure 5 that beamformer and PW-INN accurately identified two sources and recovered the source time courses, while sLORETA failed to

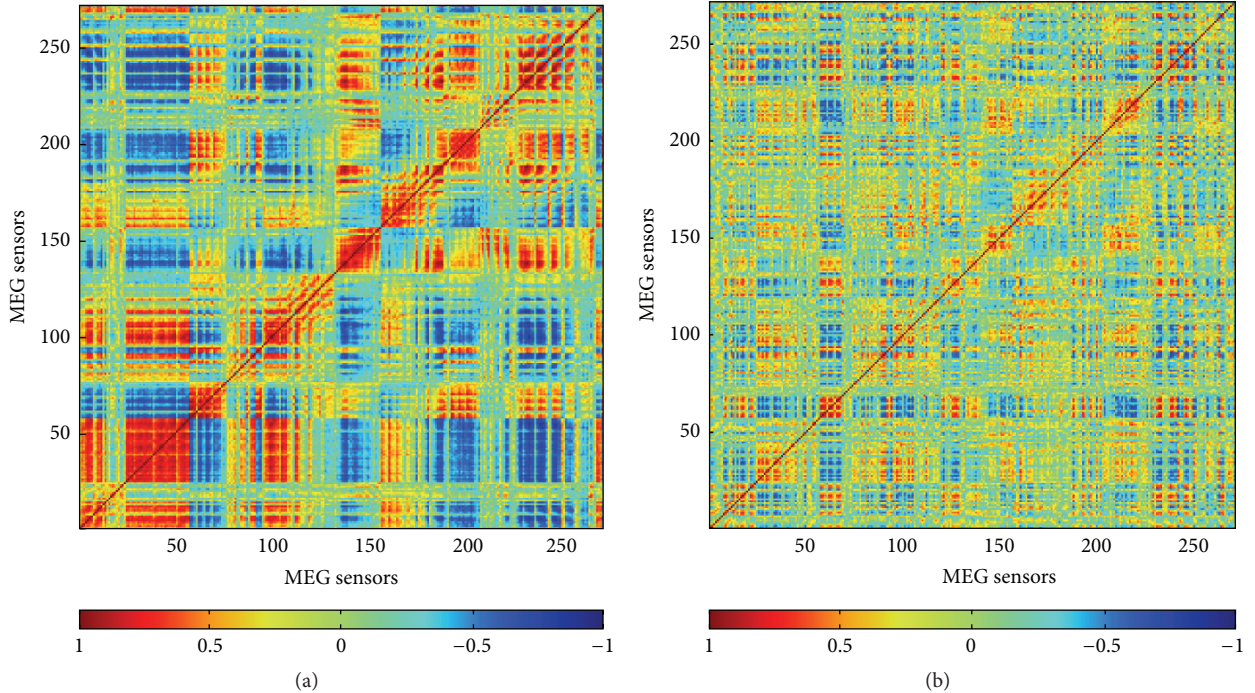


FIGURE 4: (a) Correlation coefficient matrix of real spontaneous MEG noise from a randomly selected trial. (b) Correlation coefficient matrix of real spontaneous MEG noise after being projected to a new space defined by the orthogonal complement of dominant eigenvectors of real MEG noise from another trial. The sum of absolute values of nondiagonal elements in (a) is 1.6 times larger than that in (b), implying that the spatial correlation between MEG noise can be decreased by the prewhitening operation. Colorbar indicates the values of correlation coefficient.

do so. As a comparison, Figure 6 showed source imaging and reconstruction results with a correlation of  $r^2 = 0.95$ . We can see that when the correlation between two sources is high both sLORETA and beamformer wrongly placed an equivalent source between two true sources, and, thus, they can only estimate one equivalent source time course. Under this testing condition, the proposed PW-INN method was still able to accurately identify two sources and to satisfactorily recover source time courses.

**3.2.1. Source-Level Functional Connectivity Analysis.** Once source locations and time courses were readily estimated, FC analysis can be easily implemented. Figure 7 showed the FC graph based on reconstruction results of three methods, sLORETA, beamformer, and PW-INN, when two closely spaced sources have two different correlation coefficients,  $r^2 = 0$  and  $0.95$ . It can be obviously seen that only PW-INN can accurately identify true FC patterns, while FC graphs based on sLORETA and beamformer have many spurious connections. We can also see that FC graphs of sLORETA are relatively consistent (though incorrect) for sources with different correlation coefficients, but FC graphs of beamformer show more spurious connections when the correlation between two true sources is large.

## 4. Discussion and Conclusion

**4.1. Closely Spaced Source Analysis under Real MEG Noise.** This study intensively investigated the performance of MEG

source localization methods for closely spaced source in the presence of real MEG noise and white noise.

Simulated signals with realistic characteristics are important for developing and evaluating new methods. In our previous work [15], the good performance of our proposed INN method in localizing closely spaced sources was validated in the presence of white noise only. However, the INN method is based on the assumption of uncorrelated white noise, but real MEG noise has largely different characteristics (e.g., the degree of correlations between sensors) with white noise. Figure 4 clearly showed that there are large correlations between spontaneous MEG noise at different sensors. In order to evaluate source analysis methods with more realistic signals, we used spontaneous MEG recordings to simulate real MEG noise. Although INN still outperformed beamformer and sLORETA, its performance was degraded under real MEG noise, as compared with under white noise. The newly developed PW-INN can decorrelate MEG signals, so that it can achieve better performance than INN in presence of real correlated MEG noise.

**4.2. MEG-Based Source-Level Connectivity Analysis.** Identifying connectivity between cortical sources using MEG has gained increasing popularity. Correct source localization is the prerequisite of accurate reconstruction of source time courses, which is again the prerequisite for precise inference of source-level connectivity. Many studies based on the classical beamformer have made much progress in identifying physiological and pathological MEG-based source-level FC

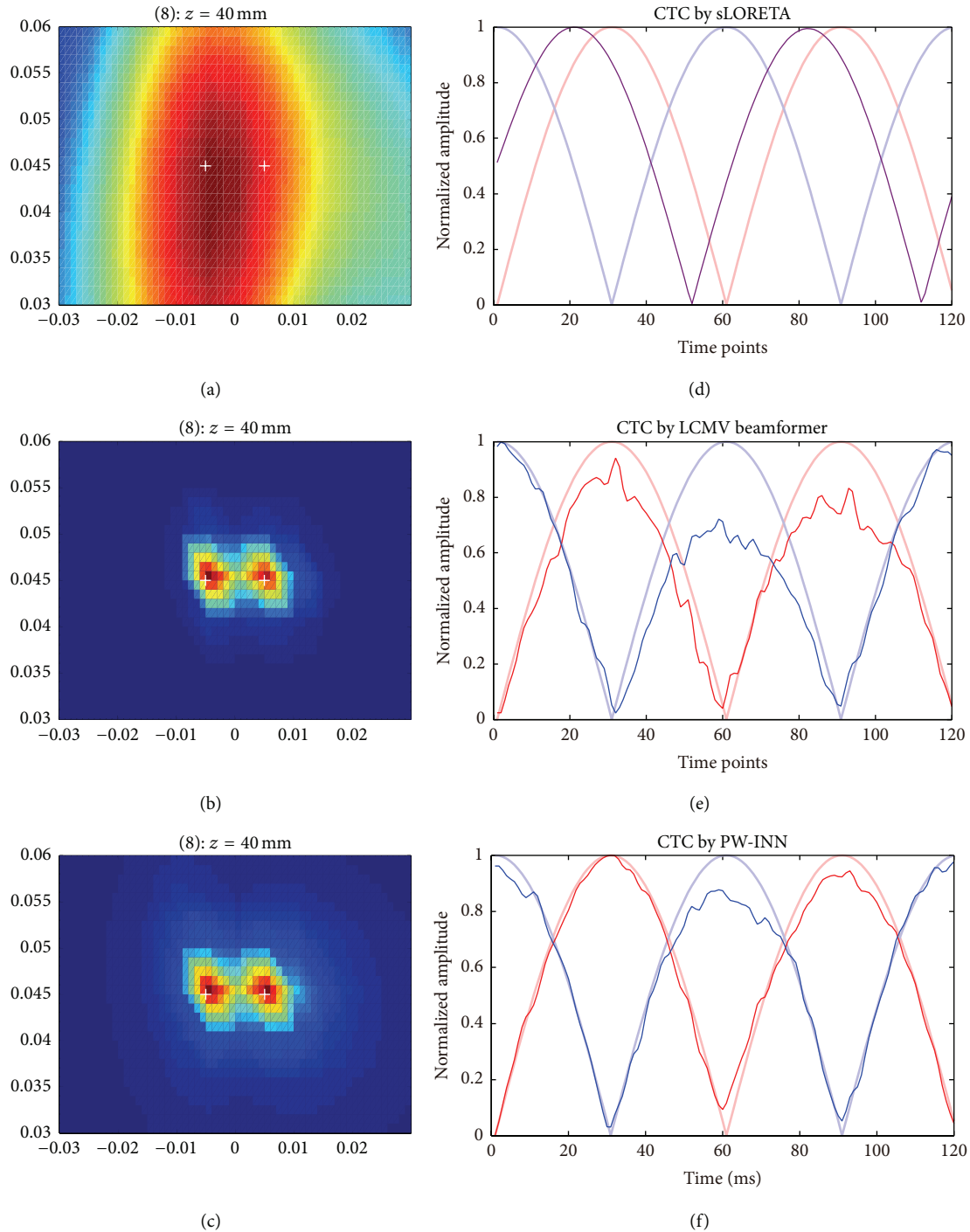


FIGURE 5: Source reconstruction using sLORETA, LCMV beamformer, and PW-INN. Source locations were the same as those in Figure 2. Real MEG noise was added such that  $\text{SNR} = 18$ . Two simulated source time courses have phase difference of 90 degrees. The correlation  $r^2$  between sources is 0. (a)–(c) Source distribution estimated from sLORETA (a), LCMV beamformer (b), and PW-INN (c). White crosses indicate the true source locations. (d)–(f) Source time courses at the peak locations estimated from sLORETA (d), LCMV beamformer (e), and PW-INN (f). The time courses in (d)–(f) are the norm of the original time courses over  $xyz$ -axis (i.e., collecting time courses, CTC). Bold lines in light red and light blue indicate the true source time courses and thin lines in red and blue indicate the estimated ones. The purple color line in (d) indicates the time course from the wrongly estimated equivalent source.

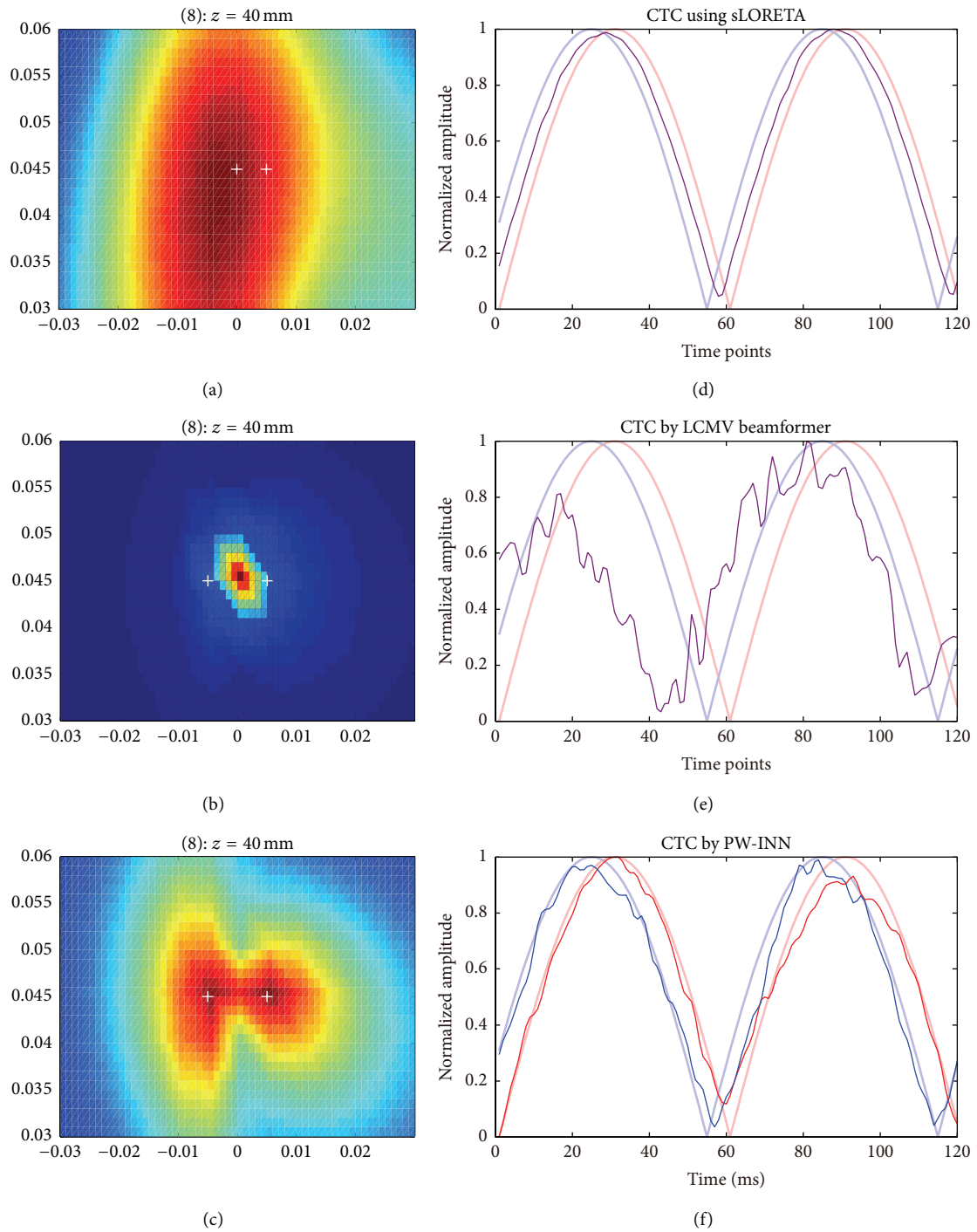


FIGURE 6: Source reconstruction using sLORETA, LCMV beamformer, and PW-INN. Source locations were the same as those in Figure 2. Real MEG noise was added such that SNR = 18. Two simulated source time courses have phase difference of 18 degrees. The correlation  $r^2$  between sources is 0.95. (a)–(c) Source distribution estimated from sLORETA (a), LCMV beamformer (b), and PW-INN (c). White crosses indicate the true source locations. (d)–(f) Source time courses at the peak locations estimated from sLORETA (d), LCMV beamformer (e), and PW-INN (f). The time courses in (d)–(f) are the norm of the original time courses over  $xyz$ -axis (i.e., collecting time courses, CTC). Bold lines in light red and light blue indicate the true source time courses and thin lines in red and blue indicate the estimated ones.

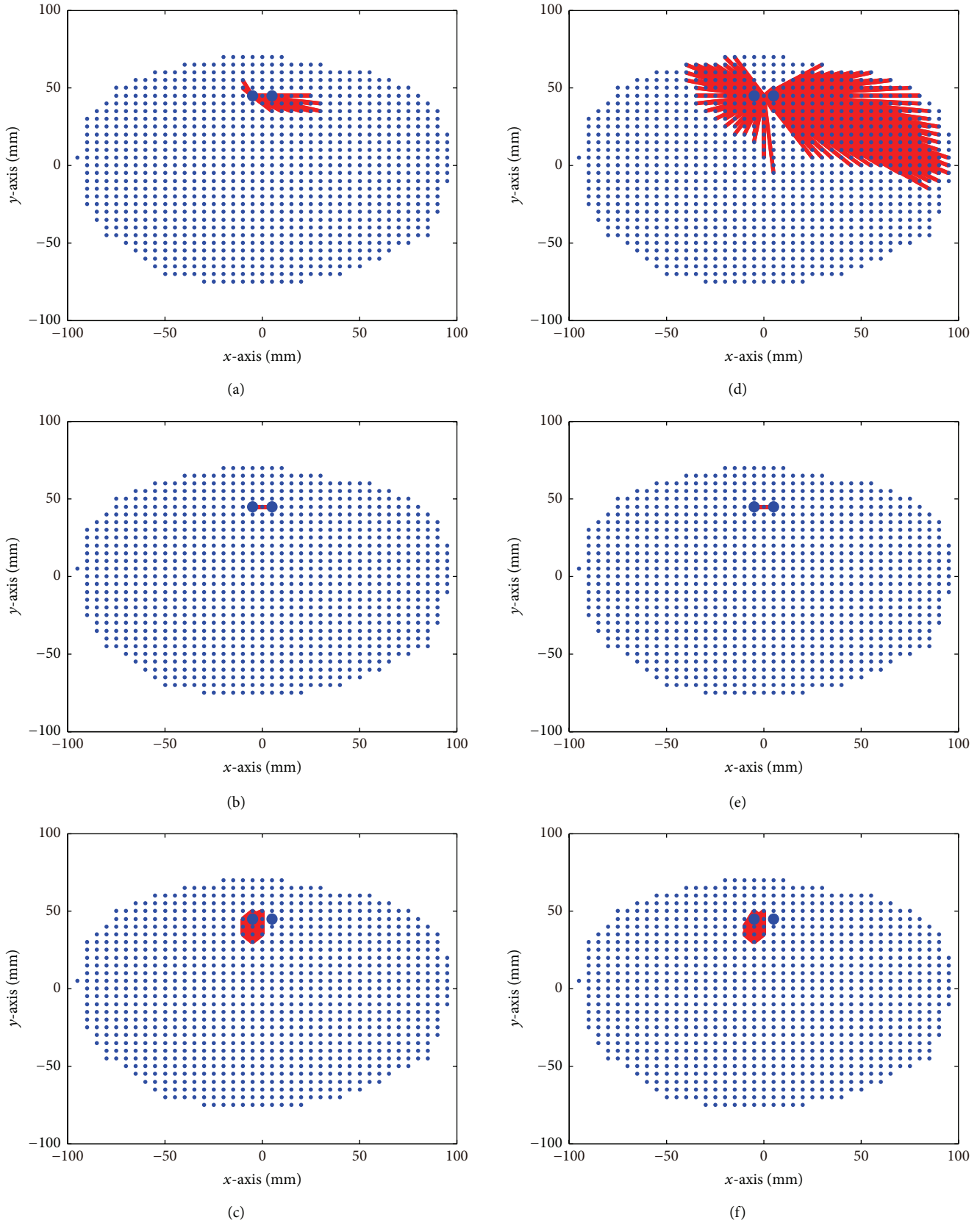


FIGURE 7: FC graphs based on source reconstruction results using sLORETA, LCMV beamformer, and PW-INN. Real MEG noise was added such that  $\text{SNR} = 18$ . Small blue dots indicate brain volume grid points, and large blue dots indicate true source locations. (a)–(c) FC graphs estimated from sLORETA (a), LCMV beamformer (b), and PW-INN (c), when  $r^2 = 0$  between two sources. (d)–(f) FC graphs estimated from sLORETA (d), LCMV beamformer (e), and IINN (f), when  $r^2 = 0.95$  between two sources.

([23] and a review in [8]). However, as discussed earlier, the beamformer has difficulty in separating closely spaced sources, especially in the case of strong intersource connectivity. As shown in Figure 5, the beamformer estimated one spurious source between two true sources, when these two true sources are highly correlated. Apparently, in such a case, source-level connectivity analysis will fail. The proposed PW-INN method inherits the advantage of the INN method, so that it can perform well in localizing highly correlated closely spaced sources and reconstructing their time courses. Therefore, based on the source reconstruction results of PW-INN, connectivity between sources can be correctly identified.

**4.3. Significance and Implications.** The present study is relevant to many important research topics in basic and clinical neuroscience, because the proposed MEG source analysis method can achieve a high spatial-temporal characterization of cortical source activity and connectivity. Nowadays, fMRI is the most popular imaging tool to construct voxel-level brain networks, because of its high spatial resolution. However, fMRI can only provide indirect measures of neural activities with a low temporal resolution, which make it not an ideal tool to investigate the highly dynamic organization of the human brain. MEG can directly detect and track neural electromagnetic activity with high temporal precision, so the proposed PW-INN and the subsequent connectivity analysis can identify cortical networks with a higher temporal resolution than fMRI, which is particularly suitable for tracking dynamic connectivity changes in sensory and cognitive experiments.

Constructing MEG brain network is attracting more and more interests. Currently, there is a huge body of publications that use sLORETA and beamformer to extract source time courses for FC analysis (i.e., [24, 25]). But, as shown in this study, sLORETA and beamformer cannot effectively resolve closely spaced sources, so that they can only be used for constructing a brain network with coarse spatial resolution (e.g., region-level FC or lobe-level FC). Another type of approach to construct MEG networks is the atlas-based MEG analysis, which can estimate FC between different brain regions or lobes [26, 27]. Thus, the spatial resolution of this atlas-based MEG networks is still coarse. So far, important information conveyed by MEG and underlying interconnection between closely spaced small cortical areas (at voxel level) [28] are generally overlooked. Actually, these voxel-level small brain regions have slightly different activities with their neighboring regions, which carry useful information for understanding cortical processing and organization. Identifying the connectivity between primary auditory cortex and secondary auditory cortex using MEG could greatly increase our understanding of auditory information processing in the brain, but it is also very challenging. Unlike previous region- or lobe-based MEG connectivity analysis, the proposed PW-INN method can resolve closely spaced sources, which enable constructing a voxel-level brain network.

In summary, this study is an important step towards a high spatial-temporal characterization of cortical activity and connectivity. In future, we plan to build a high-spatial-resolution voxel-level whole-brain connectome using MEG

and apply this MEG connectome in practical and clinical applications (e.g., to identify changes of MEG connectome for studying neural plasticity).

## Conflict of Interests

The authors declare that there is no conflict of interests regarding the publication of this paper.

## Acknowledgments

This work was supported by National Nature Science Foundation of China (Contract Grants nos. 81470085, 31271204, and 81330032), Key Technology R&D Program of Science and Technology Department of Sichuan Province (no. 2015KJT0002-2014SZ0124), National Undergraduate Training Programs for Innovation (no. 201413705025), Fund Project of Sichuan Provincial Department of Education (14ZB0241), General Research Fund of Research Grants Council of Hong Kong (785913M), Start-Up Grant from Nanyang Technological University, Singapore, MOE AcRF Tier 1 (MOE2015-T1-001-158), and MINDEF-NTU Joint Applied R&D Cooperation (JPP) Programme (MINDEF-NTU-JPP/15/01/05).

## References

- [1] M. Hämäläinen, R. Hari, R. J. Ilmoniemi, J. Knuutila, and O. V. Lounasmaa, "Magnetoencephalography—theory, instrumentation, and applications to noninvasive studies of the working human brain," *Reviews of Modern Physics*, vol. 65, no. 2, pp. 413–497, 1993.
- [2] H. Duffau, "The huge plastic potential of adult brain and the role of connectomics: new insights provided by serial mappings in glioma surgery," *Cortex*, vol. 58, pp. 325–337, 2014.
- [3] H. Duffau, "Lessons from brain mapping in surgery for low-grade gliomas: study of cerebral connectivity and plasticity," in *Medical Imaging and Augmented Reality*, vol. 4091, pp. 25–35, Springer, 2006.
- [4] H. Duffau, "New concepts in surgery of WHO grade II gliomas: functional brain mapping, connectionism and plasticity—a review," *Journal of Neuro-Oncology*, vol. 79, no. 1, pp. 77–115, 2006.
- [5] I. P. Jääskeläinen and J. Ahveninen, "Auditory-cortex short-term plasticity induced by selective attention," *Neural Plasticity*, vol. 2014, Article ID 216731, 11 pages, 2014.
- [6] P. E. Tarapore, J. Martino, A. G. Guggisberg et al., "Magnetoencephalographic imaging of resting-state functional connectivity predicts postsurgical neurological outcome in brain gliomas," *Neurosurgery*, vol. 71, no. 5, pp. 1012–1022, 2012.
- [7] Y. Zerouali, J.-M. Lina, Z. Sekerovic et al., "A time-frequency analysis of the dynamics of cortical networks of sleep spindles from MEG-EEG recordings," *Frontiers in Neuroscience*, vol. 8, article 310, 2014.
- [8] J.-M. Schoffelen and J. Gross, "Source connectivity analysis with MEG and EEG," *Human Brain Mapping*, vol. 30, no. 6, pp. 1857–1865, 2009.
- [9] L. Hu, Z. G. Zhang, and Y. Hu, "A time-varying source connectivity approach to reveal human somatosensory information processing," *NeuroImage*, vol. 62, no. 1, pp. 217–228, 2012.

- [10] B. D. Van Veen, W. Van Drongelen, M. Yuchtman, and A. Suzuki, "Localization of brain electrical activity via linearly constrained minimum variance spatial filtering," *IEEE Transactions on Biomedical Engineering*, vol. 44, no. 9, pp. 867–880, 1997.
- [11] K. Sekihara, S. S. Nagarajan, D. Poeppel, A. Marantz, and Y. Miyashita, "Reconstructing spatio-temporal activities of neural sources using an MEG vector beamformer technique," *IEEE Transactions on Biomedical Engineering*, vol. 48, no. 7, pp. 760–771, 2001.
- [12] R. D. Pascual-Marqui, "Standardized low-resolution brain electromagnetic tomography (sLORETA): technical details," *Methods and Findings in Experimental and Clinical Pharmacology D*, vol. 24, supplement, pp. 5–12, 2002.
- [13] A. Dossevi, D. Cosmelli, L. Garnero, and H. Ammari, "Multivariate reconstruction of functional networks from cortical sources dynamics in MEG/EEG," *IEEE Transactions on Biomedical Engineering*, vol. 55, no. 8, pp. 2074–2086, 2008.
- [14] J. Kujala, J. Gross, and R. Salmelin, "Localization of correlated network activity at the cortical level with MEG," *NeuroImage*, vol. 39, no. 4, pp. 1706–1720, 2008.
- [15] J. Zhang, T. Raij, M. Hämäläinen, and D. Yao, "MEG source localization using invariance of noise space," *PLoS ONE*, vol. 8, no. 3, Article ID e58408, 2013.
- [16] M. S. Hämäläinen and R. J. Ilmoniemi, "Interpreting measured magnetic fields of the brain: estimates of current distributions," Tech. Rep. TKKF-A559, Helsinki University of Technology, 1984.
- [17] C. L. Lawson and R. J. Hanson, *Solving Least Squares Problems*, SIAM, 1974.
- [18] S. S. Dalal, J. M. Zumer, V. Agrawal, K. E. Hild, K. Sekihara, and S. S. Nagarajan, "NUTMEG: a neuromagnetic source reconstruction toolbox," *Neurology & Clinical Neurophysiology*, vol. 2004, article 52, 2004.
- [19] S. S. Dalal, J. M. Zumer, A. G. Guggisberg et al., "MEG/EEG source reconstruction, statistical evaluation, and visualization with NUTMEG," *Computational Intelligence and Neuroscience*, vol. 2011, Article ID 758973, 17 pages, 2011.
- [20] F. Varela, J.-P. Lachaux, E. Rodriguez, and J. Martinerie, "The brainweb: phase synchronization and large-scale integration," *Nature Reviews Neuroscience*, vol. 2, no. 4, pp. 229–239, 2001.
- [21] M. Hassan, O. Dufor, I. Merlet, C. Berrou, and F. Wendling, "EEG source connectivity analysis: from dense array recordings to brain networks," *PLoS ONE*, vol. 9, no. 8, Article ID e105041, 2014.
- [22] O. Sporns, "Structure and function of complex brain networks," *Dialogues in Clinical Neuroscience*, vol. 15, no. 3, pp. 247–262, 2013.
- [23] M. Muthuraman, H. Hellriegel, N. Hoogenboom et al., "Beamformer source analysis and connectivity on concurrent EEG and MEG data during voluntary movements," *PLoS ONE*, vol. 9, no. 3, Article ID e91441, 2014.
- [24] F. de Pasquale, S. Della Penna, A. Z. Snyder et al., "Temporal dynamics of spontaneous MEG activity in brain networks," *Proceedings of the National Academy of Sciences of the United States of America*, vol. 107, no. 13, pp. 6040–6045, 2010.
- [25] P. Tewarie, A. Hillebrand, M. M. Schoonheim et al., "Functional brain network analysis using minimum spanning trees in Multiple Sclerosis: an MEG source-space study," *NeuroImage*, vol. 88, pp. 308–318, 2014.
- [26] A. Hillebrand, G. R. Barnes, J. L. Bosboom, H. W. Berendse, and C. J. Stam, "Frequency-dependent functional connectivity within resting-state networks: an atlas-based MEG beamformer solution," *NeuroImage*, vol. 59, no. 4, pp. 3909–3921, 2012.
- [27] B. T. Dunkley, L. Da Costa, A. Bethune et al., "Low-frequency connectivity is associated with mild traumatic brain injury," *NeuroImage: Clinical*, vol. 7, pp. 611–621, 2015.
- [28] M.-X. Huang, K. A. Yurgil, A. Robb et al., "Voxel-wise resting-state MEG source magnitude imaging study reveals neurocircuitry abnormality in active-duty service members and veterans with PTSD," *NeuroImage: Clinical*, vol. 5, pp. 408–419, 2014.

## Research Article

# Reorganization of Anatomical Connectome following Electroconvulsive Therapy in Major Depressive Disorder

Jinkun Zeng,<sup>1</sup> Qinghua Luo,<sup>1</sup> Lian Du,<sup>1</sup> Wei Liao,<sup>2</sup> Yongmei Li,<sup>3</sup> Haixia Liu,<sup>4</sup> Dan Liu,<sup>1</sup> Yixiao Fu,<sup>1</sup> Haitang Qiu,<sup>1</sup> Xirong Li,<sup>1</sup> Tian Qiu,<sup>1</sup> and Huaqing Meng<sup>1</sup>

<sup>1</sup>Department of Psychiatry, The First Affiliated Hospital of Chongqing Medical University, Chongqing 400016, China

<sup>2</sup>Center for Cognition and Brain Disorders and the Affiliated Hospital, Hangzhou Normal University, Hangzhou 310015, China

<sup>3</sup>Department of Radiology, The First Affiliated Hospital of Chongqing Medical University, Chongqing 400016, China

<sup>4</sup>Medical Psychology Department, The Third Military Medical University, Chongqing 400016, China

Correspondence should be addressed to Huaqing Meng; [mhq99666@126.com](mailto:mhq99666@126.com)

Received 29 April 2015; Revised 1 July 2015; Accepted 13 July 2015

Academic Editor: Martin Walter

Copyright © 2015 Jinkun Zeng et al. This is an open access article distributed under the Creative Commons Attribution License, which permits unrestricted use, distribution, and reproduction in any medium, provided the original work is properly cited.

**Objective.** Electroconvulsive therapy (ECT) is considered one of the most effective and fast-acting treatment options for depressive episodes. Little is known, however, about ECT's enabling brain (neuro)plasticity effects, particular for plasticity of white matter pathway. **Materials and Methods.** We collected longitudinal diffusion tensor imaging in the first-episode, drug-naïve major depressive disorder (MDD) patients ( $n = 24$ ) before and after a predefined time window ECT treatment. We constructed large-scale anatomical networks derived from white matter fiber tractography and evaluated the topological reorganization using graph theoretical analysis. We also assessed the relationship between topological reorganization with improvements in depressive symptoms. **Results.** Our investigation revealed three main findings: (1) the small-worldness was persistent after ECT series; (2) anatomical connections changes were found in limbic structure, temporal and frontal lobes, in which the connection changes between amygdala and parahippocampus correlate with depressive symptom reduction; (3) significant nodal strength changes were found in right paralimbic network. **Conclusions.** ECT elicits neuroplastic processes associated with improvements in depressive symptoms that act to specific local ventral frontolimbic circuits, but not small-world property. Overall, ECT induced topological reorganization in large-scale brain structural network, opening up new avenues to better understand the mode of ECT action in MDD.

## 1. Introduction

Patients with major depressive disorder (MDD) typically experience persistent depressed/sad mood and are highly debilitating [1]. Although antidepressant medications and psychotherapeutic treatments are currently available in many patients, electroconvulsive therapy (ECT) is thought to be the most effective and fast-acting remission for depressive episodes [2, 3]. However, little is known about ECT's enabling brain (neuro)plasticity effects [4], particular for plasticity of white matter pathway [5].

Accumulated evidence suggests that the act of ECT on brain structure associated with clinical state and treatment response in MDD [4]. The hippocampal, amygdalar, and striatal subcortical centers have shown increases in gray

matter volume after ECT series, suggesting ECT-induced brain structure neuroplasticity related to improved clinical response [6–9]. Furthermore, diffusion tensor imaging (DTI) can quantify the fiber orientation and integrity of white matter (WM) pathway within neural network. Early specific regions of interest- (ROI-) based DTI studies suggest a trend of increased WM microstructure (fractional anisotropy [FA]) in the hippocampal formation and frontal and temporal lobes following ECT treatment [10, 11]. Recently, whole-brain DTI work found increases of FA in dorsal frontolimbic circuits that are modulated by ECT therapy and relate to therapeutic response [12]. Taken together, MDD do not result from a deficit in a single brain region and local neuronal circuits which contributed to ECT-related structural plasticity. However, it is likely that a large-scale network perspective

is necessary to explain their complex etiology and ECT's enabling brain neuroplasticity.

The human brain is structurally and functionally organized into connectome [13, 14]. Depression is also associated with abnormal topological organization of brain networks [15–17], which are valuable for diagnosis neuromarkers and treatment evaluation. In the current study, we collected longitudinal DTI in the first-episode, drug-naïve MDD patients before and after a predefined time window ECT treatment. We constructed large-scale anatomical networks derived from WM fiber tractography and evaluated the dynamic alteration of global, nodal topological characteristics and the strength of each connection using graph theoretical analysis. We aimed to directly answer whether neuroplasticity of ECT related to large-scale anatomical connectome. We also assessed the relationship between topological organization with depressive severity during the ECT series, to test above ECT-related network plasticity would accounts for improvements in depressive symptoms.

## 2. Materials and Methods

**2.1. Participants.** All examinations were carried out under the guidance of the Declaration of Helsinki 1975. The protocol was reviewed and approved by the Local Medical Ethics Committee of the First Affiliated Hospital of Chongqing Medical University. All these patients were first-episode MDD, without any treatment history before. The diagnosis of MDD was confirmed with a structured clinical interview for DSM-IV-TR Disorders (SCID-I/P, Chinese version) [18], along with scores  $\geq 21$  on the 24-item Hamilton Rating Scale for Depression (HAM-D) [19]. According to the clinical guidelines of the Canadian Network for Mood and Anxiety Treatments, ECT could be considered as first-line treatment for depression with acute suicidal ideation, psychotic features, and catatonia [20]. Consequently, all the patients were required to have at least one of the above three characteristics. Patients were excluded if they (i) had any history of alcohol or drug abuse, neurological or serious physical disease, and morphological anomaly of the brain and (ii) had any surgical electronic or metal implants. MDD patients were scanned before one day of starting the ECT sessions. All the patients were scanned for the second time at least >1 day after eight ECT sessions. We did not control the medicine of subjects during this study, which was decided by their clinician independently. After the first ECT, most patients were given antidepressants over the course of ECT.

**2.2. ECT Procedures.** The patients underwent modified bitemporal ECT using a brief-pulse, constant current apparatus Thymatron (TM) DGx (Somatics LLC, Lake Bluff, IL, USA) at the Department of Psychiatry of the First Affiliated Hospital of Chongqing Medical University. The first three ECT administrations occurred on consecutive days, and the remaining ECT administrations were conducted every other day with a break of weekends until at least eight times of ECT [22]. After that, ECT treatments were continued if clinical depressive symptoms had not improved sufficiently, which

were also decided by a clinician, but lasted at most 12 times of ECTs. The initial dosage selected was normalized, based on sex, age, and weight. Anesthesia was induced with propofol (1.5–2 mg/kg) and succinylcholine (0.5–1 mg/kg). We applied a stimulus dose up to 1.5–2 times above seizure threshold [20].

**2.3. Clinical Assessments.** The patients received scanning and depressive symptoms assessments at two separate time points: (i) within one day before their first ECT session (pre-ECT) and (ii) the day after completion of eight ECT sessions (post-ECT). Ratings of depressive symptoms were collected at each time point using the 24-item HAM-D.

**2.4. Image Acquisition and Preprocessing.** We acquired imaging data using a 3.0 Tesla MRI system (GE Signa) in the First Affiliated Hospital of Chongqing Medical University. We used foam padding to minimize head motion. We acquired 3D T1-weighted anatomical images (repetition time = 8.35 ms, echo time = 3.27 ms, flip angle =  $12^\circ$ , field of view =  $240 \times 240 \text{ mm}^2$ , matrix =  $256 \times 256$ , slice thickness = 1 mm, and number of slices = 156 sagittal slices). We also acquired the diffusion-weighted images using spin echo-based echo planar imaging sequence (25 noncollinear directions,  $b = 1000 \text{ s/mm}^2$ , one volume without diffusion-weighted  $b = 0 \text{ s/mm}^2$ , number of slices = 37 axial slices, repetition time = 10000 ms, echo time = 86.7 ms, flip angle =  $90^\circ$ , field of view =  $256 \times 256 \text{ mm}^2$ , matrix =  $256 \times 256$ , slice thickness = 3 mm, and number of averages = 2).

DTI data were preprocessed and analyzed using the Pipeline for Analyzing Brain Diffusion Images toolkit (PANDA; <http://www.nitrc.org/projects/panda>) [24], which synthesizes procedures in FSL (<http://fsl.fmrib.ox.ac.uk/fsl>) and the diffusion toolkit. DTI data were coregistered to the B0 image and corrected for distortion induced by eddy currents. Diffusion tensor models were estimated by using the linear least-squares fitting method at each voxel by using the diffusion toolkit. Whole-brain MW fiber tracking was performed in the native diffusion space for each subject by using the fiber assignment with the continuous tracking algorithm. Path tracking proceeded until either the fractional anisotropy was less than 0.15 or the angle between the current and the previous path segment was greater than 35 degrees, as in our previous studies [25–27]. Fibers less than 10 mm or with obvious false paths were discarded.

**2.5. Anatomical Connectome Construction.** To determine the nodes of anatomical connectivity networks, we used the automated anatomical labelling (AAL) template [23] to parcellate the whole cerebral cortex into 90 noncerebellar anatomical ROIs. A list of anatomical labels of these ROIs are presented in Table 2. The ROIs were transformed into each subject's native diffusion space. Specifically, we coregistered the individual 3D-T1 images to B0 images and normalized the 3D T1 images to the Montreal Neurologic Institute space by a 12-parameter nonlinear transformation. These transformation parameters were inversed and applied to 90 ROIs.

In this native diffusion space, anatomical connectivity between ROI  $i$  and  $j$  was defined as the number of fibers connecting  $i$  and  $j$ . We selected fiber number as measurement because it is sensitive to the topological difference between patients with distinct outcomes. The raw network connectivity (fiber number) was scaled to the total volume of ROI  $i$  and  $j$  [25]. For each subject, the anatomical connectivity matrix “ $M$ ” had  $90 \times 90$  entries, with  $A_{ij}$  corresponding to the weighted connectivity between ROI  $i$  and  $j$ , also referred to as the link between nodes  $i$  and  $j$ .

**2.6. Graph Theoretic Measures.** Graph theory enables the quantification of network topological properties [28]. Graph measures for each individual connectivity matrix were calculated with the Brain Connectivity Toolbox (<https://sites.google.com/site/bctnet/>). Small-worldness is an optimal architecture balancing the segregation and integration of information, with similar path length ( $\lambda = L_{\text{net}}^w/L_{\text{random}}^w \approx 1$ ) but higher clustering coefficient ( $\gamma = C_{\text{net}}^w/C_{\text{random}}^w > 1$ ) than a random network [29]. We evaluated the typical properties of a small-worldness ( $\sigma = \gamma/\lambda$ ) that is typically larger than one. We selected nodal strength to estimate the topological feature of each node, because its high test-retest reliability [30] and clear neurophysiology relevance [31]. Nodal strength ( $S_i$ ) was computed as the sum of the weights of all the connections of node  $i$ . It quantifies the extent to which a node is relevant to the graph.

**2.7. Statistical Analysis.** To examine how anatomical architectures reorganized following ECT, we performed a paired  $t$ -test (post-ECT versus pre-ECT) for network measures. The anatomical connectivity edge, small-worldness, and nodal strength were analyzed, respectively. In addition, to explore associations between network measures changes (post-ECT – pre-ECT) and the depressive symptom reduction (pre-ECT – post-ECT HAMD scores) in patients after ECT ( $n = 22$ ), we calculated the Pearson correlation coefficients. We also computed the relationship between the anatomical measures of the pre-ECT data and the duration of depressive episode. As these analyses were exploratory, we used an uncorrected statistical significance level of  $P < 0.05$ .

### 3. Results

**3.1. Clinical Data.** Twenty-four first-episode, drug-naïve MDD patients (15 female, all right-handed, age [mean  $\pm$  SD]:  $28.88 \pm 10.77$  years) who received eight ECT series have enrolled (Table 1). Note that two patients’ clinical data were missed. Patients’ HAMD score before ECT was  $28.14 \pm 5.43$ , indicating severe depression. After ECT series, depressive symptoms (HAMD score) significantly reduced ( $T_{21} = 11.92$ ,  $P < 0.0001$ , paired  $t$ -test) (Table 1), indicating excellent therapeutic effects of ECT. Nineteen of the 22 patients (86.36%) were ECT responders whose depressive symptoms reduced at least to 50% compared to pre-ECT HAMD [32]. Ten of the 22 patients (45%) were in remission—that is, their HAMD scores were  $\leq 7$ —after the ECT series. After the first

TABLE 1: Demographic and clinical characteristics of patients.

Demographics	MDD ( $n = 24$ )		
Age (years)	$28.88 \pm 10.77$		
Sex (male/female)	9/15		
Education (years)	$11.96 \pm 2.79$		
Age of onset (years)*	$26.62 \pm 12.12$		
Suicidal thought or behavior (%)*	77.27		
Duration of depressive episode (months)*	$2.83 \pm 5.43$		
	Pre-ECT	Post-ECT	$P$ value
HAMD*	$28.14 \pm 5.43$	$8.81 \pm 4.20$	$<0.0001^a$

MDD, major depressive disorder; HAMD, Hamilton Rating Scale for Depression; ECT, electroconvulsive therapy.

The values are illustrated as mean  $\pm$  SD.

\*Two patients’ clinical data missed.

<sup>a</sup>Paired  $t$ -test.

ECT, 20 of the 22 patients (90.9%) were given antidepressants over the course of ECT.

**3.2. ECT Effects on Topological Reorganization.** The anatomical connectome exhibited typical features of small-world topology no matter pre- or post-ECT. However, no significant difference was found between post- and pre-ECT ( $T = 0.77$ ,  $P = 0.447$ ).

Eight anatomical connections showed reorganization feature after ECT series ( $P < 0.01$ , corrected). The six increased connections were mainly located in limbic structure, temporal and frontal lobes, for example, amygdala (AMYG) versus parahippocampal gyrus (PHG), inferior temporal gyrus (ITG) versus middle temporal gyrus (MTG), and middle temporal pole (TPOsup) versus orbital inferior frontal gyrus (ORBinf), while the two connections, including anterior cingulate cortex (ACC) versus medial superior frontal gyrus (SFGmed) and precuneus (PCUN) versus superior occipital gyrus (SOG), showed decreased connection. In addition, the connection changes between amygdala and parahippocampus correlated with depressive symptom reduction (Figure 1).

A comparison of post-ECT treatment and pre-ECT treatment on nodal strength revealed significant increases in right PHG ( $T = 2.207$ ,  $P = 0.037$ ) and ORBinf ( $T = 2.073$ ,  $P = 0.049$ ) and decreases in left fusiform gyrus (FFG) ( $T = -2.285$ ,  $P = 0.031$ ) (Figure 2). The nodal strength changes of FFG correlated with depressive symptom reduction (Figure 2).

There is no significant correlation between the anatomical measures of the pre-ECT data and the duration of depressive episode.

### 4. Discussion

We investigated the reorganization mechanism of anatomical connectome, rather than local brain structure alone, in first-episode, drug-naïve MDD patients subsequent to ECT treatments. Our investigation revealed three main findings:

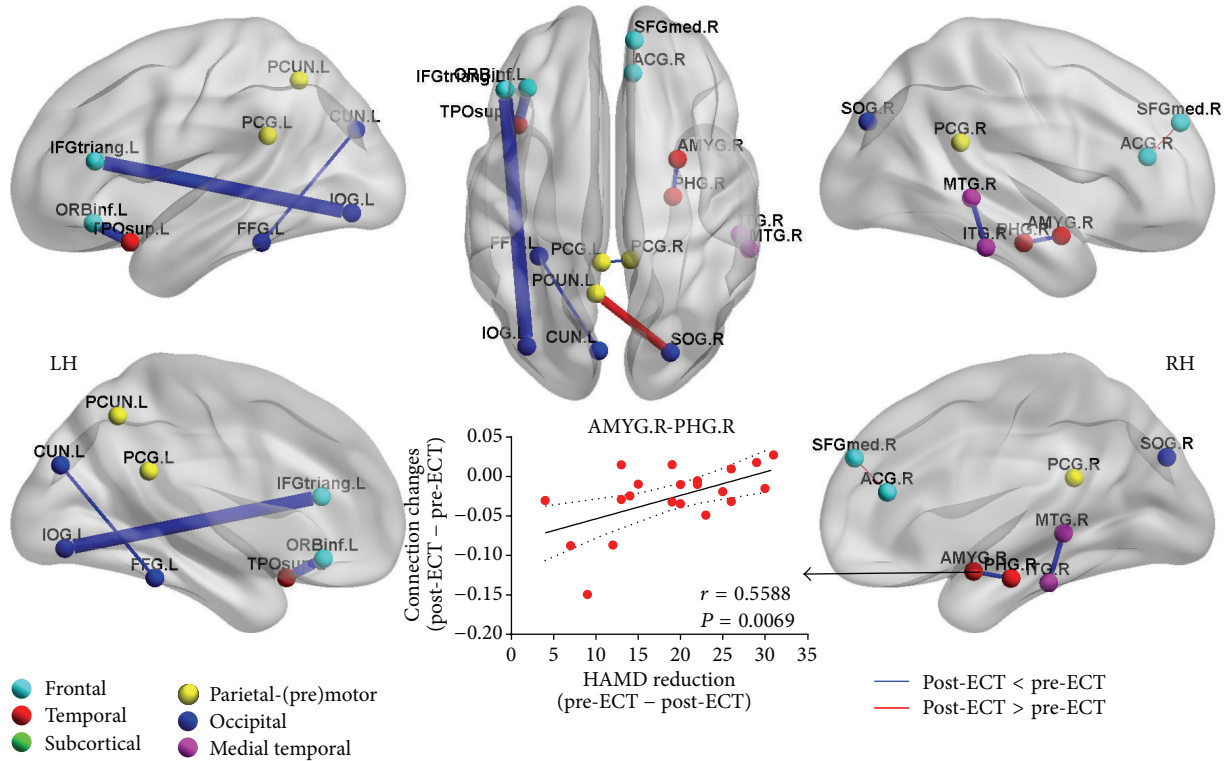


FIGURE 1: Significant differences in anatomical connection between post-ECT and pre-ECT. Nodes (individual ROIs) were differently colored according to the six anatomical modules listed in Table 2. Undirected edges were differently colored according to the significantly larger connection ( $P < 0.05$ ). Nodes and edges are presented on inflated surface maps by BrainNet Viewer (<http://www.nitrc.org/projects/bnv>) [21]. Scatter-plot indicated the changed connection (post-ECT – pre-ECT) showing significant correlation with the HAMD reduction (pre-ECT – post-ECT).

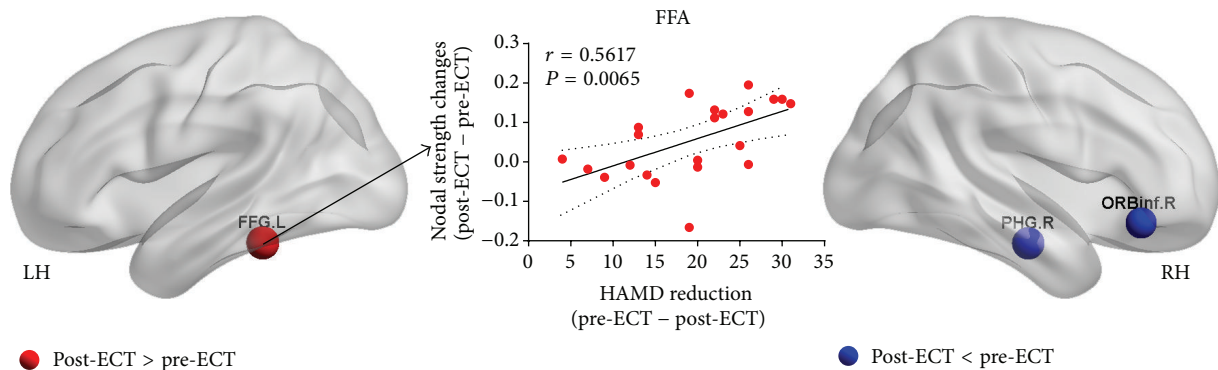


FIGURE 2: Significant differences in nodal strength between post-ECT and pre-ECT. Nodes (individual ROIs) were differently colored according to the significantly increased and decreased nodal strength ( $P < 0.05$ ). Nodes are presented on inflated surface maps by BrainNet Viewer (<http://www.nitrc.org/projects/bnv>) [21]. Scatter-plot indicated the changed nodal strength in fusiform gyrus (post-ECT – pre-ECT) showing significant correlation with the HAMD reduction (pre-ECT – post-ECT).

(1) the small-worldness was persistent after ECT series; (2) significant anatomical connections changes were found in limbic structure, temporal and frontal lobes, in which the connection changes between amygdala and parahippocampus correlated with depressive symptom reduction; and (3) significant nodal strength changes were found in right paralimbic network. These findings would support the

that ECT-induced brain structure neuroplasticity relates to improved clinical response [9].

The human brain is a complex network organized with a small-world property (high efficiency at a low wiring cost) [33]. This economic architecture was altered in the patients, suggesting a disturbance of the normal balance of segregation and integration of information in anatomical connectome in

TABLE 2: Regions of interest (ROI) in the AAL template.

Region name	Abbreviation
<i>Medial temporal</i>	
Amygdala	AMYG
Hippocampus	HIP
Parahippocampal gyrus	PHG
Middle temporal gyrus, temporal pole	TPOsup
Superior temporal gyrus, temporal pole	TPOmid
<i>Subcortical</i>	
Caudate nucleus	CAU
Olfactory cortex	OLF
Palladium	PAL
Putamen	PUT
Thalamus	THA
<i>Occipital</i>	
Calcarine fissure	CAL
Cuneus	CUN
Fusiform gyrus	FFG
Lingual gyrus	LING
Inferior occipital gyrus	IOG
Middle occipital gyrus	MOG
Superior occipital gyrus	SOG
<i>Temporal</i>	
Heschl gyrus	HES
Insula	INS
Inferior temporal gyrus	ITG
Middle temporal gyrus	MTG
Superior temporal gyrus	STG
<i>Frontal</i>	
Anterior cingulate cortex	ACC
Inferior frontal gyrus, opercular	IFGoper
Inferior frontal gyrus, orbital	ORBinf
Inferior frontal gyrus, triangular	IFGtri
Superior frontal gyrus, medial orbital	SFGmorb
Middle frontal gyrus, orbital	MFGorb
Middle frontal gyrus	MFG
Superior frontal gyrus, medial	SFGmed
Superior frontal gyrus, orbital	SFGorb
Superior frontal gyrus	SFG
Gyrus rectus	REG
<i>Parietal-(pre) Motor</i>	
Rolandic operculum	ROL
Angular gyrus	ANG
Median cingulate gyrus	MCC
Posterior cingulate gyrus	PCC
Paracentral lobule	PCL
Inferior parietal gyrus	IPG
Superior parietal gyrus	SPG
Postcentral gyrus	PoCG
Precentral gyrus	PreCG
Precuneus	PCUN
Supplementary motor area	SMA
Supramarginal gyrus	SMG

The abbreviations used in the study differ slightly from the original abbreviations by Tzourio-Mazoyer et al. [23].

depression [15, 17]. For the first time, we revealed whether the small-world property is adaptive following the ECT series. Not surprising, the small-worldness was persistent, given that

the small-world topology reflects an optimal balance between global integration and local special [34], without evidence for ECT-related change in global topology. Furthermore, the functional connectome is thought to be more flexible, while the anatomical connectome is relatively stable [25, 35]. We therefore reasoned that the anatomical connectivity network may be less affected by ECT in MDD.

Although the above-mentioned global topology was persistent, the anatomical connections showed reorganization in ventral and dorsal frontolimbic structure following ECT series. Previous cross-sectional MDD studies have consistently shown that increased anatomical connections were mainly located in cortical-limbic network, particularly in the frontolimbic network [15, 36, 37]. These prior findings support a dysregulation between underactive dorsal and overactive ventral frontolimbic circuitry [12]. Though few DTI studies have assessed treatment effects in MDD patients, our longitudinal results was compatible with prior findings. Our results further demonstrate ECT-related changes in the anatomical connections of selected frontolimbic pathways.

The amygdala and hippocampus play a pivotal role in regulation of emotion and in responses to emotion [38, 39]. The effects of ECT on amygdala and hippocampus volume suggest that ECT-induced brain gray matter structure neuroplasticity relates to improved clinical response [6–9]. We considered the anatomical basis connecting them, rather than alone, because the hippocampus connects with the amygdala and the limbic hypothalamic-pituitary-adrenal (HPA) axis, which are central to the pathophysiology of the MDD [9, 40]. In the current work, the fiber number was used to index the anatomical connection, which are closely related to neurite components of synapses (synaptogenesis) in neuroplasticity model [4]. Decreased connection would reflect axonal pruning [41], which regulate the HPA system activity [42]. Furthermore, these connection changes associate with HMDA reduction, suggesting that ECT-related anatomical connection plasticity may contribute to improvements in depressive symptoms.

The post-ECT and pre-ECT comparison of nodal topological characteristic, for example, nodal strength, revealed alterations or neuroplasticity of network hubs in MDD patients. The characteristic of nodal strength is the most fundamental network measure with high reliability [30], neurophysiology relevance [31], and sensitive neuromarkers of MDD [16]. The changes of nodal strength in right hippocampus and inferior frontal lobe, consistent with prior local brain plasticity in ventral frontolimbic structure. Rather unexpectedly, we also observed that the fusiform gyrus presented increases nodal topological characteristics following ECT series. This change was furthermore shown to be positively correlated with depressive symptoms relevance. A more recent meta-analysis in MDD patients pointed to smaller FA in fusiform gyrus that is involved in inferior longitudinal fasciculus [43]. The role of the fusiform gyrus in memory processing and face recognition may contribute to cognitive vulnerability to depression [44]. Our finding of increased nodal strength under this gyrus may provide structural evidence of white matter plasticity in the neural circuit in MDD from a connectome point of view.

Several methodological limitations need to be addressed. First, in absence of a healthy control group, we would not assess the normalization of aberrant network measures when compared post-ECT depression group and controls [45] and predict the treatment response/remission when compared pre-ECT depression group and controls [46]. Second, the patients were only scanned twice within a predefined time window. More scans would conduce to explore the relation between times of ECT and neuroimaging changes for each patient [47]. In addition, although ECT showed antidepressant therapeutic effect, the ECT-related cognitive side effects have not been considered here, which are worthy of concern in future studies [48]. Finally, although diffusion tensor modal is an effective way to investigate white matter networks, some advanced approaches (e.g., diffusion spectrum imaging) may lead to more accurate tractography results, particularly in areas with cross fibers.

## 5. Conclusion

ECT elicits neuroplastic processes associated with improvements in depressive symptoms that act to specific local ventral frontolimbic circuits, but not global small-world property. ECT-related changes in the anatomical connections of selected amygdala and hippocampus associate with axonal pruning, which regulate the HPA system activity. Our finding of increased nodal strength under fusiform gyrus may provide structural evidence of white matter plasticity in the neural circuit in MDD from a connectome point of view for adapting cognitive vulnerability. Overall, ECT induced topological reorganization in large-scale brain structural network, opening up new avenues to better understand the mode of ECT action in MDD.

## Conflict of Interests

The authors declare that there is no potential conflict of interests regarding the publication of this paper.

## Authors' Contribution

Jinkun Zeng, Qinghua Luo, and Lian Du contributed to data collection and wrote the paper. Lian Du and Wei Liao contributed to data analyses. Wei Liao, Yongmei Li, Haixia Liu, Dan Liu, Yixiao Fu, Haitang Qiu, Xirong Li, and Tian Qiu helped revise the paper. Huaqing Meng designed the experiment and revised the paper. Jinkun Zeng, Qinghua Luo, and Lian Du contributed equally to this work.

## Acknowledgments

This work was supported by the grants from the National Key Clinical Specialist Construction Programs of China ([2013] 544), the Natural Science Foundation of Chongqing Province (no. cstc2014yykfA110030), and the fund of West China Psychiatric Association (wcpafund2013-9).

## References

- [1] D. J. Kupfer, E. Frank, and M. L. Phillips, "Major depressive disorder: new clinical, neurobiological, and treatment perspectives," *The Lancet*, vol. 379, no. 9820, pp. 1045–1055, 2012.
- [2] M. Fink, "ECT has proved effective in treating depression," *Nature*, vol. 403, no. 6772, p. 826, 2000.
- [3] H.-P. Spaans, P. Sienaert, F. Bouckaert et al., "Speed of remission in elderly patients with depression: electroconvulsive therapy v. medication," *British Journal of Psychiatry*, vol. 206, no. 1, pp. 67–71, 2015.
- [4] F. Bouckaert, P. Sienaert, J. Obbels et al., "ECT: its brain enabling effects: a review of electroconvulsive therapy-induced structural brain plasticity," *Journal of ECT*, vol. 30, no. 2, pp. 143–151, 2014.
- [5] D. P. Devanand, A. J. Dwork, E. R. Hutchinson, T. G. Bolwig, and H. A. Sackeim, "Does ECT alter brain structure?" *The American Journal of Psychiatry*, vol. 151, no. 7, pp. 957–970, 1994.
- [6] P. Nordanskog, U. Dahlstrand, M. R. Larsson, E.-M. Larsson, L. Knutsson, and A. Johanson, "Increase in hippocampal volume after electroconvulsive therapy in patients with depression: a volumetric magnetic resonance imaging study," *Journal of ECT*, vol. 26, no. 1, pp. 62–67, 2010.
- [7] P. Nordanskog, M. R. Larsson, E.-M. Larsson, and A. Johanson, "Hippocampal volume in relation to clinical and cognitive outcome after electroconvulsive therapy in depression," *Acta Psychiatrica Scandinavica*, vol. 129, no. 4, pp. 303–311, 2014.
- [8] I. Tendolkar, M. van Beek, I. van Oostrom et al., "Electroconvulsive therapy increases hippocampal and amygdala volume in therapy refractory depression: a longitudinal pilot study," *Psychiatry Research—Neuroimaging*, vol. 214, no. 3, pp. 197–203, 2013.
- [9] S. H. Joshi, R. T. Espinoza, T. Pirnia et al., "Structural plasticity of the hippocampus and amygdala induced by electroconvulsive therapy in major depression," *Biological Psychiatry*, 2015.
- [10] K. Nobuhara, G. Okugawa, T. Minami et al., "Effects of electroconvulsive therapy on frontal white matter in late-life depression: a diffusion tensor imaging study," *Neuropsychobiology*, vol. 50, no. 1, pp. 48–53, 2004.
- [11] K. Szabo, J. G. Hirsch, M. Krause et al., "Diffusion weighted MRI in the early phase after electroconvulsive therapy," *Neurological Research*, vol. 29, no. 3, pp. 256–259, 2007.
- [12] H. Lyden, R. T. Espinoza, T. Pirnia et al., "Electroconvulsive therapy mediates neuroplasticity of white matter microstructure in major depression," *Translational Psychiatry*, vol. 4, article e380, 2014.
- [13] O. Sporns, G. Tononi, and R. Kötter, "The human connectome: a structural description of the human brain," *PLoS Computational Biology*, vol. 1, no. 4, article e42, 2005.
- [14] A. Fornito, A. Zalesky, and M. Breakspear, "The connectomics of brain disorders," *Nature Reviews Neuroscience*, vol. 16, no. 3, pp. 159–172, 2015.
- [15] M. S. Korgaonkar, A. Fornito, L. M. Williams, and S. M. Grieve, "Abnormal structural networks characterize major depressive disorder: a connectome analysis," *Biological Psychiatry*, vol. 76, no. 7, pp. 567–574, 2014.
- [16] Q. Gong and Y. He, "Depression, neuroimaging and connectomics: a selective overview," *Biological Psychiatry*, vol. 77, no. 3, pp. 223–235, 2015.
- [17] F. Bai, N. Shu, Y. Yuan et al., "Topologically convergent and divergent structural connectivity patterns between patients

- with remitted geriatric depression and amnesic mild cognitive impairment,” *Journal of Neuroscience*, vol. 32, no. 12, pp. 4307–4318, 2012.
- [18] M. B. First, R. L. Spitzer, M. Gibbon, and J. B. W. Williams, *Structured Clinical Interview for DSM-IV-TR Axis I Disorders—Patient Edition*, (SCID-I/P, 11/2002 Revision), New York State Psychiatric Institute, New York, NY, USA, 2002.
- [19] C. H. Kellner, R. G. Knapp, G. Petrides et al., “Continuation electroconvulsive therapy vs pharmacotherapy for relapse prevention in major depression: a multisite study from the consortium for research in electroconvulsive therapy (CORE),” *Archives of General Psychiatry*, vol. 63, no. 12, pp. 1337–1344, 2006.
- [20] S. H. Kennedy, R. Milev, P. Giacobbe et al., “Canadian Network for Mood and Anxiety Treatments (CANMAT) Clinical guidelines for the management of major depressive disorder in adults. IV. Neurostimulation therapies,” *Journal of Affective Disorders*, vol. 117, supplement 1, pp. S44–S53, 2009.
- [21] M. Xia, J. Wang, and Y. He, “BrainNet Viewer: a network visualization tool for analyzing brain connectomics,” *PLoS ONE*, vol. 8, no. 7, Article ID e68910, 2013.
- [22] E. Z. Reininghaus, B. Reininghaus, R. Ille et al., “Clinical effects of electroconvulsive therapy in severe depression and concomitant changes in cerebral glucose metabolism—an exploratory study,” *Journal of Affective Disorders*, vol. 146, no. 2, pp. 290–294, 2013.
- [23] N. Tzourio-Mazoyer, B. Landeau, D. Papathanassiou et al., “Automated anatomical labeling of activations in SPM using a macroscopic anatomical parcellation of the MNI MRI single-subject brain,” *NeuroImage*, vol. 15, no. 1, pp. 273–289, 2002.
- [24] Z. Cui, S. Zhong, P. Xu, Y. He, and G. Gong, “PANDA: a pipeline toolbox for analyzing brain diffusion images,” *Frontiers in Human Neuroscience*, vol. 7, article 42, 2013.
- [25] Z. Zhang, W. Liao, H. Chen et al., “Altered functional-structural coupling of large-scale brain networks in idiopathic generalized epilepsy,” *Brain*, vol. 134, no. 10, pp. 2912–2928, 2011.
- [26] W. Liao, Z. Zhang, Z. Pan et al., “Default mode network abnormalities in mesial temporal lobe epilepsy: a study combining fMRI and DTI,” *Human Brain Mapping*, vol. 32, no. 6, pp. 883–895, 2011.
- [27] G.-J. Ji, Z. Zhang, Q. Xu, Y.-F. Zang, W. Liao, and G. Lu, “Generalized tonic-clonic seizures: aberrant interhemispheric functional and anatomical connectivity,” *Radiology*, vol. 271, no. 3, pp. 839–847, 2014.
- [28] C. J. Stam, “Modern network science of neurological disorders,” *Nature Reviews Neuroscience*, vol. 15, no. 10, pp. 683–695, 2014.
- [29] D. J. Watts and S. H. Strogatz, “Collective dynamics of ‘small-world’ networks,” *Nature*, vol. 393, no. 6684, pp. 440–442, 1998.
- [30] J.-H. Wang, X.-N. Zuo, S. Gohel, M. P. Milham, B. B. Biswal, and Y. He, “Graph theoretical analysis of functional brain networks: test-retest evaluation on short- and long-term resting-state functional MRI data,” *PLoS ONE*, vol. 6, no. 7, Article ID e21976, 2011.
- [31] X. Liang, Q. Zou, Y. He, and Y. Yang, “Coupling of functional connectivity and regional cerebral blood flow reveals a physiological basis for network hubs of the human brain,” *Proceedings of the National Academy of Sciences of the United States of America*, vol. 110, no. 5, pp. 1929–1934, 2013.
- [32] M. M. Husain, A. J. Rush, M. Fink et al., “Speed of response and remission in major depressive disorder with acute electroconvulsive therapy (ECT): a consortium for research in ECT (CORE) report,” *Journal of Clinical Psychiatry*, vol. 65, no. 4, pp. 485–491, 2004.
- [33] E. Bullmore and O. Sporns, “The economy of brain network organization,” *Nature Reviews Neuroscience*, vol. 13, no. 5, pp. 336–349, 2012.
- [34] O. Sporns, G. Tononi, and G. M. Edelman, “Theoretical neuroanatomy: relating anatomical and functional connectivity in graphs and cortical connection matrices,” *Cerebral Cortex*, vol. 10, no. 2, pp. 127–141, 2000.
- [35] C.-H. Park, S. Y. Kim, Y.-H. Kim, and K. Kim, “Comparison of the small-world topology between anatomical and functional connectivity in the human brain,” *Physica A: Statistical Mechanics and Its Applications*, vol. 387, no. 23, pp. 5958–5962, 2008.
- [36] M. S. Korgaonkar, N. J. Cooper, L. M. Williams, and S. M. Grieve, “Mapping inter-regional connectivity of the entire cortex to characterize major depressive disorder: a whole-brain diffusion tensor imaging tractography study,” *NeuroReport*, vol. 23, no. 9, pp. 566–571, 2012.
- [37] P. Fang, L.-L. Zeng, H. Shen et al., “Increased cortical-limbic anatomical network connectivity in major depression revealed by diffusion tensor imaging,” *PLoS ONE*, vol. 7, no. 9, Article ID e45972, 2012.
- [38] N. A. Groenewold, E. M. Opmeer, P. de Jonge, A. Aleman, and S. G. Costafreda, “Emotional valence modulates brain functional abnormalities in depression: evidence from a meta-analysis of fMRI studies,” *Neuroscience and Biobehavioral Reviews*, vol. 37, no. 2, pp. 152–163, 2013.
- [39] S. J. Russo and E. J. Nestler, “The brain reward circuitry in mood disorders,” *Nature Reviews Neuroscience*, vol. 14, no. 9, pp. 609–625, 2013.
- [40] J. S. Snyder, A. Soumier, M. Brewer, J. Pickel, and H. A. Cameron, “Adult hippocampal neurogenesis buffers stress responses and depressive behaviour,” *Nature*, vol. 476, no. 7361, pp. 458–461, 2011.
- [41] K. H. Bockhorst, P. A. Narayana, R. Liu et al., “Early postnatal development of rat brain: in vivo diffusion tensor imaging,” *Journal of Neuroscience Research*, vol. 86, no. 7, pp. 1520–1528, 2008.
- [42] A. Surget, A. Tanti, E. D. Leonardo et al., “Antidepressants recruit new neurons to improve stress response regulation,” *Molecular Psychiatry*, vol. 16, no. 12, pp. 1177–1188, 2011.
- [43] Y. Liao, X. Huang, Q. Wu et al., “Is depression a disconnection syndrome? Meta-analysis of diffusion tensor imaging studies in patients with MDD,” *Journal of Psychiatry and Neuroscience*, vol. 38, no. 1, pp. 49–56, 2013.
- [44] G. A. van Wingen, P. van Eijndhoven, H. R. Cremers et al., “Neural state and trait bases of mood-incongruent memory formation and retrieval in first-episode major depression,” *Journal of Psychiatric Research*, vol. 44, no. 8, pp. 527–534, 2010.
- [45] C. C. Abbott, T. Jones, N. T. Lemke et al., “Hippocampal structural and functional changes associated with electroconvulsive therapy response,” *Translational Psychiatry*, vol. 4, article e483, 2014.
- [46] J. A. van Waarde, H. S. Scholte, L. J. B. van Oudheusden, B. Verwey, D. Denys, and G. A. van Wingen, “A functional MRI marker may predict the outcome of electroconvulsive therapy in severe and treatment-resistant depression,” *Molecular Psychiatry*, vol. 20, no. 5, pp. 609–614, 2015.
- [47] A. Merkl, F. Schubert, A. Quante et al., “Abnormal cingulate and prefrontal cortical neurochemistry in major depression after

electroconvulsive therapy,” *Biological Psychiatry*, vol. 69, no. 8, pp. 772–779, 2011.

- [48] M. Semkowska and D. M. McLoughlin, “Objective cognitive performance associated with electroconvulsive therapy for depression: a systematic review and meta-analysis,” *Biological Psychiatry*, vol. 68, no. 6, pp. 568–577, 2010.

## Research Article

# Alterations of Regional Spontaneous Brain Activity and Gray Matter Volume in the Blind

Aili Jiang,<sup>1</sup> Jing Tian,<sup>1</sup> Rui Li,<sup>1</sup> Yong Liu,<sup>2</sup> Tianzi Jiang,<sup>2</sup> Wen Qin,<sup>1</sup> and Chunshui Yu<sup>1</sup>

<sup>1</sup>Department of Radiology and Tianjin Key Laboratory of Functional Imaging, Tianjin Medical University General Hospital, Tianjin 300052, China

<sup>2</sup>Brainnetome Center, Institute of Automation, Chinese Academy of Sciences, Beijing 100190, China

Correspondence should be addressed to Wen Qin; [wayne.wenqin@gmail.com](mailto:wayne.wenqin@gmail.com)

Received 23 December 2014; Revised 20 March 2015; Accepted 25 March 2015

Academic Editor: Lucas Pozzo-Miller

Copyright © 2015 Aili Jiang et al. This is an open access article distributed under the Creative Commons Attribution License, which permits unrestricted use, distribution, and reproduction in any medium, provided the original work is properly cited.

Visual deprivation can induce alterations of regional spontaneous brain activity (RSBA). However, the effects of onset age of blindness on the RSBA and the association between the alterations of RSBA and brain structure are still unclear in the blind. In this study, we performed resting-state functional and structural magnetic resonance imaging on 50 sighted controls and 91 blind subjects (20 congenitally blind, 27 early blind, and 44 late blind individuals). Compared with the sighted control, we identified increased RSBA in the blind in primary and high-level visual areas and decreased RSBA in brain regions which are ascribed to sensorimotor and salience networks. In contrast, blind subjects exhibited significantly decreased gray matter volume (GMV) in the visual areas, while they exhibited significantly increased GMV in the sensorimotor areas. Moreover, the onset age of blindness was negatively correlated with the GMV of visual areas in blind subjects, whereas it exerted complex influences on the RSBA. Finally, significant negative correlations were shown between RSBA and GMV values. Our results demonstrated system-dependent, inverse alterations in RSBA and GMV after visual deprivation. Furthermore, the onset age of blindness has different effects on the reorganizations in RSBA and GMV.

## 1. Introduction

Visual deprivation can induce a series of structural and functional reorganizations of the brain to better adapt to external environments with the remaining modality, especially in individuals with visual deprivation at an early developmental age. For example, early visual deprivation can remold the visual areas to cross-modal process signals from non-visual modalities, such as tactile [1, 2], auditory [3–5], and even olfactory processes [6]. Furthermore, a large number of studies have demonstrated that the visual areas have increased baseline metabolism and blood flow [7–9], decreased anatomical network efficiency [10], and altered resting-state functional connectivity [11] in congenitally blind (CB) or early blind (EB) subjects. Although impaired visual areas have also been reported, limited studies have demonstrated that late blind (LB) individuals had different alteration patterns with CB/EB individuals, including the cross-modal activity [4, 12, 13], baseline glucose metabolism [9], cortical

thickness [8, 14, 15], gray matter content [16], anatomical connectivity [10], white matter integrity [17], and functional connectivity density (FCD) [18]. These findings indicate that visual deprivation at different developmental stages may influence both functional and structural organizations of the brain [19]. However, it is unclear if the age of onset of blindness influences the regional spontaneous brain activity.

Spontaneous neuronal activity can be identified by low-frequency fluctuations in the blood oxygen level dependent (BOLD) signal of functional magnetic resonance imaging (fMRI) under resting-state [20]. As a data-driven resting-state fMRI technique, regional homogeneity (ReHo) measures the functional coherence of BOLD fluctuations of a given voxel with its nearest neighbors. It can be used to evaluate the regional spontaneous brain activities based on the hypothesis that significant brain activities would more likely occur in clusters than in a single voxel [21]. This technique has been successfully applied to investigate the spontaneous brain functional organization in healthy subjects [22] and to

elucidate the neural pathological mechanisms of a variety of neurological and psychiatric diseases [23, 24]. Regarding the functional alterations of regional spontaneous brain activity after visual deprivation, one recent study demonstrated that EB had increased ReHo in the primary and higher visual areas, which indicates an abnormal cortical development and/or experience-dependent plasticity secondary to early visual deprivation [25]. However, the effects of visual deprivation during different developmental periods on the regional spontaneous brain activity are rarely known.

Another concerning issue is the potential associations between the alterations of regional spontaneous brain activity and brain structural organization in blind individuals. Although abundant studies have demonstrated that the visual-deprived brain experienced both functional and structural alterations (as described in the first paragraph), the relationships between them have not been clearly identified. In a recent study, Anurova et al. combined the measurements of cortical thickness and functional activation evoked by attention-demanding auditory tasks. They identified a significant negative correlation between the cortical thickness and cortical activation in the visual areas in the EB [3]. This finding indicates that pruning of exuberant connections during early development increases the selectivity and effectiveness of synaptic activity and therefore leads to stronger activation, which provides a structural basis for cross-modal occipital activation. Thus, clarification of the association between the alterations of regional spontaneous brain activity and brain structural organization may help our understanding of the neural mechanisms of functional alterations during the resting-state.

In this study, we combined voxel-wise ReHo and gray matter volume (GMV) approaches to investigate the alterations of the regional spontaneous brain activities and brain structures and their relationships in blind individuals. The functional and structural alterations of the brain after visual deprivation comprise the synthetic interactions among developmental, plastic, and degenerative mechanisms [14]. The developmental mechanisms play important roles in both the CB and EB; and the capacity for cross-modal plasticity is substantially stronger in the CB/EB than the LB, whereas degenerative mechanisms exert their effects on all blind subjects. Thus, we first hypothesized that visual deprivation during different developmental periods may induce diverse patterns of alterations in ReHo and GMV in the visual areas. Specifically, because earlier studies have demonstrated that the CB/EB experienced stronger increases in cross-modal activity [4, 26] and functional connectivity density [18], while they experienced smaller decreases in white matter integrity [17] than the LB in the visual pathway, we predicted that blind subjects who lost their vision at an earlier developmental age would experience a greater increase in ReHo but less degenerative-induced atrophy in the visual areas. Second, because early studies have shown increased white matter integrity in the corticospinal tract [17] and decreased long-range functional connectivity density in the primary sensorimotor area [18] in both CB and LB, we predicted significant alterations of both ReHo and GMV in the spared sensory areas in all blind groups regardless of the onset of

TABLE 1: Demographic information of the involved blind and sighted subjects.

Group	Gender	Age	Onset age
	(M/F)	Mean $\pm$ std.	Mean $\pm$ std.
CB	13/7	26.6 $\pm$ 5.0	0
EB	20/7	28.9 $\pm$ 7.4	8.0 $\pm$ 3.0
LB	30/14	30.9 $\pm$ 6.5	19.0 $\pm$ 5.3
SC	33/17	28.8 $\pm$ 7.00	/
Statistical value	$\chi^2 = 0.63$	$F = 2.07$	$F = 164.14$
<i>P</i> value	0.889	0.107	<0.001

CB: congenitally blind, EB: early blind, and LB: late blind.

age of blindness. Finally, we expected significant correlations between ReHo and GMV in these areas in the blind, which may help to elucidate the neural mechanisms of functional alteration during the resting-state.

## 2. Materials and Methods

**2.1. Subjects.** The subjects are ninety-one right-handed blind subjects (63 males and 28 females, age range from 20 to 45 years) and 50 sighted controls (SC) (33 males and 17 females, age range from 19 to 44 years) with no history of neurological and psychiatric problems; the excluded criteria included non-right handedness, different onset ages of blindness between the left and right eyes, and low-quality data. The blind subjects were further divided into three subgroups, including 20 congenital blind (CB), 27 early blind (EB) (age of onset  $\leq 12$  years), and 44 late blind (LB) (age of onset  $> 12$  years). None of the CB subjects had a history of pattern vision or memory of visual experience, and none of the acquired blind subjects had experienced pattern vision after visual deprivation. All the SC subjects had normal vision with corrected visual acuity higher than 0.8 (decimal record) [27], and subjects with history of severe ophthalmic diseases, such as glaucoma, cataract, and retinal detachment, were excluded from the study by questionnaire. The demographic and behavioral data of these subjects are shown in Table 1. The study was approved by the Ethics Committee of Tianjin Medical University, and all subjects provided written informed consent.

**2.2. MRI Data Acquisition.** The structural and functional MRI data were acquired using a 3.0-Tesla MR scanner (Magnetom Trio, Siemens, Erlangen, Germany). The subjects' heads were fixed using foam pads to minimize head motion, and earplugs were used to reduce the scanning noise. The resting-state fMRI data were obtained using a gradient echo single-shot echo planar imaging (GRE-SS-EPI) sequence with the following parameters: repetition time (TR) = 2000 ms, echo time (TE) = 30 ms, flip angle (FA) = 90°, matrix = 64  $\times$  64, field of view (FOV) = 220 mm  $\times$  220 mm, slice thickness/gap = 3/1 mm with 32 axial slices, 180 volumes (time points), and a parallel acquisition technique with an acceleration factor of 2. During fMRI scans, all subjects were instructed to keep their eyes closed, relax, do not move, think of nothing in particular, and stay awake. After the fMRI scan,

the fMRI images and subjects' conditions were checked to confirm whether they satisfied the requirements; if not, the fMRI data were abandoned and scanned again. Structural images were acquired using a 3D magnetization-prepared rapid-acquisition gradient echo sequence with the following parameters: TR/TE/inversion time = 2000/2.6/900 ms, FA = 9°, matrix = 256 × 224, FOV = 256 mm × 224 mm, and 176 continuous sagittal slices with a 1 mm thickness.

### 2.3. Data Processing

**2.3.1. Creating Customized Templates.** Data processing was performed using a self-developed software based on Matlab v2009 (MathWorks, Inc., Natick, Massachusetts, USA) and SPM8 (<http://www.fil.ion.ucl.ac.uk/spm>). First, the structural MR images for each subject were segmented into gray matter, white matter, and cerebrospinal fluid using the standard unified segmentation model in SPM8. Then the 3 tissue probabilistic maps (TPMs) of each subject were affinely coregistered with a standard TPM template implemented in SPM8, separately. After that, the 3 types of coarsely coregistered TPMs of all the blind and sighted subjects (112 cases) entered into a nonlinear image coregistration procedure using diffeomorphic anatomical registration through the exponentiated Lie algebra (DARTEL) technique [28], which involves iteratively matching all the selected images to a template generated from their own mean. This step generated 6 sets of tissue templates from coarse to refined contours. These customized DARTEL templates were used for following normalization of the structural and functional MRI data.

**2.3.2. VBM Analysis.** After an initial affine coregistration, the gray matter probabilistic map was nonlinearly warped into the customized DARTEL templates and was resliced with a resolution of 1.5 × 1.5 × 1.5 mm<sup>3</sup>. The GMV of each voxel was obtained by multiplying the gray matter concentration map by the nonlinear determinants derived from the spatial warping step, which in effect represents the relative GMV after removing the confounding effect of variance in individual brain sizes. Finally, the GMV map was smoothed with an isotropic Gaussian kernel of 6 × 6 × 6 mm<sup>3</sup> FWHM.

**2.3.3. ReHo Analysis.** The first 10 volumes of each functional time series were discarded because of the instability of the initial MRI signals caused by incomplete T1 relaxation and to allow the subjects to adapt to the scanning environments. The remaining 170 volumes were subsequently forwarded to a series of preprocessing steps, including slice timing (corrected for acquisition time delay between different slices), rigid realignment (corrected for intervolumetric head motion; all subjects' fMRI data were within the head motion thresholds for a maximum translational displacement lower than 2 mm or a maximum rotational displacement lower than 2.0°), nuisance regression (including six rigid motion parameters and their first derivatives, the mean BOLD signal of cerebrospinal fluid and white matter, and the spike time points with a mean framewise displacement higher than 0.5), band-pass filtering (0.01 to 0.08 Hz), and normalization (two-step coregistration method: first, the mean fMRI image generated

at the realignment step was affinely coregistered with individual structural images; then each filtered functional image was spatially normalized into the customized DARTEL space using the deformation determinants derived from structural normalization step and was resampled into a 3 mm cubic voxel).

The ReHo map for each subject was calculated using REST software (<http://www.restfmri.net/>). ReHo measures the Kendall correlation coefficient of a given voxel and those of its direct neighbor voxels (27 voxels) in a voxel-wise manner [21]. A higher ReHo value of a voxel indicates that the regional activity of this voxel is more similar to its neighbors. We also calculated the ReHo values with different neighboring strategies (7 voxels and 19 voxels, resp.) to explore if neighboring strategies would influence our result [21]. The calculated ReHo values for each subject were further scaled by the mean ReHo of the whole brain to reduce the effect of individual variation. Finally, the scaled ReHo maps underwent spatial smoothing using a Gaussian kernel with full width half maximum (FWHM) of 6 × 6 × 6 mm<sup>3</sup>.

**2.4. Statistical Analysis.** One-way analysis of variance (ANOVA) was conducted in a voxel-wise manner to investigate the intergroup differences in ReHo and GMV values among the four groups with age and gender as nuisance covariates within the cerebral gray matter mask. The statistical *F* map was corrected for multiple comparisons using a Monte Carlo simulation method at the cluster level (Alphasim algorithm, voxel-wise  $P < 0.01$ , iteration 5000 times, and corrected cluster-wise  $P < 0.05$ ), resulting in a corrected cluster size of 34 voxels for ReHo analyses and 260 voxels for GMV analyses. The clusters with statistical significance in ReHo and GMV values were defined as the regions of interest (ROIs). The voxels within the 9 mm radius sphere centering the peak (also second peak when the cluster occupied multiple brain regions) of each cluster, as well as surviving under the statistical threshold, were assigned to a specific ROI. The second peak was defined as the peak voxel that can be separated from the cluster containing the highest peak when we increase the statistic threshold and had distance at least 30 mm away from the highest peak. Then the mean ReHo and GMV values of each ROI in each subject were extracted. The associations between the ReHo/GMV and the age of onset of blindness were analyzed using partial correlation analyses that are controlled for gender and age effects. Finally, the associations between the ReHo and GMV values in the brain regions that exhibited altered ReHo after blindness were analyzed using partial correlation analyses controlled for age and gender effects ( $P < 0.05$ , uncorrected).

## 3. Results

**3.1. Demographic Information.** As shown in Table 1, there were no significant differences in age (one-way ANOVA,  $F = 2.07$ , and  $P = 0.107$ ) or gender (chi-square test,  $\chi^2 = 0.63$ , and  $P = 0.889$ ) among the 4 groups. There was also no significant group difference in framewise displacement (one-way ANOVA,  $F = 0.425$ , and  $P = 0.716$ ), which indicates that

gender, age, and head motion might not interpret the possible differences in ReHo among the CB, EB, LB, and SC.

**3.2. The Influence of Number of Neighboring Voxels on the ReHo Measurements.** To clarify if the number of neighboring voxels would influence the measurement of ReHo and group comparison in our study, we calculated the ReHo value using 7, 19, and 27 voxels and compared the intergroup differences in ReHo using one-way ANOVA ( $P < 0.05$ , corrected at the cluster level), respectively. We found a lower noise and higher contrast in ReHo map with higher voxel size (see Supplementary Figure S1 in Supplementary Material available online at <http://dx.doi.org/10.1155/2015/141950>). Furthermore, we compared the intergroup differences in ReHo values that were calculated using different neighboring voxels using one-way ANOVA. As shown in Supplementary Figure S2, the  $F$  distributions of intergroup differences were similar among the three datasets, and the dataset using 19 and 27 was more statistically significant in the middle cingulate cortex (MCC) than that using 7 voxels. Based on the above evidences, we chose the ReHo of 27 neighboring voxels as the functional metric in the following analyses.

**3.3. ReHo Alterations in the Blind.** Compared with the sighted subjects ( $P < 0.05$ , corrected at the cluster level), the blind subjects generally had significantly increased ReHo in the primary and higher visual pathways, including the left fusiform gyrus (FG), left superior parietal lobule (SPL), left parietooccipital sulcus (POS), right calcarine sulcus (CalS), right middle occipital gyrus (MOG), and right superior of occipital gyrus (SOG), and decreased ReHo in the sensorimotor and salience networks, including the bilateral putamen, middle cingulate cortex (MCC), bilateral anterior insula (aINS), and bilateral temporal pole (TP). In the left FG, the CB demonstrated increased ReHo compared to EB, LB, and SC. Within the blind subjects, the CB exhibited lower ReHo in the left SPL and MCC than the LB and lower ReHo in the bilateral putamen, right aINS, and right TP than the EB (Figure 1).

**3.4. GMV Alterations in the Blind.** A voxel-wise ANOVA indicated that the intergroup difference in GMV was mainly located in the visual and sensorimotor cortices ( $P < 0.05$ , corrected at the cluster level). Specifically, decreased GMV of the blind was identified in the primary and higher visual pathways relative to the SC, including the bilateral CalS, cuneus, lingual gyrus, FG, and SOG, and right intraparietal area. Furthermore, the older the age of onset of blindness is, the broader the atrophy of the visual cortex could be identified. Increased GMV was also identified in the right postcentral gyrus (PostCG) and precuneus (PreCu) of the EB, the left superior frontal gyrus (SFG) of the CB and EB, and the precentral gyrus (PreCG), medial prefrontal cortex (MPFC), and paracentral gyrus (ParaCG) of all blind groups. Within the blind subjects, the CB and EB generally had higher GMV in the visual associate areas compared with the LB. The EB had higher GMV than the CB and LB in the right PostCG, and the CB had higher GMV than the LB in the left SFG (Figure 2).

**3.5. Correlation Analyses.** Partial correlation analyses indicated that the age of onset of blindness was negatively correlated with the ReHo of the left FG but positively correlated with the MCC ( $P < 0.05$ , uncorrected) (Figure 3); moreover, the age of onset of blindness was negatively correlated with the GMV of the bilateral CalS, bilateral FG, and right IPL ( $P < 0.05$ , uncorrected) (Figure 4). In the brain regions that exhibited intergroup differences in ReHo, significant negative correlations between the ReHo and GMV values were identified in the left POS, left SPL, right CalS, right MOG, right TP, and bilateral aINS ( $P < 0.05$ , uncorrected) (Figure 5).

## 4. Discussion

In this study, we identified system-dependent inverse alterations in the regional spontaneous brain activity and gray matter volume in blind individuals: in the primary and higher visual areas, increased ReHo and decreased GMV were identified in the blind subjects, whereas in the sensorimotor related areas, decreased ReHo and increased GMV were identified. Furthermore, significant negative correlations between the ReHo and GMV values were identified in most brain regions with altered ReHo in the blind. Finally, the age of onset of blindness had different effects on the alteration of brain function and structure. Our findings provided additional information regarding the alteration patterns of the regional spontaneous brain activity and their structural bases after visual deprivation at different developmental stages.

**4.1. System-Dependent Alteration of the Regional Spontaneous Brain Activity and Structure in Blind Individuals.** The pattern of increased ReHo of the visual cortex in the CB/EB was similar to a recent study of our groups [25]. We also identified decreased GMV in the visual cortex. Combined with earlier findings of increased baseline glucose metabolism [7–9] and cortical thickness [8, 15] in the early occipital areas in this population, a potential relationship may exist between the alterations in functional and structural organizations in the deprived visual cortex. The first possible explanation is that the increased ReHo of the CB in the visual cortex reflects the retention of exuberant connections within the occipital cortex that resulted from developmental interruption. The development of the human visual cortex is characterized by an initial overproduction of synaptic connections with a maximum synaptic density at approximately 8 months, followed by the pruning of inactive synapses to reach “adult” levels at approximately 11 years [29]. Although the first phase of synaptogenesis is independent of retinal input [30], synaptic pruning is driven by visual experience [31]. Therefore, the exuberant connections caused by failed refinement can partially explain the increased ReHo, metabolism, and cortical thickness in the visual cortex. However, the “pruning interruption” hypothesis cannot solely explain the findings that a large number of concurrent reports have demonstrated that early deprived visual areas are involved in the cross-modal processing of tactile [1, 2, 32], auditory [3–5], and even olfactory tasks [6]. Thus, other mechanisms, including the establishment of new connections (rewiring theory) or

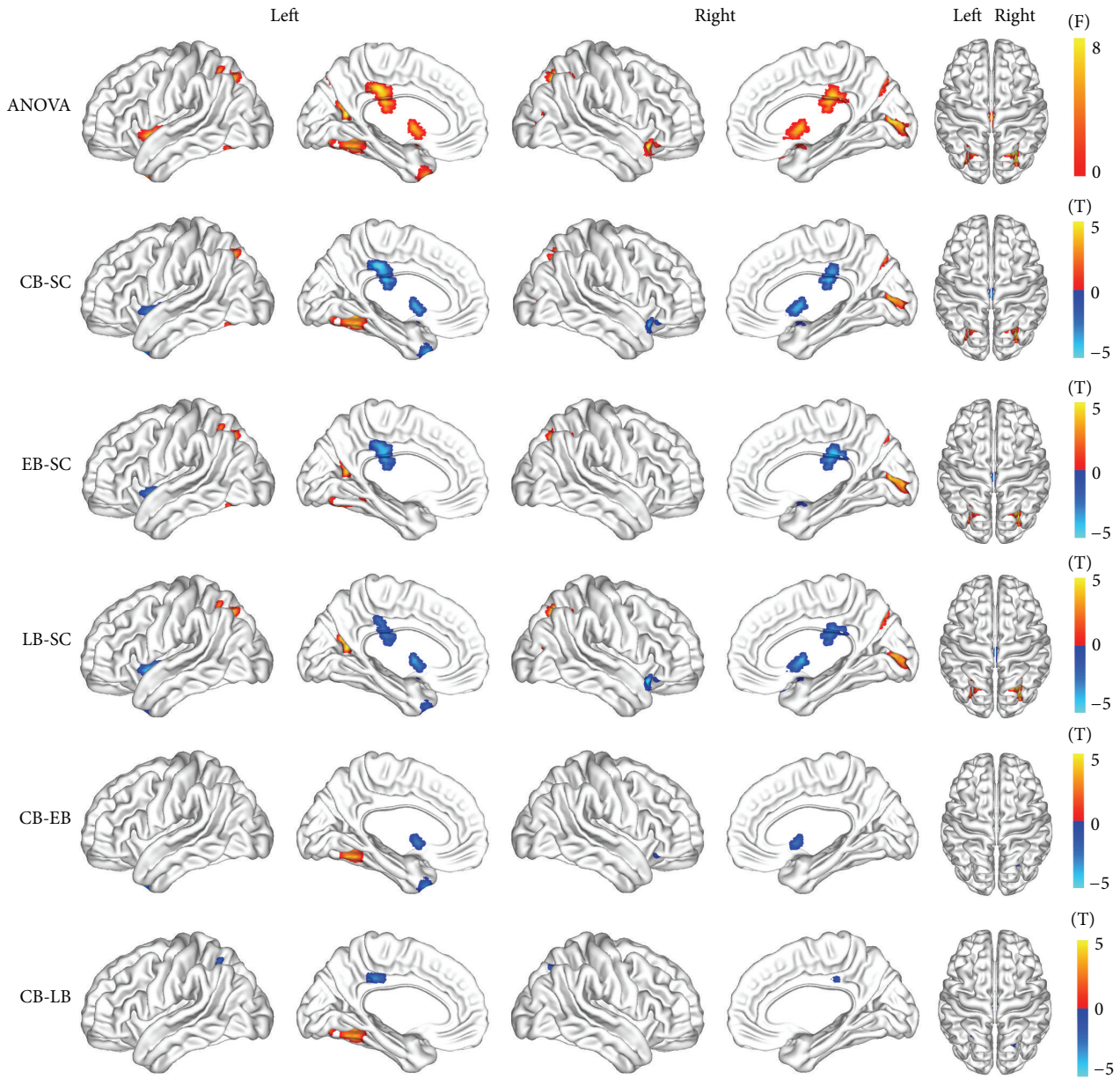


FIGURE 1: Brain regions with altered regional homogeneity in blind individuals. One-way analysis of variance was used for intergroup comparison, which was controlled for age and gender effects ( $P < 0.05$ , corrected using Monte Carlo simulation).

reinforcement of existing connections (unmasking theory) [8], may also contribute to the increased regional brain activity in the CB/EB. Finally, decreased GMV was identified in the visual cortex in the CB/EB, which is consistent with previous reports [16, 33]. In several earlier studies, thickened cortical thickness [3, 8, 14, 15, 33] and reduced cortical surface area [14, 33] were found in the occipital cortex of the CB and EB. Because the GMV is determined by both cortical thickness and cortical surface area, the reduced GMV in the visual cortex in the CB and EB might be caused by overly reduced surface area after visual deprivation, which masks the enhancing effect caused by cortical thickness. Thus, the increased ReHo might also represent a compensation for disuse-induced atrophy of the surface area of visual cortex.

Similar to the CB/EB, we also identified significantly increased ReHo of the visual cortex in the LB. To our knowledge, this is the first study to focus on the regional spontaneous brain activity in late blind subjects. This finding was consistent, in part, with a recent study that demonstrated increased functional connectivity density along the dorsal and ventral visual pathways in the LB [18]. In contrast to the CB/EB, the LB demonstrated different brain alteration patterns, including weaker cross-modal activity [4, 12, 13], higher baseline glucose metabolism [9], and thinner cortical thickness of the visual cortex [8, 14, 15]. Thus, although the LB and the CB/EB had similar increases in ReHo in the visual cortex, they might represent different neural mechanisms. The connections of visual cortex have already finished normal

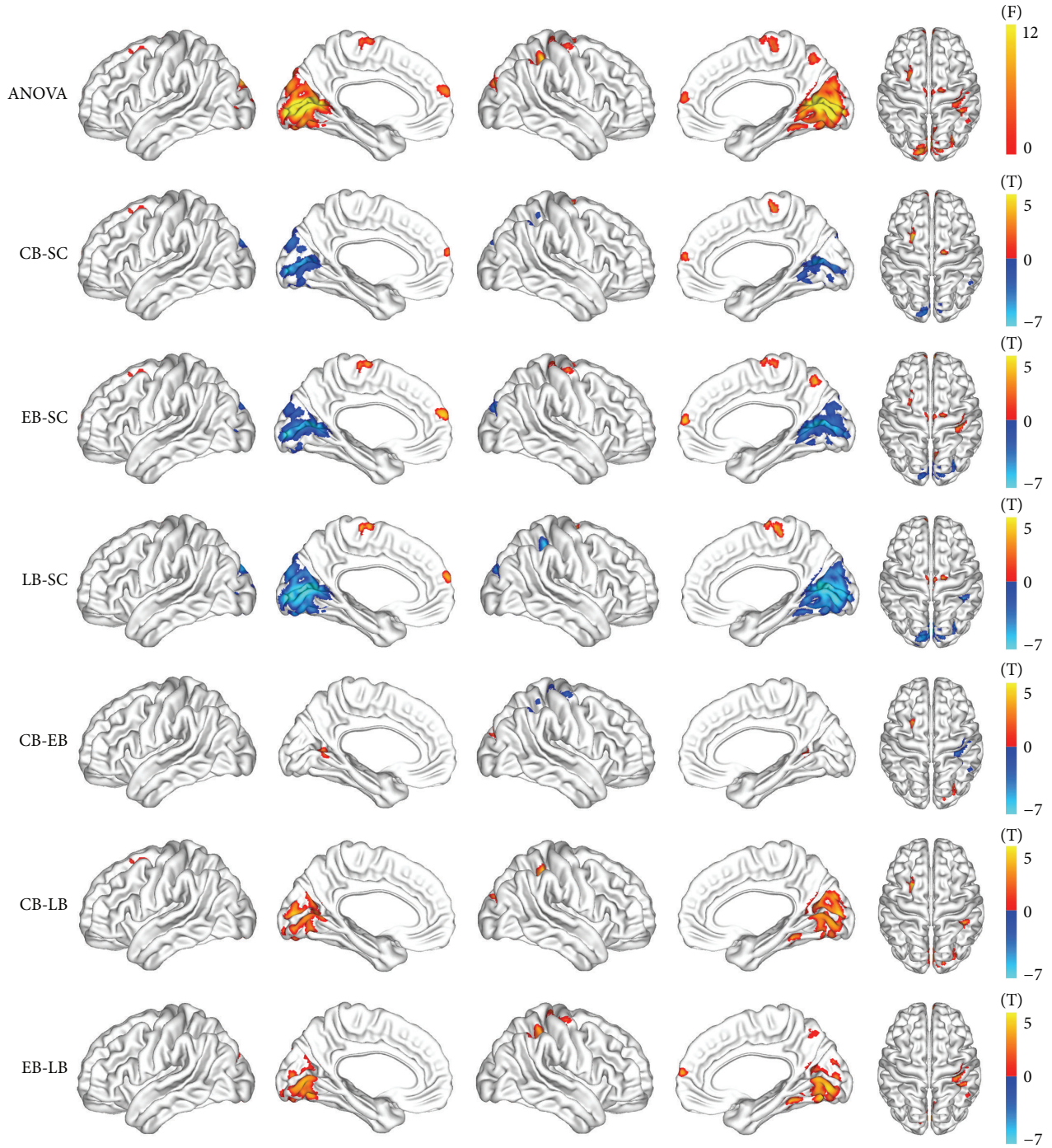


FIGURE 2: Brain regions with altered gray matter volume in blind individuals. One-way analysis of variance was used for intergroup comparison, which was controlled for age and gender effects ( $P < 0.05$ , corrected using Monte Carlo simulation).

refinement for visual processing prior to visual deprivation in the LB, so developmental factors, such as “rewiring” or “pruning interruption,” are not possible in them. Thus, the increased ReHo in the LB highly indicates the synthetic influence of plastic and degenerative factors. The plastic factor strengthened the existing intra- and intercortical connections of the occipital cortex, whereas the degenerative factor destroyed the existing connections. These synthetic

effects can explain why increased cross-modal activation [4, 34] and functional synchronization [18] are accompanied by damaged gray and white matter structures of the visual cortex in the LB [16, 17].

It should be noted that we identified an increased ReHo in the primary visual cortex in all blind subjects, whereas most previous studies have demonstrated a decreased FC (functional connectivity) of the same area [11, 12]. This

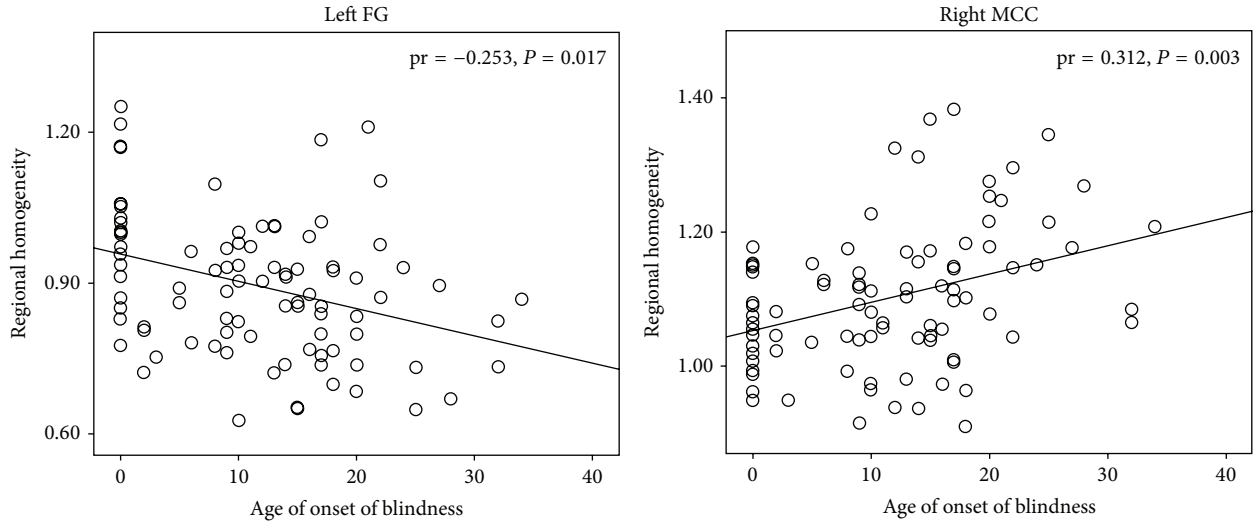


FIGURE 3: Correlation between the regional homogeneity (ReHo) and age of onset of blindness. Partial correlation analysis was performed, which was controlled for age and gender effects ( $P < 0.05$ , uncorrected). FG: fusiform gyrus; MCC: middle cingulate cortex.

disparity may be caused by the different roles of the ReHo and functional connectivity in delineating the intrinsic functional organization: ReHo specifically reflects the synergistic action of neighboring clustered neurons, whereas FC represents the intrinsic functional synchronization of the visual cortex with remote areas, such as the sensorimotor and auditory cortices. The increased ReHo in the early visual cortex and decreased FC (or FCD) between the early visual and nonvisual sensory cortices suggest that local efficiency of the early visual cortex may be strengthened to compensate for a decreased long-range transfer efficiency between visual and other sensory modalities.

With the exception of the increased ReHo in the visual cortex in the blind, we also identified decreased ReHo in the putamen and MCC, which are ascribed to the sensorimotor network (SMN). In contrast, increased GMV was also identified in the SMN (including the PostCG, PreCG, and ParaCG). The increased GMV in the SMN was consistent with previous studies that demonstrated increased white matter volume [35] in the sensorimotor system of the EB and increased white matter integrity of corticospinal tracts in both CB and LB [17]. The MCC exhibits extensive FC with brain regions that belongs to the SMN and has direct connections with the spinal cord [36], which is consistent with its function for motor and pain processes [37]. The putamen is an important hub in the complex extrapyramidal motor system. It receives inputs from many cortical areas and subcortical nuclei and principally projects to the prefrontal, premotor, and supplementary motor areas. It plays roles in motor planning, initiation, and regulation [38]. The loss of sight in the blind may require more sensorimotor and motor practice, such as Braille reading, spatial localization, and object recognition, which might induce the plasticity of the SMN, as indicated by increased GMV, white matter volume [35], and white matter integrity [17] in related structures. Thus, the decreased ReHo in the MCC and putamen may be

related to experience-dependent plasticity by extensive use of the limbs in the blind.

We also identified decreased ReHo in the anterior insula and temporal pole, which are ascribed to the salience network (SN). As a core hub of the salience network, the anterior insula serves to identify most relevant and salient stimuli from visual, auditory, and other sensory inputs and then initiates control signals to the central executive network that mediate attention, working memory, and other higher order cognitive processes while it disengages the default mode network [39]. The loss of sight makes blind subjects depend more on nonvisual inputs to efficiently interact with the environment. It is interesting to note that Wang et al. recently reported an increase in FC within the salience network and between the salience and frontoparietal networks in the CB [40]. In the present study, we also identified the alteration of the regional spontaneous brain activity within the salience network. The alteration of regional brain activity and FC in the salience network might reflect enhanced attentional ability to identify salient stimuli from the auditory, tactile, and other sensory inputs. Superior attentional performance has been reported in the CB/EB [41–43]. However, the functional roles of decreased ReHo of the salience network, the relationships between increased FC and decreased ReHo, and the relationships between spontaneous functional alteration and task-evoked activation of this network require future clarification.

**4.2. Inverse Association between Regional Spontaneous Brain Activity and Gray Matter Volume in the Blind.** One of the main findings of the present study is an inverse relationship between the alterations of ReHo and GMV in blind individuals: the increases in ReHo were accompanied by decreases in GMV of visual areas, and the decrease in ReHo was accompanied by an increase in GMV of the SMN. Furthermore, negative correlations between the ReHo and

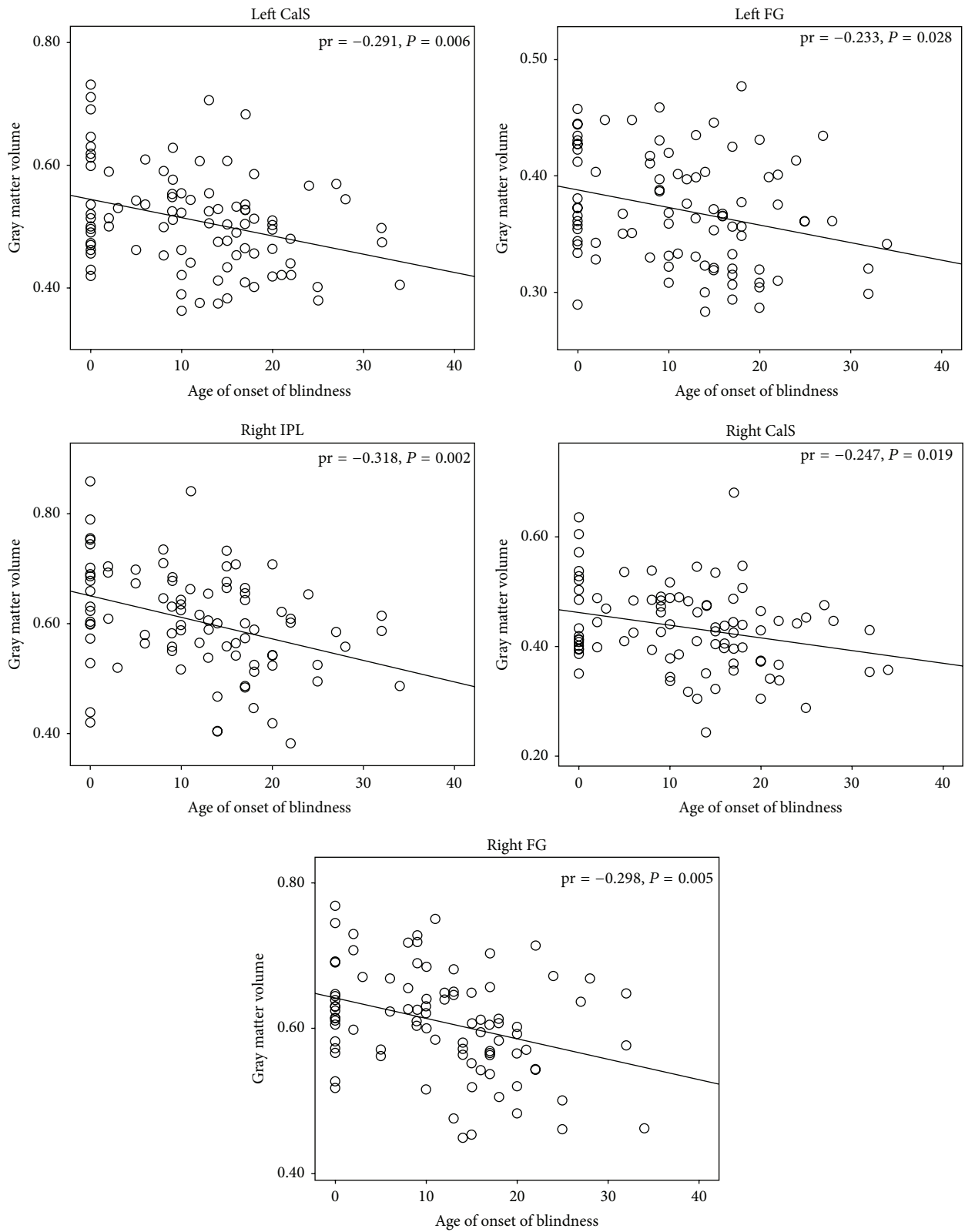


FIGURE 4: Correlation between the gray matter volume (GMV) and age of onset of blindness. Partial correlation analysis was performed, which was controlled for age and gender effects ( $P < 0.05$ , uncorrected). CalS: calcarine sulcus; FG: fusiform gyrus; IPL: inferior parietal lobe.

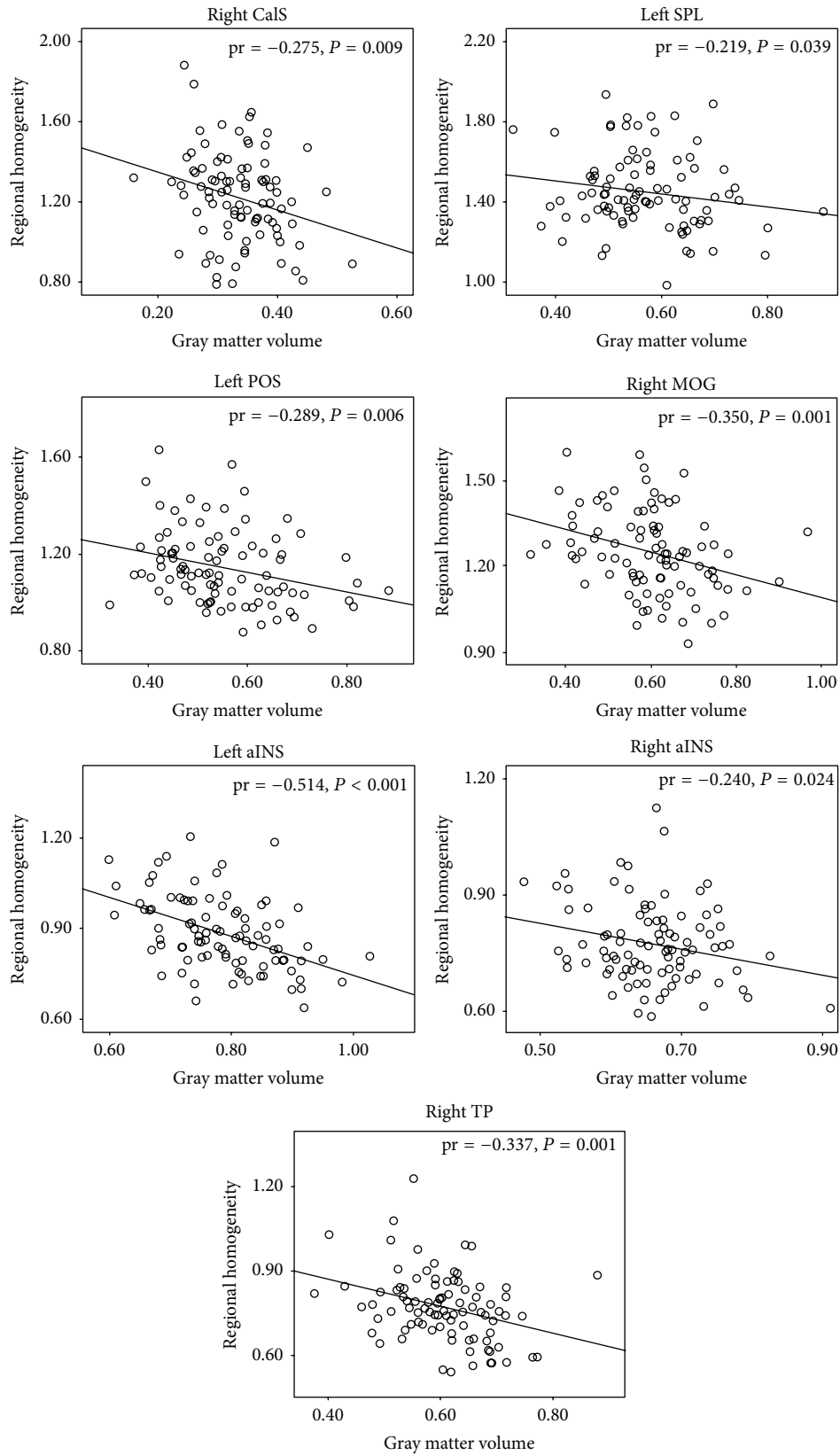


FIGURE 5: Correlation between the regional homogeneity (ReHo) and gray matter volume (GMV) in blind individuals. Partial correlation analysis was performed, which was controlled for age and gender effects ( $P < 0.05$ , uncorrected). aINS: anterior insula; CalS: calcarine sulcus; MOG: middle occipital gyrus; POS: parietooccipital sulcus; SPL: superior parietal lobule; TP: temporal pole.

GMV were identified in these visual and SMN areas. This finding was in line with a recent study that demonstrated a negative correlation between the magnitude of activation and cortical thickness of the visual cortex in EB subjects [3]. The inverse relationships between the ReHo and GMV suggest a balance between the structural and functional alterations of the brain after visual deprivation. On one hand, visual loss directly induces structural impairment of both white matter [44–46] and gray matter [15, 45] in the visual cortex. The remaining neurons may be overloaded to process the information from other modalities, which leads to an increase in neuronal activity by nonvisual stimuli [4, 26] or internally top-down signals [1, 47], and the activity status of remnant visual neurons persists at the resting-state, as indicated by increased ReHo and baseline metabolisms [7–9]. On the other hand, to adapt to the external environment without visual signals, long-term visual loss indirectly drives the experience-dependent plasticity of nonvisual structures [17]. Thus, the decreased ReHo may reflect the increased efficiency in processing nonvisual signals in these regions, which require a smaller number of neurons or lower threshold to handle the same tasks. However, this assumption should be verified by introducing the behavior performance associations.

*4.3. Effects of Age of Onset of Blindness on the Regional Spontaneous Brain Activity and Gray Matter Volume.* In this study, we demonstrated that the age of onset of blindness had a complex influence on the ReHo values of the brain. Specifically, in the left FG, the CB had higher ReHo than the EB and the LB; in the SOG, TP, putamen, and MCC, the CB generally had lower ReHo than the blind individuals who lost sight at older ages. Furthermore, the age of onset of blindness was negatively correlated with the ReHo of the left FG but positively correlated with the MCC. These findings were partially consistent with previous studies that demonstrated different alteration patterns of brain in blind individuals with lost sight at different developmental stages, including the cross-modal activity [4, 12, 13], baseline glucose metabolism [9], cortical thickness [8, 15], gray matter content [16], anatomical connectivity [10], white matter integrity [17], and FCD [18]. Our findings indicate that visual experience plays an important role in reshaping the regional spontaneous brain activity. In the ventral visual stream (as demonstrated by the left FG), only the CB (but not the EB or LB) exhibited increased ReHo compared to the SC, which was supported by a recent study that identified stronger FCD in the ventral stream of the CB relative to the LB [18]. These findings indicate that visual experience during the sensitive period is critical to normal development of the synchronization of regional clustered neurons in the ventral stream [48]. In the dorsal visual stream (as revealed by right SOG), although all blind individuals exhibited increased ReHo compared with the SC, a lower amplitude of increment was identified in the blind individuals with earlier sight lost. This finding indicates that developmental factors may not be a major determinant in reshaping these areas, which is supported by studies that demonstrate the dorsal visual stream matures more earlier than the ventral one [49, 50]. Instead, experience-dependent

plasticity and degenerative factor may exert effects. Finally, in the nonvisual areas (such as the MCC and putamen), the CB exhibited a more extended decrement in ReHo than the EB and the LB compared with the SC. Because the development of these areas is independent of visual experience and, to our knowledge, there is no report of degenerative alterations of these areas after visual deprivation, experience-dependent plasticity may be the major factor that accounts for it. However, the functional roles of the alteration in regional brain activity remain unknown and require further clarification.

In contrast to the ReHo, the blind subjects who lost their sight at earlier developmental ages demonstrated a smaller GMV decrease in the visual areas. The interactions among developmental, plastic, and degenerative factors can also explain the alterations of GMV among different blind subgroups. Degenerative factors exert their effects on all blind subjects; thus, a common decreased GMV was identified in the visual areas, especially in the primary visual cortex [16, 44]. The developmental mechanisms play important roles in both the CB and EB, and the capacity for cross-modal plasticity is substantially stronger in the CB/EB than the LB; thus, “pruning interruption,” “rewiring,” and/or “unmasking” theories may take effect in the CB and EB, which can compensate for the degeneration-induced GMV reduction.

## 5. Conclusions

In summary, the present study demonstrated that the alterations of regional spontaneous brain activity and GMV are system-dependent, and an inverse association was identified between the regional spontaneous brain activity and GMV in blind individuals. Furthermore, the age of onset of blindness has different effects on the alteration of brain regional spontaneous brain activity and GMV. Our findings provided additional information regarding the alteration patterns of the spontaneous brain activity and their structural bases after visual deprivation at different developmental stages.

## Conflict of Interests

The authors declare that there is no conflict of interests regarding the publication of this paper.

## Authors' Contribution

Aili Jiang, Jing Tian, and Rui Li contributed equally to this work.

## Acknowledgments

The work was supported by the National Natural Science Foundation of China (Grants nos. 81401394, 91332113, 81271551, 81270020, 81271564, 90920015, and 81171423) and the National Basic Research Program of China (973 program, 2011CB707800).

## References

- [1] A. Amedi, N. Raz, P. Pianka, R. Malach, and E. Zohary, “Early ‘visual’ cortex activation correlates with superior verbal

- memory performance in the blind,” *Nature Neuroscience*, vol. 6, no. 7, pp. 758–766, 2003.
- [2] M. Ptito, I. Matteau, A. Z. Wang, O. B. Paulson, H. R. Siebner, and R. Kupers, “Crossmodal recruitment of the ventral visual stream in congenital blindness,” *Neural Plasticity*, vol. 2012, Article ID 304045, 9 pages, 2012.
  - [3] I. Anurova, L. A. Renier, A. G. de Volder, S. Carlson, and J. P. Rauschecker, “Relationship between cortical thickness and functional activation in the early blind,” *Cerebral Cortex*, 2014.
  - [4] O. Collignon, G. Dormal, G. Albouy et al., “Impact of blindness onset on the functional organization and the connectivity of the occipital cortex,” *Brain*, vol. 136, no. 9, pp. 2769–2783, 2013.
  - [5] P. Voss, F. Lepore, F. Gougoux, and R. J. Zatorre, “Relevance of spectral cues for auditory spatial processing in the occipital cortex of the blind,” *Frontiers in Psychology*, vol. 2, article 48, 2011.
  - [6] R. Kupers, M. Beaulieu-Lefebvre, F. C. Schneider et al., “Neural correlates of olfactory processing in congenital blindness,” *Neuropsychologia*, vol. 49, no. 7, pp. 2037–2044, 2011.
  - [7] A. G. De Volder, A. Bol, J. Blin et al., “Brain energy metabolism in early blind subjects: neural activity in the visual cortex,” *Brain Research*, vol. 750, no. 1-2, pp. 235–244, 1997.
  - [8] R. Kupers, P. Pietrini, E. Ricciardi, and M. Ptito, “The nature of consciousness in the visually deprived brain,” *Frontiers in Psychology*, vol. 2, article 19, 2011.
  - [9] C. Veraart, A. G. De Volder, M. C. Wanet-Defalque, A. Bol, C. Michel, and A. M. Goffinet, “Glucose utilization in human visual cortex is abnormally elevated in blindness of early onset but decreased in blindness of late onset,” *Brain Research*, vol. 510, no. 1, pp. 115–121, 1990.
  - [10] J. Li, Y. Liu, W. Qin et al., “Age of onset of blindness affects brain anatomical networks constructed using diffusion tensor tractography,” *Cerebral Cortex*, vol. 23, no. 3, pp. 542–551, 2013.
  - [11] W. Qin, Y. Liu, T. Jiang, and C. Yu, “The development of visual areas depends differently on visual experience,” *PLoS ONE*, vol. 8, no. 1, Article ID e53784, 2013.
  - [12] M. Bedny, T. Konkle, K. Pelphrey, R. Saxe, and A. Pascual-Leone, “Sensitive period for a multimodal response in human visual motion area MT/MST,” *Current Biology*, vol. 20, no. 21, pp. 1900–1906, 2010.
  - [13] H. Burton, R. J. Sinclair, and D. G. McLaren, “Cortical activity to vibrotactile stimulation: an fMRI study in blind and sighted individuals,” *Human Brain Mapping*, vol. 23, no. 4, pp. 210–228, 2004.
  - [14] J. Jiang, W. Zhu, F. Shi et al., “Thick visual cortex in the early blind,” *Journal of Neuroscience*, vol. 29, no. 7, pp. 2205–2211, 2009.
  - [15] P. Voss and R. J. Zatorre, “Occipital cortical thickness predicts performance on pitch and musical tasks in blind individuals,” *Cerebral Cortex*, vol. 22, no. 11, pp. 2455–2465, 2012.
  - [16] P. Voss, B. G. Pike, and R. J. Zatorre, “Evidence for both compensatory plastic and disuse atrophy-related neuroanatomical changes in the blind,” *Brain*, vol. 137, no. 4, pp. 1224–1240, 2014.
  - [17] D. Wang, W. Qin, Y. Liu, Y. Zhang, T. Jiang, and C. Yu, “Altered white matter integrity in the congenital and late blind people,” *Neural Plasticity*, vol. 2013, Article ID 128236, 8 pages, 2013.
  - [18] W. Qin, Y. Xuan, Y. Liu, T. Jiang, and C. Yu, “Functional connectivity density in congenitally and late blind subjects,” *Cerebral Cortex*, 2014.
  - [19] P. Voss, “Sensitive and critical periods in visual sensory deprivation,” *Frontiers in Psychology*, vol. 4, article 664, 2013.
  - [20] M. D. Fox and M. E. Raichle, “Spontaneous fluctuations in brain activity observed with functional magnetic resonance imaging,” *Nature Reviews Neuroscience*, vol. 8, no. 9, pp. 700–711, 2007.
  - [21] Y. Zang, T. Jiang, Y. Lu, Y. He, and L. Tian, “Regional homogeneity approach to fMRI data analysis,” *NeuroImage*, vol. 22, no. 1, pp. 394–400, 2004.
  - [22] J. S. Anderson, B. A. Zielinski, J. A. Nielsen, and M. A. Ferguson, “Complexity of low-frequency blood oxygen level-dependent fluctuations covaries with local connectivity,” *Human Brain Mapping*, vol. 35, no. 4, pp. 1273–1283, 2014.
  - [23] A. Yoshino, Y. Okamoto, Y. Kunisato et al., “Distinctive spontaneous regional neural activity in patients with somatoform pain disorder: a preliminary resting-state fMRI study,” *Psychiatry Research—Neuroimaging*, vol. 221, no. 3, pp. 246–248, 2014.
  - [24] L. Cocchi, I. E. Bramati, A. Zalesky et al., “Altered functional brain connectivity in a non-clinical sample of young adults with attention-deficit/hyperactivity disorder,” *Journal of Neuroscience*, vol. 32, no. 49, pp. 17753–17767, 2012.
  - [25] C. Liu, Y. Liu, W. Li et al., “Increased regional homogeneity of blood oxygen level-dependent signals in occipital cortex of early blind individuals,” *NeuroReport*, vol. 22, no. 4, pp. 190–194, 2011.
  - [26] M. Bedny, A. Pascual-Leone, S. Dravida, and R. Saxe, “A sensitive period for language in the visual cortex: distinct patterns of plasticity in congenitally versus late blind adults,” *Brain and Language*, vol. 122, no. 3, pp. 162–170, 2012.
  - [27] Standardization Administration of the People’s Republic of China, *Standard for Logarithmic Visual Acuity Charts*, vol. GB 11533-2011, Standardization Administration of the People’s Republic of China, 2011.
  - [28] J. Ashburner, “A fast diffeomorphic image registration algorithm,” *NeuroImage*, vol. 38, no. 1, pp. 95–113, 2007.
  - [29] L. J. Garey, “Structural development of the visual system of man,” *Human Neurobiology*, vol. 3, no. 2, pp. 75–80, 1984.
  - [30] J.-P. Bourgeois, “Synaptogenesis in the occipital cortex of macaque monkey devoid of retinal input from early embryonic stages,” *European Journal of Neuroscience*, vol. 8, no. 5, pp. 942–950, 1996.
  - [31] M. P. Stryker and W. A. Harris, “Binocular impulse blockade prevents the formation of ocular dominance columns in cat visual cortex,” *Journal of Neuroscience*, vol. 6, no. 8, pp. 2117–2133, 1986.
  - [32] L. Gagnon, F. C. Schneider, H. R. Siebner, O. B. Paulson, R. Kupers, and M. Ptito, “Activation of the hippocampal complex during tactile maze solving in congenitally blind subjects,” *Neuropsychologia*, vol. 50, no. 7, pp. 1663–1671, 2012.
  - [33] H.-J. Park, J. D. Lee, E. Y. Kim et al., “Morphological alterations in the congenital blind based on the analysis of cortical thickness and surface area,” *NeuroImage*, vol. 47, no. 1, pp. 98–106, 2009.
  - [34] H. Burton, A. Z. Snyder, T. E. Conturo, E. Akbudak, J. M. Ollinger, and M. E. Raichle, “Adaptive changes in early and late blind: a fMRI study of Braille reading,” *Journal of Neurophysiology*, vol. 87, no. 1, pp. 589–607, 2002.
  - [35] U. Noppeney, K. J. Friston, J. Ashburner, R. Frackowiak, and C. J. Price, “Early visual deprivation induces structural plasticity in gray and white matter,” *Current Biology*, vol. 15, no. 13, pp. R488–R490, 2005.
  - [36] R. P. Dum and P. L. Strick, “The origin of corticospinal projections from the premotor areas in the frontal lobe,” *Journal of Neuroscience*, vol. 11, no. 3, pp. 667–689, 1991.

- [37] M. Beckmann, H. Johansen-Berg, and M. F. S. Rushworth, "Connectivity-based parcellation of human cingulate cortex and its relation to functional specialization," *Journal of Neuroscience*, vol. 29, no. 4, pp. 1175–1190, 2009.
- [38] M.-T. Herrero, C. Barcia, and J. M. Navarro, "Functional anatomy of thalamus and basal ganglia," *Child's Nervous System*, vol. 18, no. 8, pp. 386–404, 2002.
- [39] W. W. Seeley, V. Menon, A. F. Schatzberg et al., "Dissociable intrinsic connectivity networks for salience processing and executive control," *Journal of Neuroscience*, vol. 27, no. 9, pp. 2349–2356, 2007.
- [40] D. Wang, W. Qin, Y. Liu, Y. Zhang, T. Jiang, and C. Yu, "Altered resting-state network connectivity in congenital blind," *Human Brain Mapping*, vol. 35, no. 6, pp. 2573–2581, 2014.
- [41] B. Röder, W. Teder-Sälejärvi, A. Sterr, F. Rösler, S. A. Hillyard, and H. J. Neville, "Improved auditory spatial tuning in blind humans," *Nature*, vol. 400, no. 6740, pp. 162–166, 1999.
- [42] B. Forster, A. F. Eardley, and M. Eimer, "Altered tactile spatial attention in the early blind," *Brain Research*, vol. 1131, no. 1, pp. 149–154, 2007.
- [43] O. Collignon and A. G. de Volder, "Further evidence that congenitally blind participants react faster to auditory and tactile spatial targets," *Canadian Journal of Experimental Psychology*, vol. 63, no. 4, pp. 287–293, 2009.
- [44] M. Ptito, F. C. Schneider, O. B. Paulson, and R. Kupers, "Alterations of the visual pathways in congenital blindness," *Experimental Brain Research*, vol. 187, no. 1, pp. 41–49, 2008.
- [45] W.-J. Pan, G. Wu, C.-X. Li, F. Lin, J. Sun, and H. Lei, "Progressive atrophy in the optic pathway and visual cortex of early blind Chinese adults: a voxel-based morphometry magnetic resonance imaging study," *NeuroImage*, vol. 37, no. 1, pp. 212–220, 2007.
- [46] J. S. Shimony, H. Burton, A. A. Epstein, D. G. McLaren, S. W. Sun, and A. Z. Snyder, "Diffusion tensor imaging reveals white matter reorganization in early blind humans," *Cerebral Cortex*, vol. 16, no. 11, pp. 1653–1661, 2006.
- [47] A. A. Stevens, M. Snodgrass, D. Schwartz, and K. Weaver, "Preparatory activity in occipital cortex in early blind humans predicts auditory perceptual performance," *The Journal of Neuroscience*, vol. 27, no. 40, pp. 10734–10741, 2007.
- [48] E. M. Callaway and L. C. Katz, "Effects of binocular deprivation on the development of clustered horizontal connections in cat striate cortex," *Proceedings of the National Academy of Sciences of the United States of America*, vol. 88, no. 3, pp. 745–749, 1991.
- [49] I. Kovács, P. Kozma, Á. Fehér, and G. Benedek, "Late maturation of visual spatial integration in humans," *Proceedings of the National Academy of Sciences of the United States of America*, vol. 96, no. 21, pp. 12204–12209, 1999.
- [50] J. Wattam-Bell, D. Birtles, P. Nyström et al., "Reorganization of global form and motion processing during human visual development," *Current Biology*, vol. 20, no. 5, pp. 411–415, 2010.